AKADEMIA GÓRNICZO-HUTNICZA IM. STANISŁAWA STASZICA W KRAKOWIE

DZIEDZINA NAUK ŚCISŁYCH I PRZYRODNICZYCH

DYSCYPLINA NAUKI FIZYCZNE

ROZPRAWA DOKTORSKA

Metody spektroskopowe
w badaniach toksyczności nowotworów pierwotnych po implantacji
do mózgu szczura

Autor: Karolina Olbrich

Promotor rozprawy: dr hab. inż. Joanna Chwiej, prof. uczelni
Drugi promotor rozprawy: prof. dr hab. Zuzanna Setkowicz-Janeczko
Promotor pomocniczy: dr inż. Agnieszka Dróżdż

Praca wykonana: Akademia Górniczo-Hutnicza im. Stanisława Staszica w Krakowie,
Wydział Fizyki i Informatyki Stosowanej, Katedra Fizyki Medycznej i Biofizyki

Kraków, 2023

Oświadczenie autora rozprawy:

Oświadczam, świadomy(-a) odpowiedzialności karnej za poświadczenie nieprawdy, że niniejszą pracę doktorską wykonałem(-am) osobiście i samodzielnie i nie korzystałem(-am) ze źródeł innych niż wymienione w pracy.

data, podpis autora

Oświadczenie promotorów rozprawy:

Niniejsza rozprawa jest gotowa do oceny przez recenzentów.

data, podpis pierwszego promotora rozprawy

data, podpis drugiego promotora rozprawy

Rozprawa doktorska została zrealizowana w ramach Interdyscyplinarnych Środowiskowych Studiów Doktoranckich „Fizyczne, Chemiczne i Biofizyczne Podstawy Nowoczesnych Technologii i Inżynierii Materiałowej" (FCB) finansowanych z budżetu Programu Operacyjnego Wiedza Edukacja Rozwój (POWER), nr projektu POWR.03.02.00-00-I004/16, współfinansowanego ze środków Unii Europejskiej.

Pragnę złożyć serdeczne podziękowania Pani dr hab. inż. Joannie Chwiej, profesor uczelni, za możliwość rozpoczęcia interdyscyplinarnych studiów doktoranckich, opiekę naukową, chętne dzielenie się swoją ogromną wiedzą, zarówno naukową jak i życiową. Jestem Pani wdzięczna za czas poświęcony na planowanie badań oraz liczne dyskusje na temat ich rezultatów. Dziękuję za stałe motywowanie mnie, zrozumienie, otrzymaną od Pani życzliwość i wszystkie ciepłe słowa.

Chciałabym podziękować Pani prof. Zuzannie Setkowicz-Janeczko za umożliwienie mi podjęcia się interdyscyplinarnej tematyki studiów, wprowadzenie mnie do świata badań obejmujących pracę ze zwierzętami oraz czas poświęcony na przeprowadzenie kluczowego dla realizacji rozprawy eksperymentu implantacji. Dziękuję Pani za zaangażowanie w prowadzone badania, za wszystkie cenne uwagi dotyczące otrzymanych wyników oraz miłą atmosferę pracy.

Dziękuję serdecznie dr inż. Agnieszce Dróżdż za wszystkie istotne wskazówki dotyczące prowadzonych badań oraz ich wyników, rozmowy o nauce i o życiu oraz wsparcie.

Bardzo dziękuję Pani dr inż. Katarzynie Matusiak za pomoc w przygotowaniu próbek, szczerą życzliwość i uśmiech oraz miłą atmosferę pracy.

Serdecznie dziękuję Pani dr Beacie Ostachowicz oraz dr inż. Pawłowi Wróblowi za istotne sugestie, rozmowy oraz ogromną i życzliwą pomoc w przeprowadzeniu pomiarów.

Podziękowania kieruję również do dr Natalii Janik-Olchawy za zaangażowanie w hodowlę komórek wykorzystanych w prowadzonych badaniach, za wspólne przejście przez studia, spędzony razem czas oraz wsparcie.

Dziękuję mgr Kamilowi Kawoniowi za przeprowadzenie pomiarów oraz dyskusje dotyczące biologicznego aspektu uzyskanych wyników.

Pragnę wyrazić moją wdzięczność pracownikom linii FLUO synchrotronu KARA oraz linii XRF synchrotronu Elettra za przeprowadzenie pomiarów. W szczególności, chciałabym podziękować dr inż. Mateuszowi Czyżyckiemu za zaangażowanie w realizację badań oraz cenne uwagi i wskazówki.

Dziękuję również Pani mgr Małgorzacie Kaczyńskiej za pomoc w opiece nad zwierzętami.

Serdecznie dziękuję Panu dr hab. inż. Przemysławowi Wachniewowi, profesorowi uczelni, za możliwość wykorzystania mineralizatora do preparatyki próbek.

Dziękuję Agnieszce Treli-Makowej, Pauli Kasprzyk, Agnieszce Wochnik, Weronice Mazur, Paulinie Śliwie, Ani Ryś, Agnieszce Dołędze i Marzenie Rugieł – za liczne rozmowy, wsparcie oraz miłą atmosferę w murach Uczelni i nie tylko. Dziękuję również wszystkim pracownikom i doktorantom Katedry Fizyki Medycznej i Biofizyki, za okazywaną mi życzliwość i pomoc w trakcie realizacji studiów doktoranckich.

W tym miejscu chciałabym wspomnieć śp. dr Damiana Ryszawego, który do 2020 r. pełnił funkcję promotora pomocniczego mojej rozprawy i który swoim zaangażowaniem w hodowlę komórek przyczynił się do realizacji badań przedstawionych w pracy.

Chciałabym serdecznie podziękować mojej Rodzinie i Przyjaciołom, za szczere zainteresowanie prowadzonymi przeze mnie badaniami oraz dopingowanie mnie w ich realizacji.

Największe podziękowania składam mojemu Mężowi Marcinowi – bez Twojego zaangażowania ta praca by nie powstała. Dziękuję za ogromną cierpliwość, zrozumienie, wsparcie w chwilach zwątpienia, a przede wszystkim dziękuję za przejęcie większości obowiązków w opiece nad Kubusiem, co pozwoliło mi na przygotowanie rozprawy.

Synkowi – mojej największej Motywacji – abyś zawsze dążył do realizacji swoich marzeń.

Spis treści

Streszczenie 7
Abstract 9
Układ rozprawy 11
1. Wprowadzenie 13
2. Cele i zakres pracy 17
3. Materiały i metody 19
4. Streszczenia artykułów 21
5. Dyskusja 25
6. Podsumowanie 30
Literatura 32
Lista wystąpień konferencyjnych i seminaryjnych 37
Publikacje spoza rozprawy 37
Staże i naukowe wyjazdy zagraniczne 38
Oświadczenia współautorów publikacji oraz manuskryptów 39
Oryginalne wersje publikacji i manuskryptów stanowiących podstawę rozprawy 69

Streszczenie

Nowotwory złośliwe są drugą w kolejności przyczyną zgonów wśród kobiet i mężczyzn w Polsce, a ok. 5-10% z nich stanowią pierwotne guzy mózgu. Jednym z najbardziej agresywnych nowotworów ośrodkowego układu nerwowego, stanowiącym ok. 16% spośród wszystkich pierwotnych guzów mózgu, jest glejak wielopostaciowy (GBM, ang. *glioblastoma multiforme*). Mimo radykalnych procedur terapeutycznych, śmiertelność z powodu GBM jest wysoka, a mediana przeżycia pacjentów od momentu diagnozy wynosi nie więcej niż 2 lata. Dlatego podejmowanych jest wiele interdyscyplinarnych prac badawczych mających na celu lepsze poznanie natury glejaka oraz zdobycie nowej wiedzy na temat jego patogenezy, a ich realizacja często opiera się na wykorzystaniu modeli zwierzęcych nowotworu.

Głównym celem badań prowadzonych w ramach rozprawy doktorskiej była identyfikacja pierwiastków oraz makromolekuł biologicznych zaangażowanych w rozwój glejaka wielopostaciowego w zwierzęcych modelach tego schorzenia. Pierwszym etapem realizacji założonych celów rozprawy było przeprowadzenie eksperymentu polegającego na implantacji trzech różnych linii ludzkich komórek GBM do mózgów gryzoni. Materiał badawczy stanowiły mózgi pobrane od zwierząt, którym wszczepiono komórki glejaka. Kolejnym krokiem był wybór metody analitycznej, która pozwoliłaby na określenie składu pierwiastkowego całości materiału próbki, tj. półkul mózgu szczurów. Spośród dostępnych metod analizy pierwiastkowej próbek biologicznych wybrano spektroskopię fluorescencji rentgenowskiej z całkowitym odbiciem (TXRF, ang. *Total Reflection X-ray Fluorescence*). Poprzez wyznaczenie parametrów walidacyjnych tj. precyzja, poprawność oraz granice detekcji, a także na podstawie międzylaboratoryjnego porównania rezultatów przeprowadzonych analiz tkanek ssaków, podjęto próbę weryfikacji użyteczności analitycznej metody TXRF dla potrzeb oceny składu pierwiastkowego próbek biologicznych. Następnie, zastosowano metodę fluorescencji rentgenowskiej ze wzbudzeniem promieniowaniem synchrotronowym (SR-XRF, ang. *Synchrotron Radiation X-Ray Fluorescence*), która pozwoliła na uwidocznienie zmian w dystrybucji pierwiastków w badanych tkankach mózgu. Z kolei, anomalie w rozmieszczeniu oraz strukturze biomolekuł w tkankach zbadano wykorzystując mikrospektroskopię w podczerwieni z transformatą Fouriera (FTIR, ang. *Fourier Transform Infrared Spectroscopy*) oraz mikroskopię Ramana.

Wyniki przeprowadzonych badań potwierdziły wysoką użyteczność metody TXRF w analizie próbek pochodzenia biologicznego, przede wszystkim dla pierwiastków o wyższej liczbie atomowej. Badania przeprowadzone tą metodą pozwoliły wskazać pierwiastki potencjalnie zaangażowane w rozwój glejaka wielopostaciowego, a liczba obserwowanych anomalii w składzie pierwiastkowym próbek korelowała ze stopniem inwazyjności implantowanych do mózgu gryzoni komórek. Analiza topograficzna, wykonana z zastosowaniem metody SR-XRF, uwidoczniła rozbieżności w akumulacji pierwiastków w tkankach objętych rozwojem nowotworu oraz jego otoczeniu, a także niejednorodności w strukturze guza rozwiniętego w jednym z badanych modeli. Porównanie map rozmieszczenia pierwiastków z obrazami mikroskopowymi badanych tkanek pozwoliło na omówienie potencjalnych przyczyn obserwowanych anomalii w modelach zwierzęcych GBM, a w szczególności wskazać selen jako możliwy biomarker jego rozwoju. Analiza biochemiczna

tkanek, przeprowadzona z wykorzystaniem mikrospektroskopii FTIR i Ramana, wykazała obecność w mózgach szczurów lokalnych zmian w gromadzeniu biomolekuł spowodowanych rozwojem glejaka. W szczególności zaobserwowano, iż rejony dotknięte procesem nowotworzenia charakteryzują się zmniejszoną zawartością lipidów, kwasów nukleinowych oraz związków zawierających grupy karbonylowe, a także zmianami w zawartości i strukturze białek.

Podsumowując, w rozprawie doktorskiej, dzięki zastosowaniu metod spektroskopowych, możliwe było porównanie toksyczności glejaka wielopostaciowego rozwiniętego z różnych linii komórkowych. Otrzymane wyniki badań korelowały ze zmianami histologicznymi tkanek, powstałymi wskutek rozwoju nowotworu. Przeprowadzone analizy pozwoliły na wskazanie potencjalnych pierwiastkowych i molekularnych markerów toksyczności GBM.

Abstract

Tumors are the second leading cause of death among men and women and about 5-10% of them are primary brain tumors. One of the most aggressive central nervous system tumor, accounting for about 16% of all primary brain tumors, is glioblastoma multiforme (GBM). Despite radical therapies, mortality rate caused by GBM is high and the median survival of patients from diagnosis does not exceed 2 years. Therefore, many interdisciplinary researches are undertaken for better understanding the nature of glioblastoma as well as to get novel knowledge about its pathogenesis. These type of researches are often performed with the use of animal models.

The main purpose of the research performed in the frame of the doctoral dissertation was to identify the elements and biomolecules involved in the development of glioblastoma multiforme in the animal models of the disease. The first stage of the investigation was the implantation of three different human GBM cell lines into rat's brains. The next step was to choose an analytical tool for the determination of the elemental composition of the separate brain hemispheres taken from the rats subjected to implantation. From the various available methods of elemental analysis of biological samples, Total Reflection X-ray Fluorescence (TXRF) spectroscopy was selected. An attempt was made to verify the usefulness of the TXRF in the elemental analysis of biological samples. The investigation included the evaluation of selected validation parameters of performed measurements, i.e. precision, trueness and detection limits, as well as assessment of the inter-laboratory comparison of the results of the mammalian tissue samples analysis. Next, the method of Synchrotron Radiation based X-ray Fluorescence (SR-XRF) was used to examined changes in the distribution of elements in the rat brain tissues. In turn, anomalies in the accumulation and structure of biomolecules in the tissues were analysed using Fourier Transform Infrared Spectroscopy (FTIR) and Raman microscopy.

The obtained results confirmed the high usefulness of the TXRF method in the analysis of biological samples, especially for elements with a higher atomic number. The TXRF analysis of rat brain hemispheres allowed to indicate the elements, which potentially may be involved in the development of GBM, and the number of the observed anomalies correlated with the degree of aggressiveness of the cells used for implantation. Topographic analysis performed using the SR-XRF method, revealed changes in the accumulation of elements in the regions of the tumor and its surroundings. Analysis of the maps of elemental distribution within the examined tissues along with their microscopic evaluation allowed to discuss the potential causes of the observed elemental anomalies in the animal models of GBM. In particular, it was possible to indicate selenium as a possible biomarker of GBM development. Two-dimensional biochemical analysis performed using FTIR and Raman microspectroscopy, showed local changes in the accumulation of the main biological molecules in the rodents brains. The areas of the tissues affected by the tumor growth were characterized by a reduced content of the lipids, nucleic acids and compounds containing carbonyl groups, as well as changes in the level and structure of the proteins.

To conclude, in the frame of the doctoral dissertation, the various spectroscopic methods were used to examine the toxicity of the glioblastoma multiforme developed in the rodents

brains after implantation of human cells of the tumor. The results of elemental and biochemical analysis correlated with the histological changes of the tissues resulting from the GBM development. Furthermore, performed researches allowed to identify potential elemental and biomolecular markers of GBM toxicity.

Układ rozprawy

Rozprawę doktorską stanowi zbiór trzech publikacji podejmujących tematykę wykorzystania metod spektroskopowych dla potrzeb analizy pierwiastkowej próbek pochodzenia biologicznego [A1-A3], a w szczególności, dwa artykuły [A2,A3] opisują badania zmian pierwiastkowych zachodzących w tkance mózgowej szczura na skutek implantacji ludzkich komórek glejaka wielopostaciowego.

Do cyklu opublikowanych artykułów dołączono dwa manuskrypty, które w momencie złożenia pracy znajdują w recenzji w czasopismach Spectrochimica Acta B oraz Spectrochimica Acta A. W pierwszym opisano rezultaty międzylaboratoryjnego porównania wyników analizy pierwiastkowej próbek biologicznych [S1]. Drugi manuskrypt dotyczy zastosowania metod spektroskopii wibracyjnej dla potrzeb oceny zmian biomolekularnych będących skutkiem rozwoju GBM w mózgach gryzoni [S2].

A1 **Karolina Płaneta**, Aldona Kubala-Kukuś, Agnieszka Dróżdż, Katarzyna Matusiak, Zuzanna Setkowicz-Janeczko, Joanna Chwiej, *The assessment of the usability of selected instrumental techniques for the elemental analysis of biomedical samples,* Sci. Rep. 11: 3704 (2021); IF_{2021}=4.996, $MNiSW_{2021}$=140.

A2 **Karolina Płaneta**, Zuzanna Setkowicz, Natalia Janik-Olchawa, Katarzyna Matusiak, Damian Ryszawy, Agnieszka Dróżdż, Krzysztof Janeczko, Beata Ostachowicz, Joanna Chwiej, *Comparison of elemental anomalies following implantation of different cell lines of glioblastoma multiforme in the rat brain: a total reflection X‑ray fluorescence spectroscopy study,* ACS Chem. Neurosci. 11: 4447-4459 (2020); IF_{2021}=5.780, $MNiSW_{2021}$=100.

A3 **Karolina Płaneta**, Zuzanna Setkowicz, Mateusz Czyżycki, Natalia Janik-Olchawa, Damian Ryszawy, Krzysztof Janeczko, Rolf Simon, Tilo Baumbach, Joanna Chwiej, *Altered elemental distribution in male rat brain tissue as a predictor of glioblastoma multiforme growth — studies using SR-XRF microscopy,* Int. J. Mol. Sci. 23: 703 (2022); IF_{2021}=6.208, $MNiSW_{2021}$=140.

S1 **Karolina Olbrich**, Aldona Kubala-Kukuś, Eva Margui, Ramon Fernández Ruiz, Katarzyna Matusiak, Jolanta Wudarczyk-Mocko, Paweł Wróbel, Zuzanna Setkowicz, Joanna Chwiej, *The first total reflection X-ray fluorescence round-robin test of mammalian tissue samples: preliminary results,* (w recenzji w Spectrochimica Acta B); IF_{2021}=3.662, $MNiSW_{2021}$=100.

S2 **Karolina Olbrich**, Zuzanna Setkowicz, Kamil Kawon, Mateusz Czyzycki, Natalia Janik-Olchawa, Ilaria Carlomagno, Giuliana Aquilanti, Joanna Chwiej, *Vibrational spectroscopy methods for investigation of the animal models of glioblastoma multiforme,* (w recenzji w Spectrochimica Acta A); IF_{2021}=4.831, $MNiSW_{2021}$=140.

1. Wprowadzenie

Nowotwory stanowią drugą najczęstszą przyczynę śmierci w Polsce i odpowiadają za 21,8% zgonów wśród mężczyzn i 20% zgonów kobiet [1]. Współczynnik śmiertelności spowodowany chorobami nowotworowymi w Polsce jest jednym z najwyższych w Europie, o 15% wyższy od średniej europejskiej [2]. Według Krajowego Rejestru Nowotworów, w 2025 r. przewidywany jest ok. 1,5 krotny wzrost liczby zgonów spowodowanych chorobami nowotworowymi w porównaniu do 2006 r. [3]. Wśród osób dotkniętych chorobą nowotworową 2% cierpi na pierwotne, tzn. powstałe *de novo* w tkance, guzy mózgu. Jednymi z najczęstszych pierwotnych guzów mózgu są glejaki, które rozwinęły się z komórek glejowych - nieneuronalnych komórek wspierających funkcje neuronów. Najlepiej opisanym i najbardziej agresywnym wśród glejaków jest glejak wielopostaciowy (GBM, ang. *glioblastoma multiforme*), stanowiący ok. 54% wszystkich przypadków glejaka i 16% wszystkich guzów mózgu. GBM jest klasyfikowany przez Światową Organizację Zdrowia do nowotworów o IV, najwyższym, stopniu złośliwości [4].

Glejak wielopostaciowy jest nowotworem heterogennym, co oznacza że jego obraz makroskopowy nie jest jednorodny. W różnych obszarach tego samego nowotworu obserwowane jest duże zróżnicowanie komórek oraz ich atypia. Na złożony charakter GBM wpływa także obecność ognisk martwiczych i krwotocznych w obrębie tej samej masy guza. Charakterystycznymi cechami glejaka wielopostaciowego są również naciekający, gwałtowny wzrost, bogate unaczynienie oraz niekontrolowana zdolność do proliferacji komórek [5,6]. Wszystkie te cechy składają się na obraz nowotworu o wysokiej inwazyjności i niepomyślnym rokowaniu. Mediana przeżycia po rozpoznaniu GBM wynosi kilkanaście miesięcy, a mniej niż 10% pacjentów przeżywa 5 lat [7].

Obecnie, standardowe leczenie chorych na GBM opiera się na resekcji chirurgicznej, z maksymalnym oszczędzeniem tkanki otaczającej guz, po której wdrażana jest radioterapia oraz chemioterapia. Należy jednak mieć na uwadze, iż specyficzna lokalizacja oraz naciekający charakter guza uniemożliwiają jego całkowite usunięcie i utrudniają precyzyjne przeprowadzenie radioterapii. Ponadto, złożona struktura GBM oraz jego właściwości lekooporne zmniejszają skuteczność leczenia. Dlatego też, pomimo zastosowanego leczenia, nie obserwuje się istotnej poprawy w przeżywalności pacjentów [8]. Celem pracy wielu grup badawczych jest pogłębienie wiedzy na temat etiologii glejaka wielopostaciowego oraz opracowanie nowych, efektywnych metod jego leczenia, skutkujących wydłużeniem długości i poprawą jakości życia pacjentów.

Istotną rolę, zarówno w badaniach przedklinicznych terapii przeciwnowotworowych, jak i tych ukierunkowanych na poznanie patogenezy glejaka wielopostaciowego, mają modele zwierzęce [9-11]. Pozwalają one na ocenę działania substancji potencjalnie terapeutycznych oraz wywoływanych przez nie skutków ubocznych w organizmach, które nie były wcześniej poddawane leczeniu. Do badania zmian morfologicznych, molekularnych czy pierwiastkowych zachodzących w tkankach objętych rozwojem nowotworu wykorzystywane są próbki pochodzenia ludzkiego, jednak w tym przypadku należy mieć na uwadze, iż otrzymane wyniki mogą być obarczone wpływem stosowanych u pacjentów terapii. Dlatego, również pod tym względem, materiał badawczy pozyskany z modeli zwierzęcych stanowi bardzo cenne źródło

informacji na temat patogenezy danego schorzenia.

Istnieje wiele modeli zwierzęcych glejaka wielopostaciowego, a jeden z szeroko stosowanych opiera się na wszczepieniu do mózgu zwierząt linii ludzkich komórek nowotworowych – tzw. model ortotopowego przeszczepu ksenogenicznego. Model ten wymaga wykorzystania zwierząt o upośledzonej odporności lub poddawanych działaniu środków immunosupresyjnych [12]. Implantowane mogą być konwencjonalne linie komórkowe GBM, pochodzące z banku hodowli komórkowych. Model ten jest łatwy do wygenerowania i przez długi czas stanowił złoty standard w badaniach nad glejakiem. Obecnie wskazuje się jego wiele ograniczeń, m.in. odstępstwa od linii oryginalnej, powstałe wskutek wykształcenia specyficznych fenotypów podczas adaptacji komórek do warunków panujących w danym laboratorium, brak reprezentacji heterogeniczności komórek GBM czy brak obecności mikrośrodowiska tkankowego nowotworu [13]. Istnieje również możliwość wszczepienia komórek nowotworowych bądź fragmentów nowotworu pobranych bezpośrednio od pacjenta z rozpoznanym glejakiem (PDX, ang. *orthotopic patient-derived xenografts*). Rozwiązanie to bardzo często pozwala na zachowanie genomu oraz komórkowej i histopatologicznej struktury oryginalnego nowotworu. Model PDX, w porównaniu do modeli bazujących na hodowlanych liniach GBM, uważany jest za bardziej użyteczny w badaniach odpowiedzi na testowane środki terapeutyczne i cieszy się zainteresowaniem przy opracowywaniu strategii w medycynie spersonalizowanej [14, 15]. Ze względu na wysoką niejednorodność glejaka wielopostaciowego, obserwowaną zarówno w obrębie tego samego nowotworu jak i między różnymi pacjentami, oraz modyfikacje w środowisku tkankowym konieczne do proliferacji komórek nowotworowych, nie można wskazać modelu zwierzęcego idealnie odzwierciedlającego procesy rozwoju GBM zachodzące u ludzi. Ponadto, prawidłowa analiza wyników badań prowadzonych z wykorzystaniem modeli zwierzęcych, np. testowania nowych terapii, wymaga znajomości anomalii wywołanych samym procesem rozwoju nowotworu, które mogą być charakterystyczne dla danego modelu. Dlatego też, konieczna wydaje się weryfikacja wykorzystywanych modeli zwierzęcych glejaka wielopostaciowego, w celu oceny ich przydatności dla potrzeb planowanych badań [16–18].

Z istniejącego piśmiennictwa wynika, że stany patologiczne organizmu, w tym procesy nowotworowe, mają swoje odzwierciedlenie w zaburzeniach składu pierwiastkowego oraz molekularnego tkanek. W szczególności, informacje na temat zawartości pierwiastków w tkance zmienionej chorobowo mogą służyć jako wskaźnik rozwoju nowotworu oraz stanowić czynnik prognostyczny pozwalający przewidzieć sukces zastosowanego leczenia [19–22]. Wskazuje się również na zależności pomiędzy stopniem złośliwości nowotworu a jego składem pierwiastkowym i biochemicznym [23–32]. Informacje na temat zaangażowania określonych pierwiastków w procesy powstawania i wzrostu nowotworu, mogą zostać wykorzystane przy opracowywaniu alternatywnych, wspomagających metod terapeutycznych [33, 34]. Istotny kierunek badań stanowi także poszukiwanie biomarkerów procesu nowotworzenia, pozwalających na odróżnienie tkanek zdrowych od tych zmienionych nowotworowo, które można byłoby zastosować dla potrzeb wsparcia stosowanych obecnie procedur diagnostycznych [35–40].

Potężnym narzędziem analitycznym, pozwalającym na przeprowadzanie analiz składu

pierwiastkowego oraz biochemicznego próbek biologicznych, są metody spektroskopowe. Ich podstawą jest generowanie i interpretacja widm powstałych w efekcie oddziaływania promieniowania elektromagnetycznego z materią próbki. W szerokiej grupie metod spektroskopowych wyróżnić można spektroskopię wibracyjną, gdzie oddziaływanie promieniowania ze składnikami próbki pozwala na generację i rejestrację widm oscylacyjnych, dostarczających informacji na temat grup funkcyjnych związków chemicznych obecnych w analizowanym materiale. Do metod spektroskopii wibracyjnej należy spektroskopia w podczerwieni (IR, ang. *infrared radiation*), u podstaw której leży absorpcja promieniowania podczerwonego przez cząsteczki wchodzące w skład próbki, a także spektroskopia Ramana, bazująca na zjawisku nieelastycznego rozproszenia promieniowania w wyniku jego interakcji z molekułami próbki. Metody te są wzajemnie komplementarne, co oznacza, że pasma oscylacyjne charakterystyczne dla danej grupy funkcyjnej mogą być widoczne w widmie IR, a niewidoczne w widmie Ramana i odwrotnie. Komplementarność obu metod realizowana jest także w różnicach pomiędzy intensywnościami rejestrowanych pasm oscylacyjnych. Analiza widm powstałych z wykorzystaniem metod spektroskopii wibracyjnej pozwala na identyfikację w próbce makromolekuł tj. białka, lipidy czy kwasy nukleinowe. Obecnie, w wyniku połączenia metod spektroskopii wibracyjnej z mikroskopią optyczną, bardzo popularnymi metodami analizy biochemicznej stały się mikrospektroskopia promieniowania podczerwonego z transformatą Fouriera (FTIR, ang. *Fourier Transform Infrared Spectroscopy*) oraz mikroskopia Ramana. Metody te umożliwiają analizę składu biochemicznego badanych tkanek przy jednoczesnej ocenie ich budowy na poziomie mikroskopowym. Wysoka rozdzielczość przestrzenna obu metod pozwala na prowadzanie pomiarów składu molekularnego w mikroobszarach próbki, co przekłada się na ich szerokie zastosowanie w badaniach próbek pochodzenia biologicznego.

W przypadku analizy składu pierwiastkowego próbek, szczególnym zainteresowaniem cieszy się spektroskopia fluorescencji rentgenowskiej, należąca do grupy metod spektroskopii emisyjnej. W wyniku wzbudzenia atomów próbki wiązką pierwotnego promieniowania X, dochodzi do emisji rentgenowskiego promieniowania charakterystycznego o energii specyficznej dla danego pierwiastka. Rejestracja tego promieniowania pozwala na identyfikację pierwiastków obecnych w badanej próbce. Jednym z wariantów spektroskopii fluorescencji rentgenowskiej jest metoda fluorescencji rentgenowskiej ze wzbudzeniem promieniowaniem synchrotronowym (SR-XRF, ang. *Synchrotron Radiation X-Ray Fluorescence*). Duża intensywność oraz naturalnie wysoka kolimacja promieniowania synchrotronowego, przy zastosowaniu nowoczesnych systemów ogniskowania promieniowania rentgenowskiego, pozwala, w tym przypadku, na dwuwymiarową analizę wielopierwiastkowa z bardzo dobrą rozdzielczością przestrzenną, sięgająca nawet części mikrometrów, przy zachowaniu wysokiej czułości analitycznej dla pierwiastków śladowych. Ponadto, procedura pomiarowa jest nieniszcząca oraz nie wymaga specjalnego przygotowania próbek. Dlatego też, metoda SR-XRF stanowi cenne narzędzie w badaniach dystrybucji i akumulacji pierwiastków w próbkach pochodzenia biologicznego.

Metodą fluorescencji rentgenowskiej, szeroko stosowaną do przeprowadzania analizy pierwiastkowej całości materiału próbki, jest spektroskopia fluorescencji rentgenowskiej z zastosowaniem całkowitego odbicia promieniowania X (TXRF, ang. *Total Reflection X-ray*

Fluorescence). Efektem wykorzystania geometrii całkowitego odbicia jest podwójne wzbudzenie próbki, a także znaczna poprawa granic wykrywalności analizowanych pierwiastków, wynikająca z redukcji rejestrowanego promieniowania rozproszonego. Metoda TXRF umożliwia przeprowadzanie analiz wielopierwiastkowych w krótkim czasie oraz dla niewielkiej ilości próbki koniecznej do wykonania oznaczeń. Ponadto, pozwala na bezpośrednie pomiary próbek ciekłych, które wymagają jedynie wysuszenia. Dodatkową zaletą metody jest nieskomplikowana procedura oznaczania ilościowego pierwiastków, opierająca się na metodzie dodatku wzorca wewnętrznego. Ze względu na te właściwości, metoda TXRF stała się w ostatnich latach bardzo popularna w badaniach składu pierwiastkowego próbek biologicznych.

Istotnym elementem związanym z wiarygodnością wyników przeprowadzanych analiz jest ich walidacja. Jest to proces polegający na wyznaczeniu wartości parametrów charakteryzujących efektywność i przydatność danej metody do określonych celów badawczych. Walidacja jest przeprowadzana w celu zapewnienia, że proces analizy jest rzetelny i dokładny. W literaturze najczęściej wyznaczanymi parametrami walidacyjnymi dla ilościowych analiz pierwiastkowych są poprawność i precyzja pomiaru, a także granice wykrywalności oznaczanych pierwiastków. Znajomość możliwości analitycznych stosowanych metod stanowi kluczowy element planowania procedur badawczych.

2. Cele i zakres pracy

Głównym celem badań prowadzonych w ramach rozprawy doktorskiej była **identyfikacja pierwiastków oraz makromolekuł biologicznych zaangażowanych w rozwój glejaka wielopostaciowego w modelach zwierzęcych nowotworu**. Dla potrzeb realizacji założonych celów wykorzystano nowoczesne metody spektroskopowe, a mianowicie metodę spektroskopii fluorescencji rentgenowskiej z całkowitym odbiciem, mikrofluorescencję rentgenowską ze wzbudzeniem promieniowaniem synchrotronowym, mikrospektroskopię w podczerwieni z transformatą Fouriera oraz mikroskopię Ramana.

Jako szczegółowe cele badawcze przyjęto:

1. Ocenę użyteczności wybranych metod analizy pierwiastkowej stosowanych w badaniach próbek pochodzenia biologicznego, w tym absorpcyjnej spektrometrii płomieniowej (F-AAS, ang. *flame atomic absorption spectrometry*) i bezpłomieniowej z zastosowaniem kuwety grafitowej (GF-AAS, ang. *graphite-furnance atomic absorption spectrometry*), atomowej spektrometrii emisyjnej ze wzbudzeniem w plazmie indukcyjnie sprzężonej (ICP-OES, ang. *inductively coupled plasma optical emission spectrometry*) oraz spektrometrii masowej ze wzbudzeniem w plazmie indukcyjnie sprzężonej (ICP-MS, ang. *inductively coupled plasma mass spectrometry*).

2. Weryfikację przydatności analitycznej metody TXRF dla potrzeb oceny składu pierwiastkowego próbek biologicznych na tle wyżej wymienionych metod.

3. Ewaluację zgodności wyników analizy pierwiastkowej tkanek pochodzenia zwierzęcego uzyskanych przez różne laboratoria przy użyciu komercyjnych spektrometrów TXRF.

4. Ocenę zmian w składzie pierwiastkowym półkul mózgu szczurów zachodzących w wyniku rozwoju glejaka wielopostaciowego z zastosowaniem metody TXRF.

5. Określenie lokalnych zmian w rozmieszczeniu pierwiastków w tkankach mózgowych szczurów wywołanych rozwojem glejaka wielopostaciowego z wykorzystaniem metody SR-XRF.

6. Ocenę anomalii w dystrybucji głównych makromolekuł biologicznych w mózgach szczurów wskutek rozwoju glejaka wielopostaciowego z zastosowaniem mikrospektroskopii FTIR i Ramana.

7. Weryfikację różnic w anomaliach pierwiastkowych i molekularnych obserwowanych w badanych modelach zwierzęcych glejaka wielopostaciowego.

Zakres rozprawy doktorskiej obejmuje:

1. Przegląd literatury dotyczącej zastosowania metod spektroskopowych do analizy pierwiastkowej próbek biologicznych oraz porównanie wartości parametrów walidacyjnych wyznaczonych dla przeprowadzanych przy ich użyciu analiz.

2. Udział w eksperymencie polegającym na implantacji komórek glejaka wielopostaciowego do mózgu szczurów.

3. Preparatykę pobranych narządów szczurzych w celu przeprowadzenia pomiarów.

4. Badania składu pierwiastkowego próbek (półkule mózgu szczurów, serce, nerka, śledziona, płuca) metodą TXRF.

5. Analiza dystrybucji pierwiastków w mózgu szczurów metodą SR-XRF.

6. Badania rozmieszczenia głównych makromolekuł biologicznych oraz zmian w strukturze białek w tkance mózgowej metodą mikrospektroskopii FTIR i Ramana.

7. Podsumowanie rezultatów międzylaboratoryjnego porównania wyników analiz składu pierwiastkowego próbek biologicznych przeprowadzonych metodą TXRF.

3. Materiały i metody

W badaniach prowadzonych w ramach rozprawy doktorskiej wykorzystano narządy pochodzące od męskich osobników szczurów Wistar albino. Hodowla zwierząt oraz wszystkie procedury z ich udziałem prowadzone były w Pracowni Neuropatologii Eksperymentalnej (wcześniej Zakład Neuroanatomii) Instytutu Zoologii i Badań Biomedycznych Uniwersytetu Jagiellońskiego. Procedury te zostały zaakceptowane przez II Lokalną Komisję Etyczną do Spraw Doświadczeń na Zwierzętach w Krakowie (zgody nr 121/2015 oraz nr 119/2016) oraz przeprowadzone zgodnie z międzynarodowymi standardami.

W części eksperymentalnej pracy A1 wykorzystano tkanki pochodzące od sześciu zwierząt stanowiących grupę kontrolną we wcześniej prowadzanych badaniach, dotyczących wpływu ekspozycji na nanocząstki tlenku żelaza na skład pierwiastkowy wybranych narządów [41]. Przedmiot analizy stanowiły narządy szczurze: tkanka mięśniowa, mózg, nerka, wątroba, serce oraz śledziona.

Dla potrzeb realizacji celów postawionych w pracach A2, A3 oraz S2 zanalizowano tkanki mózgu pobrane od szczurów wykorzystanych w eksperymencie dotyczącym toksyczności glejaka wielopostaciowego. Grupy oznaczone jako T, U oraz Pa[1] reprezentowały modele zwierzęce GBM, które opierały się na implantacji wybranych komórek nowotworu do mózgu szczura. Zwierzęta z grup T oraz U poddano implantacji komercyjnie dostępnych komórek linii T98g oraz U87mg, pochodzących z banku Amerykańskiej Kolekcji Hodowli Komórkowych (ATCC, ang. *American Type Culture Collection*, USA). Zwierzęta z grupy Pa zostały poddane implantacji komórek nowotworowych pobranych od pacjenta ze zdiagnozowanym pierwotnym glejakiem wielopostaciowym. Procedura izolacji ludzkich komórek glejaka wielopostaciowego została zaakceptowana przez Komisję Bioetyki ds. wykorzystania materiału komórkowego pobranego od pacjentów podczas zabiegów neuroonkologicznych (decyzja nr 535/2017 z dnia 13 czerwca 2017, wydana przez Komisję Bioetyczną przy Uniwersytecie Mikołaja Kopernika w Toruniu). W pracach A2, A3 oraz S2 wykorzystano również tkanki pobrane od zwierząt niepoddanych procedurze implantacji komórek nowotworowych, które stanowiły w przeprowadzonych eksperymentach grupę kontrolną N. Dodatkowo, w pracy A3 analizowano tkanki mózgu pobrane od zwierząt poddanych implantacji do mózgu pożywki hodowlanej (DMEM, ang. *Dulbecco's Modified Eagle Medium*), w której zawieszone były opisane wcześniej wszystkie rodzaje komórek nowotworowych (grupa M).

Materiał badawczy w pracy S1 stanowiły narządy szczurze (nerka, serce, śledziona, płuco) pobrane od zwierząt stanowiących grupę kontrolną N w eksperymencie dotyczącym toksyczności GBM.

Do zbadania składu pierwiastkowego narządów szczurzych w pracach A1, A2 oraz S1 wykorzystano spektroskopię TXRF. W celu przygotowania pobranych narządów do analizy tą metodą, poddano je mineralizacji mikrofalowej w kwasie azotowym V przy użyciu mineralizatora SpeedWave 4. Efektem procedury mineralizacji jest usunięcie organicznej matrycy próbki oraz jej rozpuszczenie. Pomiary, tak przygotowanych ciekłych próbek tkanek, przeprowadzono przy użyciu spektrometru Picofox^{TM} S2 (Bruker) w Laboratorium Metod

[1] W oryginalnej wersji publikacji A2 grupa zwierząt „Pa" oznaczona jest jako „P".

Rentgenowskich Instytutu Fizyki na Uniwersytecie Jana Kochanowskiego w Kielcach (praca A1) oraz spektrometru Nanohunter II (Rigaku) w Laboratorium Fluorescencji Rentgenowskiej na Wydziale Fizyki i Informatyki Stosowanej AGH w Krakowie (praca A2 oraz S1). Wynikiem przeprowadzonych pomiarów było oznaczenie stężeń fosforu, siarki, potasu, wapnia, żelaza, miedzi, cynku oraz selenu w analizowanych narządach szczurzych, tj. tkance mięśniowej, mózgu, nerce, wątrobie, sercu i śledzionie (praca A1), w lewych i prawych półkulach mózgu szczurów (praca A2) oraz w nerce, śledzionie, sercu i płucu (praca S1).

Metoda SR-XRF została zastosowana do przeprowadzenia topograficznej i ilościowej analizy pierwiastkowej mózgu szczurów. Do analizy wykorzystano suche skrawki tego narządu o grubości 20 μm, obejmujące obszar implantacji komórek GBM. Dwuwymiarowe obrazowanie rozmieszczenia fosforu, siarki, potasu, wapnia, żelaza, miedzi, cynku oraz selenu przeprowadzono na linii FLUO ośrodka synchrotronowego KARA (ang. *Karlsruhe Research Accelerator*) w KIT (ang. *Karlsruhe Institute of Technology*) w Karlsruhe (praca A3). Z kolei analizę dystrybucji pierwiastków lekkich, tj. sodu, magnezu, glinu oraz chloru przeprowadzono na linii XRF synchrotronu Elettra w Trieście (praca S2).

W celu zbadania zmian w zawartości głównych makromolekuł biologicznych, a także analizy różnic w strukturze drugorzędowej białek oraz zmian strukturalnych lipidów, zastosowano dwie komplementarne metody spektroskopii wibracyjnej: mikrospektroskopię FTIR oraz mikroskopię Ramana. Analizom poddano skrawki mózgu o grubości 8 μm, które pobrano z rejonu implantacji komórek nowotworowych, a następnie wysuszono w niskiej temperaturze. Pomiary metodą mikrospektroskopii FTIR przeprowadzono z użyciem mikroskopu Nicolet iN10 MX (Thermo Fisher Scientific), a pomiary ramanowskie z wykorzystaniem mikroskopu WITec Alpha 300R. Oba mikroskopy stanowią wyposażenie Laboratorium Biospektroskopii Atomowej i Molekularnej na Wydziale Fizyki i Informatyki Stosowanej AGH w Krakowie.

4. Streszczenia artykułów

A1: "The assessment of the usability of selected instrumental techniques for the elemental analysis of biomedical samples"

Celem pracy [A1] było omówienie wybranych metod analizy instrumentalnej (F-AAS, GF-AAS, ICP-OES i ICP-MS) pod względem ich przydatności w ilościowej analizie pierwiastkowej próbek pochodzenia biologicznego. W przeprowadzonym przeglądzie literaturowym skupiono się na uzyskiwanych wartościach parametrów walidacyjnych pomiarów, tj. precyzja (powtarzalność oraz precyzja pośrednia), poprawność oraz granice detekcji pierwiastków. Szczególną uwagę poświęcono również metodom przygotowania próbek biologicznych przed wykonaniem analiz. Na podstawie danych przedstawionych w analizowanych pracach naukowych, stwierdzono, że spośród omawianych technik analizy pierwiastkowej najwięcej możliwości analitycznych oferuje metoda ICP-MS. Pozwala ona na przeprowadzanie analiz wielopierwiastkowych, a ze względu na uzyskiwane bardzo niskie granice wykrywalności, umożliwia oznaczanie pierwiastków znajdujących się w próbkach na poziomie ultraśladowym. Ponadto, otrzymywane wartości precyzji i poprawności pomiarów przeprowadzanych metodą ICP-MS są w większości przypadków lepsze niż uzyskiwane dla innych technik analizy pierwiastkowej. Zastosowanie metody ICP-MS w badaniach próbek biologicznych wydaje się jednak ograniczone, ze względu na wysokie koszty aparatury oraz procedury pomiarowej.

W drugiej, eksperymentalnej części artykułu podjęto się oceny użyteczności metody TXRF dla potrzeb analizy składu pierwiastkowego próbek pochodzenia zwierzęcego – narządów szczurzych. Wyznaczono fizjologiczne wartości stężeń fosforu, siarki, potasu, wapnia, żelaza, miedzi, cynku oraz selenu w narządach szczurzych: wątrobie, nerce, próbce mięśnia, mózgu, sercu oraz śledzionie. Porównanie otrzymanych wyników z danymi literaturowymi wykazało dobrą zgodność dla pierwiastków o wyższej liczbie atomowej. Z kolei w przypadku pierwiastków lekkich obserwowano większe rozbieżności w wartościach zmierzonych stężeń, co mogło wynikać z zastosowanej preparatyki próbek. Na ocenę przydatności metody TXRF składało się również wyznaczenie precyzji i poprawności przeprowadzonych pomiarów, a także wartości granic detekcji analizowanych pierwiastków. Granice wykrywalności wynosiły od 0,0335 μg/g (selen) do 28,6 μg/g (fosfor). Powtarzalność wyników uzyskanych metodą TXRF była dla większości pierwiastków zadowalająca i nie przekraczała 6%. Wyjątek stanowiła precyzja oznaczenia zawartości fosforu i siarki, której wartości wynosiły odpowiednio 11,7% oraz 28%. Ostatnim z elementów procedury walidacyjnej metody TXRF było wyznaczenie poprawności przeprowadzonych pomiarów, co zrealizowano poprzez analizę zawartości pierwiastków w materiale referencyjnym pochodzenia biologicznego. Zmierzone wartości stężeń różniły się od ich wartości referencyjnych dla większości analizowanych pierwiastków. W szczególności, zaobserwowano zawyżenie zawartości potasu, wapnia, żelaza, miedzi oraz cynku oraz zaniżenie stężenia fosforu. Najlepszą zgodność pomiędzy wynikami otrzymano dla siarki oraz selenu.

S1 “The first total reflection X-ray fluorescence round-robin test of mammalian tissue samples: preliminary results”

Badania przedstawione w pracy [S1] stanowiły kolejny etap weryfikacji użyteczności metody TXRF w analizie próbek pochodzenia biologicznego i zostały przeprowadzone w ramach projektu ENFORCE TXRF (*European Network for Chemical Elemental Analysis by Total Reflection X-ray Fluorescence*) COST Action 18130 (*European Cooperation in Science and Technology*). Ich celem była ocena zmienności wyników analizy pierwiastkowej tych samych próbek (narządów szczurzych: nerka, serce, śledziona, płuco), uzyskanych przez cztery laboratoria wyposażone w różne, komercyjnie dostępne spektrometry TXRF. W laboratoriach przeprowadzono pomiary stężeń fosforu, siarki, potasu, wapnia, żelaza, miedzi, cynku i selenu w analizowanych próbkach, a także wyznaczono parametry walidacyjne: granice wykrywalności badanych pierwiastków, powtarzalność oraz precyzję pośrednią pomiarów. Aby zweryfikować zgodność wyników otrzymanych przez współpracujące laboratoria określono również precyzję międzylaboratoryjną. Ponadto, wyniki pomiarów składu pierwiastkowego wybranej próbki serca przeprowadzone metodą TXRF porównano z wynikami analiz z wykorzystaniem metod ICP-OES oraz ICP-MS, które przyjęto jako metody referencyjne.

Wyniki pracy [S1] potwierdziły przydatność metody TXRF w analizie pierwiastkowej tkanek zwierzęcych. Wartości stężeń pierwiastków o wyższych liczbach atomowych zmierzone przez współpracujące laboratoria były ze sobą zgodne, natomiast widoczne rozbieżności zaobserwowano w przypadku analizy zawartości pierwiastków lekkich. Wyznaczone granice wykrywalności wynosiły od 3,92 μg/g do 22,9 μg/g dla fosforu i od 0,0147 μg/g do 0,0352 μg/g dla selenu. Zgodnie z oczekiwaniami, pod względem badanych parametrów walidacyjnych, najlepsze wyniki uzyskano dla pierwiastków o wyższych liczbach atomowych. Przeprowadzone porównanie międzylaboratoryjne wykazało bardzo dobrą poprawność (około 100% dla żelaza, miedzi i cynku) i precyzję (powtarzalność <6%, precyzja pośrednia <12% i precyzja międzylaboratoryjna <12%) wyznaczenia stężeń tych pierwiastków, co może świadczyć o wysokiej przydatności metody TXRF w ich analizie w próbkach tkanek ssaków. Wskazano również potencjalne kierunki działań dla poprawy użyteczności metody w przypadku analizy pierwiastków lekkich, a mianowicie usprawnienie procesu preparatyki próbek w celu zmniejszenia efektu samoabsorpcji, optymalizację i/lub ujednolicenie procedur kalibracji oraz dekonwolucji widm w poszczególnych laboratoriach.

A2 “Comparison of elemental anomalies following implantation of different cell lines of glioblastoma multiforme in the rat brain: a total reflection X‑ray fluorescence spectroscopy study”

W pracy [A2] skoncentrowano się na ocenie zmian w składzie pierwiastkowym mózgu szczurów poddanych implantacji różnych komórek glejaka wielopostaciowego. Badaniom poddano tkanki mózgu pochodzące od zwierząt z grup N, T, Pa oraz U. Wykorzystując metodę TXRF wyznaczono stężenia fosforu, siarki, potasu, wapnia, żelaza, miedzi, cynku oraz selenu osobno dla półkuli lewej - implantowanej oraz prawej - nieimplantowanej. W celu stwierdzenia, czy obserwowane różnice między koncentracjami pierwiastków w półkulach są istotne statystycznie zastosowano test *U*-Manna Whitneya. Stopień inwazyjności wykorzystanych linii

komórkowych glejaka, określony na podstawie przeprowadzonej analizy mikroskopowej jako potencjał do rozwoju guza, różnił się między poszczególnymi grupami eksperymentalnymi i był najwyższy dla grupy U, a najniższy dla grupy T. Ilość obserwowanych anomalii pierwiastkowych korelowała ze stopniem agresywności badanych komórek GBM i była największa dla grupy U, gdzie zaobserwowano znaczący spadek stężenia fosforu, potasu i miedzi oraz wzrost stężenia selenu w implantowanej półkuli w porównaniu do lewej półkuli zwierząt z grupy kontrolnej. Większość zmian była specyficzna dla danego modelu GBM, natomiast, wspólną cechą dla wszystkich trzech grup zwierząt implantowanych był wzrost zawartości żelaza w prawych półkulach mózgu. Poziom tego pierwiastka był podwyższony również w lewych półkulach mózgów zwierząt z grup Pa oraz T. Cechą charakterystyczną dla poszczególnych grup eksperymentalnych była akumulacja selenu w półkulach implantowanych. Zawartość selenu zaobserwowana w grupach Pa i U była, odpowiednio, niższa i wyższa w porównaniu do analogicznej półkuli zwierząt kontrolnych. Natomiast w grupie T pierwiastek ten utrzymywał się na niezmienionym poziomie.

Dodatkowo, w celu oceny wiarygodności przeprowadzonych pomiarów wyznaczono parametry walidacyjne dla zastosowanej metody TXRF, tj. granice detekcji analizowanych pierwiastków a także powtarzalność oraz precyzję pośrednią. Otrzymane wartości analizowanych parametrów były zadowalające.

A3 “Altered elemental distribution in male rat brain tissue as a predictor of glioblastoma multiforme growth — studies using SR-XRF microscopy”

Motywacją do badań przedstawionych w pracy [A3] był fakt, iż rozmieszczenie pierwiastków w tkankach objętych rozwojem nowotworu może nie być jednorodne. Dlatego, do zbadania dystrybucji pierwiastków w mózgach szczurów, a także ilościowego oznaczenia gęstości powierzchniowych pierwiastków w wybranych rejonach badanych tkanek zastosowano metodę SR-XRF. Analizowano tkanki pochodzące od zwierząt z grup N, M, T, Pa oraz U. Zaobserwowane anomalie w dystrybucji pierwiastków były skorelowane ze zmianami w morfologii tkanek, które pojawiły się wskutek rozwoju nowotworu. Podobnie jak w przypadku wyników przedstawionych w pracy [A2], największe nieprawidłowości w rozmieszczeniu pierwiastków odnotowano dla grupy U. Zmiany nowotworowe, które rozwinęły się w mózgach zwierząt należących do tej grupy, charakteryzowała niejednorodna struktura, widoczna na obrazach mikroskopowych. W jej obrębie można było zidentyfikować rejon właściwy guza oraz jego obszar szczątkowy. Rejony te wykazywały różnice w stopniu akumulacji dla większości pierwiastków, a największe rozbieżności można było obserwować w przypadku rozmieszczenia wapnia oraz żelaza. Jedynym pierwiastkiem, który akumulował się w sposób jednorodny w zmianach rozwiniętych u zwierząt z grupy U był selen.

Analiza ilościowa oraz ocena statystyczna uzyskanych wyników pozwoliły na wskazanie pierwiastków, których akumulacja różni się znacząco pomiędzy rejonem glejaka a jego otoczeniem. Nowotwory które rozwinęły się w mózgach zwierząt z grup Pa oraz U charakteryzowały się zwiększoną akumulacją żelaza oraz selenu. W bezpośrednim otoczeniu zmian powstałych w wyniku implantacji komórek U87mg zaobserwowano zwiększone gromadzenie miedzi. Zauważono, iż anomalia w morfologii oraz dystrybucji pierwiastków w tkankach pobranych od szczurów z grupy T są zbliżone do zmian obserwowanych u zwierząt

poddanych administracji pożywki hodowlanej (grupa M) i prawdopodobnie mogą one wynikać z samego uszkodzenia tkanek, do jakiego może dochodzić podczas implantacji a nie rozwoju nowotworu. Dla obu tych grup eksperymentalnych, w rejonach odpowiadających miejscu implantacji, zaobserwowano zwiększoną akumulację żelaza oraz wapnia.

Na podstawie oceny zarówno rozmieszczenia pierwiastków jak uzyskanych wyników analizy ilościowej wysunięto wniosek, iż selen mógłby być potencjalnym, pierwiastkowym markerem rozwoju glejaka wielopostaciowego w badanych modelach zwierzęcych.

S2 "Application of vibrational spectroscopy methods in the investigation of animal models of glioblastoma multiforme"

Badania w pracy [S2] miały na celu weryfikację, czy rozwój glejaka wielopostaciowego w mózgach szczurzych powoduje zmiany w zawartości oraz strukturze głównych molekuł biologicznych oraz akumulacji pierwiastków lekkich. W pierwszej kolejności, wykorzystując mikrospektroskopię FTIR, przeprowadzono dwuwymiarowe obrazowanie tkanek co pozwoliło na uzyskanie map rozmieszczenia biomolekuł oraz wskazanie różnic w ich akumulacji pomiędzy regionami zdrowymi a zmienionymi nowotworowo. Zaobserwowane anomalie w dystrybucji biomolekuł korelowały ze zmianami histologicznymi tkanki, a ich rozległość okazała się zależna od rodzaju implantowanej linii komórkowej GBM i była największa dla grupy U. Następnie, za pomocą tej metody oraz mikrospektroskopii Ramana, przeprowadzono szczegółową analizę spektralną wybranych obszarów tkanki, a mianowicie kory mózgowej, istoty białej oraz guza dla półkuli implantowanej i nieimplantowanej. Porównanie widm zarejestrowanych na terenie lewej i prawej półkuli w obszarach kory oraz istoty białej pozwoliło na stwierdzenie, że rozwój glejaka nie ma wpływu na gromadzenie biomolekuł w odległych obszarach mózgu. Skupiono się również na zbadaniu lokalnych zmian biochemicznych spowodowanych rozwojem GBM. Analiza porównawcza widm zarejestrowanych w obszarze nowotworu oraz jego otoczeniu wykazała, że rejony GBM charakteryzują się zmniejszoną zawartością lipidów, kwasów nukleinowych oraz związków zawierających grupy karbonylowe a także zmianami w zawartości i strukturze białek. W porównaniu do tkanek otaczających, w rejonach nowotworów zaobserwowano większą zawartość białek o strukturze drugorzędowej typu beta. W celu potwierdzenia istotności otrzymanych wyników poddano je zaawansowanej ocenie statystycznej z wykorzystaniem metody analizy głównych składowych (PCA, ang. *principal component analysis*). Wyniki PCA wykazały, że w przypadku grup Pa oraz U różnice między widmami IR zarejestrowanymi w rejonie nowotworu oraz kory mózgowej i istoty białej, są znaczące.

Ponadto, analiza zawartości lekkich pierwiastków przeprowadzona z wykorzystaniem metody SR-XRF ujawniła wzrost akumulacji sodu i chloru oraz zmniejszone gromadzenia magnezu w guzach rozwiniętych u zwierząt z grupy U.

5. Dyskusja

Wszelkie procesy chorobowe zachodzące w organizmie mogą mieć swoje odzwierciedlenie w składzie pierwiastkowym oraz biochemicznym tkanek, których badanie może stanowić istotny element w poznaniu patogenezy danego schorzenia. Analiza próbek biologicznych jest trudnym zagadnieniem, co wynika ze złożonej struktury ich matrycy, a także, często niskich zawartości badanych składników. Ponadto, zwykle dysponuje się niewielką ilością materiału próbki do przeprowadzenia analizy. Dokładna ilościowa analiza pierwiastkowa próbek biologicznych stanowi bardzo ważny problem biomedycyny. W tego rodzaju badaniach wykorzystywane są narzędzia analizy instrumentalnej, w tym metody spektroskopowe takie jak absorpcyjna spektrometria płomieniowa (F-AAS) i bezpłomieniowa z zastosowaniem kuwety grafitowej (GF-AAS) oraz atomowa spektrometria emisyjna ze wzbudzeniem w plazmie indukcyjnie sprzężonej (ICP-OES). Do metod analizy pierwiastkowej należy również spektrometria masowa ze wzbudzeniem w plazmie indukcyjnie sprzężonej (ICP-MS). Na podstawie przeglądu literatury przeprowadzonego dla celów publikacji A1 stwierdzono, że metodami najczęściej wykorzystywanymi do analizy pierwiastkowej próbek biologicznych są ICP-MS i ICP-OES, które w odróżnieniu od metod F-AAS i GF-AAS pozwalają na wykonywanie analiz wielopierwiastkowych. Metoda ICP-OES jest zazwyczaj wybierana jako narzędzie analizy pierwiastków głównych w próbce, z kolei metoda ICP-MS wykorzystywana jest w analizie tych o zawartościach na poziomie śladowym i ultraśladowym. Dane przedstawione w analizowanych pracach naukowych, w tym wartości precyzji i poprawności przeprowadzonych pomiarów, pozwoliły wskazać ICP-MS jako metodę o największej efektywności. Ma to związek również z osiąganiem najniższych granic wykrywalności pierwiastków spośród wymienionych metod analizy pierwiastkowej. Metoda ICP-MS jest bardziej wszechstronna, pozwala bowiem również na określenie składu izotopowego niektórych pierwiastków w próbkach. Jej wykorzystanie, jednak, może być ograniczone ze względu na wysokie koszty wykonywanych pomiarów.

Wśród metod wielopierwiastkowej analizy ilościowej, wartą do rozważenia alternatywą dla wysokokosztowych metod plazmowych jest spektrometria TXRF. Możliwości analityczne tej metody, tj. niskie granice wykrywalności pierwiastków, krótki czas analizy oraz niewielka ilość materiału konieczna do wykonania oznaczeń, jak również nieskomplikowana procedura pomiarowa i niskie koszty, wpływają na jej szerokie wykorzystanie w analizie próbek różnego pochodzenia. W badaniach prowadzonych w ramach rozprawy doktorskiej podjęto się próby oceny przydatności metody TXRF dla potrzeb analizy zawartości fosforu, siarki, potasu, wapnia, żelaza, miedzi, cynku oraz selenu w próbkach biologicznych. Wyznaczone w pracach A1, S1 oraz A2 granice detekcji pierwiastków, jak również wartości precyzji pomiarów wykonanych z użyciem metody TXRF były zadowalające oraz porównywalne z wartościami tych parametrów dla omówionych wcześniej metod analizy pierwiastkowej, przede wszystkim dla pierwiastków o wyższej liczbie atomowej. W rezultacie międzylaboratoryjnego porównania wyników analizy pierwiastkowej tkanek szczurzych przeprowadzonych metodą TXRF wykazano, iż wartości stężeń pierwiastków o wyższych liczbach atomowych zmierzone przez współpracujące laboratoria były ze sobą zgodne. Rozbieżności zaobserwowano, natomiast, w przypadku pierwiastków lekkich, zwłaszcza fosforu i siarki. Ich źródłem mogą być różne algorytmy dekonwolucji stosowane w poszczególnych laboratoriach podczas dopasowania

widm rentgenowskich w zakresie promieniowania charakterystycznego tych pierwiastków (1,5-3,0 keV). Ze względu na złożony charakter widma w tym zakresie, wynikający z obecności dodatkowych linii serii K pochodzących od krzemu, chloru oraz argonu, jest ono szczególne wrażliwe na zastosowaną procedurę dopasowania. Istotnym czynnikiem wpływającym na obserwowane rozbieżności w zawartościach fosforu i siarki może być również różna efektywność absorpcji promieniowania rentgenowskiego w suchej pozostałości próbki. Usprawnienie procesu preparatyki próbek, optymalizacja i ujednolicenie stosowanych procedur dekonwolucji widm i kalibracji mogłyby być potencjalnymi działaniami skutkującymi polepszeniem przydatności metody TXRF w przypadku analizy pierwiastków lekkich w tkankach zwierzęcych.

Głównym celem badań stanowiących przedmiot rozprawy doktorskiej była identyfikacja pierwiastków oraz biomolekuł zaangażowanych w rozwój glejaka wielopostaciowego w zwierzęcych modelach tego schorzenia. Zadanie to zrealizowano z zastosowaniem metod spektroskopowych, w szczególności metod analizy pierwiastkowej TXRF oraz SR-XRF a także metod spektroskopii wibracyjnej, tj. mikrospektroskopii FTIR oraz Ramana. Badania przeprowadzono z wykorzystaniem modeli zwierzęcych GBM określanych jako ortotopowe przeszczepy ksenogeniczne – komórki ludzkiego nowotworu wszczepiono do mózgów gryzoni. Dwa modele bazowały na rozwoju nowotworu z komercyjnie dostępnych ustalonych linii komórkowych GBM, a mianowicie U87mg (grupa U) oraz T98g (grupa T). Trzeci model powstał z wykorzystaniem komórek pobranych bezpośrednio z nowotworu rozwiniętego u pacjenta ze zdiagnozowanym GBM (grupa Pa).

Nowotworom powstałym w modelach zwierzęcych GBM towarzyszył szereg zmian pierwiastkowych i biochemicznych. Przeprowadzone badania wykazały, że ilość obserwowanych anomalii zależała od implantowanej linii komórkowej, a największe różnice między tkankami zdrowymi a nowotworowymi stwierdzono dla zmian, które rozwinęły się po implantacji komórek linii U87mg. Analiza mikroskopowa tkanek pobranych z rejonu implantacji komórek glejaka pokazała, że zarówno wszczepienie komórek U87mg, jak i tych pochodzących bezpośrednio od pacjenta, doprowadziło do rozwoju guza w obrębie implantowanej półkuli mózgowej szczura. W przypadku komórek U87mg była to masywna zmiana, niekiedy obejmująca całą implantowaną półkulę, z widoczną niejednorodną strukturą, w obrębie której zidentyfikowano rejon właściwy guza oraz jego obszar szczątkowy. Natomiast po implantacji komórek T98g nie doszło do rozwoju nowotworu w mózgach szczurów, a zmiany morfologiczne tkanek obserwowane w miejscu wszczepienia mogły wynikać z ich uszkodzenia podczas procedury implantacji.

Analiza metodą TXRF wykazała spadek zawartości fosforu w implantowanych półkulach mózgu szczurów należących do grupy U [praca A2]. Z kolei na podstawie map rozmieszczenia pierwiastków, otrzymanych z wykorzystaniem metody SR-XRF, w tkankach pobranych od zwierząt należących do tej grupy można było zaobserwować zmniejszenie akumulacji fosforu w rejonie szczątkowym nowotworu [praca A3]. Obszar ten stanowi rejon martwiczy guza, którego obecność jest jedną z charakterystycznych cech GBM, świadczącą o złym rokowaniu pacjentów [42]. Zmniejszenie dystrybucji fosforu w tym obszarze może wynikać z uszkodzenia

błon komórkowych, a w szczególności z rozpadu fosfolipidów będących składnikami budulcowymi błon, które wpływają na ich integralność [43]. Obniżoną akumulację fosfolipidów w rejonie szczątkowym guzów rozwiniętych z komórek U87mg potwierdziły badania przeprowadzone z wykorzystaniem metody FTIR. Wykazano, iż obszary te cechuje zmniejszona intensywność pasm charakterystycznych dla związków zawierających grupy fosforanowe (~1080 i 1240 cm^{-1}) oraz grupy karbonylowe (~1740 cm^{-1}) [praca S2].

Badania składu pierwiastkowego półkul mózgu pokazały wzrost zawartości wapnia oraz żelaza w nieimplantowanych półkulach dla zwierząt poddanych implantacji komórek U87mg. Ponadto, w obu półkulach mózgu szczurów z grupy Pa zaobserwowano zwiększenie poziomu żelaza w porównaniu do zwierząt kontrolnych [praca A2]. Analiza skrawków mózgu metodą SR-XRF wykazała niehomogeniczną akumulację wapnia oraz żelaza w obrębie masy guza, który rozwinął się z komórek U87mg. Istotny wzrost gęstości powierzchniowej wapnia odnotowano w rejonie szczątkowym nowotworu, natomiast żelaza w jego obszarze właściwym. Wzrost akumulacji tych dwóch pierwiastków odnotowano również w obrębie zmian które rozwinęły się po implantacji komórek pochodzących od pacjenta [praca A3]. Podejrzewa się, iż anomalie w gromadzeniu wapnia mogą być rezultatem procesu ekscytotoksyczności glutaminianu – pobudzającego neuroprzekaźnika, którego poziom w warunkach fizjologicznych regulowany jest przez astrocyty. Komórki GBM wykazują nieprawidłowości w zakresie kontroli poziomu glutaminianu. Co więcej, mogą uwalniać jego znaczne ilości do przestrzeni międzykomórkowej [44]. Nadmierna koncentracja glutaminianu aktywuje w błonach kanały przepuszczalne dla wapnia, co powoduje jego napływ do wnętrza komórki. To, z kolei, wywołuje szereg niszczących procesów prowadzących do śmierci komórki [45]. Żelazo jest mikroelementem istotnym dla wzrostu i procesów podziału komórek. Zwiększona akumulacja tego pierwiastka w obrębie zmiany powstałej z komórek pobranych od pacjenta oraz w rejonie właściwym nowotworu, który rozwinął się z komórek U87mg, może wskazywać na obszary o intensywnej proliferacji i inwazyjności.

Miedź jest mikroelementem zaangażowanym w wiele istotnych procesów fizjologicznych, w tym w proces angiogenezy. Pierwiastek ten aktywuje wiele czynników promujących powstawanie nowych naczyń krwionośnych, a także stymuluje proliferację komórek śródbłonka, które wyścielają naczynia [46]. Angiogeneza jest procesem kluczowym dla wzrostu nowotworu, ze względu na zwiększone zapotrzebowanie na składniki znajdujące się we krwi [47]. Analiza TXRF półkul mózgu szczurów poddanych implantacji komórek U87mg wykazała zmniejszenie zawartości miedzi w porównaniu do zwierząt normalnych, a także spadek koncentracji tego pierwiastka w półkulach implantowanych w odniesieniu do półkul nieimplantowanych [praca A2]. Ponadto, analiza map rozmieszczenia pierwiastków w badanych tkankach wykazała zmniejszone gromadzenie się miedzi w obrębie zmian powstałych w mózgach zwierząt z grup U oraz Pa. Z kolei, istotny statystycznie wzrost akumulacji tego pierwiastka został zaobserwowany w tkankach sąsiadujących ze zmianą nowotworową, która powstała w wyniku implantacji komórek U87mg [praca A3]. Zwiększenie gęstości powierzchniowej miedzi w rejonie otaczającym nowotwór może wskazywać na zintensyfikowanie procesów rozwoju nowych naczyń i sugerować wysoką inwazyjność zmiany.

Analiza TXRF mózgów szczurów wykazała specyficzną dla badanych modeli zwierzęcych GBM akumulację selenu. Stężenie tego pierwiastka zmierzone w półkulach implantowanych zwierząt z grup U i Pa było odpowiednio wyższe i niższe w odniesieniu do odpowiedniej półkuli zwierząt kontrolnych [praca A2]. Z kolei na podstawie map rozmieszczenia selenu zaobserwowano jego zwiększoną akumulację w obrębie nowotworów, które powstały w obu tych grupach eksperymentalnych. Istotnie podwyższona zawartość selenu wyróżniała rejony rozwiniętych zmian nowotworowych od obszarów tkanek poddanych implantacji pożywki hodowlanej jak i komórek T98g, gdzie nie zaobserwowano ekspansji nowotworu. Spośród wszystkich badanych pierwiastków, jedynie region o zwiększonej akumulacji selenu pokrywał się z obszarem nowotworu zidentyfikowanym podczas oceny mikroskopowej. Co istotne, selen był jedynym pierwiastkiem o jednorodnym rozkładzie w obrębie zmiany w grupie U, a gęstość powierzchniowa tego pierwiastka była podwyższona zarówno w obszarze właściwym nowotworu jak i w jego rejonie szczątkowym [praca A3]. Na podstawie tych wszystkich obserwacji uznano, iż selen mógłby być potencjalnym, pierwiastkowym markerem rozwoju GBM w modelach zwierzęcych. Podwyższona akumulacja selenu w rejonie nowotworu może wynikać ze zwiększonego zapotrzebowania na ten pierwiastek, które wykazują intensywnie proliferujące komórki nowotworowe i/lub może być wynikiem odpowiedzi układu immunologicznego na rozwijający się nowotwór i towarzyszący temu procesowi stan zapalny [48, 49].

W badaniach zmian zawartości i struktury biomolekuł zachodzących w mózgach szczurów poddanych implantacji komórek GBM szczególnie użyteczna okazała się metoda mikrospektroskopii FTIR. Otrzymane z jej wykorzystaniem mapy chemiczne, jak również przeprowadzona analiza spektralna, pozwoliły na wskazanie związków, które mogą mieć znaczenie dla rozwoju nowotworu w badanych modelach zwierzęcych. Przeprowadzona analiza statystyczna uzyskanych wyników potwierdziła istotność różnic pomiędzy widmami IR zarejestrowanymi dla istoty białej, kory mózgowej oraz zmiany nowotworowej rozwiniętej z komórek U87mg oraz pochodzących od pacjenta. Może to świadczyć o potencjale diagnostycznym metody FTIR w rozróżnianiu tkanek zdrowych od zmienionych nowotworowo. Dla żadnego z modeli zwierzęcych GBM nie udało się, natomiast, potwierdzić istotności statystycznej różnic pomiędzy widmami ramanowskimi zarejestrowanymi w badanych rejonach mózgu [praca S2].

Jedną z najistotniejszych obserwacji poczynionych w wyniku przeprowadzonej analizy biochemicznej, jest stwierdzony spadek akumulacji lipidów w rejonach nowotworów rozwiniętych z komórek U87mg i pochodzących od pacjenta, jak również w miejscu implantacji komórek T98g. Różnice w dystrybucji lipidów, wyraźnie widoczne na mapach topograficznych, pozwoliły na rozróżnienie obszaru nowotworu od tkanek otaczających [praca S2]. Jednym z czynników wpływających na zmniejszenie akumulacji lipidów może być wspomniana wcześniej redukcja zawartości fosfolipidów w obszarze guza. Inną z przyczyn może stanowić wysokie zapotrzebowanie energetyczne komórek nowotworowych związane z ich intensywną proliferacją [50, 51].

Obecność w widmie IR pasm absorpcji 1080 oraz 1240 cm^{-1} wynika, między innymi,

z zawartości w badanej próbce kwasów nukleinowych. Zarówno analiza topograficzna jak i spektralna przeprowadzona z wykorzystaniem metody FTIR wykazała różnice w intensywności i strukturze tych pasm pomiędzy tkankami zdrowymi a zmienionymi nowotworowo, przede wszystkim dla grup U oraz Pa [praca S2]. Ich zmniejszona intensywność może wskazywać na uszkodzenia kwasów nukleinowych w rejonach mózgu zajętych przez nowotwór [52].

Analiza biochemiczna tkanek pobranych z obszaru implantacji od zwierząt z grup Pa oraz U wykazała wzrost zawartości białek o strukturze drugorzędowej typu beta kartki w porównaniu do tych o strukturze alfa helisy w obszarach objętych rozwojem nowotworu [praca S2]. Ze względu na fakt, iż struktura protein determinuje ich funkcje biologiczne, wszelkie jej zmiany mogą mieć swoje odzwierciedlenie w funkcjonowaniu komórek. Obserwowane anomalia mogą wynikać z mutacji genów związanych z procesem rozwoju nowotworu [52–54]. Wzrost zawartości białek o drugorzędowej strukturze beta kartki może być również związany ze zwiększonym uwalnianiem przez komórki glejaka proteoglikanu NG2 do przestrzeni międzykomórkowej [55]. Związek ten posiada białkowy rdzeń o takiej właśnie strukturze drugorzędowej i wpływa m.in. na wysoką inwazyjność komórek GBM [56, 57].

6. Podsumowanie

W ramach rozprawy doktorskiej, w oparciu o zwierzęce modele GBM, zbadano zmiany pierwiastkowe i biochemiczne powstające w mózgu na skutek rozwoju tego nowotworu. Do tego celu wykorzystano metody analizy spektroskopowej: TXRF, SR-XRF, mikrospektroskopię FTIR oraz Ramana. Ponadto, poruszono problem analizy pierwiastkowej próbek pochodzenia biologicznego, a przede wszystkim skupiono się na ocenie użyteczności do tego celu wybranych metod instrumentalnych. W szczególności:

1. W przeprowadzonym przeglądzie literaturowym opisano możliwe zastosowania metod F-AAS, GF-AAS, ICP-OES oraz ICP-MS do analizy pierwiastkowej różnego rodzaju próbek biologicznych. Przedstawiono stosowane do tego celu metody preparatyki próbek. Na podstawie analizy wybranych parametrów walidacyjnych (precyzja, poprawność oraz granice detekcji pierwiastków) oceniono użyteczność poszczególnych metod w badaniach zawartości fosforu, siarki, potasu, wapnia, żelaza, miedzi, cynku oraz selenu w takich próbkach [praca A1].

2. Potwierdzono użyteczność metody TXRF w analizie pierwiastkowej próbek biologicznych, przede wszystkim dla pierwiastków o wyższej liczbie atomowej. Zrealizowano to poprzez ocenę wybranych parametrów walidacyjnych oraz weryfikację międzylaboratoryjnego porównania wyników analizy próbek ssaków. Wskazano możliwe kierunki poprawy przydatności metody dla badania zawartości pierwiastków lekkich w takich próbkach [prace A1, A2, S1].

3. Wskazano różnice w składzie i rozmieszczeniu pierwiastków oraz istotnych biologicznie molekuł w mózgu pomiędzy badanymi modelami zwierzęcymi GBM. Liczba obserwowanych anomalii korelowała z inwazyjnością implantowanych komórek glejaka i była największa dla linii U87mg, a najmniejsza dla linii T98g. Stwierdzono, że implantacja tych ostatnich nie doprowadziła do rozwoju nowotworu, a obserwowane anomalie pierwiastkowe i biochemiczne, jak również w strukturze morfologicznej, mogą wynikać z uszkodzenia tkanek spowodowanego procedurą implantacji [prace A2, A3, S2].

4. Metody wykorzystane do zobrazowania rozmieszczenia pierwiastków oraz biomolekuł w badanych tkankach, a mianowicie SR-XRF oraz FTIR, uwidoczniły zmiany nowotworowe powstałe z komórek U87mg oraz pochodzących od pacjenta. Obserwowane anomalie zwykle korelowały ze zmianami histologicznymi tkanek. Z pomocą wyżej wymienionych metod, możliwa była również identyfikacja rejonów o odmiennej strukturze morfologicznej w obrębie nowotworu który rozwinął się z komórek U87mg [prace A3, S2].

5. Zidentyfikowano pierwiastki, które mogą być zaangażowane w rozwój GBM w zwierzęcych modelach nowotworu. Istotne dla procesu wzrostu glejaka anomalie zaobserwowano dla zawartości i dystrybucji fosforu, wapnia, żelaza, miedzi oraz selenu. Wskazano selen jako możliwy pierwiastkowy marker rozwoju glejaka w mózgach gryzoni [prace A2, A3].

6. Szczególnie użyteczna w analizie biochemicznej badanych tkanek okazała się metoda mikrospektroskopii FTIR. Przy jej użyciu zaobserwowano spadek zawartości lipidów, kwasów

nukleinowych oraz związków zawierających grupy karbonylowe, jak również zmiany w strukturze drugorzędowej białek w obszarach nowotworów rozwiniętych w mózgach szczurów z implantowanych komórek glejaka [praca S2].

Literatura

1. Wojciechowska U, Barańska K, Michałek I, Olasek P, Miklewska M, Didkowska J (2022) Nowotwory złośliwe w Polsce w 2020 roku. Krajowy Rejestr Nowotworów
2. OECD, European Union (2022) Health at a Glance: Europe 2022: State of Health in the EU Cycle. OECD
3. Didkowska J, Wojciechowska U, Zatoński W (2009) Prognozy zachorowalności i umieralności na nowotwory złośliwe w Polsce do 2025 roku. Krajowy Rejestr Nowotworów
4. Hanif F, Muzaffar K, Perveen K, Malhi SM, Simjee SU (2017) Glioblastoma Multiforme: A Review of its Epidemiology and Pathogenesis through Clinical Presentation and Treatment. Asian Pac J Cancer Prev 18:3–9. https://doi.org/10.22034/APJCP.2017.18.1.3
5. Holland EC (2000) Glioblastoma multiforme: The terminator. Proc Natl Acad Sci USA 97:6242–6244
6. Rojek A, Zub WL, Waliszewska-Prosół M, Bladowska J, Obara K, Ejma M (2016) Wieloletnie przeżycie chorych z glejakiem wielopostaciowym — opisy przypadków. Polski Przegląd Neurologiczny 12:107–115
7. Czapski B, Baluszek S, Herold-Mende C, Kaminska B (2018) Clinical and immunological correlates of long term survival in glioblastoma. Contemp Oncol (Pozn) 22:81–85. https://doi.org/10.5114/wo.2018.73893
8. Urbańska K, Sokołowska J, Szmidt M, Sysa P (2014) Glioblastoma multiforme – an overview. Contemp Oncol (Pozn) 18:307–312. https://doi.org/10.5114/wo.2014.40559
9. Teicher BA, Menon K, Álvarez E, Galbreath E, Shih C, Faul MM (2001) Antiangiogenic and antitumor effects of a protein kinase Cbeta inhibitor in human T98G glioblastoma multiforme xenografts. Clinical Cancer Research 7:634–40
10. Henke G, Meier V, Lindner LH, Eibl H, Bamberg M, Belka C, Budach W, Jendrossek V (2012) Effects of ionizing radiation in combination with Erufosine on T98G glioblastoma xenograft tumours: a study in NMRI nu/nu mice. Radiation Oncology 7:172. https://doi.org/10.1186/1748-717X-7-172
11. Uchida H, Marzulli M, Nakano K, Goins WF, Chan J, Hong C-S, Mazzacurati L, Yoo JY, Haseley A, Nakashima H, Baek H, Kwon H, Kumagai I, Kuroki M, Kaur B, Chiocca EA, Grandi P, Cohen JB, Glorioso JC (2013) Effective Treatment of an Orthotopic Xenograft Model of Human Glioblastoma Using an EGFR-retargeted Oncolytic Herpes Simplex Virus. Molecular Therapy 21:561–569. https://doi.org/10.1038/mt.2012.211
12. Lenting K, Verhaak R, ter Laan M, Wesseling P, Leenders W (2017) Glioma: experimental models and reality. Acta Neuropathologica 133:263–282. https://doi.org/10.1007/s00401-017-1671-4
13. Hidalgo M, Amant F, Biankin AV, Budinská E, Byrne AT, Caldas C, Clarke RB, de Jong S, Jonkers J, Mælandsmo GM, Roman-Roman S, Seoane J, Trusolino L, Villanueva A, for the EurOPDX Consortium (2014) Patient-Derived Xenograft Models: An Emerging Platform for Translational Cancer Research. Cancer Discovery 4:998–1013. https://doi.org/10.1158/2159-8290.CD-14-0001
14. Yoshida GJ (2020) Applications of patient-derived tumor xenograft models and tumor organoids. Journal of Hematology & Oncology 13.: https://doi.org/10.1186/s13045-019-

0829-z
15. Kerstetter-Fogle AE, Harris PLR, Brady-Kalnay SM, Sloan AE (2020) Generation of Glioblastoma Patient-Derived Intracranial Xenografts for Preclinical Studies. International Journal of Molecular Sciences 21:5113. https://doi.org/10.3390/ijms21145113
16. Strojnik T, Kavalar R, Lah TT (2006) Experimental Model and Immunohistochemical Analyses of U87 Human Glioblastoma Cell Xenografts in Immunosuppressed Rat Brains. Anticancer research 26:2887–2900
17. Baklaushev VP, Kavsan VM, Balynska OV, Yusubalieva GM, Abakumov MA, Chekhonin VP (2012) New Experimental Model of Brain Tumors in Brains of Adult Immunocompetent Rats. British Journal of Medicine and Medical Research 2:206–215. https://doi.org/10.9734/BJMMR/2012/1072
18. Biasibetti E, Valazza A, Capucchio MT, Annovazzi L, Battaglia L, Chirio D, Gallarate M, Mellai M, Muntoni E, Peira E, Riganti C, Schiffer D, Panciani P, Lanotte M (2017) Comparison of Allogeneic and Syngeneic Rat Glioma Models by Using MRI and Histopathologic Evaluation. Comp Med 67:147–156
19. Callejón-Leblic B, Arias-Borrego A, Pereira-Vega A, Gómez-Ariza JL, García-Barrera T (2019) The Metallome of Lung Cancer and its Potential Use as Biomarker. Int J Mol Sci 20.: https://doi.org/10.3390/ijms20030778
20. Jouybari L, Saei Ghare Naz M, Sanagoo A, Kiani F, Sayehmiri F, sayehmiri K, hasanpour dehkordi A (2018) Toxic elements as biomarkers for breast cancer: a meta-analysis study. Cancer Management and Research 10:69–79. https://doi.org/10.2147/CMAR.S151324
21. Silva MP, Soave DF, Ribeiro-Silva A, Poletti ME (2012) Trace elements as tumor biomarkers and prognostic factors in breast cancer: a study through energy dispersive x-ray fluorescence. BMC Research Notes 5.: https://doi.org/10.1186/1756-0500-5-194
22. Zaichick V, Zaichick SV (2018) Trace Elements of Expressed Prostatic Secretions as a Source for Biomarkers of Prostate Cancer. Journal of Clinical Research in Oncology 1:1–7
23. Zoriy MV, Dehnhardt M, Reifenberger G, Zilles K, Becker JS (2006) Imaging of Cu, Zn, Pb and U in human brain tumor resections by laser ablation inductively coupled plasma mass spectrometry. International Journal of Mass Spectrometry 257:27–33. https://doi.org/10.1016/j.ijms.2006.06.005
24. Dehnhardt M, Zoriy MV, Khan Z, Reifenberger G, Ekström TJ, Sabine Becker J, Zilles K, Bauer A (2008) Element distribution is altered in a zone surrounding human glioblastoma multiforme. Journal of Trace Elements in Medicine and Biology 22:17–23. https://doi.org/10.1016/j.jtemb.2007.08.002
25. Szczerbowska-Boruchowska M, Lankosz M, Adamek D (2011) First step toward the "fingerprinting" of brain tumors based on synchrotron radiation X-ray fluorescence and multiple discriminant analysis. JBIC Journal of Biological Inorganic Chemistry 16:1217–1226. https://doi.org/10.1007/s00775-011-0810-y
26. Lankosz MW, Grzelak M, Ostachowicz B, Wandzilak A, Szczerbowska-Boruchowska M, Wrobel P, Radwanska E, Adamek D (2014) Application of the total reflection X-ray fluorescence method to the elemental analysis of brain tumors of different types and grades of malignancy. Spectrochimica Acta Part B: Atomic Spectroscopy 101:98–105.

https://doi.org/10.1016/j.sab.2014.07.019
27. Wandzilak A, Czyzycki M, Radwanska E, Adamek D, Geraki K, Lankosz M (2015) X-ray fluorescence study of the concentration of selected trace and minor elements in human brain tumours. Spectrochimica Acta Part B: Atomic Spectroscopy 114:52–57. https://doi.org/10.1016/j.sab.2015.10.002
28. Crow P, Stone N, Kendall CA, Uff JS, Farmer JAM, Barr H, Wright MPJ (2003) The use of Raman spectroscopy to identify and grade prostatic adenocarcinoma in vitro. British Journal of Cancer 89:106–108. https://doi.org/10.1038/sj.bjc.6601059
29. Tiwari S, Falahkheirkhah K, Cheng G, Bhargava R (2022) Colon Cancer Grading Using Infrared Spectroscopic Imaging-Based Deep Learning. Applied Spectroscopy 76:475–484. https://doi.org/10.1177/00037028221076170
30. Krafft C, Sobottka SB, Geiger KD, Schackert G, Salzer R (2007) Classification of malignant gliomas by infrared spectroscopic imaging and linear discriminant analysis. Analytical and Bioanalytical Chemistry 387:1669–1677. https://doi.org/10.1007/s00216-006-0892-5
31. Kopec M, Błaszczyk M, Radek M, Abramczyk H (2021) Raman imaging and statistical methods for analysis various type of human brain tumors and breast cancers. Spectrochimica Acta Part A: Molecular and Biomolecular Spectroscopy 262:120091. https://doi.org/10.1016/j.saa.2021.120091
32. Amharref N, Beljebbar A, Dukic S, Venteo L, Schneider L, Pluot M, Manfait M (2007) Discriminating healthy from tumor and necrosis tissue in rat brain tissue samples by Raman spectral imaging. Biochimica et Biophysica Acta (BBA) - Biomembranes 1768:2605–2615. https://doi.org/10.1016/j.bbamem.2007.06.032
33. Richardson DR (2002) Iron chelators as therapeutic agents for the treatment of cancer. Critical Reviews in Oncology/Hematology 42:267–281. https://doi.org/10.1016/S1040-8428(01)00218-9
34. Brewer GJ, Dick RD, Grover DK, LeClaire V, Tseng M, Wicha M, Pienta K, Redman BG, Jahan T, Sondak VK, Strawderman M, LeCarpentier G, Merajver SD (2000) Treatment of Metastatic Cancer with Tetrathiomolybdate, an Anticopper, Antiangiogenic Agent: Phase I Study. Clin Cancer Res 6:1–10
35. Bähr O, Hattingen E, Rieger J, Steinbach JP (2011) Bevacizumab-induced tumor calcifications as a surrogate marker of outcome in patients with glioblastoma. Neuro-Oncology 13:1020–1029. https://doi.org/10.1093/neuonc/nor099
36. Zhang J, Fan Y, He M, Ma X, Song Y, Liu M, Xu J (2017) Accuracy of Raman spectroscopy in differentiating brain tumor from normal brain tissue. Oncotarget 8:36824–36831. https://doi.org/10.18632/oncotarget.15975
37. Mehrotra R, Tyagi G, Jangir DK, Dawar R, Gupta N (2010) Analysis of ovarian tumor pathology by Fourier Transform Infrared Spectroscopy. J Ovarian Res 3:27. https://doi.org/10.1186/1757-2215-3-27
38. de Jong BWD, Bakker Schut TC, Maquelin K, van der Kwast T, Bangma CH, Kok D-J, Puppels GJ (2006) Discrimination between Nontumor Bladder Tissue and Tumor by Raman Spectroscopy. Anal Chem 78:7761–7769. https://doi.org/10.1021/ac061417b
39. Wehbe K, Pineau R, Eimer S, Vital A, Loiseau H, Déléris G (2010) Differentiation between normal and tumor vasculature of animal and human glioma by FTIR imaging.

Analyst 135:3052–3059. https://doi.org/10.1039/C0AN00513D
40. Kong K, Kendall C, Stone N, Notingher I (2015) Raman spectroscopy for medical diagnostics — From in-vitro biofluid assays to in-vivo cancer detection. Advanced Drug Delivery Reviews 89:121–134. https://doi.org/10.1016/j.addr.2015.03.009
41. Matusiak K, Skoczen A, Setkowicz Z, Kubala-Kukus A, Stabrawa I, Ciarach M, Janeczko K, Jung A, Chwiej J (2017) The elemental changes occurring in the rat liver after exposure to PEG-coated iron oxide nanoparticles: total reflection x-ray fluorescence (TXRF) spectroscopy study. Nanotoxicology 11:1225–1236. https://doi.org/10.1080/17435390.2017.1408151
42. Liu S, Wang Y, Xu K, Wang Z, Fan X, Zhang C, Li S, Qiu X, Jiang T (2017) Relationship between necrotic patterns in glioblastoma and patient survival: fractal dimension and lacunarity analyses using magnetic resonance imaging. Scientific Reports 7.: https://doi.org/10.1038/s41598-017-08862-6
43. Hubesch B, Sappey-Marinier D, Roth K, Meyerhoff DJ, Matson GB, Weiner MW (1990) P-31 MR spectroscopy of normal human brain and brain tumors. Radiology 174:401–409. https://doi.org/10.1148/radiology.174.2.2296651
44. Ye Z-C, Sontheimer H (1999) Glioma Cells Release Excitotoxic Concentrations of Glutamate. Cancer Res 59:4383–4391
45. Noch E, Khalili K (2009) Molecular mechanisms of necrosis in glioblastoma: The role of glutamate excitotoxicity. Cancer Biology & Therapy 8:1791–1797. https://doi.org/10.4161/cbt.8.19.9762
46. Finney L, Vogt S, Fukai T, Glesne D (2009) Copper and angiogenesis: unravelling a relationship key to cancer progression. Clinical and Experimental Pharmacology and Physiology 36:88–94. https://doi.org/10.1111/j.1440-1681.2008.04969.x
47. Denoyer D, Masaldan S, Fontaine SL, Cater MA (2015) Targeting copper in cancer therapy: "Copper That Cancer." Metallomics 7:1459–1476. https://doi.org/10.1039/C5MT00149H
48. Brozmanová J, Mániková D, Vlčková V, Chovanec M (2010) Selenium: a double-edged sword for defense and offence in cancer. Archives of Toxicology 84:919–938. https://doi.org/10.1007/s00204-010-0595-8
49. Stojsavljević A, Vujotić L, Rovčanin B, Borković-Mitić S, Gavrović-Jankulović M, Manojlović D (2020) Assessment of trace metal alterations in the blood, cerebrospinal fluid and tissue samples of patients with malignant brain tumors. Scientific Reports 10.: https://doi.org/10.1038/s41598-020-60774-0
50. Beljebbar A, Amharref N, Lévèques A, Dukic S, Venteo L, Schneider L, Pluot M, Manfait M (2008) Modeling and quantifying biochemical changes in C6 tumor gliomas by Fourier transform infrared imaging. Anal Chem 80:8406–8415. https://doi.org/10.1021/ac800990y
51. Wang J-S, Shi J-S, Xu Y-Z, Duan X-Y, Zhang L, Wang J, Yang L-M, Weng S-F, Wu J-G (2003) FT-IR spectroscopic analysis of normal and cancerous tissues of esophagus. World J Gastroenterol 9:1897–1899. https://doi.org/10.3748/wjg.v9.i9.1897
52. Depciuch J, Tołpa B, Witek P, Szmuc K, Kaznowska E, Osuchowski M, Król P, Cebulski J (2020) Raman and FTIR spectroscopy in determining the chemical changes in healthy brain tissues and glioblastoma tumor tissues. Spectrochimica Acta Part A: Molecular and

Biomolecular Spectroscopy 225:117526. https://doi.org/10.1016/j.saa.2019.117526
53. Kong D, Peng W, Zong R, Cui G, Yu X (2020) Morphological and Biochemical Properties of Human Astrocytes, Microglia, Glioma, and Glioblastoma Cells Using Fourier Transform Infrared Spectroscopy. Med Sci Monit 26:e925754. https://doi.org/10.12659/MSM.925754
54. Zhou Y, Liu C-H, Wu B, Yu X, Cheng G, Zhu K, Wang K, Zhang C, Zhao M, Zong R, Zhang L, Shi L, Alfano RR (2019) Optical biopsy identification and grading of gliomas using label-free visible resonance Raman spectroscopy. J Biomed Opt 24:1–12. https://doi.org/10.1117/1.JBO.24.9.095001
55. Jones LL, Yamaguchi Y, Stallcup WB, Tuszynski MH (2002) NG2 Is a Major Chondroitin Sulfate Proteoglycan Produced after Spinal Cord Injury and Is Expressed by Macrophages and Oligodendrocyte Progenitors. J Neurosci 22:2792–2803
56. Yadavilli S, Hwang EI, Packer RJ, Nazarian J (2016) The Role of NG2 Proteoglycan in Glioma. Transl Oncol 9:57–63. https://doi.org/10.1016/j.tranon.2015.12.005
57. Tamburini E, Dallatomasina A, Quartararo J, Cortelazzi B, Mangieri D, Lazzaretti M, Perris R (2019) Structural deciphering of the NG2/CSPG4 proteoglycan multifunctionality. The FASEB Journal 33:3112–3128. https://doi.org/10.1096/fj.201801670R

Lista wystąpień konferencyjnych i seminaryjnych

1. **Karolina Olbrich**, Zuzanna Setkowicz-Janeczko, Damian Ryszawy, Mateusz Czyżycki, Natalia Janik-Olchawa, Kamil Kawoń, Agnieszka Dróżdż, Rolf Simon, Tilo Baumbach, Joanna Chwiej, *The studies of the animal models of glioma development using the methods of atomic and molecular biospectroscopy,* Brain Tumors 2022: from Biology to Therapy, 22-24 czerwca 2022, Warszawa, Polska (plakat)

2. **Karolina Płaneta**, Zuzanna Setkowicz-Janeczko, Damian Ryszawy, Natalia Janik-Olchawa, Agnieszka Dróżdż, Mateusz Czyżycki, Ilaria Carlomagno, Giuliana Aquilanti, Joanna Chwiej, *Vibrational spectroscopy as a valuable tool for investigation of biochemical markers of glioblastoma multiforme invasiveness,* ICAVS-11: 11 International Conference on Advanced Vibrational Spectroscopy, 23-26 sierpnia 2021, online (plakat)

3. **Karolina Płaneta**, Natalia Janik-Olchawa, Joanna Chwiej, Zuzanna Setkowicz-Janeczko, Krzysztof Janeczko, Damian Ryszawy, Mateusz Czyżycki, Rolf Simon, Tilo Baumbach, *Alterations of the elemental distribution within brain tissue occurring during glioma development studied using SR-XRF method,* 2-6 sierpnia 2021, online (referat)

4. **Karolina Płaneta**, Zuzanna Setkowicz-Janeczko, Damian Ryszawy, Natalia Janik-Olchawa, Katarzyna Matusiak, Agnieszka Dróżdż, Krzysztof Janeczko, Beata Ostachowicz, Joanna Chwiej, *Elemental changes of brain accompanying the glioblastoma multiforme development – the study using the total reflection x-ray fluorescence,* ENFORCE TXRF: BIOMEDIAG subgroup workshop, 21-23 kwietnia 2021, online (plakat)

5. **Karolina Płaneta**, Zuzanna Setkowicz-Janeczko, Damian Ryszawy, Natalia Janik-Olchawa, Agnieszka Dróżdż, Joanna Chwiej, *Biomolecular topography of glioblastoma multiforme developed in the rat brain – a FTIR study,* XXII Polish Conference on Biocybernetics and Biomedical Engineering (PCBBE), 19-21 maja 2021, online (plakat)

6. **Karolina Płaneta,** *Spectroscopic methods for the determination of elemental and molecular markers of the invasiveness of different glioma cells in brain during tumour development,* Scattering/Imaging Seminar w Karlsruhe Institute of Technology, 2 luty 2021, online (seminarium)

7. **Karolina Płaneta**, Zuzanna Setkowicz, Damian Ryszawy, Natalia Janik-Olchawa, Katarzyna Matusiak, Beata Ostachowicz, Joanna Chwiej, *Application of total reflection X-ray fluorescence (TXRF) method to identify elemental changes occurring in rat organs after intracranial implantation of human glioblastoma multiforme cell line,* National Scientific Conference for PhD Students : II edition, 2 marca 2019, Kraków, Polska (plakat)

Publikacje spoza rozprawy

1. Aleksandra Wilk, Agnieszka Dróżdż, **Karolina Olbrich**, Natalia Janik-Olchawa, Zuzanna Setkowicz, Joanna Chwiej, *Influence of measurement mode on the results of glioblastoma multiforme analysis with the FTIR microspectroscopy.* Spectrochim. Acta A Mol. Biomol. Spectrosc. 287:122086 (2023); IF_{2021}=4.831, $MNiSW_{2021}$=140;

2. Natalia Janik-Olchawa, Agnieszka Dróżdż, Aleksandra Wajda, Maciej Sitarz, **Karolina**

Płaneta, Zuzanna Setkowicz, Damian Ryszawy, Angelika Kmita, Joanna Chwiej, *Biochemical changes of macrophages and U87MG cells occurring as a result of the exposure to iron oxide nanoparticles detected with the Raman microspectroscopy*, Spectrochim. Acta A Mol. Biomol. Spectrosc. 278:121337 (2022); IF_{2021}=4.831, $MNiSW_{2021}$=140;

3. Natalia Janik-Olchawa, Agnieszka Dróżdż, Damian Ryszawy, Maciej Pudelek, **Karolina Płaneta**, Zuzanna Setkowicz, Maciej Śniegocki, Magdalena Wytrwał-Sarna, Marta Gajewska, Joanna Chwiej, *The influence of IONPs core size on their biocompatibility and activity in in vitro cellular models,* Sci. Rep. 11, 21808 (2021); IF_{2021}=4.996, $MNiSW_{2021}$=140;

4. Natalia Janik-Olchawa, Agnieszka Dróżdż, Damian Ryszawy, Maciej Pudełek, **Karolina Płaneta**, Zuzanna Setkowicz, Maciej Śniegocki, Andrzej Żądło, Beata Ostachowicz, Joanna Chwiej, *Comparison of ultrasmall IONPs and Fe salts biocompatibility and activity in multi-cellular in vitro models*, Sci. Rep. 10, 15447 (2020); IF_{2021}=4.996, $MNiSW_{2021}$=140;

5. Joanna G. Chwiej, Stanisław W. Ciesielka, Agnieszka K. Skoczeń, Krzysztof J. Janeczko, Christophe Sandt, **Karolina L. Płaneta**, Zuzanna K. Setkowicz, *Biochemical changes indicate developmental stage in the hippocampal formation,* ACS Chem. Neurosci. 10(1):628-635 (2019); IF_{2021}=5.780, $MNiSW_{2021}$=100.

Staże i naukowe wyjazdy zagraniczne

1. Staż zagraniczny w Elettra-Sincrotrone Trieste (Włochy) w terminie 15-27.09.2019 finansowany w ramach Programu Operacyjnego Wiedza Edukacja Rozwój, nr projektu POWR.03.02.00-00-I004/16.

2. Pobyt naukowy w ośrodku badawczym promieniowania synchrotronowego DESY w Hamburgu (Niemcy) 18-24.06.2019 w ramach programu PROM, NAWA.

Oświadczenia współautorów publikacji oraz manuskryptów

Autorzy (alfabetycznie)	A1	A2	A3	S1	S2	strony
Aquilanti Giuliana				+		40
Baumbach Tilo			+			41
Carlomagno Ilaria				+		42
Chwiej Joanna	+	+	+	+	+	43-45
Czyżycki Mateusz			+	+		46-47
Dróżdż Agnieszka	+	+				48
Fernández-Ruiz Ramón					+	49
Janeczko Krzysztof		+	+			50
Janik-Olchawa Natalia		+	+	+		51-52
Kawoń Kamil				+		53
Kubala-Kukuś Aldona	+				+	54-55
Margui Eva					+	56
Matusiak Katarzyna	+	+			+	57-58
Olbrich Karolina	+	+	+	+	+	59-61
Ostachowicz Beata		+				62
Ryszawy Damian†		+	+			-
Setkowicz Zuzanna	+	+	+	+	+	63-65
Simon Rolf			+			66
Wróbel Paweł					+	67
Wudarczyk-Moćko Jolanta					+	68

† dr Damian Ryszawy zmarł nagle 11.09.2020 r.

Trieste, 16/02/2023

Dr. Giuliana Aquilanti
Elettra-Sincrotrone Trieste
SS 14 km 163.5 Basovizza (TS) 34149 Italy

CO-AUTHOR CONFIRMATION

As a co-author of publication entitled
"Vibrational spectroscopy methods for investigation of the animal models of glioblastoma multiforme" (in review),

I declare that my contribution to the creation of the above-mentioned work included
Support for data acquisition, review of the manuscript

I declare that a separate part of the above-mentioned work demonstrate the individual contribution from **Karolina Olbrich** in developing the research concept, conducting the experimental part as well as analyzing and interpreting the results. I give my permission for the above-mentioned work to be submitted by **Karolina Olbrich** as part of a doctoral dissertation in the form of a thematically coherent collection of articles published in scientific journals.

Giuliana Aquilanti
(Signature)

Karlsruhe, 06. February 2023
(Place and date)

Prof. Dr. Tilo Baumbach
(Professional title, name and surname)

Karlsruhe Institute of Technology
Institute for Photon Science and Synchrotron Radiation
(Institution)

Hermann-von-Helmholtz-Platz 1
76344 Eggenstein-Leopoldshafen, Germany
(Address)

CO-AUTHOR CONFIRMATION

As a co-author of the publication entitled

"Altered Elemental Distribution in Male Rat Brain Tissue as a Predictor of Glioblastoma Multiforme Growth—Studies Using SR-XRF Microscopy" (Int. J. Mol. Sci. 2022),

Hereby, I declare that my contribution to the above-mentioned paper was to grant a beamtime at the beamline FLUO at the KIT Synchrotron Light Source.

I declare that a separatable part of the above-mentioned paper demonstrates the individual contribution from **Karolina Olbrich** in developing the research concept, conducting the experiment as well as analyzing and interpreting the results. I give my permission for the above-mentioned paper to be submitted by **Karolina Olbrich** as a part of her doctoral dissertation in the form of a thematically coherent collection of papers published in scientific journals.

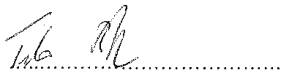

(Signature)

Trieste, 16/02/2023

Dr. Ilaria Calromagno
Elettra-Sincrotrone Trieste
SS 14 km 163.5 Basovizza (TS) 34149 Italy

CO-AUTHOR CONFIRMATION

As a co-author of publication entitled
"Vibrational spectroscopy methods for investigation of the animal models of glioblastoma multiforme" (in review),

I declare that my contribution to the creation of the above-mentioned work included
Support for data acquisition, review of the manuscript

I declare that a separate part of the above-mentioned work demonstrate the individual contribution from **Karolina Olbrich** in developing the research concept, conducting the experimental part as well as analyzing and interpreting the results. I give my permission for the above-mentioned work to be submitted by **Karolina Olbrich** as part of a doctoral dissertation in the form of a thematically coherent collection of articles published in scientific journals.

(Signature)

Kraków, dnia 27.02.2023

Dr hab. inż. Joanna Chwiej, prof. uczelni
(tytuł zawodowy, imię i nazwisko)
WFiIS AGH
(instytucja)
Al. Mickiewicza 30, 30-059 Kraków
(adres)

OŚWIADCZENIE

Jako współautor prac pt.:

1. "Comparison of Elemental Anomalies Following Implantation of Different Cell Lines of Glioblastoma Multiforme in the Rat Brain: A Total Reflection X-ray Fluorescence Spectroscopy Study" (ACS Chem. Neurosci. 2020),
2. "The assessment of the usability of selected instrumental techniques for the elemental analysis of biomedical samples" (Sci Rep 2021),
3. "Altered Elemental Distribution in Male Rat Brain Tissue as a Predictor of Glioblastoma Multiforme Growth—Studies Using SR-XRF Microscopy" (Int. J. Mol. Sci. 2022),

oświadczam, że mój wkład w powstanie każdej z ww. prac obejmował udział w opracowaniu koncepcji i metodologii badań oraz nadzór nad ich realizacją i publikacją uzyskanych wyników.

Oświadczam także, że samodzielna oraz możliwa do wyodrębnienia część ww. prac wykazuje indywidualny wkład mgr **Karoliny Olbrich** przy opracowywaniu koncepcji badań, przeprowadzeniu części eksperymentalnej, analizie i interpretacji wyników niniejszych prac. Jednocześnie wyrażam zgodę na przedłożenie ww. prac przez mgr **Karolinę Olbrich** jako część rozprawy doktorskiej w formie spójnego tematycznie zbioru artykułów opublikowanych w czasopismach naukowych.

Joanna Chwiej
.....
(podpis współautora)

Kraków, dnia 27.02.2023

Dr hab. inż. Joanna Chwiej, prof. uczelni
(tytuł zawodowy, imię i nazwisko)
WFiIS AGH
(instytucja)
Al. Mickiewicza 30, 30-059 Kraków
(adres)

OŚWIADCZENIE

Jako współautor pracy pt.:
"Vibrational spectroscopy methods for investigation of the animal models of glioblastoma multiforme" (w recenzji),

oświadczam, że mój wkład w powstanie ww. pracy obejmował udział w opracowaniu koncepcji i metodologii badań oraz nadzór nad ich realizacją i publikacją uzyskanych wyników.

Oświadczam także, że samodzielna oraz możliwa do wyodrębnienia część ww. pracy wykazuje indywidualny wkład mgr **Karoliny Olbrich** przy opracowywaniu koncepcji badań, przeprowadzeniu części eksperymentalnej, analizie i interpretacji wyników niniejszej pracy. Jednocześnie wyrażam zgodę na przedłożenie ww. pracy przez mgr **Karolinę Olbrich** jako część rozprawy doktorskiej w formie spójnego tematycznie zbioru artykułów opublikowanych w czasopismach naukowych.

Joanna Chwiej

(podpis współautora)

Kraków, dnia 27.02.2023

Dr hab. inż. Joanna Chwiej, prof. uczelni
(tytuł zawodowy, imię i nazwisko)
WFiIS AGH
(instytucja)
Al. Mickiewicza 30, 30-059 Kraków
(adres)

OŚWIADCZENIE

Jako współautor pracy pt.:
"The first total reflection X-ray fluorescence round-robin test of mammalian tissue samples: preliminary results" (w recenzji),

oświadczam, że mój wkład w powstanie ww. pracy obejmował udział w opracowaniu koncepcji i metodologii badań oraz nadzór nad ich realizacją i publikacją uzyskanych wyników.

Oświadczam także, że samodzielna oraz możliwa do wyodrębnienia część ww. pracy wykazuje indywidualny wkład mgr **Karoliny Olbrich** przy opracowywaniu koncepcji badań, przeprowadzeniu części eksperymentalnej, analizie i interpretacji wyników niniejszej pracy. Jednocześnie wyrażam zgodę na przedłożenie ww. pracy przez mgr **Karolinę Olbrich** jako część rozprawy doktorskiej w formie spójnego tematycznie zbioru artykułów opublikowanych w czasopismach naukowych.

.....
(podpis współautora)

Hamburg, 14 lutego 2023
(miejscowość, data)

Dr inż. Mateusz Czyżycki
(tytuł zawodowy, imię i nazwisko)

Akademia Górniczo-Hutnicza
Wydział Fizyki i Informatyki Stosowanej
(instytucja)
Al. A. Mickiewicza 30
30-059 Kraków
(adres)

Karlsruhe Institute of Technology
Institute for Photon Science and Synchrotron Radiation
KIT Synchrotron Laboratory at PETRA III in Hamburg
(instytucja)
Hermann-von-Helmholtz-Platz 1
76344 Eggenstein-Leopoldshafen, Niemcy
(adres)

OŚWIADCZENIE

Jako współautor pracy pt.:
"Altered Elemental Distribution in Male Rat Brain Tissue as a Predictor of Glioblastoma Multiforme Growth—Studies Using SR-XRF Microscopy" (Int. J. Mol. Sci. 2022),
oświadczam, że mój wkład w powstanie ww. pracy obejmował wykonanie eksperymentu w KIT Synchrotron Light Source w Karlsruhe w Niemczech na linii pomiarowej FLUO.

Oświadczam także, że samodzielna oraz możliwa do wyodrębnienia część ww. pracy wykazuje indywidualny wkład mgr **Karoliny Olbrich** przy opracowywaniu koncepcji badań, przeprowadzeniu części eksperymentalnej, analizie i interpretacji wyników niniejszej pracy. Jednocześnie wyrażam zgodę na przedłożenie ww. pracy przez mgr **Karolinę Olbrich** jako część rozprawy doktorskiej w formie spójnego tematycznie zbioru artykułów opublikowanych w czasopismach naukowych.

.....
(podpis współautora)

Hamburg, 14 lutego 2023
(miejscowość, data)

Dr inż. Mateusz Czyżycki
(tytuł zawodowy, imię i nazwisko)

Akademia Górniczo-Hutnicza
Wydział Fizyki i Informatyki Stosowanej
(instytucja)
Al. A. Mickiewicza 30
30-059 Kraków
(adres)

Karlsruhe Institute of Technology
Institute for Photon Science and Synchrotron Radiation
KIT Synchrotron Laboratory at PETRA III in Hamburg
(instytucja)
Hermann-von-Helmholtz-Platz 1
76344 Eggenstein-Leopoldshafen, Niemcy
(adres)

OŚWIADCZENIE

Jako współautor pracy pt.:
"Vibrational spectroscopy methods for investigation of the animal models of glioblastoma multiforme" (w recenzji),

oświadczam, że mój wkład w powstanie ww. pracy obejmował wykonanie eksperymentu w Elettra Sincrotrone Trieste we Włoszech na linii pomiarowej XRF/IAEA.

Oświadczam także, że samodzielna oraz możliwa do wyodrębnienia część ww. pracy wykazuje indywidualny wkład mgr **Karoliny Olbrich** przy opracowywaniu koncepcji badań, przeprowadzeniu części eksperymentalnej, analizie i interpretacji wyników niniejszej pracy. Jednocześnie wyrażam zgodę na przedłożenie ww. pracy przez mgr **Karolinę Olbrich** jako część rozprawy doktorskiej w formie spójnego tematycznie zbioru artykułów opublikowanych w czasopismach naukowych.

.....
(podpis współautora)

Kraków, dnia 20.02.2023

Dr inż. Agnieszka Dróżdż
(tytuł zawodowy, imię i nazwisko)
Wydział Fizyki i Informatyki Stosowanej
Akademia Górniczo-Hutnicza
im. Stanisława Staszica w Krakowie
(instytucja)
Al. Adama Mickiewicza 30
30-059 Kraków
(adres)

OŚWIADCZENIE

Jako współautor prac pt.:

1. "Comparison of Elemental Anomalies Following Implantation of Different Cell Lines of Glioblastoma Multiforme in the Rat Brain: A Total Reflection X-ray Fluorescence Spectroscopy Study" (ACS Chem. Neurosci. 2020),
2. "The assessment of the usability of selected instrumental techniques for the elemental analysis of biomedical samples" (Sci Rep 2021)

oświadczam, że mój wkład w powstanie ww. prac obejmował:

1. współudział w opracowaniu metodologii badań oraz prowadzeniu badań
2. współudział w opracowaniu metodologii, prowadzeniu badań oraz walidacji otrzymanych wyników.

Oświadczam także, że samodzielna oraz możliwa do wyodrębnienia część ww. prac wykazuje indywidualny wkład mgr **Karoliny Olbrich** przy opracowywaniu koncepcji badań, przeprowadzeniu części eksperymentalnej, analizie i interpretacji wyników niniejszych prac. Jednocześnie wyrażam zgodę na przedłożenie ww. prac przez mgr **Karolinę Olbrich** jako część rozprawy doktorskiej w formie spójnego tematycznie zbioru artykułów opublikowanych w czasopismach naukowych.

Agnieszka Dróżdż
(podpis współautora)

Madrid, 28th February 2023

Universidad Autónoma de Madrid

Dr. Ramón Fernandez Ruiz
Universidad Autónoma de Madrid
Facultad de Ciencias. SIdI, C13
Avd. Francisco Tomas y Valiente, 7
28049-Madrid

CO-AUTHOR CONFIRMATION

As a co-author of publication entitled
"The first total reflection X-ray fluorescence round-robin test of mammalian tissue samples: preliminary results" (in review),

I declare that my contribution to the creation of the above-mentioned work included experimental measurements as well as writing-review & editing.

I declare that a separate part of the above-mentioned work demonstrate the individual contribution from **Karolina Olbrich** in developing the research concept, conducting the experimental part as well as analyzing and interpreting the results. I give my permission for the above-mentioned work to be submitted by **Karolina Olbrich** as part of a doctoral dissertation in the form of a thematically coherent collection of articles published in scientific journals.

Firmado digitalmente por FERNANDEZ RUIZ RAMON - 22975511Y
Nombre de reconocimiento (DN): c=ES, serialNumber=IDCES-22975511Y, givenName=RAMON, sn=FERNANDEZ RUIZ, cn=FERNANDEZ RUIZ RAMON - 22975511Y
Fecha: 2023.02.28 12:54:51 +01'00'

Kraków, dnia 07.03.23

Prof. dr hab.Krzysztof Janeczko
(tytuł zawodowy, imię i nazwisko)
Instytut Zoologii i Badań Biomedycznych
Uniwersytet Jagielloński
(instytucja)
Kraków, ul. Gronostajowa 9
(adres)

OŚWIADCZENIE

Jako współautor prac pt.:

1. "Comparison of Elemental Anomalies Following Implantation of Different Cell Lines of Glioblastoma Multiforme in the Rat Brain: A Total Reflection X-ray Fluorescence Spectroscopy Study" (ACS Chem. Neurosci. 2020),
2. "Altered Elemental Distribution in Male Rat Brain Tissue as a Predictor of Glioblastoma Multiforme Growth—Studies Using SR-XRF Microscopy" (Int. J. Mol. Sci. 2022)

oświadczam, że mój wkład w powstanie ww. prac obejmował twórczą dyskusję manuskryptu

Oświadczam także, że samodzielna oraz możliwa do wyodrębnienia część ww. prac wykazuje indywidualny wkład mgr **Karoliny Olbrich** przy opracowywaniu koncepcji badań, przeprowadzeniu części eksperymentalnej, analizie i interpretacji wyników niniejszych prac. Jednocześnie wyrażam zgodę na przedłożenie ww. prac przez mgr **Karolinę Olbrich** jako część rozprawy doktorskiej w formie spójnego tematycznie zbioru artykułów opublikowanych w czasopismach naukowych.

Elektronicznie podpisany przez Krzysztof Janeczko
Data: 2023.03.07 23:34:59 +01'00'

.....
(podpis współautora)

Kraków, dnia 1.03.2023

Dr Natalia Janik-Olchawa
(tytuł zawodowy, imię i nazwisko)
Instytut Zoologii i Badań Biomedycznych UJ
(instytucja)
Gronostajowa 9
(adres)

OŚWIADCZENIE

Jako współautor prac pt.:

1. "Comparison of Elemental Anomalies Following Implantation of Different Cell Lines of Glioblastoma Multiforme in the Rat Brain: A Total Reflection X-ray Fluorescence Spectroscopy Study" (ACS Chem. Neurosci. 2020),
2. "Altered Elemental Distribution in Male Rat Brain Tissue as a Predictor of Glioblastoma Multiforme Growth—Studies Using SR-XRF Microscopy" (Int. J. Mol. Sci. 2022),

oświadczam, że mój wkład w powstanie obu ww. prac obejmował:

- prowadzenie hodowli komórkowych i przygotowanie materiału biologicznego do doświadczeń

Oświadczam także, że samodzielna oraz możliwa do wyodrębnienia część ww. prac wykazuje indywidualny wkład mgr **Karoliny Olbrich** przy opracowywaniu koncepcji badań, przeprowadzeniu części eksperymentalnej, analizie i interpretacji wyników niniejszych prac. Jednocześnie wyrażam zgodę na przedłożenie ww. prac przez mgr **Karolinę Olbrich** jako część rozprawy doktorskiej w formie spójnego tematycznie zbioru artykułów opublikowanych w czasopismach naukowych.

Janik-Olchawa
(podpis współautora)

Kraków, 1.03.2023
(miejscowość, data)

Dr Natalia Janik-Olchawa
(tytuł zawodowy, imię i nazwisko)
Instytut Zoologii i Badań Biomedycznych UJ
(instytucja)
Gronostajowa 9
(adres)

OŚWIADCZENIE

Jako współautor pracy pt.:
"Vibrational spectroscopy methods for investigation of the animal models of glioblastoma multiforme" (w recenzji),

oświadczam, że mój wkład w powstanie ww. pracy obejmował:
- prowadzenie hodowli komórkowych i przygotowanie materiału biologicznego do doświadczeń

Oświadczam także, że samodzielna oraz możliwa do wyodrębnienia część ww. pracy wykazuje indywidualny wkład mgr **Karoliny Olbrich** przy opracowywaniu koncepcji badań, przeprowadzeniu części eksperymentalnej, analizie i interpretacji wyników niniejszej pracy. Jednocześnie wyrażam zgodę na przedłożenie ww. pracy przez mgr **Karolinę Olbrich** jako część rozprawy doktorskiej w formie spójnego tematycznie zbioru artykułów opublikowanych w czasopismach naukowych.

Janik-Olchawa
.....
(podpis współautora)

Kraków, 20.02.2023
(miejscowość, data)

mgr Kamil Kaczor
(tytuł zawodowy, imię i nazwisko)
Wydział Fizyki i Informatyki Stosowanej AGH
(instytucja)
al. Mickiewicza 30, 30-059 Kraków
(adres)

OŚWIADCZENIE

Jako współautor pracy pt.:
"Vibrational spectroscopy methods for investigation of the animal models of glioblastoma multiforme" (w recenzji),

oświadczam, że mój wkład w powstanie ww. pracy obejmował: przeprowadzenie części eksperymentalnej, analizę i interpretację wyników niniejszej pracy

Oświadczam także, że samodzielna oraz możliwa do wyodrębnienia część ww. pracy wykazuje indywidualny wkład mgr **Karoliny Olbrich** przy opracowywaniu koncepcji badań, przeprowadzeniu części eksperymentalnej, analizie i interpretacji wyników niniejszej pracy. Jednocześnie wyrażam zgodę na przedłożenie ww. pracy przez mgr **Karolinę Olbrich** jako część rozprawy doktorskiej w formie spójnego tematycznie zbioru artykułów opublikowanych w czasopismach naukowych.

Kamil Kaczor
(podpis współautora)

Kielce, dnia 01.03.2023

Dr hab. Aldona Kubala-Kukuś, prof. UJK
(tytuł zawodowy, imię i nazwisko)
Instytut Fizyki, Uniwersytet Jana Kochanowskiego w Kielcach
(instytucja)
Ul. Uniwersytecka 7, 25-435 Kielce
(adres)

OŚWIADCZENIE

Jako współautor pracy pt.:
"The assessment of the usability of selected instrumental techniques for the elemental analysis of biomedical samples" (Sci Rep 2021),

oświadczam, że mój wkład w powstanie ww. pracy obejmował:
..... wstępną redakcję manuskryptu .....

Oświadczam także, że samodzielna oraz możliwa do wyodrębnienia część ww. pracy wykazuje indywidualny wkład mgr **Karoliny Olbrich** przy opracowywaniu koncepcji badań, przeprowadzeniu części eksperymentalnej, analizie i interpretacji wyników niniejszej pracy. Jednocześnie wyrażam zgodę na przedłożenie ww. pracy przez mgr **Karolinę Olbrich** jako część rozprawy doktorskiej w formie spójnego tematycznie zbioru artykułów opublikowanych w czasopismach naukowych.

Aldona Kubala-Kukuś
(podpis współautora)

Kielce, 01.03.2023
(miejscowość, data)

Dr hab. Aldona Kubala-Kukuś, prof. UJK
(tytuł zawodowy, imię i nazwisko)
Instytut Fizyki, Uniwersytet Jana Kochanowskiego w Kielcach
(instytucja)
Ul. Uniwersytecka 7, 25-435 Kielce
(adres)

OŚWIADCZENIE

Jako współautor pracy pt.:
"The first total reflection X-ray fluorescence round-robin test of mammalian tissue samples: preliminary results" (w recenzji),

oświadczam, że mój wkład w powstanie ww. pracy obejmował:
..... wykonanie części pomiarów TXRF .....

Oświadczam także, że samodzielna oraz możliwa do wyodrębnienia część ww. pracy wykazuje indywidualny wkład mgr **Karoliny Olbrich** przy opracowywaniu koncepcji badań, przeprowadzeniu części eksperymentalnej, analizie i interpretacji wyników niniejszej pracy. Jednocześnie wyrażam zgodę na przedłożenie ww. pracy przez mgr **Karolinę Olbrich** jako część rozprawy doktorskiej w formie spójnego tematycznie zbioru artykułów opublikowanych w czasopismach naukowych.

Aldona Kubala-Kukuś
(podpis współautora)

Girona, 28th of February 2023

Universitat de Girona

Dr. Eva Marguí
Department of Chemistry
University of Girona
C/M.Aurèlia Capmany, 69
17003-Girona

CO-AUTHOR CONFIRMATION

As a co-author of publication entitled
"The first total reflection X-ray fluorescence round-robin test of mammalian tissue samples: preliminary results" (in review),

I declare that my contribution to the creation of the above-mentioned work included experimental measurements as well as writing-review & editing.

I declare that a separate part of the above-mentioned work demonstrate the individual contribution from **Karolina Olbrich** in developing the research concept, conducting the experimental part as well as analyzing and interpreting the results. I give my permission for the above-mentioned work to be submitted by **Karolina Olbrich** as part of a doctoral dissertation in the form of a thematically coherent collection of articles published in scientific journals.

EVA MARGUÍ GRABULOSA - DNI 43632717S

Firmado digitalmente por EVA MARGUÍ GRABULOSA - DNI 43632717S
Fecha: 2023.02.28 10:21:28 +01'00'

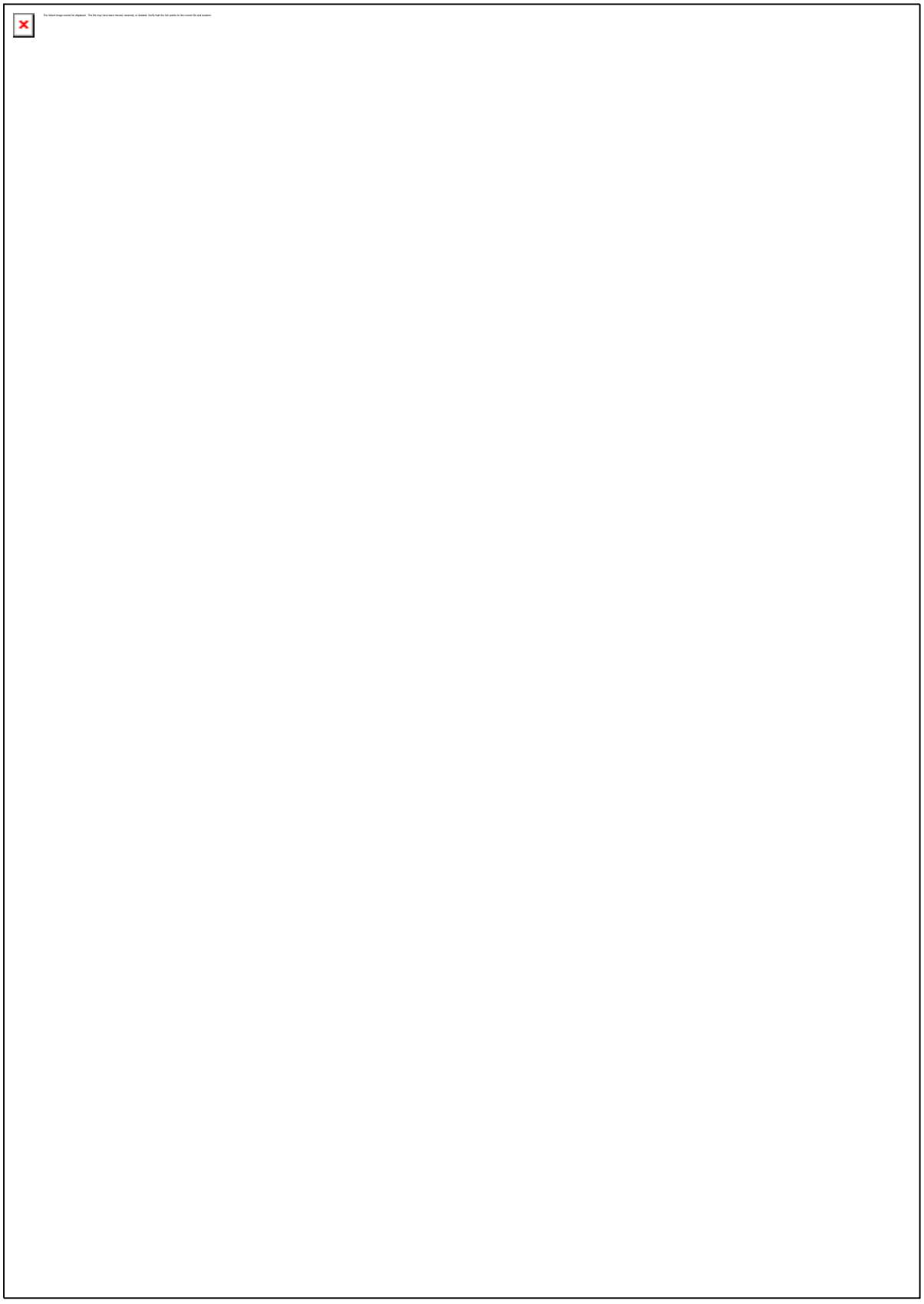

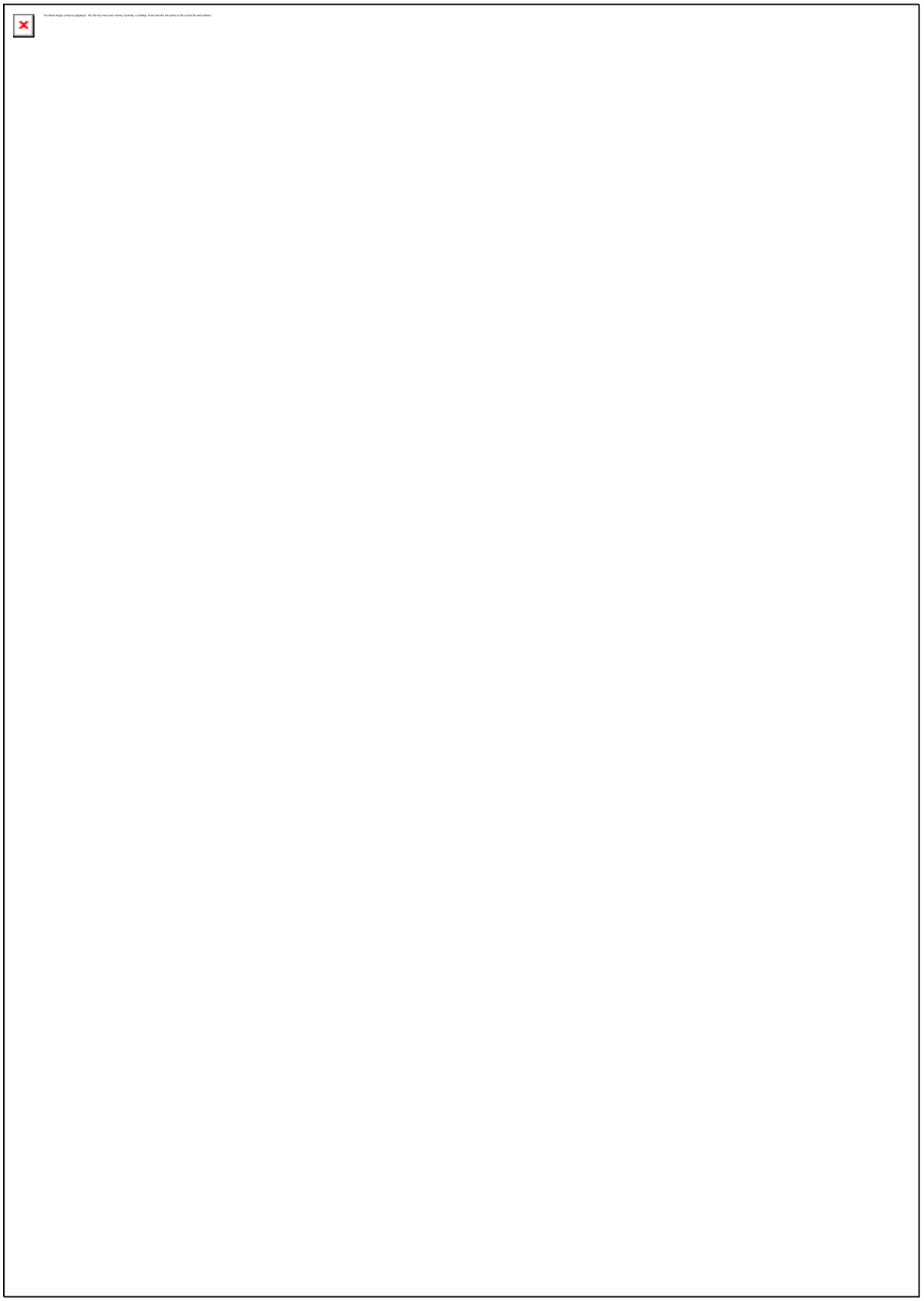

Kraków, dnia 28.02.2023

Mgr inż. Karolina Olbrich
(tytuł zawodowy, imię i nazwisko)
WFiIS AGH
(instytucja)
Al. Mickiewicza 30, 30-059 Kraków
(adres)

OŚWIADCZENIE

Jako współautor prac pt.:

1. "Comparison of Elemental Anomalies Following Implantation of Different Cell Lines of Glioblastoma Multiforme in the Rat Brain: A Total Reflection X-ray Fluorescence Spectroscopy Study" (ACS Chem. Neurosci. 2020),
2. "The assessment of the usability of selected instrumental techniques for the elemental analysis of biomedical samples" (Sci Rep 2021),
3. "Altered Elemental Distribution in Male Rat Brain Tissue as a Predictor of Glioblastoma Multiforme Growth—Studies Using SR-XRF Microscopy" (Int. J. Mol. Sci. 2022),

oświadczam, że mój wkład w powstanie ww. prac obejmował:

1. udział w koncepcji i metodologii badań, udział w eksperymencie ze zwierzętami, przygotowanie próbek, wykonanie pomiarów, analiza i dyskusja wyników, walidacja, przygotowanie tekstu publikacji;
2. udział w koncepcji i metodologii badań, przeprowadzenie przeglądu literatury, analiza danych, porównanie parametrów walidacyjnych, przygotowanie tekstu publikacji;
3. udział w koncepcji i metodologii badań, udział w eksperymencie ze zwierzętami, analiza i dyskusja wyników, przygotowanie tekstu publikacji.

Oświadczam także, że samodzielna oraz możliwa do wyodrębnienia część ww. prac wykazuje mój indywidualny wkład przy opracowywaniu koncepcji badań, przeprowadzeniu części eksperymentalnej, analizie i interpretacji wyników niniejszych prac.

Karolina Olbrich
(podpis współautora)

Kraków, dnia 28.02.2023

Mgr inż. Karolina Olbrich
(tytuł zawodowy, imię i nazwisko)
WFiIS AGH
(instytucja)
Al. Mickiewicza 30, 30-059 Kraków
(adres)

OŚWIADCZENIE

Jako współautor pracy pt.:
"Vibrational spectroscopy methods for investigation of the animal models of glioblastoma multiforme" (w recenzji),

oświadczam, że mój wkład w powstanie ww. pracy obejmował:
udział w koncepcji i metodologii badań, udział w eksperymencie ze zwierzętami, wykonanie pomiarów metodą FTIR, analiza i dyskusja wyników, przygotowanie tekstu publikacji.

Oświadczam także, że samodzielna oraz możliwa do wyodrębnienia część ww. pracy wykazuje mój indywidualny wkład przy opracowywaniu koncepcji badań, przeprowadzeniu części eksperymentalnej, analizie i interpretacji wyników niniejszej pracy.

Karolina Olbrich
(podpis współautora)

Kraków, dnia 28.02.2023

Mgr inż. Karolina Olbrich
(tytuł zawodowy, imię i nazwisko)
WFiIS AGH
(instytucja)
Al. Mickiewicza 30, 30-059 Kraków
(adres)

OŚWIADCZENIE

Jako współautor pracy pt.:
"The first total reflection X-ray fluorescence round-robin test of mammalian tissue samples: preliminary results" (w recenzji),

oświadczam, że mój wkład w powstanie ww. pracy obejmował:
udział w koncepcji i metodologii badań, przygotowanie próbek, wykonanie części pomiarów, analiza i podsumowanie wyników, walidacja, przygotowanie tekstu publikacji.

Oświadczam także, że samodzielna oraz możliwa do wyodrębnienia część ww. pracy wykazuje mój indywidualny wkład przy opracowywaniu koncepcji badań, przeprowadzeniu części eksperymentalnej, analizie i interpretacji wyników niniejszej pracy.

Karolina Olbrich
(podpis współautora)

Kraków, dnia 27.02.2023

Dr Beata Ostachowicz
(tytuł zawodowy, imię i nazwisko)
WFiIS, AGH
(instytucja)
30-040 Kraków, Al. Mickiewicza 30
(adres)

OŚWIADCZENIE

Jako współautor pracy pt.:
"Comparison of Elemental Anomalies Following Implantation of Different Cell Lines of Glioblastoma Multiforme in the Rat Brain: A Total Reflection X-ray Fluorescence Spectroscopy Study" (ACS Chem. Neurosci. 2020),

oświadczam, że mój wkład w powstanie ww. pracy obejmował:
udział w pomiarach składu pierwiastkowego próbek metodą całkowitego odbicia promieniowania rentgenowskiego (TXRF).

Oświadczam także, że samodzielna oraz możliwa do wyodrębnienia część ww. pracy wykazuje indywidualny wkład mgr **Karoliny Olbrich** przy opracowywaniu koncepcji badań, przeprowadzeniu części eksperymentalnej, analizie i interpretacji wyników niniejszej pracy. Jednocześnie wyrażam zgodę na przedłożenie ww. pracy przez mgr **Karolinę Olbrich** jako część rozprawy doktorskiej w formie spójnego tematycznie zbioru artykułów opublikowanych w czasopismach naukowych.

Beata Ostachowicz
.....
(podpis współautora)

Kraków, dnia……..

Prof. dr hab. Zuzanna Setkowicz-Janeczko
(tytuł zawodowy, imię i nazwisko)
Instytut Zoologii i Badań Biomedycznych
Uniwersytet Jagielloński
(instytucja)
Ul. Gronostajowa 9…
(adres)

OŚWIADCZENIE

Jako współautor prac pt.:

1. "Comparison of Elemental Anomalies Following Implantation of Different Cell Lines of Glioblastoma Multiforme in the Rat Brain: A Total Reflection X-ray Fluorescence Spectroscopy Study" (ACS Chem. Neurosci. 2020),
2. "The assessment of the usability of selected instrumental techniques for the elemental analysis of biomedical samples" (Sci Rep 2021),
3. "Altered Elemental Distribution in Male Rat Brain Tissue as a Predictor of Glioblastoma Multiforme Growth—Studies Using SR-XRF Microscopy" (Int. J. Mol. Sci. 2022),

oświadczam, że mój wkład w powstanie ww. prac obejmował:

1. Przeprowadzenie części eksperymentu na zwierzętach
2. Twórczą dyskusję manuskryptu

Oświadczam także, że samodzielna oraz możliwa do wyodrębnienia część ww. prac wykazuje indywidualny wkład mgr **Karoliny Olbrich** przy opracowywaniu koncepcji badań, przeprowadzeniu części eksperymentalnej, analizie i interpretacji wyników niniejszych prac. Jednocześnie wyrażam zgodę na przedłożenie ww. prac przez mgr **Karolinę Olbrich** jako część rozprawy doktorskiej w formie spójnego tematycznie zbioru artykułów opublikowanych w czasopismach naukowych.

Zuzanna Setkowicz-Janeczko

Elektronicznie podpisany przez Zuzanna Setkowicz-Janeczko
Data: 2023.08.07 14:05:17 +01'00'

(podpis współautora)

.....
(miejscowość, data)

Prof. dr hab. Zuzanna Setkowicz-Janeczko
(tytuł zawodowy, imię i nazwisko)
Instytut Zoologii i Badań Biomedycznych
Uniwersytet Jagielloński
(instytucja)
Ul. Gronostajowa 9…
(adres)

OŚWIADCZENIE

Jako współautor pracy pt.:
"Vibrational spectroscopy methods for investigation of the animal models of glioblastoma multiforme" (w recenzji),
oświadczam, że mój wkład w powstanie ww. pracy obejmował:

1. Przeprowadzenie części eksperymentu na zwierzętach
2. Twórczą dyskusję manuskryptu

Oświadczam także, że samodzielna oraz możliwa do wyodrębnienia część ww. pracy wykazuje indywidualny wkład mgr **Karoliny Olbrich** przy opracowywaniu koncepcji badań, przeprowadzeniu części eksperymentalnej, analizie i interpretacji wyników niniejszej pracy. Jednocześnie wyrażam zgodę na przedłożenie ww. pracy przez mgr **Karolinę Olbrich** jako część rozprawy doktorskiej w formie spójnego tematycznie zbioru artykułów opublikowanych w czasopismach naukowych.

Zuzanna Setkowicz-Janeczko
Elektronicznie podpisany przez Zuzanna Setkowicz-Janeczko
Data: 2023.03.07 14:04:48 +01'00'

.....
(podpis współautora)

.....
(miejscowość, data)

Prof. dr hab. Zuzanna Setkowicz-Janeczko
(tytuł zawodowy, imię i nazwisko)
Instytut Zoologii i Badań Biomedycznych
Uniwersytet Jagielloński
(instytucja)
Ul. Gronostajowa 9…
(adres)

OŚWIADCZENIE

Jako współautor pracy pt.:
"The first total reflection X-ray fluorescence round-robin test of mammalian tissue samples: preliminary results" (w recenzji),
oświadczam, że mój wkład w powstanie ww. pracy obejmował:

1. Przeprowadzenie części eksperymentu na zwierzętach
2. Twórczą dyskusję manuskryptu

Oświadczam także, że samodzielna oraz możliwa do wyodrębnienia część ww. pracy wykazuje indywidualny wkład mgr **Karoliny Olbrich** przy opracowywaniu koncepcji badań, przeprowadzeniu części eksperymentalnej, analizie i interpretacji wyników niniejszej pracy. Jednocześnie wyrażam zgodę na przedłożenie ww. pracy przez mgr **Karolinę Olbrich** jako część rozprawy doktorskiej w formie spójnego tematycznie zbioru artykułów opublikowanych w czasopismach naukowych.

Zuzanna Setkowicz-Janeczko
Elektronicznie podpisany przez Zuzanna Setkowicz-Janeczko
Data: 2023.03.07 14:04:19 +01'00'

.....
(podpis współautora)

Karlsruhe, 06. February 2023
(Place and date)

Dr. Rolf Simon
(Professional title, name and surname)

Karlsruhe Institute of Technology
Institute for Photon Science and Synchrotron Radiation
(Institution)

Hermann-von-Helmholtz-Platz 1
76344 Eggenstein-Leopoldshafen, Germany
(Address)

CO-AUTHOR CONFIRMATION

As a co-author of the publication entitled

"Altered Elemental Distribution in Male Rat Brain Tissue as a Predictor of Glioblastoma Multiforme Growth—Studies Using SR-XRF Microscopy" (Int. J. Mol. Sci. 2022),

Hereby, I declare that my contribution to the above-mentioned paper was to prepare the beamline FLUO at the KIT Synchrotron Light Source for the experiment.

I declare that a separatable part of the above-mentioned paper demonstrates the individual contribution from **Karolina Olbrich** in developing the research concept, conducting the experiment as well as analyzing and interpreting the results. I give my permission for the above-mentioned paper to be submitted by **Karolina Olbrich** as a part of her doctoral dissertation in the form of a thematically coherent collection of papers published in scientific journals.

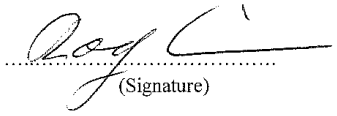

(Signature)

KRAKÓW 06.03.2023
(miejscowość, data)

DR INŻ. PAWEŁ WRÓBEL
(tytuł zawodowy, imię i nazwisko)
AGH WFiIS
(instytucja)
REYMONTA 19, 30-059 KRAKÓW
(adres)

OŚWIADCZENIE

Jako współautor pracy pt.:
"The first total reflection X-ray fluorescence round-robin test of mammalian tissue samples: preliminary results" (w recenzji),
oświadczam, że mój wkład w powstanie ww. pracy obejmował:
PRZEPROWADZENIU WALIDACJI I REDAGOWANIU MANUSKRYPTU

Oświadczam także, że samodzielna oraz możliwa do wyodrębnienia część ww. pracy wykazuje indywidualny wkład mgr **Karoliny Olbrich** przy opracowywaniu koncepcji badań, przeprowadzeniu części eksperymentalnej, analizie i interpretacji wyników niniejszej pracy. Jednocześnie wyrażam zgodę na przedłożenie ww. pracy przez mgr **Karolinę Olbrich** jako część rozprawy doktorskiej w formie spójnego tematycznie zbioru artykułów opublikowanych w czasopismach naukowych.

Paweł Wróbel
(podpis współautora)

Kielce, 01.03.2023
(miejscowość, data)

Mgr Jolanta Wudarczyk-Moćko
(tytuł zawodowy, imię i nazwisko)
Świętokrzyskie Centrum Onkologii
(instytucja)
Ul. Artwińskiego 3, 25-734 Kielce
(adres)

OŚWIADCZENIE

Jako współautor pracy pt.:
"The first total reflection X-ray fluorescence round-robin test of mammalian tissue samples: preliminary results" (w recenzji),

oświadczam, że mój wkład w powstanie ww. pracy obejmował:
……wykonanie części pomiarów TXRF ……..

Oświadczam także, że samodzielna oraz możliwa do wyodrębnienia część ww. pracy wykazuje indywidualny wkład mgr **Karoliny Olbrich** przy opracowywaniu koncepcji badań, przeprowadzeniu części eksperymentalnej, analizie i interpretacji wyników niniejszej pracy. Jednocześnie wyrażam zgodę na przedłożenie ww. pracy przez mgr **Karolinę Olbrich** jako część rozprawy doktorskiej w formie spójnego tematycznie zbioru artykułów opublikowanych w czasopismach naukowych.

Jolanta Wudarczyk-Moćko
……
(podpis współautora)

Oryginalne wersje publikacji i manuskryptów stanowiących podstawę rozprawy

A1 Karolina Płaneta, Aldona Kubala-Kukuś, Agnieszka Dróżdż, Katarzyna Matusiak, Zuzanna Setkowicz-Janeczko, Joanna Chwiej, *The assessment of the usability of selected instrumental techniques for the elemental analysis of biomedical samples*, Sci. Rep. 11, 3704 (2021) - **strony 70-100.**

Suplement do pracy A1 - **strony 101-120.**

A2 Karolina Płaneta, Zuzanna Setkowicz, Natalia Janik-Olchawa, Katarzyna Matusiak, Damian Ryszawy, Agnieszka Dróżdż, Krzysztof Janeczko, Beata Ostachowicz, Joanna Chwiej, *Comparison of elemental anomalies following implantation of different cell lines of glioblastoma multiforme in the rat brain: a total reflection X‑ray fluorescence spectroscopy study*, ACS Chem. Neurosci. 11(24):4447-4459 (2020) - **strony 121-133.**

Suplement do pracy A2 - **strony 134-135.**

A3 Karolina Płaneta, Zuzanna Setkowicz, Mateusz Czyżycki, Natalia Janik-Olchawa, Damian Ryszawy, Krzysztof Janeczko, Rolf Simon, Tilo Baumbach, Joanna Chwiej, *Altered elemental distribution in male rat brain tissue as a predictor of glioblastoma multiforme growth — studies using SR-XRF microscopy*, In. J. Mol. Sci. 23,703 (2022) - **strony 136-155.**

S1 Karolina Olbrich, Aldona Kubala-Kukuś, Eva Margui, Ramon Fernández Ruiz, Katarzyna Matusiak, Jolanta Wudarczyk-Mocko, Paweł Wróbel, Zuzanna Setkowicz, Joanna Chwiej, *The first total reflection X-ray fluorescence round-robin test of mammalian tissue samples: preliminary results*, (w recenzji) - **strony 156-175.**

S2 Karolina Olbrich, Zuzanna Setkowicz, Kamil Kawon, Mateusz Czyzycki, Natalia Janik-Olchawa, Ilaria Carlomagno, Giuliana Aquilanti, Joanna Chwiej, *Vibrational spectroscopy methods for investigation of the animal models of glioblastoma multiforme*, (w recenzji) - **strony 176-200.**

scientific reports

Check for updates

OPEN

The assessment of the usability of selected instrumental techniques for the elemental analysis of biomedical samples

Karolina Planeta[1], Aldona Kubala-Kukus[2,3], Agnieszka Drozdz[1], Katarzyna Matusiak[1], Zuzanna Setkowicz[4] & Joanna Chwiej[1]✉

The fundamental role of major, minor and trace elements in different physiological and pathological processes occurring in living organism makes that elemental analysis of biomedical samples becomes more and more popular issue. The most often used tools for analysis of the elemental composition of biological samples include Flame and Graphite Furnace Atomic Absorption Spectroscopy (F-AAS and GF-AAS), Inductively Coupled Plasma Optical Emission Spectroscopy (ICP-OES) and Inductively Coupled Plasma Mass Spectrometry (ICP-MS). Each of these techniques has many advantages and limitations that should be considered in the first stage of planning the measurement procedure. Their reliability can be checked in the validation process and the precision, trueness and detection limits of elements belong to the most frequently determined validation parameters. The main purpose of this paper was the discussion of selected instrumental techniques (F-AAS, GF-AAS, ICP-OES and ICP-MS) in term of the achieved validation parameters and the usefulness in the analysis of biological samples. The focus in the detailed literature studies was also put on the methods of preparation of the biomedical samples. What is more based on the own data the usefulness of the total reflection X-ray fluorescence spectroscopy for the elemental analysis of animal tissues was examined. The detection limits of elements, precision and trueness for the technique were determined and compared with the literature data concerning other of the discussed techniques of elemental analysis. Reassuming, the following paper is to serve as a guide and comprehensive source of information concerning the validation parameters achievable in different instrumental techniques used for the elemental analysis of biomedical samples.

Instrumental techniques are a group of research tools applied for investigation of analytes in various types of matter. These include i.a. spectroscopic techniques and mass spectrometry. Spectroscopic techniques are based on the generation and interpretation of the atomic spectra obtained as a result of the interaction of electromagnetic radiation with the analyte. These interactions involve physical phenomena such as absorption or emission and depending on the type of interaction, spectroscopic techniques are distinguished[1]. Mass spectrometry is based on the ionization of atoms contained in the analysed sample and separation of the formed charged particles based on their mass to charge ratio[2]. Both atomic and mass spectra allow obtaining qualitative and quantitative information on the composition of the analyte. Atomic absorption spectroscopy (AAS), inductively coupled plasma optical emission spectroscopy (ICP-OES) and inductively coupled plasma mass spectrometry (ICP-MS) are widely used in the studies on the elemental composition of samples of various origin, including biomedical samples[3–9].

An important issue related to the reliability of the results of analyses is their validation. It is a process of determining the values of parameters characterizing the efficiency of operation and the suitability of a given technique for the research purposes set. Validation is carried out to ensure that the analysis process is fair and precise. Demonstrating the reliability of the results obtained in this way is very important both for their correct interpretation and for the possibility of their future use by other research groups. In the literature, the most

[1]Faculty of Physics and Applied Computer Science, AGH University of Science and Technology, Krakow, Poland. [2]Institute of Physics, Jan Kochanowski University, Kielce, Poland. [3]Holly Cross Cancer Centre, Kielce, Poland. [4]Institute of Zoology and Biomedical Research, Jagiellonian University, Krakow, Poland. ✉email: joanna.chwiej@fis.agh.edu.pl

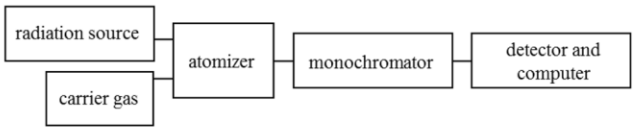

Figure 1. Block diagram of a typical instrument used for atomic absorption spectroscopy.

frequently appearing validation parameters for quantitative elemental analyses are the accuracy and precision of the measurement as well as the detection limit of the determined elements[10–13].

The biomedical samples can be divided into three main categories. The first category are liquid samples, which include blood and its liquid components[14], urine[15], cerebrospinal[16] or amniotic fluid[17]. There is also a group of soft tissues, which are mainly organ or skin samples[18–22]. The third category includes hard tissues, i.e. hair[23], nails[24], kidney stones[25], teeth[26] and bones[12]. These samples can be of both human and animal origin, and the latter especially in the case of in vivo experiments[27–31]. The elements that they contain perform many important functions, and maintaining their content at the appropriate levels is crucial for the proper functioning of the living organism[32–35]. What is more, the changes in their tissue concentrations may reflect physiological and pathological processes occurring in the body[36–39]. Besides the analysis of essential elements, their physiological concentration and changes occurring during different pathological states, the investigations are focused on the evaluation of the content of toxic elements in case of poisoning or environmental exposure[7,8,40–42].

Elemental analysis of biological samples is a difficult issue, mainly, due to their complex composition and to the low levels of the elements[43,44]. Therefore, among different factors that should be taken into account when choosing an analytical tool, the most important are: minimum detectable element concentrations, the number of elements one want to determine, the expected accuracy and precision of measurements or the available amount of research material[45–48]. Awareness of the analytical capabilities of a given technique is a key element to correctly plan the measurement procedure.

The following work was divided into two parts. The purpose of the first one was to discuss the use of AAS, ICP-OES and ICP-MS in the quantitative elemental analysis of biomedical samples. The values of accuracy, precision and detection limits of elements for various techniques were compared and discussed. What is more, the summary concerning the methods of preparation of biomedical samples was presented. The second part of the work was the evaluation of the usefulness of the total reflection X-ray fluorescence (TXRF) technique for elemental analysis of tissue samples. The TXRF, due to its analytical capabilities and sample preparation requirements, is similar to the discussed instrumental techniques of elemental analysis and therefore was chosen from the collection of methods based on X-ray fluorescence for comparison with other presented techniques. The principles of the TXRF and examples of its use for analysis of biomedical samples were discussed. The validation parameters for the technique were determined and compared with the values achieved for other of the discussed analytical techniques.

Selected instrumental techniques and their use for elemental analysis of biomedical samples

Atomic absorption spectroscopy (AAS). Atomic absorption spectroscopy is one of the most commonly used technique in analytical laboratories. Due to its simplicity and low operating costs, AAS in widely applied in single-elemental analysis. The basic principle of the AAS technique is that energy-characteristic radiation is selectively absorbed by free atoms of elements. The number of free atoms in the absorbing medium is proportional to the concentration of the element in the analysed sample. The absorbance, measured in the AAS technique, depends on the number of free atoms and thus on their concentration in the sample. This dependence is the basis for quantitative analyses carried out by AAS. Depending on the atomization method, two types of AAS are distinguished: flame (F-AAS) and graphite-furnace (GF-AAS). In the F-AAS, sample in an aerosol form is introduced into a burning flame, while in GF-AAS sample is transferred into a special cuvette, heated and gradually evaporated[49,50]. The block diagram of the apparatus used in the AAS technique is shown in the Fig. 1.

GF-AAS is based on the use of flameless atomizer, usually graphite cuvette to which sample is introduced and gradually heated. Increasing temperature results in drying the sample, removal of its matrix and atomization. Before measurement, substances reducing the volatility of the analysed element are added to the sample. These substances are called modifiers and their used make easier to separate analysed element from the matrix. Sometimes, interactions between free atoms and atomizer occur and it is the main disadvantage of this technique[49]. Xu et al. analysed the concentration of Al in human brain tissue. Due to serious interferences occurring between Al and P, which content is high in this type of samples, potassium dichromate as a chemical modifier was applied. It resulted in a decrease of elemental disturbances and improvement of Al determination[51]. Dudek-Adamska et al. investigated how the addition of chemical modifier influences the determination of Ni in human organ samples. For this purpose, magnesium nitrate, palladium nitrate and mixture of magnesium nitrate and ammonium dihydrogen phosphate were tested as chemical modifiers. Based on the performed validation tests they found that the determination of Ni was the best without any matrix modifiers and at temperatures 1300 °C and 2400 °C for pyrolysis and atomization, respectively[19]. A similar study performed for Cr showed better accuracy when magnesium nitrate was used as chemical modifier at temperatures of pyrolysis equals 1400 °C and atomization—2500 °C[52]. Application of palladium or magnesium nitrate as chemical modifiers for Al and Mn determination in human hair samples decreased the influence of background on the obtained results[53]. In turn,

in case of Al analysis in human bone samples, there was no need to use an additional modifier because its function was fulfilled by Ca present at high concentration in bones[12].

The type of used flame in F-AAS measurements depends on the elements under analysis. Goldberg et al. determined physiological concentrations of Cu, Mn, Fe and Ca in six regions of human brain. To analyse Cu and Mn, they used graphite furnace, while for Fe and Ca, air-acetylene and nitrous oxide-acetylene flames, respectively[54]. Flame AAS was used to determine the concentration of potentially toxic elements (Fe, Mg, Ca, Cu, Zn, Cr, Cd and Pb) in human hair samples. The technique was not useful for Cd and Pb determination due to the fact that results obtained for these elements were below the detection limits[34]. By using the GF-AAS technique human breast samples were analysed by Leung et al. The authors investigated the differences in Si concentration between tissues taken from women with and without silicone implants[55]. In cancerous breast tissue concentrations of Cd, Pb[56] and Al[57] were investigated. Villeneuve et al. determined levels of Fe in liver needle-biopsy samples taken from patients who suffered from cirrhosis and they assessed the variability of Fe content depending on the region of tissue origin[58]. Using the GF-AAS the possible exposure of steel industry workers on trace and toxic elements, produced in manufactures processes, was investigated. Pb, Cd, Ni, Cr[59] as well as As, Cu, Co and Mn[60] concentrations were determined in their blood, urine and hair samples. Campillo et al. developed a fast method for Mo, Cr and Al determination in human urine by GF-AAS. The procedure did not require the sample pre-treatment and the background signal was reduced by addition of hydrogen pyroxide and nitric acid to the sample[15]. Khlifi et al. analysed the content of As, Cd, Cr and Ni in healthy and cancerous tissue from patients suffering from head and neck cancers[61].

Various methods are used for improving the sensitivity of measurements with AAS. Yaman et al. analyzed differences in concentrations of Cd, Cu, Zn, Fe, Mg, Ca and Ni between the cancerous and non-cancerous tissues taken from ovary and endometrium. For better sensitivity of Cd and Cu determination, they used the slotted tube atom trap (STAT)[62]. This device significantly increased the time of residence of the free atoms in the measurement area and allowed to obtain lower detection limits comparing to conventional F-AAS[50]. A very common procedure, leading to sample preconcentration and allowing the determination of elements at the ultra-trace levels, is cloud point extraction (CPE). This method involves adding to the sample some chemical compounds, mostly nonionic surfactants, which at high temperature forms a separate phase in the sample solution. The analyte, found in the acid solution of the sample previously subjected to digestion, concentrates together with the surfactant in a small volume of new established phase and thus it is separated from the sample. The surfactant-rich phase containing an analyte is then subjected to further analysis. CPE was used, among others, by Arain et al. for measurements of Ni content in blood and serum of patients who suffered from oropharyngeal cancer[63]. In turn, Shemirani et al. applied CPE for sample preconcentration analysing the content of Bi in human urine and hair[44]. Dual-cloud point extraction (d-CPE) used for the preconcentration of hair samples before Mn determination by F-AAS allowed to improve the recovery value from 97.1% (without preconcentration) to 99.2% (d-CPE)[64]. Another procedure used for sample preconcentration is solid-phase extraction. Baghban et al. applied it for human hair and nail samples before Cd and Pb determination by F-ASA. To verify the obtained results also GF-AAS measurements were performed[24].

In some studies, different techniques are chosen for the analysis of individual element. Jablonska et al. determined Cd, As, Se and Fe concentrations in the tissue of human breast cancer trying to indicate whether there are relationships between their contents. For Cd and Se, GF-AAS was used with palladium and palladium-magnesium matrix modifier, respectively. Flame AAS was used for Fe determination whilst As concentration was measured using ICP-MS with kinetic energy discrimination chamber, which allowed for the decrease of the influence of polyatomic interferences[65].

The elements such as As, Sb, Pb, Bi, Te, Se and Sn have a properties to form, with a hydrogen, volatile hydrides. This reaction coupled with an atomic absorption spectroscopy constitutes the basis of hydride generation atomic absorption spectroscopy (HG-AAS). Volatile hydrides of elements, which are formed by adding a reducing agent to the sample, are directed to the atomizer in the stream of carrier gas. As the element is isolated from the sample, matrix effects are reduced, what results in the improvement of detection limits. A technique basing on similar operating principles which allows for the determination of mercury, is called the Cold vapour atomic absorption spectroscopy (CV-AAS). Lech et al. used ICP-OES and CV-AAS for Hg determination in human organs and blood. CV-AAS is one of the primary tools applied for mercury determination. Due to the fact that this element might occur as the free atoms at room temperature, application of furnace is not necessary. As a result of adding a reducing agent to acid environment of analysed sample solution, the mercury ions contained in sample are reduced to its elemental form. Then they are transported in the stream of carrier gas to the measuring chamber. In this case, CV-AAS turned out to be a more sensitive technique of Hg determination in blood, characterized with the lowest detection limit of the element[46].

Inductively coupled plasma optical emission spectroscopy (ICP-OES). Inductively coupled plasma optical emission spectroscopy is currently one of the most sensitive and precise technique of instrumental analysis. It is based on the measurement of radiation emitted by atoms (in the gaseous form) passing from excited to the lower energy state. Plasma, electrically neutral gas consisting of free electrons and positive ions, is the source of atoms excitations and it is generated by inductively coupled system. The resulting emission spectrum is linear, i.e. it consist of series of lines corresponding to specific wavelengths of radiation emitted by atom during transition between energy levels. The arrangement of emission lines is unique for particular element, therefore it is possible to identify it and determine its content in the sample.

ICP-OES apparatus consists of a sample supply system, plasma generation system, analyzer, detector and computer. Its block diagram is presented in Fig. 2. The sample supply system is usually based on nebulization or thermal evaporation. In the first case, the sample in the form of solution is dispersed into the carrier gas stream

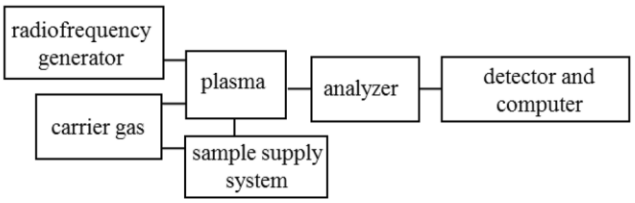

Figure 2. Block diagram of a typical instrument used for ICP-OES.

and form an aerosol. In thermal evaporation, sample is heated which results in its evaporation and introduction into plasma with gas[66]. The technique of generating volatile hydrides is also used[67]. Radiation emitted by excited atoms goes to the analyzer, usually monochromators or polychromators and then it is registered by detector (photomultipliers or multi-channel spectrometers).

ICP-OES was used to determine physiological concentrations of 13 trace elements (Al, B, Ba, Cd, Co, Cr, Cu, Fe, Mn, Ni, Pb, Se, Sr and Zn) in human autopsy samples taken from cerebellum, heart, kidneys, liver, pancreas, spleen and ovary[3]. Other research aimed to find if there are any correlations between concentrations of different trace elements (Cu, Co, Cr, Fe, Mn, Ni, Se, Zn, Al, Ba, Cd, Pb, Sr) within particular organ and between different organs collected during autopsy. Such information may contribute to better understanding of interactions between trace elements and their distribution in human organs[20]. Chen et al. applied electrothermal vaporization as a sample supply method for determination of Ti, Cu, Cr, Fe, Zn and Ca in human hair and serum. The use of thermal evaporation minimizes matrix effects, allows to measure small amounts of sample and limits the need of its chemical pre-treatment[47]. ICP-OES was one of the techniques used to analyze organ samples taken from a person suspected to mercury poisoning. Blood, stomach, liver and kidney were examined for the content of this element. The technique proved to be useless in case of blood tests, where the Hg level was below the detection limit[46]. Tohno et al. analysed concentrations of Ca, P and Mg in various types of human arteries. It was investigated whether there are dependencies between the contents of particular elements and whether the obtained elemental levels correlate with the age of examined patients[68]. Similar study was carried out by Yang et al. They determined the content of Ca, Mg and Fe in rabbit arteries and developed analytical procedure allowing determination of the elemental composition for very small amount of the sample of biological origin[69]. Naganuma et al. determined the content of S, Mg, Ca, P, Zn, Fe and Al in human round ligaments. They analyzed the elemental changes occurring in tissues with age and the relationships between the contents of particular elements[70]. ICP-OES was one of the techniques used to examine the content of heavy metals (Cu, Fe, Mn, Zn, Cd, Pb) in human brain. This technique, however, did not prove to be useful in assessing of the Pb content, which was lower than the achieved detection limit[45]. Andrasi et al. used the ICP-OES to determine Al, Mg, P and Al, Zn, Cu, Mn and Fe levels in different regions of human brain. They verified differences in concentrations of these elements in samples taken from healthy people and those suffering from Alzheimer's disease[71,72] and analysed the concentrations of Na, K, Mg, Fe, Cu, Mn Zn P and S in normal human brain[73]. The other research concerned the determination of the content of Ca, P, S, Fe, Mg, Zn and Cu in 28 regions of the brain taken from patient suffered from Wilson's disease[74]. The differences in the content of 21 elements (Ag, Al, As, Ba, Ca, Cd, Co, Cr, Cu, Fe, Mg, Mn, Na, Ni, Pb, Sb, Se, Sr, Tl, V and Zn) between healthy liver, breast and lungs and tissues taken from the tumor-altered organs were also examined[75]. ICP-OES was also used by Mohammadi et al. to determine the concentration of Se in human breast cancer tissues[56].

Using the ICP-OES MacLachlan et al. determined the contents of Cu and Zn in liver, kidney and muscle of Australian sheep[76]. The concentrations of Ba, Cd, Co, Cr, Cu, Fe, Hg, Li, Mn, Mo, Ni, Pb, Sr and Zn in wolf liver samples were also evaluated[77]. Due to the extensive use of rats in laboratory experiments, their organs are often the subject of elemental analysis, also using the ICP-OES. Leblondel et al. measured concentrations of 14 elements (Na, K, Ca, Mg, S, P, Fe, Sr, Mn, Cu, Zn, Mo and Ba) in whole blood, plasma, liver, kidney, brain, heart, spleen, skeletal muscle, thymus and bone of rat[78]. In turn, Shapira et al. analyzed whether ketamine affects Ca and Mg concentrations in the brain of head trauma rats[27]. The effect of furosemide on Cd, Cu, Fe, Mg, Pb, Se and Zn contents in rat liver, kidney, lung and serum was also investigated[79]. The ICP-OES was also used in the assessment of the impact of arsenic, administered orally to rats, on the concentration of Cu, Zn and Mn in the liver and kidney[21].

ICP-OES is often used along with the ICP-MS. Using the first technique, the contents of the major elements are determined, whilst ICP-MS is used for trace elements determination. Using such a solution, Takahashi et al. determined the content of P, K, Na, Fe, Mg and Ca in the liver of the Wistar rat[13]. Similarly, concentrations of the major elements (Na, Mg, Si, P, K, Ca, Fe and Zn) in the rat kidney were determined by Shimamura et al.[28] whilst Sivrikaya et al. analysed the influence of Zn supplementation on Pb, Co, Mo, Cr, B, Mg, Fe, Cu, Ca, Zn and Se distribution in this organ[80]. In the literature one can find also information concerning the use of the ICP-OES in the analysis of liquid clinical samples. Korvela et al. checked whether there are differences in the concentration of Ca, Mg, P, K and Na in the cerebrospinal fluid of people suffering from neuropathic pain, subjected to spinal cord stimulation[16]. Cerebrospinal fluid, serum, blood and urine were the subject of investigation of Forte et al. who examined whether there are differences in concentrations of Ca, Cu, Fe, Mg, Si and Zn between the samples of biological fluids taken from healthy people and those suffering from Parkinson's disease[81]. Human blood and plasma were also analysed by Harrington et al. in terms of Ca, Fe, K, Mg and Na contents[32] whilst Chen et al. used electrothermal vaporization to analyse the human serum and determine the content of Ti, Cu, Cr, Fe, Zn

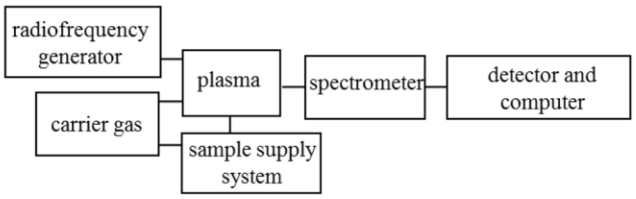

Figure 3. Block diagram of a typical instrument used for ICP-MS.

and Ca. The applied technique of sample introduction allowed for direct analysis of samples with low mass and contributed to the improvement of the detection limits of elements and minimized the matrix effect[47]. Bianchi et al. have undertaken to optimize the ICP-OES measurement procedure aiming at the determination of the content of Li, Na, K, Al, Fe, Mn and Zn in the human serum[82] whilst Rahil-Khazen et al. carried out validation of the procedure of trace elements analysis (Al, B, Ba, Be, Cd, Co, Cr, Cu, Fe, Li, Mn, Ni, Pb, Se, Sr and Zn) in such samples. It was found that ICP-OES cannot be used as a routine technique of human plasma analysis in case of Al, Be, Co, Cd Cr, Ni and Pb as the concentrations of these elements are below the detection or quantification limits. However, the analysis of the mentioned elements could be possible when their concentrations would increase due to the toxication. The other way to get an information about concentrations of these elements, presented by authors, is application of standard addition method. In this method, increasing amounts of analyte are adding to the sample and the signal intensity for a given analyte concentration is measured. Then, a regression line is created and by extrapolation, knowing the signal intensity in the original sample, one can read the element concentration[83]. Hasegawa et al. examined the elemental composition of bone-marrow fluid. Using the ICP-OES, they determined concentrations of Na, K, Fe, P, Ca, Mg, Al and Zn in the samples[35].

The ICP-OES is also used for the elemental analysis of hard biological samples. Sahuquillo et al. determined concentrations of Cu, Fe, Mn and Zn in human gallstones previously prepared using the focused-microwave wet digestion method. They analysed the impact of Ca on the determination of other elements. They found that high Ca level in samples influenced the measured Fe and Zn concentrations and in order to reduce this effect they recommended to prepare a calibration solution with a concentration of Ca similar to those of the sample[25]. ICP-OES has also been used to determine the content of Al, B, Ba, Ca, Cu, Fe, K, Li, Mg, Mn, Na, P, S, Sr, V and Zn in human bone of the ribs. It was checked whether there are dependencies between the levels of elements and the age and sex of people from whom samples were taken[84]. Animal bones (domestic dog) were analysed for Zn, Cu, Pb, Cd and Hg content[85]. Chew et al. used the ICP-OES to analyse Zn, Pb and Cu concentrations in human teeth[26]. The discussed technique was also used to investigate the level of selected elements in human hair[47,86].

Inductively coupled plasma mass spectrometry (ICP-MS). Inductively coupled plasma mass spectrometry is an elemental analysis technique that derives from the ICP-OES. ICP is used here to ionize the atoms of the sample which are afterwards separated and identified based on their mass-to-charge ratio. The composition of ions in plasma is proportional to their concentration in the original sample solution. ICP-MS allows for precise identification as well as quantitative multi-elemental analysis and what is more, it makes possible to measure particular isotopes of the analyzed element. Another important feature of the ICP-MS is the ability to detect and measure elements occurring in the sample in very low concentrations. Therefore, it significantly exceeds the capabilities of other techniques of elemental analysis. Also, analysis of non-metals can be carried out with very good sensitivity. Additional advantages, such as high accuracy and precision of measurements as well as minimal disturbances, make ICP-MS one of the most important and useful technique of trace analysis of biomedical samples[2].

The basis of analysis using mass spectrometry is to obtain the mass spectra of the analysed sample showing the distribution of ions (or other charged particles) as a function of their mass-to-charge ratio. The apparatus for ICP-MS measurements consists of an ICP forming module, a sample introduction system, a mass spectrometer with an ion detector and data acquisition system. It is presented in Fig. 3.

ICP-MS was applied for multielemental (Al, As, Ba, Ca, Cd, Co, Cr, Cu, Mg, Mn, Ni, Pb, Sb, Se, Sr, U, V and Zn) analysis of amniotic fluid[17]. It was also used to determine the concentrations of Rb, Cu, Se, Ba, Sr, Zr, Cs, Sb, Sn, Mo, Ag and W in human bone-marrow fluid samples[35]. Korvela et al. analysed Ti, As, Rb, Sr and Ba contents in cerebrospinal fluid of patients with neuropathic pain, who were subjected to spinal cord stimulation[16]. Cerebrospinal fluid as well as blood, serum and urine were the subject of investigation of Forte et al., who determined Al and Mn concentrations in these samples. The purpose of their study was the comparison of elemental composition of samples taken from healthy people and patients diagnosed with Parkinson disease[81]. ICP-MS was also used by Harrington et al. for determination of mineral elements (Na, Ca, Mg, K, Fe, Zn, Cu and Se) content in human blood and serum samples. The authors presented the methodological approach for the analysis of small sample volumes (about 250 µl) and the obtained results were with agreement with the literature data[32]. The concentration of Sb was examined in blood, serum, urine and hair of patients with parasitic disease[87]. The technique was also used for determination of 37 trace elements in more than a hundred human blood samples and the obtained results are to help toxicologist in the assessment of health effects caused by possible environmental exposure to metals[88]. ICP-MS, with high resolution magnetic sector, was applied for determination of physiological concentrations of 16 trace elements in children plasma. For most samples, Cd, Pb, V, Cr and As contents were very low, even below the calculated limits of quantification[89]. Human plasma was also the subject

of the study carried out by Meyer et al., who used ICP-MS for analysis of significant (Mg, Ca, Fe, Cu, Zn, Mo, Se, I) and toxic (As and Cd) elements[90]. Heitland et al. studied the case of child poisoned with hexavalent chromium and inorganic arsenic. They used ICP-MS to determine a concentration of Cr (VI) in erythrocytes and total Cr and As content in blood, plasma, urine and liver tissue taken from the child. Using high-performance liquid chromatography (HPLC) that allowed to separate the inorganic species of As from sample, they also managed to determine its concentration in urine. The addition of ethanol to urine before measurement reduced non-spectral interferences caused by the presence of carbon. Additionally, this procedure increased the efficiency of nebulization and therefore gave the higher sensitivity of the As determination[8]. The ICP-MS analysis of trace elements in urine was carried out to designate the differences in their concentrations between adults and children[91]. ICP-MS is also used to determine particular isotopes of elements in a sample. Among others, abundances of Fe isotopes in human blood[92] and uranium in human urine samples were analysed[93].

ICP-MS was used for Fe, Cu, Mg, Mn, Ca and Zn analysis in samples taken from 13 regions of human brain. The correlations between elemental composition and age as well as inter-hemispherical differences were investigated[9]. ICP-MS was also applied for quantitative analysis of gadolinium in different regions of the brain taken post-mortem from patients in which Gd was used as a contrast agent during MRI examination[94]. Panayi et al. determined concentrations of Cd and Zn in brain samples taken from patients who suffered from Alzheimer's disease and from senile involution cortical changes[95]. ICP-MS was used also for multielemental (48 elements) analysis of human lung samples collected during surgical procedures. Dependencies between elemental composition and the patient gender, nicotine smoking and occupational exposure to metals were examined[18]. Boulyga et al. performed elemental analysis of thyroid tissue taken from people living in the Chernobyl area. Despite the small quantities of examined material (down to 1 mg) they obtained high sensitivity of measurements. In the case of iodine determination, they observed losses of this element due to its volatility and high ionization potential. Based on the results obtained from the measurements of certified reference materials (CRM) they calculated correction factor for quantitative analysis of iodine in sample[38]. The ICP-MS was also applied for multielemental analysis of esophageal tissues taken from patients suffered from esophageal squamous cell carcinoma. Concentrations of elements in normal tissue, cancerous tissue and its surrounding area were compared[96]. Using ICP-MS the content of Ca, Cu, Fe, As, Mg, Ni, Cd and Cr in stomach tissue taken from patients with cancer was also determined[97]. In turn, Jablonska et al. measured the concentrations of Cd, As, Se and Fe in breast cancer tissue[65]. Varga et al. examined concentrations of Cr, Mn, Fe, Ni, Cu, Zn, Rb and Pb in liver samples taken from patients suspected with chronic diffuse liver disease[39] whilst Sahin et al. determined Al, Fe, Cd, Mn, Cr, Cu, Pb, Ni, Zn, Ag and Co concentrations in liver of patients suffered from hepatitis B[98]. The technique was also used for determination of Cr, Co and V concentrations in heart samples[99].

Batista et al. used ICP-MS for multielemental analysis of human hair, previously prepared for analysis using ultrasound extraction. However, the method was not useful for Ag, Se and Mo determinations[100]. Prejac et al. analysed human hair and blood for strontium content, assuming that hair can be a long-term biological indicator of nutrition in case of this element[23]. Using ICP-MS, MacLachlan et al. determined the content of As, Cd, Co, Pb, Hg, Mo and Se in liver, kidney and muscle from Australian sheep[76] whilst Garcia-Vaquero et al. examined changes of As, Ca, Cd, Co, Cr, Fe, Hg, Mn, Mo, Ni, Pb, Se, Sn and Zn concentrations in organs of beef calves which were induced by Cu dietary supplementation[101]. In turn, Gui et al. used ICP-MS to measure the concentration of Zr in liver, kidney and urine of rats[102].

Based on the available literature data, charts were prepared to show the frequency of application of selected analytical techniques for the determination of particular elements in biomedical samples. They are placed in the Fig. 4.

As it can be seen from the Fig. 4, the most commonly used techniques of elemental analysis of biomedical samples are ICP-MS and ICP-OES. Probably this results from the fact that they make possible simultaneous multielemental analysis, in contrast to AAS technique usually allowing the determination of single elements. ICP-OES is usually selected for the analysis of major and minor elements, while ICP-MS for trace and ultra-trace ones. This is because ICP-MS offers the lowest detection limits amongst other discussed techniques of elemental analysis. ICP-MS is more versatile, however it is also more complicated and much more expensive comparing to ICP-OES. Therefore, ICP-OES can be a good alternative to ICP-MS, especially in case of analysis of elements occurring in samples at higher concentrations. Such approach was utilized by Harrington et al. who performed a multielemental analysis of human blood and serum. For this purpose, they used the ICP-OES to determine Ca, Mg, Na, K, and ICP-MS for Co, Zn, Cu, Se, Mo, Cr, Mn and Fe[32]. Forte et al. determined Ca, Cu, Fe, Mg, Si and Zn in human body fluids using ICP-OES, whilst concentrations of Al and Mn with the use of ICP-MS[81]. Similar approaches were applied in the works of Korvela et al.[16], Shimamura et al.[28,103], Takahashi et al.[13], MacLachlan et al.[76] and Alimonti et al.[37].

Preparation of biological samples for elemental analysis

In order to enable the analysis of biomedical samples using discussed instrumental techniques removing of its organic matrix is a crucial step. This process is called mineralization and results in oxidation of the hydrogen contained in sample to water, carbon to carbon dioxide and appearing of the free nitrogen. Usually, the sample is decomposed with the use of oxidizing acids in conditions of higher temperature. As a result of mineralization, the volatile, organic components are removed from the sample whilst its inorganic part is transformed to solution which can be analysed.

Based on the information contained in the papers dealing with the elemental analysis of biomedical samples, a summary concerning the used sample preparation methods was made and is placed in Table 1. It can be seen that the most popular is microwave-assisted acid digestion, which is used for liquids and soft or hard tissues dissolution. Microwave energy is supplied directly to the sample, which causes its effective heating and improves

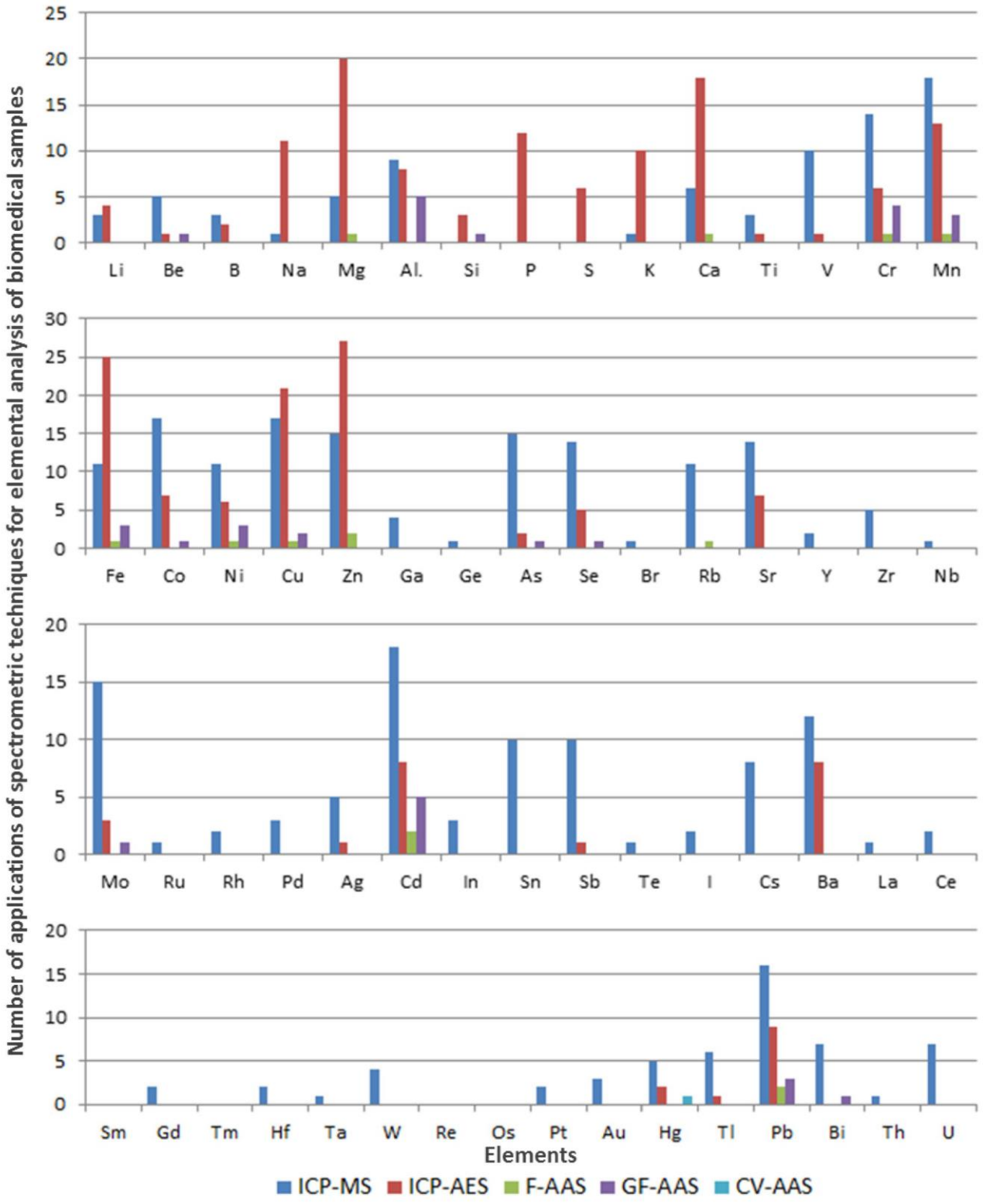

Figure 4. Number of applications of particular analytical technique for elemental analysis of biomedical samples depending on the determined element (based on the papers cited in the following article).

its decomposition. The conditions of microwave heating process, such as temperature and duration is very different. Slightly less often the mineralization of samples in acids with the use of thermal conductivity is used. For this purpose, samples with acid addition are heated either in laboratory ovens or on hotplates. Since the thermal

Sample preparation (method of digestion)		Type of sample
Microwave-assisted acid digestion	Wet sample	Brain[19, 20, 101], stomach[19, 46, 97], liver[19, 20, 46, 77, 101, 102], kidney[19, 20, 46, 101, 102], pancreas[20], spleen[20, 101], heart[19, 20], lung[19], diaphragm[101], breast[65], hair[42, 46, 64, 100], blood[23, 32, 46, 59, 60, 81, 92], serum[32, 82, 83], amniotic fluid[17], urine[59, 60, 102, 104]
	Dry sample	Brain[9, 45, 51, 71, 72, 95, 105], liver[13, 39, 41, 58, 79], kidney[79, 80], heart[79, 99], thyroid[38], lung[18, 79], esophageal[96], muscle[41], breast[57], arteries[69], hair[23, 59, 60], gallstones[25], bone[12]
Thermal-heating acid digestion	Wet sample	Brain[78, 94, 106], cerebrum[21], liver[8, 21, 78], kidney[21, 28, 78], spleen[21], colon[36], heart[78], lung[21], muscle[78], breast[22], skin[21], hair[86], blood[59, 63, 107], serum[63, 90], bone-marrow fluid[35], urine[44, 59], teeth[26], bone[78, 84]
	Dry sample	Brain[27, 45, 71–73], liver[98, 108], muscle[108], breast[55, 56, 109], arteries[68], uteri round ligaments[70], hair[24, 34, 44, 59], fingernail[24], bone[6]
Acid digestion	Wet sample	Stomach[46], liver[46, 76], kidney[46, 76], muscle[76], hair[46, 47], blood[46]
	Dry sample	Liver[110], bone[85]
Sample preparation without digestion procedure		
Preparation of powdered sample followed by dilution in water to obtain slurry		Hair[53]
Dilution with Triton X-100 and chemical modifier		Serum[12]
Dilution with matrix modifier		Serum[55]
Dilution with PTFE emulsion, Triton X-100 and water		Serum[47]
Dilution with Triton X-100		Serum[79]
Dilution with acid and internal standard		Plasma[89]
Dilution with Triton X-100, diammonium hydrogen phosphate (as matrix modifier) and acid		Blood[14]
Dilution with internal standard and Triton X-100		Blood[107]
Dilution with Triton X-100, internal standard and ammonia solution		Blood[8, 88], plasma[8], erythrocytes[8]
Dilution with acid		Cerebrospinal fluid[16]
Dilution with hydrogen peroxide, acid and Triton X-100		Urine[15]
Dilution with acid and water		Urine[81, 91]
Dilution with acid, internal standard and ethanol		Urine[8]
Dilution with water		Serum[81], cerebrospinal fluid[37, 81], urine[8]
Dilution with internal standard		Serum[111], cerebrospinal fluid[111]

Table 1. Summary of methods used for preparation of biomedical samples for elemental analysis (based on the literature data).

energy is not transferred directly to the sample, this method is less effective than the one using microwave energy. The digestion using both microwave energy and thermal conductivity, can be carried out in open and closed systems (the samples are placed in Teflon vessels and sealed). The advantage of the method based on a closed system is that in such conditions, high pressure is generated in the vessel due to the evolution of gases (volatile components of the sample). With increasing pressure in the vessel, the boiling point of acids used for digestion also increases, which in turn makes possible to use higher temperatures for sample decomposition than in open systems. This allows to decompose the sample more efficiently and faster than in traditional open systems. Also, the probability of sample contamination with components from the environment is much lower. Since direct information about whether digestions were carried out in an open or closed system is rarely placed in papers, such a distinction has not been prepared. The mineralization of biomedical samples by using only acid digestion, without microwave or thermal support, is the least common method. However, one can find examples of its use for mineralization of blood, organ tissues and bones.

As one can notice from Table 1, a very popular procedure of body fluids preparation is the dilution of samples (with distilled water or acid) or adding to them various compounds. However, it should be remembered that the dilution of samples can be a problem when the elements under analysis occur in the sample at very low concentrations. Matrix modifiers are added to samples before GF-AAS analysis to reduce the measurement interferences[53,55,57,59,108]. PTFE (polytetrofluoroethylene) slurry is used as a chemical modifier for direct serum analysis by ICP-OES with electrothermal vaporization as a method of sample introduction[47]. Triton X-100 is a detergent applied to dissolve proteins and lipids of cell membranes, often used for blood[8,14,88,107], serum[12,47,79] and plasma[8] preparation. For these types of samples, ammonium compounds are often added as they prevent the coagulation of sample components[8,14,88].

Parameters used for validation of analytical techniques

Precision. Precision is a parameter that characterizes the closeness between the results of independently carried out measurements. It is the result of random errors occurring during the measurement procedure by using the given analytical technique[112]. It is expressed as a standard deviation (SD), relative standard deviation (RSD, which is equal to SD divided by the mean measurement result) and most often as a coefficient of variance (CV or also VC, CV[%] = RSD*100). Repeatability, intermediate precision and reproducibility are distinguished in term of precision[113]. It is said repeatability when there is no long-time interval between the considered measurements and they are performed on the same equipment in a laboratory by one operator[114]. In the literature, repeatability is also referred to as intra-day precision (for measurements performed on the same day), intra-assay precision

(or within-run—repeatability of results obtained in a given measurement series) or inter-assay precision. Intermediate precision refers to the deviation between the results obtained in the same laboratory when the measurements were carried out over a longer period of time (e.g. several weeks). In addition, it is not necessary for the measurements to be carried out by the same operator using the same instrument. Different laboratory reagents and accessories may also be used[114]. The terms commonly used in the literature in respect to inter-mediate precision are inter-day precision, within-laboratory reproducibility, day-to-day precision. The least used term in the literature in relation to precision is reproducibility. It expresses a standard deviation of the results obtained by a given technique in different laboratories. It is recommended that the determination of the measurement precision should be carried out using the test sample, with matrix and the concentration of the elements as similar as possible to the authentically analysed sample[115]. In the literature, however, one can find out the values of measurement precision for reference and standard materials as well. There are many recommendations for determining precision and there is no single fixed formula. It is important, however, that the experimentalists put in their work information how this validation parameter was obtained. Discrepancies that can be observed concern the type of sample for which measurements are made, the number of measurements carried out in a given series and the number of series as well as concentration levels for which precision is determined.

Trueness. Trueness is a parameter that defines the closeness of the obtained result, understood as the average value from the measurement series, to the expected value. It expresses the systematic error of measurement appearing with the use of a given analytical technique[114]. In order to determine the trueness, certified reference materials are most frequently used. The value of trueness for a given technique can be obtained also using another analytical technique, called the reference. Often, instead of determining the trueness using CRMs, or as an additional option, the "spike and recovery" method is used. It involves adding a known quantity of the analyte to the previously measured sample and afterwards its re-measuring. In such a case, the trueness is referred to as recovery. If the enrichment of the sample with the analyte took place at an early stage of its pre-treatment, calculated trueness also takes into account the procedure of sample preparation[113,115]. Often in scientific articles, only experimental and certified values are given, without indicating the value of trueness. The most often used formula for trueness calculation is Trueness[%] = (experimental value/certified value)*100. Then, the result closer to 100% indicates better trueness. The same dependence occurs for recovery (Recovery[%] = ((c1−c2)/c3)*100, where c1 is the concentration of the analyte after sample spiking, c2 is the concentration of the analyte before sample spiking and c3 is a concentration of spiked analyte). One can also meet the trueness expressed as Bias or Mean Relative Error and calculated according to the formula Bias[%] = [experimental value of concentration-certified value of concentration (or known, added concentration)]/certified value (or added)*100. In this case, a smaller measurement error will result in a closer to 0% Bias value. In literature, the word "accuracy" is often used instead of trueness. This is improper, due to the fact that accuracy concerns the correspondence between the true value and the result of a single measurement (not an average value). The accuracy of the measurement (the magnitude of the total error) consists of trueness (systematic error) as well as precision (random error)[112,116]. Both accuracy and trueness, as well as trueness and recovery seem to be often used interchangeably in scientific articles, which is also not correct. Therefore, the details concerning the method of their determination is very important for proper interpretation of the results.

Limit of detection. Limit of detection (LOD) is a parameter that indicates the smallest content of an analyte that can be detected with a certain probability and by using a given analytical procedure but not necessarily quantified[117]. It can be expressed as micrograms per gram or micrograms per litre units. In the literature, various possibilities to calculate the limit of detection can be found. The most common formula used for LOD calculations is LOD = 3*SDblank, where SDblank is the standard deviation of the analyte content in blank. It is recommended to calculate the standard deviation for 10 independent measurements[115] however in scientific articles their number differs. One can also find the following formula for LOD calculation LOD=$\bar{x}$blank + 3*SDblank. It is used when the level of the determined analyte is measurable in blank solution[110]. The detection limit can also be expressed in the signal domain according to the formula: yd=$\bar{x}$blank + 2*t*SDblank, where yd is the average value of a signal for a blank and t is Student's t-distribution coefficient. Then, from the calibration curve and based on the detection limit in the signal domain, the value corresponding to the concentration unit of the measured analyte is read[82]. Discussing the detection limit, one can also distinguish the value associated with used instrument (Instrument Detection Limit, IDL) and the applied measurement method (Method Detection Limit, MDL). The first one is determined on the basis of measurements made for standard solutions (blank measurement), which have not been subjected to any preparation. In turn, MDL determines the limit of detection for the method, thus it is influenced by all stages of sample preparation for analysis. MDL values are always greater than those of IDL (determined for the same analytical technique)[17,114].

The comparison of the discussed techniques of elemental analysis in respect of their use for the analysis of biological samples and achievable validation parameters

Tables 2, 3, and 4 summarize the values of selected validation parameters determined in research papers dealing with the elemental analysis of biomedical samples using various instrumental techniques. Additionally in the Table S1 and S2 of Supplementary materials, the details concerning the type of samples and the methods of their preparation as well as used instrument and experimental conditions in particular papers were placed. The validation parameters taken into account during data collection were the precision of measurements, the trueness and the limit of detection for the analysed element. When it was possible, an attempt was made to distinguish the parameter characterizing precision into repeatability, inter-day (assay) precision and reproducibility. For the trueness, based on the information contained in the papers, it was indicated whether it was calculated based on

Element	Precision (%CV) a: intra-day precision b: inter-day precision c: reproducibility	Trueness (%) a: calculated with CRM b: as recovery	Limit of detection a: in blank solution b: in real sample
CV AAS			
Hg	a: below 3.7[46]	a: 100.0–104.5[46] b: 89.9–99.2[46]	a: 0.0003 µg/mL[46] 0.00019 µg/mL[46]
F AAS			
Mg		b: 98.1[34]	a: 0.05 µg/mL[34]
Ca		b: 102.4[34]	a: 0.01 µg/g[34]
Cr		b: 102.4[34]	a: 0.05 µg/g[34]
Mn	a: 3.2[64]	a: 97.1–99.2[64] b: 99.4[64] 99.3[64]	a: 0.000097 µg/mL[64]
Fe		b: 97.8[34]	a: 0.08 µg/g[34]
Ni		a: 98.8[63] 99.2[63]	a: 0.00052 µg/mL[63]
Cu		b: 104.1[34]	a: 0.03 µg/g[34]
Zn		a: 95.9[110]* 95.1[110]* b: 95.2[34]	a: 0.03 µg/g[34]
Cd	nd: 2.1[24]	b: 96.0–99.0[24] 94.6[34]	a: 0.00011 µg/mL[24] 0.03 µg/g[34]
Pb	nd: 1.9[24]	b: 95.8–101.2[24] 96.0[34]	a: 0.0003 µg/mL[24] 0.03 µg/g[34]
GF AAS			
Be			b: 0.000007 µg/mL[5] 0.000002 µg/mL[5]
Al	a: 1.9–9.0[53] 0.8–2.8[12] b: 5.8–7.2[12] nd: ± 7.15[15]	a: 83.3[15] 100[15] 42.8[51] 97.6[51] 52[57] b: 67–98[51] 97.0 ± 3.8–103.4 ± 2.8[53] 98–109[12] 103[57]	a: 0.9 µg/mL[53] 0.00023 µg/mL[12] 0.00035 µg/mL[12] 0.00048 µg/mL[57] 0.0011 µg/mL[15] b: 0.000023 µg/mL[12] 0.001 µg/mL[12]
Si	nd: 8.4[55] 5.9[55]	b: 97–104[55]	
Cr	a: 2.0–2.9[108] c: 5.35–6.59[59] 1.9–4.1[108] nd: ±4.37[15]	a: 101.2[15] 107.7[15] 99.0–99.9[59]* 91.76–102.49[108] b: 83.1–86.3[108]	a: 0.0000062 µg/mL[59] 0.00042 µg/mL[15] nd: 0.001 µg/g[108]
Mn	a: 0.5–3.3[53] nd: 7.26–9.17[60]	a: 99–99.3[60]* 98[45]* 99.1[110]* 95.3[110]* b: 99.5 ± 0.8–103.3 ± 1.2[53]	a: 27.6 µg/g[53] 0.00013 µg/g[60] nd: 0.6 µg/g[45]
Fe		a: 97[45]* 106[105]* 101[105]*	nd: 1.6 µg/g[45]
Co	nd: 7.69[60] 0.80[60] 6.30[60]	a: 98.9–99.6[60]*	a: 0.0013 µg/g[60]
Continued			

Element	Precision (%CV) a: intra-day precision b: inter-day precision c: reproducibility	Trueness (%) a: calculated with CRM b: as recovery	Limit of detection a: in blank solution b: in real sample
Ni	c: 3.06–8.24[59] nd: 1.52[19] (standard solution) 10.4[19] (sample) 4.38[19] (sample)	a: +27.4[19#] −2.9[19#] +52.5[19#] +41.7[19#] +8.1[19#] −24.3[19#] +59.3[19#] 99.8–100.3[59]* b: 92.1–123.5[19]	a: 0.00023 µg/mL[19] 0.000025 µg/g[59]
Cu	nd: 7.35[60] 1.29[60] 6.1[60]	a: 96.4–99.8[60]* 99[45]* 102.5[110]* 103.8[110]*	a: 0.00000017 µg/g[60] nd: 0.2 µg/g[45]
Zn		a: 97[45]*	nd: 0.3 µg/g[45]
As	nd: 4.73[60] 6.2[60]	a: 99.4[60]* 103.2[60]*	a: 0.0000159 µg/g[60]
Mo	nd: ± 5.9[15]	b: 95.3–103.0[15]	a: 0.00081 µg/mL[15]
Cd	c: 4.72–7.69[59] nd: 3.6[14] 3.2[14] (standard material)	a: 100.3–102[59]* 86[45]* 105[14] 115[14]	a: 0.00018 µg/g[56] 0.00002 µg/g[59] 0.005 µg/mL[14] nd: 0.02 µg/g[45]
Pb	c: 3.63–7.76[59]	a: 100.5–100.9[59]* 106[45]*	a: 0.00157 µg/g[56] 0.001 µg/g[59] nd: 0.1 µg/g[45]
Bi	nd: 4.3[44] 4.7[44]	a: 96.8[44] b: 97.7[44] 101.1[44]	a: 0.00002 µg/mL[44] 0.0015 µg/mL[44]

Table 2. Values of precision, trueness and detection limit for different elements determined by using AAS. *nd* method of parameter determination was not defined; #Trueness expressed as a Bias; *Calculated based on the literature data.

the CRM measurements or using the sample spiking method. If the publications contained only information on the certified and measured value of the concentration of the analysed element, to enable the comparisons, the trueness was calculated according to the following formula Trueness[%] = (experimental value/certified value)*100. It was also marked if trueness was calculated as Bias. A large variety of methods for calculating the detection limits of elements was noticed. Therefore, only the type of matrix for which the detection limit of the analysed element was indicated, whether it was a blank solution or the analysed real biomedical sample. Also, values of LODs are expressed in both volume and mass units. Since there is a lack of information necessary to standardize them, the original format of units has been left.

Unfortunately, especially in the case of precision and limit of detection, a clear information on the procedure for calculating a validation parameter is not provided by the authors. Very often only its value is indicated. Furthermore, the measurement conditions (i.e. the number of repetitions) applied in the analysed research work are very different. Therefore, the prepared summary is intended to provide a general view of the analytical capabilities of selected instrumental techniques in studying the elemental composition of biomedical samples based on its validation results.

The focus was on the discussion of validation parameters obtained for selected elements, which are very often the subject of analysis in case of biomedical samples due to their significant importance for the proper functioning of living organisms. These include P, S, K, Ca, Fe, Cu, Zn and Se.

The data concerning P found for ICP-OES and ICP-MS show that both techniques are characterized by very good precision values. In case of determination of P using ICP-OES, the precision is in the range from 1% (calculated as RSD of mean value in five independent measurements of pork liver and bovine liver reference materials)[13] to 3% (calculated as RSD from 3 independent measurements of human bone marrow fluid sample)[35]. In turn, for ICP-MS, one can see strong dependence of precision values from the matrix of studied sample. In the work of Takasaki et al. the precision of P concentration measurement for the reference material (NIST SRM 1577b bovine liver) is 0.9%, while for the sample of *E. coli* cells is 3.9%[119]. Analysis of P content carried out using ICP-OES and ICP-MS is characterized by a high value of the trueness of the obtained results. The best value of

Element	Precision (%CV) a: intra-day precision b: inter-day precision c: reproducibility	Trueness (%) a: calculated with CRM b: as recovery	Limit of detection a: in blank solution b: in real sample
Li	a: 12.9[83] b: 9.0[83]	b: 90.2[82] 110[83]	a: 0.0033 µg/mL[82] 0.000278 µg/mL[83]* nd: 0.042 µg/mL[77]
Be		b: 103[83]	a: 0.000216 µg/mL[83]*
B	a: 2.0[83] b: 4.5[83]	b: 96[83]	a: 0.002162 µg/mL[83]*
Na	nd: 0.8–3.6[13] 3[16] 2[35]	a: 91[71]* 96–103[13] b: 89.1[82]	a: 0.402 µg/mL[13] b: 0.4 µg/mL[16] 0.013 µg/mL[82] nd: 0.11 µg/mL[78]
Mg	nd: 1.7–2.0[13] 7[16] 3[35]	a: 99[69] 100[71]* 97[79] 95[13] 98.5[84]* b: 92–104[69] 83[79]	a: 0.02 µg/mL[79] 0.931 µg/mL[13] b: 0.04 µg/g[69] 0.1 µg/mL[16] nd: 0.000015 µg/mL[78]
Al	nd: 60[35]	a: 101[3]* 96[3]* b: 88.9[82] 107[83]	a: 0.0005 µg/mL[82] 0.0243 µg/mL[83]*
Si	nd: 5.3[81]		
P	nd: 1.0[13] 2.0[16] 3.0[35]	a: 90–98[13] 99.8[84]*	a: 0.23 µg/mL[13] b: 2.0 µg/mL[16] nd: 0.033 µg/mL[78]
S			nd: 0.035 µg/mL[78]
K	nd: 2.0–4.7[13] 2[16] 0.6[35]	a: 98[71]* 72–73[13] 104[84]* b: 89.3[82]	a: 0.065 µg/mL[82] 1.146 µg/mL[13] b: 5.9 µg/mL[16] nd: 0.41 µg/mL[78]
Ca	nd: 5[13] 6[16] 2.0[35]	a: 96[47] 102[69] 94[71]* 101–104[13] 100.6[84]* b: 96–105[69] 101[81]	a: 0.023 µg/mL[13] b: 0.005 µg/g[69] 0.1 µg/mL[16] nd: 0.00001 µg/mL[78]
Ti		a: 89[47]	
Cr	a: 7.8[83] b: 39.6[83]	a: 111[47] 98[3]* 84[3]* b: 100[83]	a: 0.00364 µg/mL[83]* nd: 0.000366 µg/mL[77]
Mn	a: 14.7[83] b: 26.6[83] nd: 10–15[25]	a: 88–103[3]* 98[45]* 112[71]* 85.7[83]* 96[86]* 88[86]* b: 88.6[82] 96[83]	a: 0.00054 µg/mL[82] 0.00011 µg/mL[83]* nd: 0.4 µg/g[45] 0.000403 µg/mL[77] 0.00025 µg/mL[78]
Continued			

Element	Precision (%CV) a: intra-day precision b: inter-day precision c: reproducibility	Trueness (%) a: calculated with CRM b: as recovery	Limit of detection a: in blank solution b: in real sample
Fe	a: 0.5[83] b: 1.9[83] nd: 1.9–2.2[13] 2[35] 25[25]	a: 113[47] 100.3–104.9[3]* 99.7[69] 90[79] 94–98[13] 91.2[83]* 93[84]* 106[86]* 92[86]* b: 91[79] 93–105[69] 91.5 ± 1.8[82] 95[83]	a: 0.038 µg/mL[79] 0.459 µg/mL[13] 0.00091 µg/mL[82] 0.001117 µg/mL[83]* b: 0.5 µg/g[69] nd: 2.3 µg/g[45] 0.000562 µg/mL[77] 0.0009 µg/mL[78]
Co		a: 105[3]* 99[3]* 100[83]* 95[86]* 97[86]* b: 91[83]	a: 0.00825 µg/mL[83]* nd: 0.00024 µg/mL[77]
Ni		a: 103[3]* 92[3]* 96[86]* 109[86]* b: 93[83]	a: 0.002935 µg/mL[83]* nd: 0.00114 µg/mL[77]
Cu	a: 0.6[83] b: 2.3[83] c: 11.1[26] nd: 2.9[81] below 5[25]	a: 90[47] 101–107[3]* 99[45]* 106[71]* 102[76]* 94[79] 91–107[81] 103.4[83]* 99[86]* 108[86]* b: 95[79] 95[81] 97[83]	a: 0.0109 µg/g[76] 0.003 µg/mL[79] 0.003178 µg/mL[83]* nd: 2.1 µg/g[45] 0.000588 µg/mL[77] 0.0004 µg/mL[78]
Zn	a: 0.3[83] b: 1.3[83] c: 1.55[26] nd: 10–15[25]	a: 108[47] 93–101[3]* 103[45]* 113[71]* 103[76]* 87[79] 92–105[81] 101[83]* 97[84]* 93[86]* 106[86]* b: 87[79] 90.7[82] 110[83]	a: 0.0357 µg/g[76] 0.012 µg/mL[79] 0.0039 µg/mL[82] 0.000981 µg/mL[83]* nd: 1.1 µg/g[45] 0.000391 µg/mL[77] 0.0014 µg/mL[78]
Se	a: 9.3[83] b: 9.1[83]	a: 95–109[3]* 94.5[83]* b: 91[83]	a: 0.036 µg/mL[79] 0.022898 µg/mL[83]* nd: 0.0002 µg/g[56]
Sr	a: 2.3[83] b: 4.6[83]	a: 88–101[3]* 95[84]* b: 104[83]	a: 0.000175 µg/mL[83]* nd: 0.00138 µg/mL[77] 0.00002 µg/mL[78]
Mo			nd: 0.000784 µg/mL[77] 0.0006 µg/mL[78]
Continued			

Element	Precision (%CV) a: intra-day precision b: inter-day precision c: reproducibility	Trueness (%) a: calculated with CRM b: as recovery	Limit of detection a: in blank solution b: in real sample
Cd	a: 23.7[83] b: 18.0[83]	a: 92–102[3]* 91[45]* 112[79] 115[86]* 85[86]* b: 90[83] 116[79]	a: 0.001 µg/mL[79] 0.000337 µg/mL[83]* nd: 0.1 µg/g[45] 0.000132 µg/mL[77]
Ba	a: 0.6[83] b: 1.5[83] nd: below 6[118]	a: 4[118]# 7[118]# b: 105[83] 76–104[118] 85–101[118]	a: 0.000412 µg/mL[83]* 0.00011 µg/mL[118] nd: 0.000531 µg/mL[77] 0.00006 µg/mL[78]
Hg	a: below 6[46]	a: 80[46]	a: 0.00002 µg/mL[46] 0.000007 µg/mL[46] 0.023 µg/g[46] nd: 0.00553 µg/mL[77]
Pb	c: 10.3[26]	a: 102–113[3]* 83[86]* b: 103[83]	a: 0.019 µg/mL[79] 0.007874 µg/mL[83]* nd: 2.0 µg/g[45] 0.00343 µg/mL[77]

Table 3. Values of precision, trueness and detection limit for different elements determined by using ICP-OES. *nd* method of parameter determination was not defined; #Trueness expressed as a Bias; *Calculated based on the literature data.

trueness, equal to 99.8%, was obtained in the work of Zaichick et al. who were studying using the ICP-OES the correlation between elemental composition of bones and age/sex of people. Trueness was calculated there based on the measurement of the reference material (SRM NIST 1486 Bone Meal)[84]. The values of limit of detection obtained for P using both discussed techniques are satisfactory. The lowest LOD for this element (found based on referenced papers) is 0.000012 µg/ml and it was obtained by Takasaki et al. using ICP-MS. The authors conducted a multielemental analysis of a very small amount of analyte (20 µl) using a highly effective sample introduction system. Compared to the conventional technique, requiring about 2 ml of sample, they achieved a significant improvement in the absolute detection limit value (from 28 to 0.2 pg) for P[119]. Based on the results for real biomedical samples (human cerebrospinal fluid) Korvela et al. received a LOD for P equals to 2 µg/ml[16].

In the work of Takasaki et al. the precision of S measurement performed using ICP-MS depended on the sample type. For the reference material (NIST SRM 1577b bovine liver) it was 0.8%, while for the sample of *E. coli* cells was 3.6%[119]. In this study also trueness was determined and equaled 100%[119]. The detection limit of S obtained using ICP-MS was two order of magnitude smaller than that in the ICP-OES technique and these values equaled 0.0003 µg/ml[119] and 0.035 µg/ml[78], respectively.

The precision values obtained for K using ICP-OES varied from 0.6%[35] to 4.7%[13]. As in the case of P and S, the precision of K measurements carried out using ICP-MS depended on the matrix and was equal to 1.2% for reference material and to 3.1% for *E. coli* cells[119]. The best trueness of the obtained results of K concentration, amounting to 98.7%, was obtained in the work of Boulyga et al. which regarded the multielemental analysis of small amounts of pathologically changed thyroid tissue carried out using the ICP-MS. Trueness was tested based on measurements of the reference material NIST SRM 1566a (oyster tissue). The LOD of K obtained by Boulyga et al. for thyroid samples was 3 µg/g[38]. In turn, this determined by Korvela et al. for cerebrospinal fluid using the ICP-OES was 5.9 µg/ml[16]. The lowest detection limit of the element, similarly as for P and S, was obtained in the work of Zaichack et al. using ICP-MS and it was equal to 0.01 µg/ml[84].

In presented examples of Ca determination in biological samples, the ICP-OES, ICP-MS, and F-AAS were used for elemental analysis. The accuracy of the results obtained using the ICP-OES ranged from 2% (calculated as RSD of 3 measurements of human bone marrow-fluid)[35] to 6% (determined as RSD of mean values of Ca content in human cerebrospinal fluid)[16]. The values of precision for Ca determinations using the ICP-MS was similar and did not exceed 9.5%. The best value for this validation parameter (1.2%), was obtained in the work of Meyer et al. as an intra-day precision (three samples of human serum were separately digested on one day and measured)[90]. Determination of Ca concentration in biomedical samples using all of the three mentioned techniques is generally characterized by a very good value of trueness which usually falls within the range from 93%[119] to 105%[39,69]. The best trueness for Ca determination (100%) was obtained in the work of Krebs et al. It was calculated based on the comparison of the certified and the measured value of this element concentration in the

Element	Precision (% CV) a: repeatability b: inter-day (assay) c: reproducibility	Trueness (%) a: calculated with CRM b: as recovery	Limit of detection a: in blank solution b: in real sample
Li	nd: 5.6[37]	a: 105[37]* b: 102[37]*	a: 0.004 µg/g[18] 0.000007 µg/mL[37]
Be			a: 0.0001 µg/g[18] 0.00009 µg/g[100]
B	a: 3.7[89] b: 10.8[89]	b: 98.04[89]	a: 0.47 µg/g[18]
Na	nd: 1.0[119] 1.2[119]	a: 103.1[38]* 94[39]* 108[119]	a: 1 µg/g[38] nd: 0.0002 µg/mL[119]
Mg	a: 4.0[17] 0.79[96] 0.6[90] b: 1.6[90] 5.0[17] nd: 1.5[119]	a: 93[17] 99[9]* 93. 2[38]* 95[96]* 99[39]* 103.3[90]	a: 0.0004 µg/mL[17] (IDL) 0.00088 µg/mL[17] (MDL) 5 µg/g[38] b: 0.00234 µg/mL[90] nd: 0.0004218 µg/mL[96] 0.00007 µg/mL[119]
Al	a: 1.6[17] 1.28[96] 7.4[89] b: 2.3[17] 12.7[89] nd: 6.2–6.7[13]	a: 66[13] 113[17] 115[96]* b: 89.82[89]	a: 0.000029 µg/mL[13] 0.00081 µg/mL[17] (IDL) 0.0026 µg/mL[17] (MDL) 0.388 µg/g[18] 0.0001 µg/g[100] nd: 0.0023464 µg/mL[96] 0.00174 µg/g[120]
P	nd: 0.9[119] 3.9[119]	a: 104[119]	nd: 0.000012 µg/mL[119]
S	nd: 0.8[119] 3.6[119]	a: 100[119]	nd: 0.0003 µg/mL[119]
K	nd: 1.2[119] 3.1[119]	a: 98.7[38]* 98[119]	a: 3 µg/g[38] nd: 0.011 µg/mL[119]
Ca	a: 1.2[90] 5.2[17] 3.61[96] b: 6.4[17] 2.5[90] nd: 2.1[119] 9.5[119]	a: 95[17] 100[9]* 96.9[38]* 64[96]* 105[39]* 103.9[90] 93[119]	a: 0.015 µg/mL[17] (IDL) 0.056 µg/mL[17] (MDL) 0.801 µg/g[101] b: 0.04088 µg/mL[90] nd: 0.0025794 µg/mL[96] 0.00003 µg/mL[119]
Ti	a: 3.90[96] nd: 4[16]		a: 0.048 µg/g[18] b: 0.5 µg/mL[16] nd: 0.0001132 µg/mL[96]
V	a: 5.2[17] 1.91[96] 4.7[89] b: 10.9[89] 8.4[17]	a: 107[17] 104.7[38]* 67[96]* 111.22[89]	a: 0.0000017 µg/mL[17] (IDL) 0.0000027 µg/mL[17] (MDL) 0.014 µg/g[18] 0.005 µg/g[38] 0.0001 µg/g[100] nd: 0.0000038 µg/mL[96] 0.000135 µg/mL[99]
Continued			

Element	Precision (% CV) a: repeatability b: inter-day (assay) c: reproducibility	Trueness (%) a: calculated with CRM b: as recovery	Limit of detection a: in blank solution b: in real sample
Cr	a: 3.4[17] 3.31[96] 3.8[89] b: 4.4[17] 5.6[89] nd: 3.1[119]	a: 88[17] 125.9[38]* 100[96]* 106.25[89] 63[101]*	a: 0.000042 µg/mL[17] (IDL) 0.000052 µg/mL[17] (MDL) 0.024 µg/g[18] 0.3 µg/g[38] 0.0001 µg/g[100] 0.0014 µg/g[101] b: 0.00005 µg/mL[8] 0.0001 µg/mL[8] 0.0001 µg/mL[8] 0.00025 µg/mL[8] nd: 0.0000649 µg/mL[96] 0.00113 µg/g[98] 0.000116 µg/mL[99] 0.0000014 µg/mL[119]
Mn	a: 4.5[17] 2.05[96] 3.3[89] b: 10.0[17] 4.5[89] nd: 2.1–3.6[13] 1.1[100] 1.1[100] 2.9[119] 2.7[119]	a: 99–110[13] 94[17] 97[9]* 97.6[38]* 87[96]* 97[39]* 99[100]* 93[100]* 104[101]* 104[119] b: 102.52[89]	a: 0.000071 µg/mL[13] 0.000012 µg/mL[17] (IDL) 0.000025 µg/mL[17] (MDL) 0.018 µg/g[18] 0.07 µg/g[38] 0.0016 µg/g[101] 0.001 µg/g[100] nd: 0.0000194 µg/mL[96] 0.00021 µg/mL[98] 0.000003 µg/mL[119]
Fe	a: 1.13[96] 1.5[89] 2.4[90] b: 3.7[89] 4.1[90] nd: 2.5[119] 4.1[119]	a: 98[9]* 102.0[38]* 97[96]* 95[39]* 97.9[90] 111[101]* 71[101]* 104[119] b: 102.66[89]	a: 0.089 µg/g[18] 4 µg/g[38] 0.136 µg/g[101] b: 0.00205 µg/mL[90] nd: 0.0001827 µg/mL[96] 0.00149 µg/g[98] 0.00002 µg/mL[119]
Co	a: 3.5[17] 4.10[96] 3.7[89] b: 5.6[17] 9.6[89] nd: 1.1–8.2[13] 4.6[119]	a: 92[76]* 92–100[13] 96[17] 77.2[38]* 110[39]* 105.09[89] b: 89[101]*	a: 0.004 µg/g[76] 0.000016 µg/mL[13] 0.0000043 µg/mL[17] (IDL) 0.0000061 µg/mL[17] (MDL) 0.001 µg/g[18] 0.007 µg/g[38] 0.00004 µg/g[100] 0.0002 µg/g[101] nd: 0.0000061 µg/mL[96] 0.00024 µg/g[98] 0.000177 µg/mL[99] 0.0000008 µg/mL[119]
Ni	a: 2.8[17] 5.40[96] b: 6.2[17] nd: 5.6[119]	a: 110[17] 88.9[38]* 100[96]* 138[101]*	a: 0.0004 µg/mL[17] (IDL) 0.00051 µg/mL[17] (MDL) 0.016 µg/g[18] 0.1 µg/g[38] 0.0025 µg/g[101] nd: 0.0000405 µg/mL[96] 0.00064 µg/g[98] 0.00002 µg/mL[119]
Cu	a: 2.1[17] 1.26[96] 1.3[89] 1.5[90] b: 3.9[17] 9.7[89] 4.2[90] nd: 1.3–4.1[13] 2[35] 1.9[100] 0.7[100] 2.9[119] 2.9[119]	a: 89–97[13] 92[9]* 96.5[38]* 125[101]* 100[101]* 94[39]* 100[96]* 107.5[90] 95.87[89] 89[17] 95[100]* 81[100]* 107[119]	a: 0.000017 µg/mL[13] 0.000039 µg/mL[17] (IDL) 0.000072 µg/mL[17] (MDL) 0.049 µg/g[18] 0.1 µg/g[38] 0.0029 µg/g[100] 0.0304 µg/g[101] b: 0.00010 µg/mL[90] nd: 0.0000399 µg/mL[96] 0.00059 µg/g[98] 0.000007 µg/mL[119]
Continued			

Element	Precision (% CV) a: repeatability b: inter-day (assay) c: reproducibility	Trueness (%) a: calculated with CRM b: as recovery	Limit of detection a: in blank solution b: in real sample
Zn	a: 5.3[17] 0.90[96] 1.1[89] 3.6[90] b: 7.5[17] 8.7[89] 5.3[90] nd: 1.5–3.4[13] 22.8[95] 16.3[95] 1.2[100] 0.2[100] 2.4[119] 5.3[119]	a: 93–97[13] 88[17] 116[9]* 101–104[95]* 101.2[38]* 102[96]* 102[39]* 94.39[89] 97.3[90] 110[101]* 91[101]* 97[100]* 98[100]* 108[119] b: 111 ± 30[95] 99 ± 12[95]	a: 0.000017 µg/mL[13] 0.00096 µg/mL[17] (IDL) 0.002 µg/mL[17] (MDL) 0.0107 µg/g (32 µg/mL)[95] 0.58 µg/g[18] 0.2 µg/g[38] 0.0042 µg/g[100] 0.9 µg/g[101] b: 0.00024 µg/mL[90] nd: 0.0005154 µg/mL[96] 0.00251 µg/g[98] 0.00002 µg/mL[119]
Ga	a: 2.47[96]		a: 0.0007 µg/g[18] nd: 0.0000452 µg/mL[96]
Ge			a: 0.001 µg/g[18]
As	a: 4.4[17] 4.14[96] 7.7[89] 3.6 b: 10[17] 10.9[89] 3.7[90] nd: 4[16]	a: 96[76]* 97[17] 86.4[38]* 45[96]* 110.36[89] 98.7[90] 83[101]* 88[101]*	a: 0.0047 µg/g[76] 0.000037 µg/mL[17] (IDL) 0.000043 µg/mL[17] (MDL) 0.016 µg/g[18] 0.002 µg/g[38] 0.0004 µg/g[100] 0.0003 µg/g[101] b: 1.0 µg/mL[16] 0.00001 µg/mL[90] 0.00005 µg/mL[8] nd: 0.0009148 µg/mL[96]
Se	a: 1.8[17] 5.47[96] 9.0[89] 2.1[90] b: 2.9[17] 11.2[89] 3.0[90] nd: 30[35] 10[100] 6.4[100]	a: 95[76]* 119[17] 81.4[38]* 69[96]* 119.15[89] 101.5[90] 125[101]* 64[100]* 62[100]*	a: 0.017 µg/g[76] 0.000062 µg/mL[17] (IDL) 0.000094 µg/mL[17] (MDL) 0.12 µg/g[18] 0.04 µg/g[38] 0.0015 µg/g[101] b: 0.00004 µg/mL[90] nd: 0.0003438 µg/mL[96]
Br			a: 2.168 µg/g[18]
Rb	a: 2.8[89] b: 9.6[89] nd: 1.4–2.7[13] 4[16] 0.7[35]	a: 1.01[13] 103.3[38]* 106[39]* b: 104.06[89]	a: 0.000012 µg/mL[13] 0.021 µg/g[18] 0.002 µg/g[38] b: 1.0 µg/mL[16]
Sr	a: 2.6[17] 1.0[96] 2.4[89] b: 4.6[17] 7.9[89] nd: 6.9–16.8[13] 8[16] 0.4[35] 2.9[37]	a: 125[13] 110[17] 99.1[38]* 135[96]* b: 92.03[89] 98[37]*	a: 0.000017 µg/mL[13] 0.000014 µg/mL[17] (IDL) 0.000037 µg/mL[17] (MDL) 0.036 µg/g[18] 0.05 µg/g[38] 0.00001 µg/mL[37] b: 1.0 µg/mL[16] nd: 0.0000190 µg/mL[96]
Y	nd: 12.1[119]		a: 0.0006 µg/g[18] nd: 0.0000012 µg/mL[119]

Continued

Element	Precision (% CV) a: repeatability b: inter-day (assay) c: reproducibility	Trueness (%) a: calculated with CRM b: as recovery	Limit of detection a: in blank solution b: in real sample
Zr	a: 1.7–4.2[102] b: 2.0–6.1[102] nd: 10[35] 3.0[37]	b: 0.1–7.2[102#] 91.0 -118[102] 106[37*]	a: 0.000055 µg/mL[102] 0.000002 µg/mL[37] 0.008 µg/g[18]
Nb			a: 0.0005 µg/g[18]
Mo	a: 4.25[96] 3.2[89] 3.5[90] b: 8.8[89] 7.9[90] nd: 1.1–3.0[13] 5[35] 2.8[37] 2.9[119]	a: 102[76*] 102–107[13] 95[96*] 102[37*] 108.7[90] 110[119] 105.49[8,9] b: 96[101*] 104[37*]	a: 0.0057 µg/g[76] 0.000008 µg/mL[13] 0.01 µg/g[18] 0.006 µg/g[38] 0.0048 µg/g[101] 0.000005 µg/mL[37] b: 0.000025 µg/mL[90] nd: 0.0000194 µg/mL[96] 0.0000012 µg/mL[119]
Ru			a: 0.017 µg/g[18]
Pd			a: 0.002 µg/g[18]
Ag	nd: 8[35]		nd: 0.00013 µg/g[98]
Cd	a: 6.1[17] 1.96[96] 4.1[89] 5.8[90] b: 10.0[17] 9.3[89] 6.3[90] nd: 1.1–2.6[13] 6.6[95] 4.2[95] 4.6[14] 9.5[14] 0.3[119]	a: 106[76*] 94–114[13] 83[17] 99[95*] 96[95*] 91.6[38*] 40[96*] 94.73[89] 98.8[90] 93[14] 101[14] 120[101*] 95[101*] 111[119] b: 102 ± 7[95] 102 ± 3[95]	a: 0.0029 µg/g[76] 0.000001 µg/mL[13] 0.0000088 µg/mL[17] (IDL) 0.000013 µg/mL[17] (MDL) 0.00006 µg/g[95] (0.017 µg/mL) 0.002 µg/g[18] 0.001 µg/g[38] 0.00008 µg/g[100] 0.0001 µg/g[101] 0.0001 µg/mL[14] b: 0.000001 µg/mL[90] nd: 0.0000032 µg/mL[96] 0.00047 µg/g[98] 0.0000006 µg/mL[119]
In			a: 0.0002 µg/g[18]
Sn	a: 0.57[96] nd: 30[35] 5.2[37]	a: 73.3[38*] b: 104[37*]	a: 0.004 µg/g[18] 0.04 µg/g[38] 0.00003 µg/mL[37] 0.0001 µg/g[101] nd: 0.0000139 µg/mL[96]
Sb	a: 2.8[17] 0.85[96] b: 3.6[17] nd: 10[35] 2.3[37]	a: 104[17] 90.0[38*] b: 96[37*]	a: 0.000017 µg/mL[17] (IDL) 0.000028 µg/mL[17] (MDL) 0.002 µg/g[18] 0.0006 µg/g[38] 0.000002 µg/mL[37] nd: 0.0000193 µg/mL[96]
Te			a: 0.006 µg/g[18]
I	a: 3.1[90] b: 4.7[90]	a: 98.7[38*] 94.5[90]	b: 0.00010 µg/mL[90]
Cs	nd: 2.9–4.3[13] 20[35]		a: 0.000001 µg/mL[13] 0.0009 µg/g[18]

Continued

Element	Precision (% CV) a: repeatability b: inter-day (assay) c: reproducibility	Trueness (%) a: calculated with CRM b: as recovery	Limit of detection a: in blank solution b: in real sample
Ba	a: 4.4[17] 1.19[96] b: 6.0[17] nd: 4[16] 3[35] 4.7[37] 1.5[119]	a: 110[17] 92[96]* b: 92[37]*	a: 0.000011 µg/g[17] (IDL) 0.00038 µg/mL[17] (MDL) 0.025 µg/g[18] 0.03 µg/g[38] 0.0002 µg/g[100] 0.00001 µg/mL[37] b: 0.5 µg/mL[16] nd: 0.0011218 µg/mL[96] 0.0000014 µg/mL[119]
Ce		a: 82.5[38]*	a: 0.0008 µg/g[18] 0.002 µg/g[38]
Sm			a: 0.002 µg/g[18]
Gd			a: 0.001 µg/g[18]
Tm			a: 0.0006 µg/g[18]
Hf			a: 0.0002 µg/g[18]
Ta			a: 0.002 µg/g[18]
W	nd: 9[35] 4.2[37]	b: 98[37]*	a: 0.000001 µg/mL[37] 0.074 µg/g[18]
Re			a: 0.0002 µg/g[18]
Os			a: 0.013 µg/g[18]
Pt			a: 0.0005 µg/g[18]
Au			a: 0.001 µg/g[18]
Hg		a: 100[76]* 84.1[38]* 97[101]* 74[101]*	a: 0.0011 µg/g[76] 0.037 µg/g[18] 0.007 µg/g[38] 0.0002 µg/g[101]
Tl	nd: 3.4[37]	a: 99[37]* b: 94[37]*	a: 0.0005 µg/g[18] 0.000001 µg/mL[37] 0.00004 µg/g[100]
Pb	a: 5.2[17] 1.28[96] 4.8[89] b: 8.3[17] 8.6[89] nd: 10.0–10.5[13]	a: 96[76]* 109–112[13] 125[17] 94.3[38]* 93[39]* 86[101]* b: 92.85[89]	a: 0.0079 µg/g[76] 0.00001 µg/mL[13] 0.000099 µg/mL[17] (IDL) 0.00016 µg/mL[17] (MDL) 0.002 µg/g[18] 0.005 µg/g[38] 0.0009 µg/g[100] 0.0013 µg/g[101] nd: 0.0000414 µg/mL[96] 0.00036 µg/g[98] 0.000004 µg/mL[119]
Bi	nd: 4.3[37]	a: 102[37]* b: 110[37]*	a: 0.000001 µg/mL[37] 0.002 µg/g[18] 0.004 µg/g[38]
U	a: 2.3[17] b: 3.1[17]	a: 111[17] 106.1[38]*	a: 0.00000029 µg/mL[17] (IDL) 0.00000045 µg/mL[17] (MDL) 0.0002 µg/g[38] 0.00005 µg/g[100]

Table 4. Values of precision, trueness and detection limit for different elements determined by using ICP-MS. *nd* method of parameter determination was not defined; # Trueness expressed as a Bias; *Calculated based on the literature data.

certified material NIST RM 8414 (bovine muscle) using ICP-MS[9]. The lowest detection limit for Ca (0.00001 µg/ml) was obtained in the work of Leblondel et al. who have studied the distribution of elements in rat tissues using ICP-OES[78]. In turn, in the work of Yang et al. a limit of detection of Ca obtained for sample of rabbit artery using ICP-OES was 0.005 µg/g (calculated as 3*SD from 16 measurements)[69].

Fe is very often the subject of studies carried out using the F-AAS, GF-AAS, ICP-OES and ICP-MS. In general, it can be stated that for techniques using plasma for analytes determination the obtained values of precision are very good and do not exceed 4.1%. The highest value of this parameter in case of Fe determination (25%) was contained in the work of Sahuquilo et al. concerning the elemental analysis of human gallstones using the ICP-OES. It was pointed out that this may be caused by the low content of this element in the analysed sample (pure cholesterol gallstone sample)[25]. For all discussed techniques of Fe determination very good results of trueness were obtained, calculated both with spike sample methods and based on measurements of reference materials. The highest agreement between the measured and certified values of Fe concentration was obtained using the ICP-OES in the works of Rahil-Khazen et al. (100.3% for human hair reference material GBW 09101 measurements)[3] and Yang et al. (99.7% for NIST bovine liver standard reference material measurements)[69]. The best value of Fe recovery for the real sample matrix was obtained with the use of F-AAS (97.8%) in the work of Fakayode et al., where the contents of trace elements in human hair samples were examined[34]. Based on the analysed papers it can be said that the lowest detection limit for Fe is 0.0001827 µg/ml and was obtained by Xie et al. during measurements of standard solution using ICP-MS[96]. For the same technique, the value of Fe detection limit determined based on the measurements of real sample of human serum was 0.00205 µg/ml in the work of Meyer et al.[90].

All techniques selected for the discussion were used to determine the content of Cu in biomedical samples. Performed measurements are characterized by good precision values, ranging from 0.6% (within-run precision calculated based on 20 measurements of a digested human serum sample using ICP-OES)[83] to 11.1% (reproducibility determined based on 6 measurements, done with the use of ICP-OES, of Cu concentration in the solution of digested tooth samples)[26]. In most cases, the trueness obtained for Cu ranges from 81% (ICP-MS)[100] to 108% (ICP-OES)[86]. Also, the values of recovery parameter are satisfactory for these techniques and range from 95% (ICP-OES)[81] to 104.1% (F-AAS)[34]. Both the best and the worst agreement between measured and certified Cu concentration values were obtained in the work of Garcia-Vaquero et al. The trueness of 100% was obtained when measuring DORM-3 CRM (fish protein), whilst 125% when analysing CRM 186 (pig kidney)[101]. The lowest LOD for Cu was obtained in the work of Afridi et al. based on blank solution GF-AAS measurements and this value is 0.00000017 µg/g[60]. Analysing the real sample (human serum) and using for this purpose ICP-MS, Meyer et al. obtained LOD for Cu equal to 0.0001 µg/ml[90].

Zn is an element frequently examined in biomedical samples. The precision of Zn measurements performed using ICP techniques is satisfactory for most of the discussed papers and ranges from 0.3% (ICP-OES)[83] to 8.7% (ICP-MS)[89]. In the work of Panayi et al., where Cd and Zn contents in brain tissue were measured using ICP-MS, the precision of Zn determination was 22.8% and 16.3% depending on the type of tissue examined[95]. Observed higher values of this parameter in case of results obtained for real samples reflect possible non-homogeneity in their elemental composition. Also the trueness of the results obtained using the discussed techniques can be considered as satisfactory. When comparing certified and measured values, the trueness ranges from 87% (measurements of standard reference material CRM 1577-bovine liver using ICP-OES)[79] to 116% (calculated based on measurements of standard tissue of bovine muscle with the use of ICP-MS)[9]. The obtained recovery values range from 87% (2 µg of the analyte added to rat liver samples and reanalysed using ICP-OES)[79] to 111% (analysed samples spiked with a known amount of an element and measured with the use of ICP-MS)[95]. The lowest LOD for Zn is 0.000017 µg/ml and was determined using the ICP-MS by Takahashi et al. It was calculated as the concentration of the element for which the number of counts is three times higher than the standard deviation of the background counts[13]. The lowest LOD of Zn for the matrix constituting the biomedical sample was 0.00024 µg/ml and was calculated based on results obtained for human serum using the ICP-MS[90].

The presented validation parameters regarding the determination of Se in biomedical samples refer to the use of the ICP-OES and ICP-MS. In most cases, obtained results are characterized by very good precision from 1.8% (expressed as repeatability calculated from 6 measurements of CRM Seronorm Trace Elements Serum L-2 carried out on the same day)[17] to 11.2% (inter-day precision expressed as the relative standard deviation of 10 measurements of CRM Clinchek Blood Plasma Control level 1)[89]. The highest value of the precision for Se found in discussed papers, equals to 30%, was obtained by Hasegawa et al. who have studied the elemental composition of human bone-marrow fluid[35]. The parameter was calculated as RSD of 3 replicated measurements of the sample done using ICP-MS. The values of the trueness in case of Se determination ranged from 62 to 125% and depended on the applied analytical technique. The best agreement between the measured and certified Se concentrations, equals to 101.5%, was obtained in the work of Meyer et al. for human blood serum reference material with the use of ICP-MS[90]. The lowest LOD for Se, achieved also by Meyer et al., was equal to 0.00004 µg/ml for human serum samples[90].

Evaluation of the usefulness of the total reflection X-ray fluorescence (TXRF) for the elemental analysis of animal tissues

The total reflection X-ray fluorescence is a technique of quantitative elemental analysis and it is based on the registration of fluorescent radiation emitted by atoms excited as a result of ionization of their inner shell. The fundamental principle of TXRF is application of measurement geometry, which allows for the occurrence of total X-ray reflection phenomena. Primary, X-ray radiation is used for atoms ionization and it falls on a sample surface at very small glancing angle and is totally reflected from a sample carrier. Thus allows for double excitation of atoms, first by primary, incident beam and then by reflected beam. The energy of emitted fluorescent

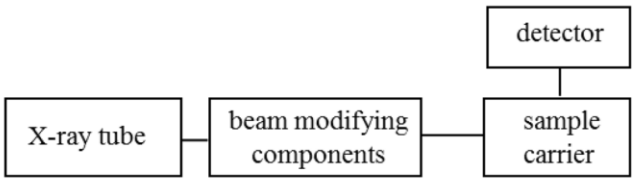

Figure 5. Block diagram of a typical instrument used for TXRF.

radiation is characteristic for each element and depends on the atomic number. Therefore, the measurement of the fluorescent radiation energy, allows identifying elements present in the sample[121].

A layout of the experimental setup used for TXRF measurements is presented in Fig. 5. X-ray tubes with molybdenum anode are most often used as X-ray sources for the TXRF. The spectrum of the beam generated in the lamp is continuous and requires monochromatization to reduce background radiation. Therefore, the beam passes through the set of modifying components, like shut-off reflectors and crystalline or multilayer monochromators. The most commonly used detectors for TXRF are semiconductor detectors (mainly Silicon Drift Detector or Si(Li)). The detector, sample carrier and source of radiation are arranged at angle 90°, ant that geometry allows for a significant decrease of the background of the recorded spectrum To improve the detection of low-energy characterisctic radiation, if possible, the analysis should be conducted in a vacuum to reduce the absorption of radiation in the air. It is also important to provide a suitably thin layer of the sample, which also affects the elimination of radiation absorption effects[122].

The TXRF is widely used in the analysis of biomedical samples, both solid and liquid[123,124]. For liquid samples, such as body fluids, the measurement can be carried out directly[111,125,126] or after appropriate dilution of the sample[107,127]. Solid samples, both soft (such as organ tissues[106,128]) and hard (e.g. bones[6]) require sample preparation. Its purpose is to conduct the sample into the liquid form and to remove the organic matrix, which could contribute to the increase of scattered radiation and worsening of the detection limits of the elements.

Ostachowicz et al. used the TXRF to determine concentrations of Na, Mg, Cl, K, Ca, Cu, Zn and Br in serum and cerebrospinal fluid taken from patients suffering from amyotrophic lateral sclerosis and healthy people constituting a control group[111]. Margui et al. have performed a multi-elemental analysis of whole blood taken from patients with thyroid diseases. For this purpose, they examined the influence of different dilution procedures and sample volume deposited on the reflector on the carried elemental analysis[107]. Sanchez et al. have analysed oral fluids of women with osteoporosis and osteopenia in terms of P, S, Cl, K, Ca, Cr, Fe, Ni, Cu and Zn contents[129]. Martinez et al. have determined the concentration of Fe in the blood of people living in the Mexico Valley metropolitan zone. Before analysis, Fe was extracted from the samples, which allowed to reduce the detection limit of the element and the obtained results were compared with the levels of Fe in environmental samples[124]. Majewska et al. have used the TXRF to determine the reference values of K, Ca, Ce, Mn, Fe, Ni, Cu, Zn, Br, Rb and Sr in human urine[104]. Another study concerned the determination of gadolinium content in urine and blood plasma using the TXRF. The same samples were also measured using ICP-MS in order to perform a comparison with results obtained by TXRF. Concentrations of Gd determined by both techniques showed very good correlations[125]. It was found that TXRF can be considered as a simple technique for routine analysis of gadolinium levels in body fluids in clinical laboratories[125]. Abraham et al. have analysed the concentration of Ti, V and Al in oral fluids taken from patients with dental implants. The study was performed in order to explore the possibility of corrosion effect of metals in implanted materials. As an X-ray source for the TXRF, they used synchrotron radiation (SR-TXRF, Total Reflection X-ray fluorescence with Synchrotron Radiation). The use of a linearly polarized synchrotron radiation in TXRF reduces the influence of scattered radiation on the recorded spectrum. High intensity and monochromatization of the exciting synchrotron beam lead to further improvement of the detection limits of analysed elements[126].

Wagner et al. have performed a multielemental analysis of muscle and liver fish tissues. The objective of their study was investigation of the influence of environmental pollution caused by the local coal industry on the fish tissues and find out if it may stands a potential danger for the consumers[41]. Marco et al. have analysed the contents of Cu and Zn in human brain and Fe, Cu, Zn, Se and Pt in human serum. Different procedures of sample pretreatment, including digestion and preparing slurries, as well as methods of standardization were investigated[130]. Serpa et al. have studied the content of Al, P, S, Cl, K, Ca, Ti, Fe, Cu, Zn, Br and Rb in different parts of rat brain. They indicated how the concentrations of the elements change with the age of the animal[106]. In turn, Varga et al. analysed content of Cr, Mn, Fe, Ni, Cu, Zn, Rb and Pb in the samples of liver biopsy taken from patients suffered from chronic diffuse liver disease[39]. There are many studies where TXRF is used for the comparison of elemental composition of cancerous and healthy tissues. Such studies were done for colon[131], breast[22,109,131], stomach[131], uterus[132], prostate[128], intestine[36] and the corresponding healthy tissues of these organs. Other investigation concerned the elemental analysis of brain tumours of various types and grades[133] as well as breast, lung and intestinal cancer tissues[134]. Using the TXRF, attempts were also made to find correlations between the concentrations of trace elements in samples of cancerous and benign tissues of the rectum, colon, thyroid, kidneys, larynx and lung[134]. Czarnowski et al. have analysed the distribution of trace elements in normal and cancerous tissues of the human stomach, colon and rectum. The frozen samples were not digested but were cut in a microtome and directly put on the reflector[135]. Using the TXRF, the concentrations of elements (P, S, K, Ca, Fe, Ni, Zn, Cu, Br) were compared in cancerous and healthy breast tissues. Several fragments were taken from each tissue to determine the variability of elemental distribution in the obtained samples[123]. The technique

has also been successfully used to determine the platinum content in biological samples. These were the tissues collected during biopsy of patients subjected to Cisplatin chemotherapy at different times from its administration. The obtained detection limit of platinum was 0.1 ppm[136]. Due to the TXRF analysis speed, uncomplicated measurement process and accuracy, this technique was considered suitable for carrying out trace analyses of small amounts of samples in medical and clinical trials[136].

Carvalho et al. have analysed distribution of Ca, Mn, Fe, Cu, Zn, Sr, Ba and Pb in human femur originated from archaeological excavations[6]. Rodriguez et al. have investigated whether the dog hair may be considered as potential biomarker of environmental arsenic exposure. Samples were measured using TXRF and the ICP-OES to check the accuracy of proposed methodology and there were no significant differences between the results obtained with these two techniques[42].

Experimental animals and sample preparation. The subject of the study was a group of six male Wistar rats, which were originated from the colony of the Department of Neuroanatomy, Institute of Zoology and Biomedical Research, Jagiellonian University, Krakow. The animals constituted a control group in our previous experiment focused on the elemental anomalies occurring in rat organs after the systemic exposure to iron oxide nanoparticles[7].

All procedures in which animals were involved were carried out with the approval of the Bioethical Commission of the Jagiellonian University (agreement no. 121/2015) and were performed in accordance with the international standards. The rats were housed in cages, with the access to water and standard rodent diet ad libitum. On the 60th day of their postnatal development, the animals were euthanized and perfused with 0.9% saline of high analytical purity. Muscle, brain, kidney, liver, heart and spleen were excised from the bodies, weighted and quickly frozen in liquid nitrogen. Removed organs, packed in sterile Whirl-pack bags, were stored in temperature − 80 °C.

For elemental analysis of rat organs the TXRF was applied. Before measurements, the tissues were weighted and digested. The organ weights were in range of 0.417–0.610 g for muscle, 1.722–1.923 g for brain, 2.126–2.806 g for kidney, 8.713–14.880 g for liver, 0.805–1.116 g for heart and 0.498–0.773 g for spleen. The removed livers, compared to the other organs, were significantly larger in weight. Therefore, each individual liver was cut into 5 or 6 separate pieces and separately subjected to mineralization. Digestion process was performed in few steps and the maximum achieved temperature was equal 190 °C at pressure 30 bar. Each organ was placed in a separate teflon vessel adding high purity 65% nitric acid (100,441/Suprapur, Merck Group). The typical volume of nitric acid was about 2.5 ml per 1 g of tissue. Microwave-assisted digestion was performed with the use of mineralizer SpeedWave 4 (Berghof). The conditions of the mineralization process were chosen according to the recommendations of the mineralizer manufacturer. After digestion, the teflon vessels were cooled down and their contents were separately poured to the test tubes. The samples were stored at a low temperature until analysis.

Basis of quantitative elemental analysis. The quantitative analysis was carried out with the use of the internal standard method. For this purpose gallium solution at concentration of 10 ppm was used. Typically, 0.3 ml of such solution was added to 1 ml of the digested sample and the content of the test tube was thoroughly mixed using a laboratory shaker to ensure the homogeneity of the solution. Afterwards, 2 µl of sample solution was transferred onto quartz glass carrier (Bruker Nano) and dried on a heating plate. Before this procedure the sample carriers were cleaned according to the producer recommendations and tested through the control measurements of background.

Analysis of the element contents in the liquid sample, using the internal standard method, is based on the relation (1):

$$C_i = \frac{C_{IS} * N_i}{N_{IS} * S_i} \tag{1}$$

where, C_i concentration of the element i in the liquid sample [ppm], C_{IS} known concentration of the internal standard [ppm], N_i and N_{IS} the numbers of counts for the element i and for the internal standard, S_i relative sensitivity for the element i determined by the analysis of calibration standards solutions.

In order to calculate the content of the element in the liquid sample of tissue, the dilution resulting from the addition of the internal standard has to be taken into account. The concentration of the element i in the liquid sample of the tissue is, then, expressed by the formula (2):

$$C_i^s = d * C_i \tag{2}$$

where, d coefficient of the dilution equal to the sum of the volume of the liquid sample and the volume of the solution of the internal standard.

To determine the concentration of the element in the organ, the mass conversion factor k_n for the organ n should also be taken into account which is expressed by the Eq. (3):

$$k_n = \frac{m_n + m_a}{m_n} \tag{3}$$

where, m_n mass of the organ n, m_a mass of the nitric acid added during mineralization.

As a result, the concentration C_i^n of the element i in the organ n is calculated based on the dependence (4):

$$C_i^n = C_i^s * k. \tag{4}$$

Evaluation of validation parameters. Limit of detection LOD_{ij} [ppm] for the element i in the organ j was calculated based on the results obtained for six samples of each organ in accordance with the formula (5):

$$LOD_{ij} = \frac{3 * C_{ij} * \sqrt{N_{BG}}}{N_{ij}} \tag{5}$$

where, C_{ij} concentration of the element i in the organ j [ppm], N_{BG} area of the background under K_α line for the element i in the organ j [a.u.], N_{ij} area of the peak for K_α line of the element i in the organ j [a.u.].

Final values of the detection limits of the examined elements for each organ were calculated as an average of the results obtained for six analysed samples.

Both precision and trueness of the technique were determined using standard reference material IAEA-A-13—the freeze dried animal blood. Six SRM samples weighing 200 mg were prepared, placed in separate teflon vessels with 5 ml of high purity 65% nitric acid and digested. Before elemental analysis of the reference material, 0.3 ml of the solution of the internal standard was added to each 1 ml of the sample. Similarly, as in the case of animal samples, the solution contained Ga at concentration of 10 ppm. For TXRF analysis 2 µl of sample solution was deposited on quartz glass pad (Bruker Nano) and dried on a heating plate. In order to determine the repeatability, first the coefficient of variation CV^i for the element i was determined in each measurement series as:

$$CV^i = \frac{1}{\bar{x}^i} * \sqrt{\frac{\sum_{j=1}^{n} \left(x_j^i - \bar{x}^i\right)^2}{n-1}} * 100\% \tag{6}$$

where, $\bar{x}^i$ the average concentration of the element i in a given measurement series [ppm], x_j^i the concentration of the element i obtained for single measurement j [ppm], n number of measurements in single series.

Repeatability of the analytical technique, express as coefficient of variation CV_g^i and taking into account all measurement series for each element i is defined as:

$$CV_g^i = \sqrt{\frac{1}{k}\sum_{j=1}^{k}\left(CV_j^i\right)^2} \tag{7}$$

where, k the number of measurement series.

Trueness for used analytical technique was calculated for every element according to the formula (8):

$$T = \frac{\bar{a}^i}{a_{ref}^i} * 100\% \tag{8}$$

where, $\bar{a}^i$ the average concentration of the element i calculated for all measurement series, a_{ref}^i the reference value of the concentration of the element i in IAEA-A-13 SRM.

Instrument and measurements conditions. The measurements were carried out in the Laboratory of X-ray Methods of the Institute of Physics at the Jan Kochanowski University in Kielce. For this purpose, S2 PICOFOX (Bruker Nano) TXRF spectrometer was used. The instrument is equipped with an air cooled X-ray tube with molybdenum anode and multilayer monochromator. The energy of the exciting beam was 17.5 keV and the focal spot was equal to 1.2×0.1 mm^2.

Samples on the quartz glass carriers were placed in 25-position spectrometer cassette. The measurement time was 20 min per sample and each of six SRM samples were measured 10 times.

Elemental composition of the normal rat organs. Energy calibration of the obtained TXRF spectra, carried out in the PyMCA program, allowed us to identify the elements present in the examined tissues. As an example, the spectrum of selected liver sample is shown in the Fig. 6. The identification and quantification of elements was performed based on their K_α lines and the following elements: P, S, K, Ca, Fe, Cu, Zn and Se were the subject of further quantitative study. As one can notice, Si line was also present in the spectrum, the source of which was the used quartz sample carrier, the Ar line from the air and Ga, which was added to the sample as an internal standard.

The quantitative analysis, performed on the way described earlier, allowed us to obtain information about the concentrations of P, S, K, Ca, Fe, Cu, Zn and Se in the examined organs of normal rats and the obtained data were used to prepare Fig. 7 and placed in the Table 5 which contains also the comparison of the recorded concentrations with the available literature data from various techniques of elemental analysis.

Based on the data presented in the Fig. 7 and Table 5, the analyzed elements can be classified into three groups: macroelements (with concentration higher than 1000 ppm), microelements (with concentration higher than 100 ppm and lower than 1000 ppm) and trace elements (with concentration lower than 100 ppm). The elements that in all organs persisted at the level of macroelements were: P, S and K. In case of Ca, the concentration above 1000 ppm was observed in the liver, muscle and spleen. In the three remaining organs, Ca was qualified to the micronutrient group. Fe and Zn concentrations above 100 ppm were recorded for liver and spleen. In the remaining organs, their contents were determined as trace. Cu and Se in all the examined organs were classified into the group of trace elements. The TXRF results, presented in the Table 5, pointed also at high variability in

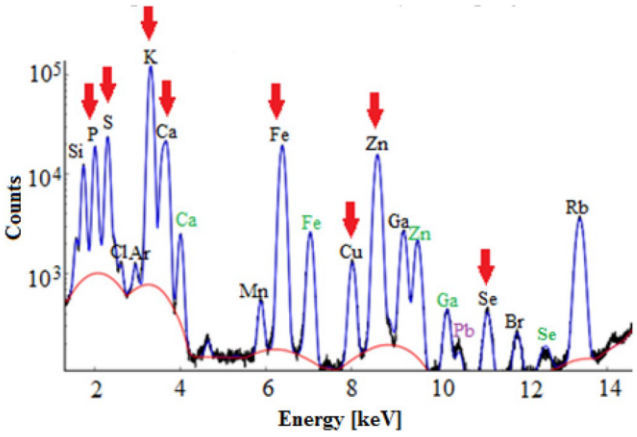

Figure 6. An example of X-ray fluorescence spectrum registered for liver sample. Kα, Kβ and L spectral lines were marked with black, green and purple colours, respectively. Lines of the analysed elements were marked with red arrows.

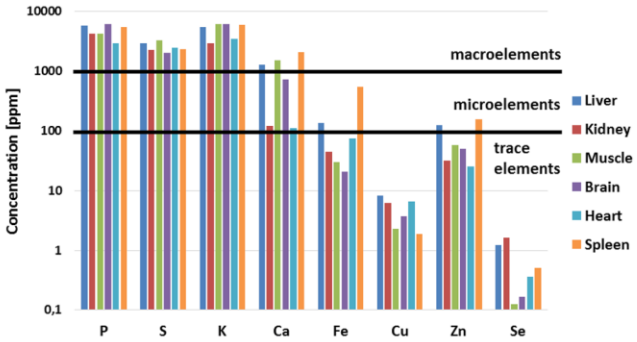

Figure 7. The contents of elements in every organ determined using TXRF.

the concentrations of the studied elements in tissues taken from individual animals. The high population variability concerned, mainly, the accumulation of Ca and Zn, and in some organs also Fe.

The aim of the study was also to compare the results of the elemental analysis of rat organs carried out using the TXRF with available literature evidence. The elemental data obtained using the techniques of AAS, ICP-OES and ICP-MS were used for this purpose. In the case of light elements, the concentrations determined using the TXRF were compared with the results obtained with ICP-OES technique by Leblondel et al.[78] and Shimamura et al.[28,103]. It was noted that in all organs, the P, S, K and Ca concentrations obtained using the TXRF were higher than those determined with ICP-OES[28,78,103] or consistent with them within the limits of observed population dispersion (concentration of S in kidney and heart[78]). The higher levels of light elements measured in our study may be influenced by the sample preparation method. Leblondel et al. used digestion of sample for 3 h at room temperature and then next 3 h at 70 °C in the presence of HNO_3[78]. Shimamura et al. performed sample decomposition using HNO_3 and H_2O_2 in high temperature (180 °C) conditions and they repeated that procedure 2 or 3 times[28,103]. No clear information on whether the digestion was performed in a close or open system was found in the mentioned papers. In our study, for tissue digestion we applied wet mineralization in a closed system using microwave energy. The technique is very often used to digest biomedical samples of different types, including the samples of organs[20,52,101,102], body fluids[17,32,83] or bones[12]. To its advantages one can include small amount of sample required for analyte preparation as well as the limitation of the risks of sample contamination and loss of light elements by limiting their volatility during digestion[10,38].

Concentrations of Fe, Cu, Zn and Se measured with TXRF were also confronted with the literature values obtained with various analytical techniques. In contrary to macroelements, the values determined with TXRF and measured with other techniques were usually in quite good accordance. The highest agreement was observed for Ca, Zn and Se levels for all the organs, excluding liver.

Comparison of validation parameters obtained for TXRF with other techniques of elemental analysis. Based on the obtained results, for each organ the detection limits of the elements were calculated and compared with the values of LODs obtained for other analytical techniques and published in the literature (Table 6). The detection limits of elements are expressed either in mass or volume units. For general compari-

Element	Liver		Kidney		Muscle		Brain		Heart		Spleen	
	Measured by TXRF	Literature data	Measured by TXRF	Literature data	Measured by TXRF	Literature data	Measured by TXRF	Literature data	Measured by TXRF	Literature data	Measured by TXRF	Literature data
P	5750 (704)	ICP-OES 2983.44 ± 163.37[78] 3900 ± 400[103] 3700[103]	4250 (280)	ICP-OES 3300 ± 20[28] 3400[28] 2531.77 ± 167.09[78]	4270 (120)	ICP-OES 1971.29 ± 121.21[78]	6110 (390)	ICP-OES 2521.85 ± 99.51[78]	2970 (270)	ICP-OES 2129.39 ± 94.55[78]	5460 (860)	ICP-OES 3188.04 ± 241.8[78]
S	2980 (150)	ICP-OES 2346.88 ± 202.56[78]	2290 (150)	ICP-OES 2327.04 ± 210.56[78]	3260 (150)	ICP-OES 2417.92 ± 194.24[78]	2030 (160)	ICP-OES 1320.64 ± 73.28[78]	2490 (310)	ICP-OES 2524.16 ± 113.92[78]	2370 (460)	ICP-OES 1953.6 ± 122.88[78]
K	5440 (610)	ICP-OES 3197.22 ± 152.88[78] 3300 ± 300[103] 3000[103]	2920 (200)	ICP-OES 2600 ± 20[28] 2600[28] 2467.14 ± 166.14[78]	6110 (380)	ICP-OES 3460.47 ± 231.66[78]	6100 (520)	ICP-OES 3084.51 ± 180.96[78]	3470 (180)	ICP-OES 2760.81 ± 157.95[78]	5920 (1060)	ICP-OES 4034.16 ± 253.5[78]
Ca	1300 (630)	ICP-OES 30.28 ± 2.48[78] 36.6 ± 4.3[103] 37.5[103]	120 (210)	ICP-OES 81 ± 9[28] 104[28] 54.52 ± 5.08[78]	1530 (3300)	ICP-OES 41.12 ± 3.48[78]	730 (1540)	ICP-OES 33.04 ± 3.52[78]	112 (320)	ICP-OES 25.72 ± 2.16[78]	2070 (6060)	ICP-OES 32.92 ± 5[78]
Fe	137 (17)	ICP-OES 531.0 ± 18.0[79] 1023.5 ± 95.9[79] 71.064 ± 8.43[78] 598 ± 102[103] 643[103] ASA: 73.4 ± 10.4[137]	45.3 (4.9)	ICP-OES 361.2 ± 9.4[79] 416.3 ± 97.1[79] 170 ± 22[28] 267[28] 40.88 ± 5.08[78]	30.1 (4.3)	ICP-OES 9.52 ± 2.07[78]	20.6 (4.4)	ICP-OES 11.48 ± 0.95[78]	75 (13)	ICP-OES 643.1 ± 31.3[79] 454.2 ± 9.4[79] 57.12 ± 6.26[78] ASA: 62.4 ± 6.0[137]	547 (200)	ICP-OES 185.19 ± 41.61[78] ASA: 173.3 ± 32.2[137]
Cu	8.37 (0.78)	ICP-OES 13.3 ± 0.2[79] 17.0 ± 0.3[79] 3.65 ± 0.31[78] 3.82 ± 0.2[21] 3.16 ± 0.2[21] 5.4 ± 0.8[103] 5.2[103] ASA: 6.50 ± 0.55[137]	6.37 (0.69)	ICP-OES 29.4 ± 1.1[79] 48.7 ± 5.8[79] 7.44 ± 1.41[78] 8.84 ± 0.5[21] 6.78 ± 0.8[21] ICP-MS 25 ± 5[28] 28[28]	2.35 (0.052)	ICP-OES 0.95 ± 0.18[78]	3.78 (0.61)	ICP-OES 1.951 ± 0.204[78]	6.61 (0.25)	ICP-OES 18.4 ± 0.5[79] 21.6 ± 0.6[79] 4.52 ± 0.35[78] ASA: 9.04 ± 1.25[137]	1.90 (0.15)	ICP-OES 1.107 ± 0.069[78] ASA: 2.34 ± 0.44[137]
Zn	125 (29)	ICP-OES: 103.0 ± 0.4[79] 92.7 ± 0.7[79] 24.39 ± 1.62[78] 30.91 ± 1.7[21] 29.43 ± 1.8[21] 32.8 ± 3.6[103] 32.3[103] ASA: 25.3 ± 3.8[137]	32 (13)	ICP-OES 80.4 ± 1.2[79] 74.0 ± 0.3[79] 29 ± 2[28] 32[28] 18.79 ± 1.52[78] 18.67 ± 1.1[21] 17.96 ± 1.5[21]	58 (180)	ICP-OES 10.59 ± 2.93[78]	50 (110)	ICP-OES 10.77 ± 0.72[78]	25.4 (5.1)	ICP-OES 62.9 ± 0.3[79] 68.7 ± 0.4[79] 14.502 ± 0.75[78] ASA: 17.9 ± 1.1[137]	159 (360)	ICP-OES 16.98 ± 1.23[78] ASA: 20.4 ± 1.7[137]
Se	1.25 (0.11)	ASA: 0.720 ± 0.030[137] 0.65 ± 0.06[138] ICP-MS: 1.4 ± 0.2[103] 1.4[103]	1.64 (0.15)	ICP-MS 1.6 ± 0.2[28] 1.9[28]	0.120 (0.019)		0.160 (0.033)		0.364 (0.032)	ASA: 0.430 ± 0.110[137]	0.520 (0.019)	ASA: 0.500 ± 0.080[137]

Table 5. The median value [μg/g] of P, S, K, Ca, Fe, Cu, Zn and Se concentrations obtained for each organ using TXRF together with corresponding literature data. In the parentheses the interquartile range of the concentration value is shown.

	LOD calculated for TXRF measurements						Literature values of LOD for other techniques			
	Liver	Brain	Heart	Kidney	Muscle	Spleen	F-AAS	GF-AAS	ICP-OES	ICP-MS
P	19.5 (4.9)[#]	13.3 (1.4)	11.7 (1.9)	14.1 (3.5)	28.6 (7.5)	19.8 (3.9)	n.f.	0.5 μg/g[a139]	0.68 μg/g[a140]	n.f.
S	5.0 (1.0)	4.96 (0.50)	4.80 (0.61)	5.3 (1.7)	10.2 (2.5)	6.79 (0.61)	30 μg/g[a141]	n.f.	8.7 μg/g[a142]	0.004 μg/g[a143]
K	2.37 (0.59)	2.16 (0.26)	1.76 (0.30)	1.88 (0.57)	4.5 (1.3)	3.06 (0.51)	0.01 μg/g[a144] 0.1 μg/g[a144]	0.0032 μg/g[a145]	0.68 μg/g[a140]	3 μg/g[38]
Ca	1.49 (0.51)	0.74 (0.25)	0.66 (0.25)	0.72 (0.23)	1.9 (1.1)	1.44 (0.71)	0.01 μg/g[34]	n.f.	0.005 [69]	0.801 μg/g[101]
Fe	0.24 (0.18)	0.116 (0.014)	0.111 (0.015)	0.129 (0.040)	0.266 (0.082)	0.229 (0.035)	0.08 μg/g[34]	1.6 μg/g[45]	0.5 μg/g[69]–2.3 μg/g[45]	0.00149 μg/g[98]–4 μg/g[38]
Cu	0.095 (0.021)	0.0764 (0.0084)	0.067 (0.011)	0.080 (0.025)	0.174 (0.058)	0.116 (0.024)	0.03 μg/g[34]	0.00000017 μg/g[60]–0.2 μg/g[45]	0.0109 μg/g[76]–2.1 μg/g[45]	0.00059 μg/g[98]–0.1 μg/g[38]
Zn	0.092 (0.021)	0.0722 (0.0080)	0.065 (0.014)	0.082 (0.027)	0.176 (0.054)	0.123 (0.026)	0.03 μg/g[34]	0.3 μg/g[45]	0.0357 μg/g[76]–1.1 μg/g[45]	0.00251 μg/g[98]–0.9 μg/g[101]
Se	0.0413 (0.0058)	0.0403 (0.0055)	0.0335 (0.0035)	0.043 (0.013)	0.090 (0.026)	0.0527 (0.0052)	0.0032 μg/g[ab146]	0.26–1.0[a147]	0.0002 μg/g[56]	0.0015 μg/g[101]–0.12 μg/g[18]

Table 6. Comparison of LODs of elements in [μg/g] obtained for examined organs using TXRF with the literature values for other analytical techniques. [#]LOD in [μg/g] together with the uncertainty calculated as standard deviation; [a]Value from the paper that does not concern the analysis biomedical samples; [b]Determined using HG-AAS; *n.f.* value not found in the discussed papers or not expressed in consistent unit.

Element	Recommended value [µg/g]	95% Confidence Interval [µg/g]	Measured value [µg/g]	TXRF	F-AAS	GF-AAS	ICP-OES	ICP-MS
P	940#	690–1120	653	69	n.f.	99.7[139]**	90[13]–99.8[84]*	104[119]
S	6500	6000–7000	6219	95	96.1–109.4[a141]	n.f.	99 ± 14[a148], 91 ± 2[a148]	100[119]
K	2500	2100–2700	2877	115	94–101[a144]	88 ± 7–104 ± 8[a145]	72[13]–104[84]*	98[119]–98.7[38]*
Ca	286	226–332	469	164	102.4[34]	n.f.	94[71]*–105[69]	64[96]*–105[39]*
Fe	2400	2200–2500	3048	127	97.8[34]	97[45]*–106[105]*	91.5 ± 1.8[82]–113[47]	71[101]*–111[101]*
Cu	4.3	3.7–4.8	5.6	130	104.1[34]	96.4[60]*–103.8[110]*	90[47]–108[86]*	81[100]*–125[101]*
Zn	13	12–14	18	140	95.1[110]*–95.9[110]*	97[45]*	87[79]–113[71]*	111 ± 30[95]
Se	0.24	0.15–0.31	0.22	92	97.8 ± 5.2[a,b146], 102.2 ± 5.3[a,b147]	89.4–98.8[a147]	91[83]–109[3]*	62[100]*–125[101]*

Table 7. Values of trueness [%] obtained using TXRF for the reference material IAEA-A-13 together with the lowest and highest values of the parameter met in examined literature. #Information value; *Calculated based on the literature data; [a]Value from the paper that does not concern the analysis biomedical samples; [b]Determined using HG-AAS; *n.f.* Value not found in discussed papers or not expressed in consistent unit.

Element	TXRF	F-AAS	GF-AAS	ICP-OES	ICP-MS
P	11.7	n.f.	n.f.	1.0[13]–3.0[35]	0.9[119]–3.9[119]
S	5.1	n.f.	n.f	5.7[a148], 1.1[a148]	0.8[119]–3.6[119]
K	2.9	0.7–9.4[a149]	4–7[a145]	0.6[35]–4.7[13]	1.2[119]–3.1[119]
Ca	5.4	0.7–4.3[a150]	n.f	2.0[35]–6[16]	1.2[90]–9.5[119]
Fe	5.1	1.2–10.0[a149]	< 7[a151]	0.5[83]–25[25]	1.13[96]–4.1[90]
Cu	5.7	3.4[a152], 7.2[a152]	1.29[60]–7.35[60]	0.6[83]–11.1[26]	0.7[100]–9.7[89]
Zn	4.1	0.8–8.6[a149]	8–15[a153]	0.3[83]–15[25]	0.2[100]–22.8[95]
Se	28.0	1.4–11.7[a,b146]	< 10[a147]	9.1[83]–9.3[83]	1.8[17]–30[35]

Table 8. Values of repeatability [%] obtained using TXRF for the reference material IAEA-A-13 with the lowest and highest values of these parameters met in examined literature. [a]Value from the paper that does not concern the analysis biomedical samples; [b]Determined using HG-AAS; *n.f.* Value not found in discussed papers or not expressed in consistent unit.

sons between TXRF and the discussed techniques, only LODs values expressed in mass units are useful and therefore they are placed in the Table 6. Additionally, the values of LODs determined for real biological samples are underlined. The remaining, not underlined values were in most cases determined in blank measurements. Additionally, when the detection limits for the element was not found in the papers dealing with the analysis of biomedical samples, the investigations concerning environmental or food samples were used for comparisons.

As one can notice from Table 6, the lowest limits of detection in our study were found for heart samples. They ranged from 0.0335 µg/g in case of Se to 11.7 µg/g for P. For most of the elements, the direct comparison between values of LODs obtained in the frame of our work and found in the literature is difficult, due to different sample matrices (real biological samples or blank samples) and/or inconsistent units. The exceptions are Ca and Fe, for which one can find the literature values of this parameter determined by Yang et al. for ICP-OES. The values of LODs were obtained there for the biological matrix, namely rabbit arteries sample, and were expressed in µg/g[69]. The Ca detection limits obtained for examined organs using TXRF are higher than determined for ICP-OES. In turn, those obtained for Fe are better than presented in the work of Yang et al.[69].

The general insight into the data presented in the Table 6 allows to conclude that the LODs received using TXRF for P are worse comparing to GF-AAS and ICP-OES, for which this parameter was obtained based on blank measurements. In the case of S, values of LODs received in our work are better than those of F-AAS for all examined organs and of ICP-OES for most of them, but much worse than obtained for ICP-MS. The LODs of K are similar to the values found for the ICP-MS but worse than for other discussed techniques in case of which the parameter was calculated for blank measurements. The Ca LODs for the TXRF are worse comparing to F-AAS and ICP-OES but similar to those of ICP-MS. The LODs of Fe achieved using TXRF are better than those of GF-AAS and ICP-OES and are within the range of values obtained for ICP-MS. They are, however, worse than Fe LODs achieved using F-AAS. Similar conclusions can be made for Cu, Zn and Se. However, for the last element better detection limits were obtained using ICP-OES than for TXRF.

To assess the reliability of the used analytical technique, the quantitative analysis of IAEA-A-13 reference material was performed. The values of trueness and repeatability calculated for TXRF are placed in Tables 7 and 8, respectively. The Tables contain also the lowest and highest values of the parameters found in the examined literature. If information about repeatability or trueness of techniques was not found in the papers concerning the analysis of biomedical samples, the data from environmental or food samples were used.

Based on the data presented in Table 7 it can be seen that for most of the elements, the values of trueness obtained using TXRF are a little worse than those received using other instrumental techniques. The exception

is the values of trueness for S and Se which in case of the TXRF, were equalled to 95% and 92%, respectively. In turn, the greatest discrepancies were observed for Ca (164%) and Zn (140%).

As one can notice from Table 8, for most of the elements the repeatability of the technique was in the range 2.9–5.7%. The values of this parameter calculated for S, K, Ca, Fe, Cu and Se were in good agreement or were slightly higher than that met in literature for other techniques. Exceptions were the values obtained for P and Se, in case of which this parameter was equal to 11.7 and 28.0%, respectively. Such high spread of results for Se may be connected with its low concentration in analysed reference material.

Conclusions

The comparison of the validation parameters of the discussed instrumental techniques, done based on the literature studies, pointed out that ICP-MS offers the best analytical possibilities. The technique allows multielemental analysis, including the determinations of ultra-trace elements due to the very low detection limits. Also precision and trueness of the results for ICP-MS are usually better than for other techniques of elemental analysis which makes it a powerful tool in case of biomedical samples examinations. Its widespread use in research is, however, limited, due to the high costs of both the instrument and the analysis of a sample. A very good analytical tool in term of the achieved detection limits of elements is GF-AAS and the detection limits of Be, Cr, Ni or As obtained using this technique are lower or comparable with the values for the plasma techniques.

The physiological concentrations of P, S, K, Ca, Fe, Cu, Zn and Se were determined using TXRF in the rat livers, kidneys, muscles, brains, hearts and spleens and compared with the literature data. Some discrepancies were observed for light elements (P, S, K, Ca) which may be connected with the used methods of tissue preparation. For higher-Z elements (Fe, Cu, Zn, Se) the differences were smaller and the results obtained using TXRF usually agreed with the data from other techniques within the limits of observed population dispersions.

Due to inconsistences in the type of matrices of examined samples and units in which detection limits were expressed, direct comparison of LODs values received for TXRF and the discussed techniques was difficult. The exceptions are detection limits of Ca and Fe achieved in ICP-OES for biomedical sample. LODs of Fe received in our work was better than found in the literature. In turn, the detection limits of Ca were higher for TXRF than for ICP-OES. The general comparison of discussed analytical techniques in respect of achieved LODs, showed that the values obtained using TXRF are usually better than those of GF-AAS for Fe, Zn and Se, than F-AAS for S and ICP-OES for Fe. The detection limits calculated in this work are within the range of the values determined for ICP-MS in case of Fe, Cu, Zn and Se, for ICP-OES in case of Cu and Zn, and for GF-AAS in case of Cu. TXRF, in terms of LODs, occurred to be worse than F-AAS for K, Ca, Fe, Cu, Zn and Se, than GF-AAS for P and K, than ICP-OES for P, K, Ca and Se and than ICP-MS for S.

Our results showed that the precision of the TXRF is comparable with those of other discussed instrumental techniques. The repeatability of the technique is good and for most of the examined elements is within the range of 2.9–5.7%. Some discrepancies between the reference and the measured values of concentrations for the IAEA-A-13 reference material were, however, observed.

Received: 8 October 2020; Accepted: 18 January 2021
Published online: 12 February 2021

References

1. Penner, M. H. Basic principles of spectroscopy. In *Food Analysis* (Springer International Publishing, Berlin, 2017).
2. Taylor, H. E. *Inductively Coupled Plasma-Mass Spectrometry. Practices and Techniques* (Academic Press, New York, 2001).
3. Rahil-Khazen, R., Bolann, B. J., Myking, A. & Ulvik, R. J. Multi-element analysis of trace element levels in human autopsy tissues by using inductively coupled atomic emission spectrometry technique (ICP-AES). *J. Trace Elem. Med Biol.* **16**, 15–25 (2002).
4. Zimmermann, S., Messerschmidt, J., von Bohlen, A. & Sures, B. Determination of Pt, Pd and Rh in biological samples by electrothermal atomic absorption spectrometry as compared with adsorptive cathodic stripping voltammetry and total-reflection X-ray fluorescence analysis. *Anal. Chim. Acta* **498**, 93–104 (2003).
5. Stephan, C. H., Fournier, M., Brousseau, P. & Sauvé, S. Graphite furnace atomic absorption spectrometry as a routine method for the quantification of beryllium in blood and serum. *Chem. Central J.* https://doi.org/10.1186/1752-153X-2-14 (2008).
6. Carvalho, M. L., Marques, A. F., Lima, M. T. & Reus, U. Trace elements distribution and post-mortem intake in human bones from middle age by total reflection X-ray fluorescence. *Spectrochim. Acta Part B* **59**, 1251–1257 (2004).
7. Matusiak, K. *et al.* The elemental changes occurring in the rat liver after exposure to PEG-coated iron oxide nanoparticles: Total reflection X-ray fluorescence (TXRF) spectroscopy study. *Nanotoxicology* **11**, 1225–1236 (2017).
8. Heitland, P. *et al.* Application of ICP-MS and HPLC-ICP–MS for diagnosis and therapy of a severe intoxication with hexavalent chromium and inorganic arsenic. *J. Trace Elem. Med Biol.* **41**, 36–40 (2017).
9. Krebs, N. *et al.* Assessment of trace elements in human brain using inductively coupled plasma mass spectrometry. *J. Trace Elem. Med Biol.* **28**, 1–7 (2014).
10. Roa, E., Capangpangan, M. & Schultz, M. Modification and validation of a microwave-assisted digestion method for subsequent ICP-MS determination of selected heavy metals in sediment and fish samples in Agusan River Philippines. *J. Environ. Chem. Ecotoxicol.* **2**, 141–151 (2010).
11. Espinoza-Quiñones, F. R., Módenes, A. N., dos Santos, J., Obregón, P. L. & de Pauli, A. R. Insights on limits of detection, precision and accuracy in TXRF analysis of trace and major elements in environmental solid suspensions. *Appl. Radiat. Isot.* **137**, 80–90 (2018).
12. Tang, S., Parsons, P. J. & Slavin, W. Rapid and reliable method for the determination of aluminium in bone by electrothermal atomic absorption spectrometry. *Analyst* **121**, 195 (1996).
13. Takahashi, S. *et al.* Determination of major and trace elements in the liver of Wistar rats by inductively coupled plasma-atomic emission spectrometry and mass spectrometry. *Lab. Anim.* **34**, 97–105 (2000).
14. Fukui, Y., Ohashi, F., Sakuragi, S., Moriguchi, J. & Ikeda, M. Comparative evaluation of GFAAS and ICP-MS for analyses of cadmium in blood. *Ind. Health* **49**, 338–343 (2011).
15. Campillo, N. Determination of molybdenum, chromium and aluminium in human urine by electrothermal atomic absorption spectrometry using fast-programme methodology. *Talanta* **48**, 905–912 (1999).

16. Korvela, M. *et al.* Quantification of 10 elements in human cerebrospinal fluid from chronic pain patients with and without spinal cord stimulation. *J. Trace Elem. Med Biol.* **37**, 1–7 (2016).
17. Markiewicz, B. *et al.* Multielemental analysis of 18 essential and toxic elements in amniotic fluid samples by ICP-MS: Full procedure validation and estimation of measurement uncertainty. *Talanta* **174**, 122–130 (2017).
18. Morton, J., Tan, E. & Suvarna, S. K. Multi-elemental analysis of human lung samples using inductively coupled plasma mass spectrometry. *J. Trace Elem. Med Biol.* **43**, 63–71 (2017).
19. Dudek-Adamska, D., Lech, T. & Kościelniak, P. Optimization and validation of an ETAAS method for the determination of nickel in postmortem material. *J. Anal. Toxicol.* **39**, 460–464 (2015).
20. Rahil-Khazen, R., Bolann, B. J. & Ulvik, R. J. Correlations of trace element levels within and between different normal autopsy tissues analyzed by inductively coupled plasma atomic emission spectrometry (ICP-AES). *Biometals* **15**, 87–98 (2002).
21. Cui, X. & Okayasu, R. Arsenic accumulation, elimination, and interaction with copper, zinc and manganese in liver and kidney of rats. *Food Chem. Toxicol.* **46**, 3646–3650 (2008).
22. Piacenti da Silva, M., Zucchi, O. L. A. D., Ribeiro-Silva, A. & Poletti, M. E. Discriminant analysis of trace elements in normal, benign and malignant breast tissues measured by total reflection X-ray fluorescence. *Spectrochim. Acta, Part B* **64**, 587–592 (2009).
23. Prejac, J. *et al.* Hair for a long-term biological indicator tissue for assessing the strontium nutritional status of men and women. *J. Trace Elem. Med Biol.* **42**, 11–17 (2017).
24. Baghban, N., Haji Shabani, A. M. & Dadfarnia, S. Solid phase extraction and flame atomic absorption spectrometric determination of trace amounts of cadmium and lead in water and biological samples using modified TiO2 nanoparticles. *Int. J. Environ. Anal. Chem.* **93**, 1367–1380 (2013).
25. Sahuquillo, A., Rubio, R., Ribó, J. M., Ros, E. & Vela, M. Application of focused-microwave wet digestion to the determination of trace metals in human gallstones by ICP/AES. *J. Trace Elem. Med Biol.* **14**, 96–99 (2000).
26. Chew, L., Bradley, D., Mohd, A. Y. & Jamil, M. M. Zinc, lead and copper in human teeth measured by induced coupled argon plasma atomic emission spectroscopy (ICP-AES). *Appl. Radiat. Isot.* **53**, 633–638 (2000).
27. Shapira, Y., Lam, A. M., Artru, A. A., Eng, C. & Soltow, L. Ketamine alters calcium and magnesium in brain tissue following experimental head trauma in rats. *J. Cereb. Blood Flow Metab.* **13**, 962–968 (1993).
28. Shimamura, T. *et al.* The concentrations of major and trace elements in rat kidney: Aging effects and mutual relationships. *J. Trace Elem. Med Biol.* **27**, 12–20 (2013).
29. Chwiej, J. *et al.* Various ketogenic diets can differently support brain resistance against experimentally evoked seizures and seizure-induced elemental anomalies of hippocampal formation. *J. Trace Elem. Med Biol.* **42**, 50–58 (2017).
30. Chwiej, J. *et al.* Elemental anomalies in the hippocampal formation after repetitive electrical stimulation: An X-ray fluorescence microscopy study. *J. Biol. Inorg. Chem.* **19**, 1209–1220 (2014).
31. Chwiej, J. *et al.* Neuroprotective action of FK-506 (tacrolimus) after seizures induced with pilocarpine: Quantitative and topographic elemental analysis of brain tissue. *J. Biol. Inorg. Chem.* **15**, 283–289 (2010).
32. Harrington, J. M., Young, D. J., Essader, A. S., Sumner, S. J. & Levine, K. E. Analysis of human serum and whole blood for mineral content by ICP-MS and ICP-OES: Development of a mineralomics method. *Biol. Trace Elem. Res* **160**, 132–142 (2014).
33. Kubala-Kukuś, A. *et al.* Determination of lead at physiological level in human biological materials using the total reflection X-ray fluorescence analysis. *X-Ray Spectrom.* **45**, 318–324 (2016).
34. Fakayode, S. O., Owen, S. L., Pollard, D. A. & Yakubu, M. Use of flame atomic absorption spectroscopy and multivariate analysis for the determination of trace elements in human scalp. *Am. J. Anal. Chem.* **04**, 348–359 (2013).
35. Hasegawa, T., Matsuura, H., Inagaki, K. & Haraguchi, H. Major-to-ultratrace elements in bone-marrow fluid as determined by ICP-AES and ICP-MS. *Anal. Sci.* **19**, 147–150 (2003).
36. Benninghoff, L., von Czarnowski, D., Denkhaus, E. & Lemke, K. Analysis of human tissues by total reflection X-ray fluorescence. Application of chemometrics for diagnostic cancer recognition. *Spectrochim. Acta Part B* **52**, 1039–1046 (1997).
37. Alimonti, A. *et al.* Elemental profile of cerebrospinal fluid in patients with Parkinson's disease. *J. Trace Elem. Med Biol.* **21**, 234–241 (2007).
38. Boulyga, S. F., Becker, J. S., Malenchenko, A. F. & Dietze, H.-J. Application of ICP-MS for multielement analysis in small sample amoun ts of pathological thyroid tissue. *Mikrochim. Acta* **134**, 215–222 (2000).
39. Varga, I., Szebeni, Á., Szoboszlai, N. & Kovács, B. Determination of trace elements in human liver biopsy samples by ICP–MS and TXRF: Hepatic steatosis and nickel accumulation. *Anal. Bioanal. Chem.* **383**, 476–482 (2005).
40. Skoczeń, A. *et al.* Low doses of polyethylene glycol coated iron oxide nanoparticles cause significant elemental changes within main organs. *Chem. Res. Toxicol.* **31**, 876–884 (2018).
41. Wagner, A. & Boman, J. Biomonitoring of trace elements in muscle and liver tissue of freshwater fish. *Spectrochim. Acta, Part B* **58**, 2215–2226 (2003).
42. Rodriguez Castro, M. C., Andreano, V., Custo, G. & Vázquez, C. Potentialities of total reflection X-ray fluorescence spectrometry in environmental contamination: Hair of owned dogs as sentinel of arsenic exposure. *Microchem. J.* **110**, 402–406 (2013).
43. Acar, O. Determination of lead chromium, manganese and zinc in slurries of botanical and biological samples by electrothermal atomic absorption spectrometry using tungsten-containing chemical modifiers. *Microchim. Acta* **151**, 53–58 (2005).
44. Shemirani, F., Baghdadi, M., Ramezani, M. & Jamali, M. R. Determination of ultra trace amounts of bismuth in biological and water samples by electrothermal atomic absorption spectrometry (ET-AAS) after cloud point extraction. *Anal. Chim. Acta* **534**, 163–169 (2005).
45. Andrási, E., Igaz, S., Szoboszlai, N., Farkas, É. & Ajtony, Z. Several methods to determine heavy metals in the human brain. *Spectrochim. Acta, Part B* **54**, 819–825 (1999).
46. Lech, T. ICP OES and CV AAS in determination of mercury in an unusual fatal case of long-term exposure to elemental mercury in a teenager. *Forensic Sci. Int.* **237**, e1–e5 (2014).
47. Chen, S., Jiang, Z., Hu, B., Liao, Z. & Ajtony, Z. Direct determination of trace elements in micro amounts of biological samples using electrothermal vaporization coupled to ICP-AES | request PDF. *At. Spectrosc.* **23**, 86–91 (2002).
48. Trzcinka-Ochocka, M., Brodzka, R. & Janasik, B. Useful and fast method for blood lead and cadmium determination using ICP-MS and GF-AAS validation parameters: Fast method for lead and cadmium determination in blood. *J. Clin. Lab. Anal.* **30**, 130–139 (2016).
49. Sanz-Medel, A. & Pereiro, R. *Atomic Absorption Spectrometry: An Introduction* 2nd edn. (Momentum Press, New York, 2014).
50. Lajunen, L. H. J. & Peramaki, P. *Spectrochemical Analysis by Atomic Absorption and Emission* 2nd edn. (The Royal Society of Chemistry, Londin, 2004).
51. Xu, N., Majidi, V., Ehmann, W. D. & Markesbery, W. R. Determination of aluminium in human brain tissue by electrothermal atomic absorption spectrometry. *J. Anal. At. Spectrom.* **7**, 749–751 (1992).
52. Lech, T. & Dudek-Adamska, D. Optimization and validation of a procedure for the determination of total chromium in post-mortem material by ETAAS. *J. Anal. Toxicol.* **37**, 97–101 (2013).
53. Bermejo-Barrera, P. Determination of aluminium and manganese in human scalp hair by electrothermal atomic absorption spectrometry using slurry sampling. *Talanta* **45**, 1147–1154 (1998).
54. Goldberg, W. J. & Allen, N. Determination of Cu, Mn, Fe, and Ca in six regions of normal human brain, by atomic absorption spectroscopy. *Clin. Chem.* **27**, 562–564 (1981).

55. Leung, F. Y. & Edmond, P. Determination of silicon in serum and tissue by electrothermal atomic absorption spectrometry. *Clin. Biochem.* **30**, 399–403 (1997).
56. Mohammadi, M., Riyahi Bakhtiari, A. & Khodabandeh, S. Concentration of Cd, Pb, Hg, and Se in different parts of human breast cancer tissues. *J. Toxicol.* **2014**, 1–5 (2014).
57. House, E. *et al.* The aluminium content of breast tissue taken from women with breast cancer. *J. Trace Elem. Med Biol.* **27**, 257–266 (2013).
58. Villeneuve, J.-P., Bilodeau, M., Lepage, R., Côté, J. & Lefebvre, M. Variability in hepatic iron concentration measurement from needle-biopsy specimens. *J. Hepatol.* **25**, 172–177 (1996).
59. Afridi, H. I. *et al.* Evaluation of toxic metals in biological samples (scalp hair, blood and urine) of steel mill workers by electrothermal atomic absorption spectrometry. *Toxicol. Ind. Health* **22**, 381–393 (2006).
60. Afridi, H. *et al.* Evaluation of arsenic, cobalt, copper and manganese in biological samples of steel mill workers by electrothermal atomic absorption spectrometry. *Toxicol. Ind. Health* **25**, 59–69 (2009).
61. Khlifi, R. *et al.* Arsenic, cadmium, chromium and nickel in cancerous and healthy tissues from patients with head and neck cancer. *Sci. Total Environ.* **452–453**, 58–67 (2013).
62. Yaman, M., Kaya, G. & Simsek, M. Comparison of trace element concentrations in cancerous and noncancerous human endometrial and ovary tissues. *Int. J. Gynecol. Cancer* **17**, 220–228 (2007).
63. Arain, S. S. *et al.* Determination of nickel in blood and serum samples of oropharyngeal cancer patients consumed smokeless tobacco products by cloud point extraction coupled with flame atomic absorption spectrometry. *Environ. Sci. Pollut. Res.* **21**, 12017–12027 (2014).
64. Arain, M. S. *et al.* Preconcentration and determination of manganese in biological samples by dual cloud point extraction and coupled with flame atomic absorption spectrometry. *J. Anal. At. Spectrom.* https://doi.org/10.1039/C4JA00266K (2020).
65. Jablonska, E. *et al.* Cadmium, arsenic, selenium and iron—Implications for tumor progression in breast cancer. *Environ. Toxicol. Pharmacol.* **53**, 151–157 (2017).
66. Montaser, A. & Golightly, D. W. *Inductively Coupled Plasmas in Analytical Spectrometry* (VCH Publishers, Weinheim, 1987).
67. Gómez, L. R., Márquez, G. D. & Chirinos, J. R. Dual nebulizer sample introduction system for simultaneous determination of volatile elemental hydrides and other elements. *Anal. Bioanal. Chem.* **386**, 188–195 (2006).
68. Tohno, Y. *et al.* Simultaneous accumulation of calcium, phosphorus, and magnesium in various human arteries. *Biol. Trace Elem. Res.* **82**, 021–028 (2001).
69. Yang, Z. *et al.* Determination of calcium, iron and magnesium in rabbit arteries by inductively coupled plasma atomic emission spectrometry. *Microchem. J.* **72**, 49–54 (2002).
70. Naganuma, T. *et al.* Age-dependent decreases of sulfur and magnesium in human round ligaments of the uterus and relationships among elements. *Biol. Trace Elem. Res.* **102**, 73–82 (2004).
71. Andrási, E., Farkas, É., Scheibler, H., Réffy, A. & Bezúr, L. Al, Zn, Cu, Mn and Fe levels in brain in Alzheimer's disease. *Arch. Gerontol. Geriatr.* **21**, 89–97 (1995).
72. Andrási, E., Páli, N., Molnár, Z. & Kösel, S. Brain aluminum, magnesium and phosphorus contents of control and Alzheimer-diseased patients. *J. Alzheimer's Dis.* **7**, 273–284 (2005).
73. Andrási, E., Nádasdi, J., Molnar, Z., Bezur, L. & Ernyei, L. Determination of main and trace element contents in human brain by NAA and ICP-AES methods. *Biol. Trace Elem. Res.* **26**, 691–698 (1990).
74. Faa, G. *et al.* Brain copper, iron, magnesium, zinc, calcium, sulfur and phosphorus storage in Wilson's disease. *J. Trace Elem. Med Biol.* **15**, 155–160 (2001).
75. Farah, I. O., Nguyen, P. X., Arslan, Z., Ayensu, W. & Cameron, J. A. Significance of differential metal loads in normal versus cancerous cadaver tissues. *Biomed. Sci. Instrum.* **46**, 404–409 (2010).
76. MacLachlan, D. J. *et al.* Arsenic, cadmium, cobalt, copper, lead, mercury, molybdenum, selenium and zinc concentrations in liver, kidney and muscle in Australian sheep. *J. Food Compos. Anal.* **50**, 97–107 (2016).
77. Subotić, S., Višnjić-Jeftić, Ž, Penezić, A. & Čirović, D. Concentrations of selected elements in liver tissue of grey wolves (Canis lupus) from Serbia. *Bull. Environ. Contam. Toxicol.* **99**, 701–705 (2017).
78. Leblondel, G., Mauras, Y. & Allain, P. Tissue distribution of some elements in rats. *Biol. Trace Elem. Res.* **10**, 327–333 (1986).
79. dos Santos, L. R. S. S. R., de Freitas Santos, A. & das Andrade Korn,. Effects of furosemide administration on the concentration of essential and toxic elements in Wistar rats by inductively coupled plasma optical emission spectrometry. *J. Trace Elem. Med. Biol.* **48**, 25–29 (2018).
80. Sivrikaya, A., Bicer, M., Akil, M., Baltaci, A. K. & Mogulkoc, R. Effects of zinc supplementation on the element distribution in kidney tissue of diabetic rats subjected to acute swimming. *Biol. Trace Elem. Res.* **147**, 195–199 (2012).
81. Forte, G. *et al.* Trace and major elements in whole blood, serum, cerebrospinal fluid and urine of patients with Parkinson's disease. *J. Neural Trans.* https://doi.org/10.1007/s00702-004-0124-0 (2020).
82. Bianchi, F., Maffini, M., Mangia, A., Marengo, E. & Mucchino, C. Experimental design optimization for the ICP-AES determination of Li, Na, K, Al, Fe, Mn and Zn in human serum. *J. Pharm. Biomed. Anal.* **43**, 659–665 (2007).
83. Rahil-Khazen, R. & Henriksen, H. Validation of inductively coupled plasma atomic emission spectrometry technique (ICP-AES) for multi-element analysis of trace elements in human serum. *Scand. J. Clin. Lab. Investig.* **60**, 677–686 (2000).
84. Zaichick, V., Zaichick, S., Karandashev, V. & Nosenko, S. The effect of age and gender on Al, B, Ba, Ca, Cu, Fe, K, Li, Mg, Mn, Na, P, S, Sr, V, and Zn contents in rib bone of healthy humans. *Biol. Trace Elem. Res.* **129**, 107–115 (2009).
85. Lanocha, N., Kalisinska, E., Kosik-Bogacka, D. I. & Budis, H. Evaluation of dog bones in the indirect assessment of environmental contamination with trace elements. *Biol. Trace Elem. Res.* **147**, 103–112 (2012).
86. Sreenivasa Rao, K., Balaji, T., Prasada Rao, T., Babu, Y. & Naidu, G. R. K. Determination of iron, cobalt, nickel, manganese, zinc, copper, cadmium and lead in human hair by inductively coupled plasma-atomic emission spectrometry. *Spectrochim. Acta Part B Atomic Spectrosc.* **57**, 1333–1338 (2002).
87. Miekeley, N., Mortari, S. & Schubach, A. Monitoring of total antimony and its species by ICP-MS and on-line ion chromatography in biological samples from patients treated for leishmaniasis. *Anal. Bioanal. Chem.* **372**, 495–502 (2002).
88. Heitland, P. & Köster, H. D. Biomonitoring of 37 trace elements in blood samples from inhabitants of northern Germany by ICP–MS. *J. Trace Elem. Med Biol.* **20**, 253–262 (2006).
89. Liu, X. *et al.* Determination of 16 selected trace elements in children plasma from China economical developed rural areas using high resolution magnetic sector inductively coupled mass spectrometry. *J. Anal. Methods Chem.* **2014**, 1–6 (2014).
90. Meyer, S. *et al.* Development, validation and application of an ICP-MS/MS method to quantify minerals and (ultra-)trace elements in human serum. *J. Trace Elem. Med Biol.* **49**, 157–163 (2018).
91. Heitland, P. & Köster, H. D. Biomonitoring of 30 trace elements in urine of children and adults by ICP-MS. *Clin. Chim. Acta* **365**, 310–318 (2006).
92. Benkhedda, K., Chen, H., Dabeka, R. & Cockell, K. Isotope ratio measurements of iron in blood samples by multi-collector ICP-MS to support nutritional investigations in humans. *Biol. Trace Elem. Res.* **122**, 179–192 (2008).
93. Arnason, J. G., Pellegri, C. N. & Parsons, P. J. Determination of total uranium and uranium isotope ratios in human urine by ICP-MS: results of an interlaboratory study. *J. Anal. At. Spectrom.* **30**, 126–138 (2015).
94. McDonald, R. J. *et al.* Gadolinium deposition in human brain tissues after contrast-enhanced MR imaging in adult patients without intracranial abnormalities. *Radiology* **285**, 546–554 (2017).

95. Panayi, A. E., Spyrou, N. M., Iversen, B. S., White, M. A. & Part, P. Determination of cadmium and zinc in Alzheimer's brain tissue using inductively coupled plasma mass spectrometry. *J. Neurol. Sci.* **195**, 1–10 (2002).
96. Xie, B. *et al.* Differential diagnosis of multielements in cancerous and non-cancerous esophageal tissues. *Talanta* **196**, 585–591 (2019).
97. Kohzadi, S. *et al.* Evaluation of trace element concentration in cancerous and non-cancerous tissues of human stomach. *Chemosphere* **184**, 747–752 (2017).
98. Şahin, M., Karayakar, F., Erdogan, K. E., Bas, F. & Colak, T. Liver tissue trace element levels in HepB patients and the relationship of these elements with histological injury in the liver and with clinical parameters. *J. Trace Elem. Med Biol.* **45**, 70–77 (2018).
99. Day, P. L., Eckdahl, S. J., Maleszewski, J. J., Wright, T. C. & Murray, D. L. Establishing human heart chromium, cobalt and vanadium concentrations by inductively coupled plasma mass spectrometry. *J. Trace Elem. Med Biol.* **41**, 60–65 (2017).
100. Batista, B. L., Rodrigues, J. L., de Oliveira Souza, V. C. & Barbosa, F. A fast ultrasound-assisted extraction procedure for trace elements determination in hair samples by ICP-MS for forensic analysis. *Forens. Sci. Int.* **192**, 88–93 (2009).
101. García-Vaquero, M. *et al.* Influence of Cu supplementation on toxic and essential trace element status in intensive reared beef cattle. *Food Chem. Toxicol.* **49**, 3358–3366 (2011).
102. Gui, J. *et al.* Handy cloud point extraction coupled with inductively coupled plasma mass spectrometry for analysis of trace zirconium in complex biological samples. *Microchem. J.* **138**, 190–196 (2018).
103. Shimamura, T. *et al.* Age-related effects of major and trace element concentrations in rat liver and their mutual relationships. *J. Trace Elem. Med Biol.* **27**, 286–294 (2013).
104. Majewska, U. *et al.* Total reflection X-ray fluorescence medical applications: Elemental analysis of human urine. *Spectrochim. Acta, Part B* **147**, 121–131 (2018).
105. Ramos, P. *et al.* Iron levels in the human brain: A post-mortem study of anatomical region differences and age-related changes. *J. Trace Elem. Med Biol.* **28**, 13–17 (2014).
106. Serpa, R. F. B. *et al.* Elemental concentration analysis in brain structures from young, adult and old Wistar rats by total reflection X-ray fluorescence with synchrotron radiation. *Spectrochim. Acta Part B Atomic Spectrosc.* **61**, 1205–1209 (2006).
107. Marguí, E. *et al.* Critical evaluation of the use of total reflection X-ray fluorescence spectrometry for the analysis of whole blood samples: Application to patients with thyroid gland diseases. *Anal. Bioanal. Chem.* **411**, 1659–1670 (2019).
108. Nawrocka, A. & Szkoda, J. Determination of chromium in biological material by electrothermal atomic absorption spectrometry method. *Bull. Vet. Inst. Pulawy* **56**, 585–589 (2012).
109. Mirji, S. *et al.* Determination of trace elements in normal and malignant breast tissues of different age group using total reflection X-ray fluorescence spectrometer. *X-Ray Spectrom.* **47**, 432–440 (2018).
110. Treble, R. G., Thompson, T. S. & Lynch, H. R. Determination of copper, manganese and zinc in human liver. *Biometals* **11**, 49–53 (1998).
111. Ostachowicz, B. *et al.* Analysis of some chosen elements of cerebrospinal fluid and serum in amyotrophic lateral sclerosis patients by total reflection X-ray fluorescence. *Spectrochim. Acta, Part B* **61**, 1210–1213 (2006).
112. Menditto, A., Patriarca, M. & Magnusson, B. Understanding the meaning of accuracy, trueness and precision. *Accred. Qual. Assur.* **12**, 45–47 (2007).
113. Huber, L. *Validation and Qualification in Analytical Laboratories* 2nd edn. (CRC Press, Boca Raton, 2007).
114. Konieczka, P. & Namiesnik, J. *Quality Assurance and Quality Control in the Analytical Chemical Laboratory: A Practical Approach* 2nd edn, 411 (CRC Press, Boca Raton, 2018).
115. Thompson, M., Ellison, S. L. R. & Wood, R. Harmonized guidelines for single-laboratory validation of methods of analysis (IUPAC technical report). *Pure Appl. Chem.* **74**, 835–855 (2002).
116. BIPM - International Vocabulary of Metrology (VIM), https://www.bipm.org/en/publications/guides/vim.html, (accessed 22 September 2020).
117. Shrivastava, A. & Gupta, V. Methods for the determination of limit of detection and limit of quantitation of the analytical methods. *Chron. Young Sci.* **2**, 21 (2011).
118. Lech, T. Application of ICP-OES to the determination of barium in blood and urine in clinical and forensic analysis. *J. Anal. Toxicol.* **37**, 222–226 (2013).
119. Takasaki, Y. *et al.* Multielement analysis of micro-volume biological samples by ICP-MS with highly efficient sample introduction system. *Talanta* **87**, 24–29 (2011).
120. Sahin, D., Ilbay, G. & Ates, N. Changes in the blood-brain barrier permeability and in the brain tissue trace element concentrations after single and repeated pentylenetetrazole-induced seizures in rats. *Pharmacol. Res.* **48**, 69–73 (2003).
121. Wobrauschek, P. Total reflection X-ray fluorescence analysis—a review. *X-Ray Spectrom.* **36**, 289–300 (2007).
122. Klockenkämper, R. & von Bohlen, A. (eds) *Total-Reflection X-ray Fluorescence Analysis and Related Methods* (John Wiley & Sons Inc, Hoboken, 2014).
123. Magalhães, T., Becker, M., Carvalho, M. L. & von Bohlen, A. Study of Br, Zn, Cu and Fe concentrations in healthy and cancer breast tissues by TXRF. *Spectrochim. Acta Part B* **63**, 1473–1479 (2008).
124. Martinez, T. *et al.* Determination of lead in blood by TXRF and its correlation to environmental lead. *Nucl. Instrum. Methods Phys. Res., Sect. B* **213**, 584–589 (2004).
125. Telgmann, L. *et al.* Simple and rapid quantification of gadolinium in urine and blood plasma samples by means of total reflection X-ray fluorescence (TXRF). *Metallomics* **3**, 1035 (2011).
126. Abraham, J. A., Sánchez, H. J., Grenón, M. S. & Pérez, C. A. TXRF analysis of metals in oral fluids of patients with dental implants: TXRF analysis of oral fluids. *X-Ray Spectrom.* **43**, 193–197 (2014).
127. Stosnach, H. & Mages, M. Analysis of nutrition-relevant trace elements in human blood and serum by means of total reflection X-ray fluorescence (TXRF) spectroscopy. *Spectrochim. Acta Part B* **64**, 354–356 (2009).
128. Leitão, R. G. *et al.* Elemental concentration analysis in prostate tissues using total reflection X-ray fluorescence. *Radiat. Phys. Chem.* **95**, 62–64 (2014).
129. Sánchez, H. J., Valentinuzzi, M. C., Grenón, M. & Abraham, J. Total reflection X-ray fluorescence analysis of oral fluids of women affected by osteoporosis and osteopenia. *Spectrochim. Acta, Part B* **63**, 1485–1488 (2008).
130. Marcó, L. M., Greaves, E. D. & Alvarado, J. Analysis of human blood serum and human brain samples by total reflection X-ray fluorescence spectrometry applying Compton peak standardization. *Spectrochim. Acta Part B* **54**, 1469–1480 (1999).
131. Magalhães, T., Carvalho, M. L., Von Bohlen, A. & Becker, M. Study on trace elements behaviour in cancerous and healthy tissues of colon, breast and stomach: Total reflection X-ray fluorescence applications. *Spectrochim. Acta Part B* **65**, 493–498 (2010).
132. Magalhães, T., von Bohlen, A., Carvalho, M. L. & Becker, M. Trace elements in human cancerous and healthy tissues from the same individual: A comparative study by TXRF and EDXRF. *Spectrochim. Acta Part B* **61**, 1185–1193 (2006).
133. Lankosz, M. W. *et al.* Application of the total reflection X-ray fluorescence method to the elemental analysis of brain tumors of different types and grades of malignancy. *Spectrochim. Acta Part B* **101**, 98–105 (2014).
134. Majewska, U. *et al.* Trace element concentration distributions in breast, lung and colon tissues. *Phys. Med. Biol.* **52**, 3895–3911 (2007).
135. von Czarnowski, D., Denkhaus, E. & Lemke, K. Determination of trace element distribution in cancerous and normal human tissues by total reflection X-ray fluorescence analysis. *Spectrochim. Acta Part B* **52**, 1047–1052 (1997).

136. Suzuki, T., Sasaki, A. & Nakai, I. Total reflection X-ray fluorescence analysis of cisplatin platinum in human cancerous tissues obtained by biopsy. *J. Trace Microprobe Tech.* **19**, 547–561 (2001).
137. Yiin, S.-J., Chern, C.-L., Sheu, J.-Y. & Lin, T.-H. Cadmium-induced liver, heart, and spleen lipid peroxidation in rats and protection by selenium. *Biol. Trace Elem. Res.* **78**, 219–230 (2000).
138. El-Boshy, M. E., Risha, E. F., Abdelhamid, F. M., Mubarak, M. S. & Hadda, T. B. Protective effects of selenium against cadmium induced hematological disturbances, immunosuppressive, oxidative stress and hepatorenal damage in rats. *J. Trace Elem. Med Biol.* **29**, 104–110 (2015).
139. de Campos, R. C. *et al.* Direct determination of P in biodiesel by high-resolution continuum source graphite furnace atomic absorption spectrometry. *Spectrochim. Acta Part B Atom. Spectrosc.* **66**, 352–355 (2011).
140. da Silva, I. J. S., Lavorante, A. F., Paim, A. P. S. & da Silva, M. J. Microwave-assisted digestion employing diluted nitric acid for mineral determination in rice by ICP OES. *Food Chem.* **319**, 126435 (2020).
141. Ozbek, N. & Baysal, A. A new approach for the determination of sulphur in food samples by high-resolution continuum source flame atomic absorption spectrometer. *Food Chem.* **168**, 460–463 (2015).
142. Oliveira, J. S. S. *et al.* Microwave-assisted ultraviolet digestion of petroleum coke for the simultaneous determination of nickel, vanadium and sulfur by ICP-OES. *Talanta* **144**, 1052–1058 (2015).
143. Resano, M., Verstraete, M., Vanhaecke, F., Moens, L. & Claessens, J. Direct determination of sulfur in Bisphenol A at ultratrace levels by means of solid sampling-electrothermal vaporization-ICP-MS. *J. Anal. At. Spectrom.* **16**, 793–800 (2001).
144. Lyra, F. H., Carneiro, M. T. W. D., Brandão, G. P., Pessoa, H. M. & de Castro, E. V. Determination of Na, K, Ca and Mg in biodiesel samples by flame atomic absorption spectrometry (F AAS) using microemulsion as sample preparation. *Microchem. J.* **96**, 180–185 (2010).
145. Seeger, T. S., Machado, E. Q., Flores, E. M. M., Mello, P. A. & Duarte, F. A. Direct sampling graphite furnace atomic absorption spectrometry—feasibility of Na and K determination in desalted crude oil. *Spectrochim. Acta, Part B* **141**, 28–33 (2018).
146. Pistón, M., Silva, J., Pérez-Zambra, R. & Knochen, M. Determination of total selenium by multicommutated-flow hydride generation atomic absorption spectrometry. Application to cow's milk and infant formulae. *Anal. Methods* **1**, 139–143 (2009).
147. da Silva, N., Baccan, N. & Cadore, S. Determination of selenium, chromium and copper in food dyes by GF AAS. *J. Braz. Chem. Soc.* **24**, 1267–1275 (2013).
148. Souza, S. O. *et al.* Optimization of sample preparation procedures for evaluation of the mineral composition of fish feeds using ICP-based methods. *Food Chem.* **273**, 106–114 (2019).
149. Pereira, C. C. *et al.* Decomposition method in semi-closed system with cold finger for evaluation of Ca, K, Na, Mg, Zn and Fe in colostrum silage by F AAS and F AES. *Microchem. J.* **129**, 293–296 (2016).
150. Zmozinski, A. V., de Jesus, A., Vale, M. G. R. & Silva, M. M. Determination of calcium, magnesium and zinc in lubricating oils by flame atomic absorption spectrometry using a three-component solution. *Talanta* **83**, 637–643 (2010).
151. Ghisi, M. *et al.* Simple method for the determination of Cu and Fe by electrothermal atomic absorption spectrometry in biodiesel treated with tetramethylammonium hydroxide. *Microchem. J.* **98**, 62–65 (2011).
152. Coelho, L. M., Bezerra, M. A., Arruda, M. A. Z., Bruns, R. E. & Ferreira, S. L. C. Determination of Cd, Cu, and Pb after cloud point extraction using multielemental sequential determination by thermospray flame furnace atomic absorption spectrometry (TS-FF-AAS). *Sep. Sci. Technol.* **43**, 815–827 (2008).
153. Bai, J. *et al.* Determination of zinc in marine/lacustrine sediments by graphite furnace atomic absorption spectrometry using Pd/Mg chemical modifier and slurry sampling. *Int. J. Environ. Anal. Chem.* **91**, 856–865 (2011).

Acknowledgements
This work was partially financed by the Polish Ministry of Science and Higher Education and the first author Karolina Planeta has been partially supported by the EU Project POWR.03.02.00-00-I004/16.

Author contributions
K.P.: conceptualization, methodology, investigation, validation, writing original draft; A.K.-K.: investigation, validation, writing original draft; A.D.: methodology, investigation, validation; K.M.: methodology, investigation; Z.S.: resources, methodology, reviewing manuscript; J.C.: conceptualization, resources, methodology, supervision, writing original draft, corresponding author.

Competing interests
The authors declare no competing interests.

Additional information
Supplementary Information The online version contains supplementary material available at https://doi.org/10.1038/s41598-021-82179-3.

Correspondence and requests for materials should be addressed to J.C.

Reprints and permissions information is available at www.nature.com/reprints.

Publisher's note Springer Nature remains neutral with regard to jurisdictional claims in published maps and institutional affiliations.

Supplementary materials

Table S1 – Details concerning the type of sample and preparation methods in particular papers discussed in current work.

Ref.	Type of sample	Preparation
3.	human brain, heart, muscle, kidney, liver, ovary, pancreas and spleen	Organs were pre-washed and surround surface tissues, fatty tissues, membranes and blood vessels were removed. Approximately 1 g of wet tissue was digested with 5 ml of HNO_3 and 2 ml of H_2O_2 using microwave-assisted system. Then, sample solutions were evaporated to volume 0.3 - 0.9 ml and diluted up to 3 ml with deionized water. Yttrium was used as internal standard and added to sample prior to mineralization. The reference materials were prepared in the same way.
5.	human blood and serum	Blood and serum samples were prepared by a 8-fold and 5-fold dilution with a Nash Reagent (containing nitric acid, ammonium hydroxide, Triton X-100, antifoam B and EDTA). Magnesium nitrate and palladium/citric acid were tested as chemical modifiers
8.	human erythrocytes, blood, plasma, urine and liver	1-2 ml of blood were mixed gently before preparation. 500 µl of blood sample was diluted with 500 µl solution of Triton X-100 (0.02%) and internal standard (25 µg/l Rh). Then, 150 µl of ammonia solution (20%, v:v) was added and finally sample was diluted to 5 ml. Plasma samples were prepared in the same way as blood. Erythrocytes, after isolation from blood, were washed three times with 1 ml of 0.9% NaCl (m:v). Then, solution with cells was filled up to 1 ml with Triton-X-100 (1%, v:v) and mixed. Prior to analysis, 500 µl of the sample solution and 500 µl of internal standard solution (25 µg/l Rh) were diluted to 5 ml with ammonia solution (0.5%). Urine samples were prepared in both ways. For total As and Cr determination urine was diluted 1:10 (v:v) in a solution of HNO3 (1%), internal standard (2.5 µg/l Rh) and ethanol (1%, v:v). For As species determination, 500 µl of urine was diluted to 4.5 ml with deionized water. Liver tissue samples were placed in tube and dissolved with 2 ml of 32% nitric acid (v:v) at 90 °C for 1 h. 500 µl of resulting solution was diluted with 500 µl of internal standard solution and filled up with deionized water to 4 ml.
9.	human brain	Brains were fixed in formalin and stored at least 27 days. After that time, they were dissected into slices and tissue specimens (0.011-3.370 g wet mass) were taken. Then, tissue specimens were transferred into polypropylene container and freeze-dried. Amount of 0.1 mg of each sample was digested with nitric acid in microwave-heated autoclave.
12.	human bone, serum and dialysis fluid	Bone samples were washed, defatted, freeze-dried and stored at -70 °C. About 0.2 - 0.5 g segments of bone were put in Teflon vessels to which concentrated nitric acid V (10 ml) was added and then closed microwave digestion were performed. Serum and dialysis fluid were diluted (1+2) with a solution containing Triton X-100 (0.15%, v:v) and Ca (as $Ca(N0_3)_2$, used as chemical modifier).
13.	rat liver	Frozen liver tissues were cut into small pieces, freeze dried at -20 °C for 12 h and then dried in oven at 70 °C for 3h. 200 mg of the sample were pre-digested with mixture of HNO_3 (68%, 7.5 ml) and HF (38%, 1.0 ml) in a Teflon beaker at 80 °C for 3h. Sample solutions were then transferred to Teflon vessels and heated in microwave digester. After cooling, the content of vessels were evaporated at 150 °C to dryness. Then HNO_3 (1.0 ml) and $HClO_4$ (0.5 ml, 70%) were added to samples and dried again. The obtained sediment was dissolved in 1ml of HNO_3 (27%) and then diluted up to 20 ml. The reference samples were prepared in a similar way.

14.	human blood	For GF-AAS: 200 µl of blood was mixed with 100 µl of Triton (10%), 200 µl of diammonium hydrogen phosphate (10%) and 200 µl of nitric acid (0.1 N). 10 µl of resulting solution was used for analysis. For ICP-MS: 100 µl of blood sample was digested in 500 µl of 68% nitric acid using closed-vessel microwave digestion. The resulting solution was diluted to 5 ml with ultra-pure water.
15.	human urine	10 ml of urine was mixed with concentrated hydrogen peroxide (0.5 ml), concentrated nitric acid (100 µl) and Triton X-100 (100 µl of a 10%, w:v).
16.	human cerebrospinal fluid	For ICP-AES: 100 µl of fluid were placed in tube and diluted with 80 mM HNO_3 to 2.5 ml. Then, 0.5 ml of the acidified sample was transferred to tube and diluted to 5 ml with solution of Y (1 µg/ml in 80 mM HNO_3). For ICP-MS: 100 µl of fluid were placed in tube and diluted with 80 mM HNO3 to 2.5 ml.
17.	human amniotic fluid	Each amniotic fluid sample (5 ml) was centrifuged for 10 min (at 3000 rpm, 4 °C), placed in Eppendorf tubes and frozen at -80 °C. Before analysis, amniotic fluids were defrosted and 1 ml of sample were microwave digested with HNO3 (0.5 ml, 65%) and H2O2 (0.5 ml, 30%). The resulting solutions were transferred to flasks and diluted to 10 ml with demineralized water. In the case of determination of Ca and Mg, samples were diluted 100-fold. The certified reference material was digested in a microwave digestion system and diluted with demineralized water to 10 ml.
18.	human lung	The samples of tissues were dried in oven at 70 °C for three days until they reached constant weight. Then, each sample was divide into three small sub-samples (average weight was 10±0.6 mg) and individually transferred into microwave vessels, to which 2 ml of concentrated nitric acid and 1 ml of hydrogen peroxide were added. Then, vessels were sealed and microwave digested. The resulting solution was diluted to 10 ml with water.
19.	human brain, stomach, liver, kidneys, heart, lungs and blood	Tissues were homogenized, while blood were mixed on a vortex. 1.5 ml of blood and 1.5 g of organ tissue were treated with mixture of nitric acid V and hydrogen peroxide (30%, v/v) in ratio 5:1 and digested for 24 h. The resulting solutions were diluted up to 10 ml with deionized water. The certified reference materials were treated in the same way.
24.	human hair and fingernails	The samples were washed with acetone, chloroform and distilled water and then dried overnight at 60 °C. Dried samples were placed in beaker, to which 2 ml of concentrated HClO4 and 12 ml of concentrated HNO3 were added, and they were heated for 30 min at 150 °C. Next, about 5 ml of 30% hydrogen peroxide was added to samples and heated at 200 °C to dryness. To the residue, 10 ml of HNO3 (0.1 ml/l) was added and heated again for 10 min at 100 °C. The solution was diluted to final volume 200 ml, pH was adjusted to 5.5 and then solution was passed through the microcolumn, where metal ions where retained and then eluted with HCl solution.
25.	human gallstones	Gallstones were crushed and homogenized and then 0.1 - 0.2 g of sample were dried in oven at 100±5 °C to constant weight. 0.1 - 0.2 g amount of dried sample was transferred into Pyrex vessels and digested using open-focused microwave digester. 5 ml of HNO_3, 3 ml and 2 ml of H_2O_2 were added to the sample at next steps of digestion procedure which total time was 1 h 30 min. The resulting solution was filtered and diluted to 25 ml with double deionized water.

26.	human teeth	After extraction, teeth were treated with Clorox solution to remove blood or germs and rinsed with triply distilled ultrapure water. Then, teeth were put for 5 min into 25 ml of 40% HNO3 and rinsed again with ultrapure water and acetone. Next, teeth were dried in oven for 5 min at 133 °C, weighted and transferred to test tube together with 25 ml of 10% HNO3. Test tubes were heated in water bath for 1 h at 80 °C and left overnight in room temperature. Then they were again heated to 80 °C for 1 h and cooled down. The resulting solutions were filtered and diluted to 25 ml with ultrapure water.
34.	human scalp hair	The samples were washed with acetone and ethanol and rinsed with deionized water, then dried in oven (90 °C, 20 min). Amount of 1.0 g of dried hair samples were digested with nitric acid V (15 ml), then filtered and diluted to 25 ml with deionized water.
35.	human bone-marrow fluid	Human bone-marrow fluid; the fluid samples were diluted with 1ml of 0.1 M Tris-HCl and centrifuged for 15 min at 3000 rpm to exclude bone pieces. Then, the 0.3 g of supernatant was digested with concentrated HNO3 (0.5 ml) at 100 °C. Samples were heated almost to dryness and then dissolved with 5 ml of mixture HNO3 (0.1 M) and internal standards.
37.	human cerebrospinal fluid	After collection, samples of cerebrospinal fluid were stored in tubes at -20 °C. Before analysis, samples were diluted with deionized water as 1+4 (v+v).
38.	human and animal thyroid tissue	Human dried thyroid tissue samples (10 - 30 mg) were digested in microwave oven with 0.5 ml of concentrated subboiled nitric acid and 0.2 ml of hydrogen peroxide (30%). Animal dried thyroid tissue samples (1 - 2 mg) were dissolved in 0.2 ml of ultrapure nitric acid (65%). The standard reference material (20 mg) were treated in the same way as human thyroid samples.
39.	human liver	The freeze-dried human liver samples (0.5 – 2.0 mg) were placed into PFA vessels to which 100 µl of concentrated nitric acid was added. Then, vessels were closed, transferred in digestion vessels containing high-purity water (10ml) and microwave-assisted digestion was performed. The resulting solution was adjusted to 1 ml and before analysis diluted in 1:20.
44.	human hair and urine	10 ml of urine sample together with 10 ml mixture of concentrated 63% HNO3 and 70% HClO4 (2:1) were heated on a hot plate, Then, the acid was evaporated to dryness and to resulting residue 3 ml of HClO4 was added and heated again to dryness at 160 °C. Next, 5 ml of H2SO4 was added and heated for 1 min at 150 °C. The resulting solution was diluted to 50 ml. Human hair samples were cut into small pieces, washed (acetone and distilled water) and dried in oven at 100 °C. To 0.2 mg of dried hair sample, 12 ml of concentrated nitric acid and 2 ml of concentrated HClO2 were added. The solution was heated on a hot plate for 90 min and then cooled to 70 °C. 5 ml of 30% H2O2 was added to the sample solution, which was next heated at 200C to dryness. To the residue 10 ml of 1 M H2SO4 was added and heated at 100 °C for 1 h. Finally, it was dissolved in water and diluted to 50 ml. For sample preconcentration, cloud point extraction was performed. 10 ml aliquots of sample, Triton-X-114 (0.05%, w:v), dithizone (5x10-6 mol/l) and sulfuric acid were heated at 50 °C for 5 min. After phase separation, the supernatant phase was completely separated by a syringe. To the surfactant-rich phase 50 µl of THF (tetrahydrofuran) was added. 20 µl of final solution was mixed with 10 µl of chemical modifier (Pd(NO3)2, 0.1%, w:v).

45.	human brain	Tissues were dried at 105 °C to constant weight and 0.1 g were used for further preparation. Then, for comparison, two different digestion methods were used: 1) thermal heating in stainless-steel acid digestion Parr bomb with 2.5 ml of 65% nitric acid (2 hours at 150 °C), 2) microwave-assisted digestion in a Teflon PFA vessels with 3.0 ml of 65% of nitric acid. The digested solutions were diluted to 50 ml with deionized water.
46.	human blood, hair, stomach, liver, kidneys	For GF-AAS: The samples of organ tissues (10 g; previously homogenized in the case of liver and kidney), hair samples (0.25 g; washed and cut into small parts), blood and urine (5 ml) were digested twice in closed glass vessels in the mixture of nitric and sulfuric acids (2 ml and 10 ml, respectively). For ICP-AES: Internal organs tissues (2 g), blood (2 ml) and urine (5 ml) were digested in microwave oven in high pressure Teflon vessels with mixture of nitric acid V (3 ml) and hydrogen peroxide (1 ml).
47.	human hair and serum	Hair samples were washed, dried and chopped into small pieces. 5 mg of sample was placed into test tube together with 20 µl of concentrated HNO3. After 3 hours, to the tube with the sample 5.0 µl of PTFE emulsion (60%, m:v) and 2.0 µl of Triton X-100 (0.1%) were added. Solution was diluted with double distilled water to 50 µl. To 20 µl of serum 5.0 µl of PTFE emulsion (60%, m:v) and 2.0 µl of Triton X-100 (0.1%) were added, and then diluted to 50 µl with double distilled water.
51.	human brain	The samples were chopped into small pieces during freeze drying. 20 mg of tissue were placed in a Teflon vessel in which 1.0 ml of HNO_3 was added. Then heating of sealed vessels in microwave oven was performed until completely digestion of samples. The obtained solutions were cooled down and diluted to 5 ml. Potassium dichromate was used as chemical modifier.
53.	human scalp hair	hair samples were washed with acetone and ultrapure water and dried in oven at 100 °C. Then, samples were pulverized (mean particle diameter of 0.8 µm was obtained). Hair powder (0.1 g) was suspended in ultrapure water and diluted to 25 ml. Palladium and magnesium nitrate were used as chemical modifiers and glycerol (0.4 % (m/v)) as wetting agent.
55.	serum and fibrous breast capsule tissue	The serum and standard silicon solution were diluted with matrix modifier (200 µl + 800 µl, respectively). Tissues were dried at 90 °C to constant weight and then digested in nitric acid (about 1 g of tissue in 0.5ml of acid) at 90 °C for 1h. The resulting solutions were diluted with water (3.5 ml) and potassium hydroxide (50%, 1 ml). Lanthanum oxide and ammonium phosphate were used as chemical modifier and added during dilution of samples before analysis.
56.	human breast cancer tissue	Different separated regions of breast tissue were freeze-dried at -64 °C for 2-30 hours. About 1 g of each sample was placed in digestion tube together with 5 ml of concentrated HNO_3 for 3 hours at 100 °C on hot block digester. Then, 1 - 3 ml of H_2O_2 (30%) was added and heated again for 1 hour. The resulting solution was cooled down, filtered and diluted to 25 ml with deionized water.
57.	human cancer breast tissue	The samples were placed in microwave vessels and dried at 37 °C to constant weight. 1 ml of HNO_3 and 1 ml of H_2O_2 were added to the dried sample and digested in a microwave oven. Digestion solutions were cooled down and diluted to 5 ml with ultrapure water.
59.	human blood, urine and scalp hair	Blood samples, after collection, were stored at -4 °C. Urine samples were filtered and acidified with concentrated HNO_3 (65%) and stored at -4 °C. Hair samples were cut into pieces and washed with mixture of diethyl ether-acetone, non-ionic detergent solution and ultra-pure water.

		Then, they were dried for 6 h at 80 °C. Two methods of digestion were tested, conventional and microwave assisted. In the first case, 0.5 ml of blood and urine or 0.2 mg of human hair were placed into flasks, in which 5 ml of mixture HNO_3 and H_2O_2 (2:1, v/v) was added. Then, samples were heated on a hot plate for 2 - 3 h at 80 °C. The resulting solutions were diluted up to 10 ml with 2 M HNO_3 and stored in flasks. For microwave-assisted acid digestion, 200 mg of dried hair, 0.5 ml of blood and 1.0 ml of urine were placed into Teflon PFA vessels. Into each vessel 2 ml of HNO_3 and 1 ml of H_2O_2 (30%) were added and left for 10 min. Then, vessels were sealed and heated in microwave digester. After cooling, the resulting solutions were evaporated almost to dryness and diluted with HNO_3 to 10 ml. The certified reference materials were treated in the same way.
60.	human blood, urine and scalp hair	Venous blood samples, after collection, were stored at -4 °C. Urine samples were acidified with concentrated HNO_3 and stored at -4 °C. Prior to subsampling, the samples were shaken to ensure homogeneity. Hair samples were cut into pieces and washed. Duplicate samples of dried hair were placed in PTFE flasks, while 0.5 ml of blood and urine samples were transferred into Teflon PTFE flasks. To each flask, 2 ml of mixture of concentrated HNO_3 and H_2O_2 (2:1, v/v) was added and stored for 10 min at room temperature. Then, flasks were placed in covered PTFE container and microwave digested (2 - 4 min for blood and urine and 5 - 8 min for hair). After cooling, the resulting solutions were evaporated to remove acid. Then, 10 ml of nitric acid (0.1 M) was added to the residue, mixed and filtered. The certified reference materials were treated in the same way. For Co and Mn determination Mg (NO3)2 was used as chemical modifier, while Mg (NO3)2 + Pd (NO3)2 was used for As.
63.	human blood and serum	Whole blood and serum samples (0.5 ml) were placed in PTFE flask with 3 ml mixture of HNO_3 and H_2O_2 (2:1, v:v) and left for 10 min at room temperature. Then, flasks were placed in PTFE container and heated for 3 - 4 min. The resulting sample solutions were diluted with HNO_3 to 10 ml. Then, cloud-point extraction procedure was performed. Digested samples were placed in tubes where 0.2 - 1.0 ml of APDC (0.1 - 0.5%), 2 ml of buffers (0.1 mol/l HNO_3 and NaOH) and 2 ml of Triton X-114 (0.1 - 1%, v/v) were added. Then, tubes were heated at 40 - 60 °C for 10 - 30 min in ultrasonic bath. Phase separation was accelerated by centrifuging at 3500 rpm for 5 min. After cooling the solutions, the upper aqueous phase was decanted and to surfactant-rich phase acidic ethyl alcohol (0.5 ml, 0.1 mol/L HNO_3) was added.
64.	human scalp hair	200 mg of samples were treated with 2 ml mixture of HNO3 and H2O2 (2:1, v:v) and left for 10 min; then they were digested by heating in PTFE container. The obtained solution was evaporated to dryness and diluted with HNO3 to 10 ml. Dual-cloud point extraction was performed in two steps. First, liquid sample was transferred to centrifuge tubes, into which 0.5 ml of PAN, 2 ml of Triton X-112 (0.1 - 0.5 %, v:v) and 2 ml of phosphate buffer were added. The pH of the solution was adjusted to range 7 - 11. The tubes were heated at 30 - 60 °C for 2 - 20 min. After centrifugation (5 min at 3500 rpm) separation of the phases was obtained. The aqueous phase was removed and surfactant-rich phase was treated with 2 ml mixture of HCl and HNO3 (0.5 - 2.0 mol/l) and heated at 30 - 60 °C for 5 - 20 minutes. Then, tubes were centrifuged (5 min at 3500 rpm) and supernatant was analysed. Standard solutions and blanks were prepared in the same way.

69.	rabbit arteries	The samples were washed and dried at 60 °C for 48 h to constant weight. Then, they were placed in PFA Teflon vessels together with 2 ml of nitric acid (50%, v:v) and digested using close-vessel microwave system. The resulting solutions were cooled to room temperature, transferred to sterile tubes and diluted with distilled and deionized water to 5 ml. Before analysis, sample solutions were mixed by hand-shaking. A standard reference material was prepared in the same way.
71.	human brain	The samples of brain tissue were dried in oven at 105 °C for 36 h till they reach constant mass. Two types of digestion were tested: 1) 100 mg of sample and 2.5 ml of nitric acid (65%) were digested in a Parr high-pressure bomb at 150 °C for 2 h, 2) 100 mg of sample was heated in microwave digester with 3 ml of nitric acid (65%). After cooling, the obtained solutions were diluted to 5 ml with distilled water.
76.	sheep liver, kidney and muscle	Tissues were thawed and homogenized. For each type of tissue, 1 g of sub-sample were digested using nitric acid.
77.	wolves liver	To 0.3 - 0.5 g portions of wet liver tissue 9 ml of HNO_3 (65%) and 1 ml of H_2O_2 (30%) were added. Then samples were digested using microwave-assisted system. After digestion, samples were cooled down to room temperature and diluted to 25 ml with a distilled water.
78.	rat whole blood, plasma, brain, heart, skeletal muscle, liver, kidney, spleen, thymus and bone	Organs tissues were first digested at room temperature for 3 h and then at 70 °C for another 3 h in nitric acid (about 1 ml of acid per 300 mg of tissue). The obtained solutions were diluted 1:10 with deionized water (1:1000 for determination of Ca in digested bone). The standard solutions were prepared in the same way. Analysis of blood and plasma were performed immediately without digestion.
79.	rat liver, kidney, heart, lung and serum	Organ tissues were washed, dried and stored at -80 °C for further lyophilisation. About 0.5 g of each tissue were placed into PTFE vials together with 3.5 ml HNO3 (65%, v:v), 3.5 ml of H2O and 1 ml of H2O2 (30%, v:v). Then, the flasks were closed and microwave-assisted digestion was perform. After mineralization, the obtained solutions were diluted to 20 ml with deionized water. Samples of serum and plasma (aliquots of 0.1 ml) were diluted 100-fold with Triton X-100 (0.01%, v:v) to final volume 10 ml.
81.	human whole blood, serum, cerebrospinal fluid and urine	1 ml of blood was digested in microwave oven together with 2 ml of HNO_3. To 1ml of urine 0.25 ml of HNO_3 was added and diluted with water. Serum and cerebrospinal fluid were diluted with high purity deionized water.
82.	human serum	2g of serum was microwave digested with mixture of HNO_3 (65%, 6 ml, v:v) and H_2O_2 (30%, 1 ml, v:v).
83.	human serum	To 3 ml of serum sample 2ml of nitric acid, 1 ml of hydrogen peroxide and yttrium (11.2 μmol/l) were added. Sample solutions were digested in microwave oven. Then, the resulting solutions were cooled down, placed in vacuum module and evaporated till 0.6 – 1.0 ml volume of sample was obtained. The content of vessels was diluted to 3 ml with deionized water. The control and reference materials were prepared in the same way.
84.	human rib bone	Tamples were transferred into one-chamber autoclaves together with 1.5 ml of concentrated HNO3 (65%) and 0.3 ml of H2O2. Then, they were heated at 160 – 200 °C for 3 h. After cooling the autoclaves to room temperature, sample solutions were diluted to 20 ml with deionized water and placed in measuring bottles. The standard reference material was treated in the same way.
86.	human hair	The samples were dissolved by using nitric acid and hydrogen peroxide at higher temperature condition. Different temperature and time of

		digestion as well as composition of acid mixture were tested and optimized. For 1 g of hair sample, best results of mineralization were obtained for temperature in the range of 120-200 °C (150 °C was chosen), minimum 30 min of digestion time and 12 ml of HNO3-H2O2 at mixture ratio 2:1.
89.	human plasma	The plasma samples were stored at -80 °C and prior to analysis they were reconstituted at room temperature. Then, samples were shaken and centrifuged for 15 min at 2000 g. 0.1 ml of plasma supernatant was diluted to 2 ml with HNO3 (0.5 %, v:v) and internal standard solutions in 1:20. The certified reference material was prepared according to manufacturer instructions, further diluted with HNO3 (0.5%, v:v).
90.	human serum	200 µl of serum were mixed with 250 µl of HNO_3, 250 µl of H_2O_2, 250 µl of deionized water and 25 µl of an internal standard solutions (100 µg/l Rh and 1000 µg/l Se). Blank samples and reference materials were prepared in the same way, but instead the sample volume, 200 µl of deionized water or 200 µl of reference serum were used. The solutions were heated and shaken at 65 °C for 30 min and at 95 °C for another 30 - 45 min. After cooling, solutions volume loss was refilled using 25% HNO_3. The resulting solution was diluted with 1.5 ml of deionized water. In the case of I determination, 25 µl of serum was diluted with NaOH (0.1 M) containing Rh (at 1 µg/l) up to 1 ml.
95.	human brain	The samples were freeze-dried at -80 °C for 5 days until they reached constant weight and then they were removed from surface tissues and meninges. 50 - 150 mg of dried brain tissue were placed in Teflon vessels together with 2 ml of HNO3 and microwave digested. The resulting solutions were cooled down, transferred to tubes and diluted to 10 ml with MilliQ water. All analysed samples were diluted 1+4.
96.	human esophagus tissue	About 0.1 g of dried tissues were placed into Teflon PFA vessels to which 8 ml of concentrated nitric acid was added. Then, microwave-assisted digestion of samples was performed. The resulting solutions were diluted to a final volume 10 ml with ultrapure water.
98.	human liver	The samples were dried for 72 h at 105 °C to constant weight. Next, they were transferred to experimental tubes to which 2 ml of nitric acid of HNO3 (65%) and 1 ml of HClO4 (60%) were added. Samples then were heated for 8 h at 120 °C. The resulting solutions were diluted to 10 ml with deionized water.
99.	human heart	Tissues were removed from paraffin wax, first mechanically with spatulas and then by immersing in xylene. Next, samples were dried in oven for minimum 3 h at 90 °C to completely dryness. Samples weighted 0.05-0.2 g were placed in microwave digestion vials to which 1 ml of hydrochloric acid and 4 ml of nitric acid were added. Each vessel was capped and samples were digested in microwave digestion system. The resulting solution was diluted up to 25 ml with reagent grade water. The certified reference materials were prepared in the same way, but without xylene treatment and drying steps.
100.	human hair	25 mg of ground hair samples were placed in tubes together with 2 ml of HNO_3 (20%) and sonicated at 2 min (50 W, 100% amplitude). Then, liquid sample was diluted with aqueous solution of Rh (10µg/L) to 10 ml. The resulting diluted slurries were centrifuged (for 2 min at 900 x g) and analysis of supernatant was directly performed.
101.	liver, diaphragm, brain and spleen of beef calves	About 1 g of tissue sub-sample were digested using microwave-digestion system together with 5 ml of concentrated nitric acid and 3 ml of hydrogen peroxide (30%, w:v). The resulting solutions were diluted with ultrapure water up to 15 ml.

102.	rat livers, kidneys and urines	Rat organs were cut into small pieces and homogenized. Samples, each weighted 0.5 g, were placed in microwave digestion tank to which 4 ml of HNO_3 and 1 ml of H_2O_2 were added. Then, microwave assisted digestion was performed. The resulting solution was evaporated at 150 °C for 2.5 h and the residue was dissolved in 2 ml 8-HQ solution and diluted with ammonium buffer solution to 50 ml. Aliquot of 40 ml was transferred into centrifuged tube, in which Triton-X-100 was added. Then the tube was shaken on vortex for 20 s and heated at 90 °C for 90 min. After a cloudy state was formed, the upper aqueous phase was removed and the gel-like sediment was obtained. Before analysis, sediment was dissolved with 1 ml of HNO_3 (1%).
105.	human brain	Brains were washed and removed from meninges. From different brain regions tissue fragments were collected and stored at -4 °C. After defrosting, samples were washed and dried in oven at 110 °C until they reached constant weight. Dried samples (100 - 500 mg) were placed in vessels, to which 2.5 ml of concentrated HNO_3 (≥ 65%, w:w) and 1.0 ml of H_2O_2 (≥30%, v:v) were added. Samples were digested using microwave oven and, after cooling, diluted up to 50 ml with ultrapure water. Until analysis, the resulting solutions were stored in tubes at 4 °C. The certified reference materials were prepared in the same way. $Mg(NO_3)_2$ was used as matrix modifier.
108.	animal muscle and liver	2 - 10 g of homogenized sample was dried overnight in oven at 120±20 °C and then at 450 °C. After cooling the sample, 1 ml of concentrated nitric acid was added and dried on a hot plate. Then, sample was again heat at 450 °C for 1 h. After cooled the sample to room temperature, the carbon-free ash was dissolved in hydrochloric acid, transferred into flasks and diluted with 0.2 % nitric acid. Magnesium nitrate (1%) was used as a matrix modifier.
110.	human liver	1 - 2 g of wet liver samples were placed in tube and dried at 60 °C for 90 h. Then, 5 ml of nitric acid were added and solution was left for 72 h at room temperature. The standard reference material (0.5 g) was treated in the same way.
118.	human blood, serum and urine	2 ml of blood, 0.5 ml of serum and 20 ml of urine were digested with 3 ml of concentrated nitric acid V and 1 ml of 30% hydrogen peroxide using microwave digestion system. Before measurement, samples were diluted with deionized water. The reference materials were treated in a similar way.
119.	E. coli cells	The cells were incubated at 37 °C for 24 h, suspended with 10 ml of 0.9% NaCl (g:g) and centrifuged at 4 °C for 5 min at 4500 x g. These steps were performed two times. After centrifugation, 10 mg of cells were transferred into vessel to which 1.45 ml of HNO_3, 0.5 ml of H_2O_2 and 50 mg of internal standard solution (Rh and Re, 20 µg/l) were added. Then, samples were microwave digested. After mineralization, the solution was cooled down and mixed with 0.5 ml of water. The standard reference material were digested using microwave digestion system. Then, internal standard solutions were added and sample was diluted with MilliQ water up to 20 g.

Table S2 - Details concerning the instrument and operating parameters in particular papers discussed in current work.

Ref.	Technique	Instrument details	Operating parameters
3.	ICP-OES	Ash IRIS/AP (Thermo Jarell, MA, USA) ICP-AES spectrometer; charged	plasma frequency: 27.12 MHz; Rf power: 1150 W; gas flow rates: 0.56 L/min (torch), 0.5 L/min (auxiliary), 0.56 L/min (nebulizer); nebulizer

		injection device detector; axial viewing mode; the Micromist nebulizer (Glass Expansion Pty. Ltd., Australia); spray chamber: cyclone;	uptake: 0.5 ml/min; sample volume: 1.5 ml for 2 repeats; flush time: 40 s; purge time: 90 s; signal integration time: 60 s (high wavelength), 10 s (low wavelength);
5.	GF-AAS	Varian AA280Z Zeeman atomic absorption spectrometer with a Zeeman background correction; GTA 120 graphite tube atomizer; PSD 120 programmable sample dispenser; beryllium hollow cathode lamp (Varian, Part No. 5610100500);	analytical spectral lines: 309.3 nm (Al), 234.9 nm (Be), 228.9 nm (Cd), 357.9 nm (Cr), 253.7 nm (Hg), 279.5 nm (Mn), 232.0 nm (Ni), 283.3 nm (Pb), 276.8 nm (Tl); argon flow rate: 0.3 L/min; operating conditions: 1) drying: 5 s at 85 °C, 30 s at 95 °C, 20 s at 120 °C, 2) pre-pyrolysis 450 °C for 22 s, 3) pyrolysis: 17 s at 1000 °C (serum) and 800 °C (blood), 4) atomizing: 3 s at 2900 °C (serum) and 2900 °C (blood), 5) cleaning: 2900 °C for 2 s; three experimental setups were tested: without modifier and with magnesium nitrate or palladium/citric acid as modifiers;
8.	ICP-MS	total As and Cd determination - Agilent 7700x (Agilent Technologies, Waldbronn, Germany) spectrometer; Cetac ASX-500 Series autosampler (Cetac Technologies, Omaha, USA) set up in a laminar flow box FB 24 (Spetec, Erding, Germany); Babington nebulizer; Scott spray chamber (Agilent Technologies); injector tube with an inner diameter 2.5 mm; As species determination - Agilent 1200 Series HPLC (Agilent Technologies); isocratic pump; autosampler, vacuum degasser; anion exchange column and HPLC column (Hamilton, PRPX100, 250x4 mm, particle size 10 µm);	isotopes: 52-Cr, 75-As; total As and Cd determinations - collision cell gas: 4 ml/min of He; collision/reaction gas: 1.4 ml/min of He and 4 ml/min of H_2; generator power: 1500 W; gas flow rates: 15 L/min (outer); 1 L/min (intermediate), 1.2 L/min (nebulizer); As species determination - mobile phase (Solution of 20 mM NH4HCO3, 8mM CH3COONa, 2.4 mM of NaNO3 and 1% ethanol, adjusted to pH 8.9) flow rate: 1.5 ml/min; sample injection volume: 50 µl;
9.	ICP-MS	Agilent 7500ce (Agilent Technologies) spectrometer;	m/z: 56-Fe, 43-Ca, 65-Cu, 66-Zn, 24-Mg, 55-Mn; collision gas flow rate: 5.3 ml/min, He;
12.	GF-AAS	Z5100 atomic absorption spectrophotometer (Perkin-Elmer, Norwalk, CT, USA); HGA 600 furnace system; transverse Zeeman-effect background correction system; AS-60 autosampler; pyrolytic graphite-coated graphite tubes with solid pyrolytic graphite L'vov platforms	operating conditions: 1) dry: 230 °C, ramp 2 s, hold 30 s, Ar flow rate 300 ml/min, 2) pyrolysis: 1400 °C, ramp 3 s, hold 20 s, Ar flow rate 300 ml/min, 3) atomization: 2400 °C, ramp 0 s, hold 4 s, Ar flow rate 0 ml/min, 4) clean: 2650 °C, ramp 1 s, hold 10 s, Ar flow rate 300 ml/min; injection temperature: 100 °C; injection volume: 10 µl;
13.	ICP-MS	HP4500 (Yokogawa-Hewlett Co. Ltd, Tokyo, Japan);	Plasma frequency: 27.12 MHz; Rf power 1.2 kW; argon flow: 14 L/min; sampling distance: 4.8 mm.

	ICP-OES	SPS7000A (Seiko Electric Co. Ltd, Tokyo, Japan) spectrometer;	
14.	GF-AAS	Hitachi polarized Zeeman atomic absorption spectrophotometer (Z-5710, Hitachi High-technologies Corp., Tokyo, Japan); autosampler;	Analytical spectral line: 288.8 nm (Cd);
	ICP-MS	Thermo Scientific ELEMENT2 High Performance High Resolution ICPMS (Thermo Fisher Scientific Inc, Bremen, Germany);	Rf power: 1.250 kW; nebulizer: micro-uptake concentric nebulizer; plasma gas: argon; gas flow rate: cool gas 16 L/min, auxiliary gas 0.87 L/min, sample gas 0.979 - 1.190 L/min, additional gas 0.005 - 0.120 L/min; diameter of sampling cone orifice: 1.0 mm; diameter of skimmer cone orifice: 0.8 mm; mass resolution: medium resolution R=4,000; Samples per peak: 20; integration window: 60%; fore vacuum: 2-3 E-4 mbar; high vacuum: 1-2 E-7 mbar;
15.	GF-AAS	Perkin-Elmer Model 1100B atomic absorption spectrometer equipped with deuterium-arc background correction; HGA-400 graphite-furnace atomizer (Perkin-Elmer); pyrolytic graphite coated tubes (part number B013-5653) and pyrolytic graphite platforms (part number B012-1092) (Perkin-Elmer); ATI-Unicam 939QZ spectrometer (Unicam Atomic Absorption, Cambridge, UK); GF90 graphite furnace; FS90 Plus autosampler; Pyrolytic tubes (Unicam); Zeeman correction;	analytical spectral lines: 313.3 nm (Mo), 309.3 nm (Al), 357.9 nm (Cr); lamp current: 12 mA (Mo), 10 mA (Al), 15 mA (Cr); wall atomization for Mo and Cr; platform atomization for Al; bandwidth: 0.7 nm; inert gas flow rate: Ar, 300 ml/min;
16.	ICP-MS	NexION 300D ICP-MS (Perkin Elmer, USA); 1.1 version of the control software; nickel cones; cyclonic spray chamber; Meinhardt nebulizer (type-C); standard factory tubing;	isotopes: 47-Ti, 51-V, 55-Mn, 61-Ni, 66-Zn, 75-As, 85-Rb, 88-Sr, 107-Ag, 118-Sn, 138-Ba, 208-Pb; 3 readings of 30 sweeps; integration time: 75 ms; sample aspiration rate: 0.3 ml/min; sample pre-flush: 60 s;
	ICP-OES	Spectro Ciros CCD ICP-AES; modified Lichte nebulizer; cyclonic spray-chamber;	analytical spectral lines: Ca 396.847 nm, Cu 324.754 nm, Fe259.941 nm, Mg 279.553 nm, P 177.495 nm, S 180.731 nm, Si 251.612 nm, Sr 407.771 nm, Zn 213.856 nm, K 766.491 nm, Na 330.237, Y 371.030 nm; aspiration of samples and standards: 2 ml/min; argon flow rates: 0.9 ml/min (nebulization), 0.9 ml/ min (auxiliary), 14.0 ml/min (coolant); plasma power: 1400W at

			27 MHz; sample aspiration prior to collection for 45 s; signals collection: 3 x 24 s;
17.	ICP-MS	ICP-MS Elan DRC II (PerkinElmer SCIEX, Canada); cyclonic spray chamber; concentric glass nebulizer; quartz torch with an injector; quadrupole mass analyzer with gold coated rods; calibrated autolens; Pt sampler and skimmer cones; detector mode: dual (pulse counting and analog mode);	isotopes: 24-Mg, 27-Al, 44-Ca, 51-V, 52-Cr, 55-Mn, 59-Co, 60-Ni, 63-Cu, 66-Zn, 78-Se, 88-Sr, 91-AsO, 111-Cd, 121-Sb, 138-Ba, 208-Pb, 238-U; DRC reaction gases: NH_3, O; gas flow rates: 0.89 – 0.91 L/min (nebulizer),1.2 L/min (auxiliary), 16 L/min (plasma); Rf power: 1050 - 1150 W; scan mode: peak hopping; Dwell time: 50 ms per mass;
18.	ICP-MS	X Series 2 ICP–MS and ICAP Q ICP–MS (ThermoFisher Scientific, Bremen, Germany);	four measurement methods: 1) standard mode - Thermo X Series 2 with 1% v/v nitric acid solution; calibration range 0.01 - 10 µg/L, 2) collision cell mode - kinetic energy discrimination with a collision cell gas (7% hydrogen in helium at a flow of 3.5 ml/min) using Thermo X Series 2 with 1% v/v nitric acid solution; calibration range 0.001 - 100 µg/L, 3) standard mode - ICAP Q with 1% v/v nitric acid solution; calibration range 0.002 - 0.2 µg/L, 4) standard mode - ICAP Q with 1%v/v HCl solution; calibration range 0.01 - 2.5 µg/L;
19.	GF-AAS	Solaar MQZe atomic absorption spectrometer with Zeeman background correction; heated graphite atomizer (GF95) and autosampler (FS95) (Thermo Electron, Waltham, MA);	analytical spectral line: 232.0 nm (Ni); slit width 0.2 nm; sample solution volume: 20 µl; heating program details: 1) drying - 100 °C, ramp 10 s, hold 30 s, Ar flow 200 ml/min, 2) pyrolysis - 1,000 °C (1,300 °C) , ramp 150 s, hold 20 s, Ar flow 200 ml/min, 3) atomization - 2,500 °C (2,400 °C) , ramp 0 s, hold 3 s, Ar flow 0 ml/min, 4) cleaning - 2,600 °C, ramp 0 s, hold 3 s, Ar flow 200 ml/min;
24.	F-AAS	Analytik Jena model nova 300 (Jena, Germany) F-AAS spectrometer; acetylene-air burner; single-element hollow cathode lamp (Cd and Pb);	analytical spectral lines: 228.8 nm (Cd), 283.3 nm (Pb); spectral slit: 1.2 nm;
25.	ICP-OES	Thermo Jarell Ash model 25 ICP-AES (Waltham, MA, USA); cross-flow nebulizer; 2 mm i. d. plasma torch; polychromator with 2400 grooves/mm;	Rf: 27.12 MHz; Rf power: 1150 W; analytical spectral lines: 228.6 nm (Co), 267.7 nm (Cr), 324.7 nm (Cu), 259.9 nm (Fe), 257.6 nm (Mn), 231.6 nm (Ni), 213.8 nm (Zn)
26.	ICP-OES	Perkin-Elmer Plasma 40 ICP-OES spectrometer;	analytical spectral lines: 324.754 nm and 224.700 nm (Cu), 213.856 nm and 202.548 nm (Zn), 220.353 nm and 216.999 nm (Pb); measurement time of each sample: the order of 2 min.
34.	F-AAS	AA-6300 F-AAS spectrophotometer (Shimadzu); pre-mixed burner air-acetylene flame;	analytical spectral lines: Fe 248.3 nm, Cd 228.8 nm, Ca 422.7 nm, Zn 213.9 nm, Cu 309.93 nm, Pb 283.3 nm, Mg 285.2 nm, Cr 357.9 nm;

35.	ICP-OES	Plasma AtomComp MkII (Jarrell-Ash, Franklin, MA, USA); Pashen-Runge type of polychromator with 39 channels; fassel type torch; single type spray chamber; cross-flow type nebulizer.	plasma Rf frequency: 27.12 MHz; plasma incident Rf power: 1.0 kW; Ar gas flow rates: 20 l/min (outer), 1.0 l/min (intermediate), 0.5 l/min (carrier); sampling observation height: 18 mm above work coil; sampling uptake rate: 1.2 ml/min; analytical spectral lines: Na 589.0 nm, K 788.4 nm, Fe 259.9 nm, P 213.6 nm, Ca 317.9 nm, Mg 279.0 nm, Al 308.2 nm, Zn 213.8 nm.
	ICP-MS	Model SPQ 8000A (Seiko Instruments, Chiba) with quadrupole mass spectrometer; fassel type torch; scott type spray chamber; concentric type nebulizer; skimmer cone: Cu;	plasma Rf frequency: 27.12 MHz; plasma incident Rf power: 1.0 kW; Ar gas flow rates: 16 l/min (outer), 1.0 l/min (intermediate), 0.95 l/min (carrier); sampling depth: 12 mm from work coil; sample uptake rate: 0.8 ml/min; sampling cone: Cu, 1.1 mm orifice diameter;, 0.35 orifice diameter; data accumulation: 20 times; dwell time: 10 ms; repetition: 5 times; channel width: 3 channels; m/z: 85-Rb, 65-Cu, 82-Se, 138-Ba, 88-Sr, 91-Zr, 133-Cs, 121-Sb, 120-Sn, 98-Mo, 107-Ag, 184-W;
37.	ICP-OES	Optima 3100 XL spectrometer (Perkin Elmer, Norwalk, CT, USA); cross-flow nebulizer with Ryton Scott chamber; polychromator equipped with an echelle grating; detector: simultaneous solid-state Segmented-array Charged-coupled device;	Rf power: 1.3 kW; Ar gas flow rates: 13.0 L/min (plasma), 0.5 L/min (auxiliary), 0.7 L/min (nebulizer); max. resolution: 0.006 nm at 200 nm; analytical spectral lines: 393.3 nm (Ca), 324.7 nm (Cu), 259.9 nm (Fe), 279.5 nm (Mg), 251.6 nm (Si), 213.8 nm (Zn);
	ICP-MS	SF-ICP-MS ELEMENT model (Thermo Finnigan, Bremen, Germany); Guard Electrode device; nebulizer: Meinhardt glass type; water-cooled Scott type spray chamber; interface: Pt cones;	Rf power: 1200 W; gas flow rates: 14 L/min (plasma), 0.9 L/min (auxiliary), 0.85 L/min (nebulizer); low resolution (LR): 300 m/Δm; medium resolution (MR): 3000 m/Δm; isotopes: 27-Al (MR), 9-Be (LR), 114-Cd (LR and MR), 59-Co (MR), 52-Cr (MR), 202-Hg (LR), 55-Mn (MR), 60-Ni (MR), 208-Pb (LR), 51-V (MR); mass window: 150% (LR), 100% (MR); search window: 100% (LR), 80% (MR); integration window: 80% (LR), 60% (MR); scans (number): electric (25);
	ICP-MS	SF-ICP-MS (ELEMENT 2, Thermo Finnigan, Bremen, Germany); torch guard electrode device; Meinhardt-type glass nebulizer; water-cooled Scott chamber;	isotopes: 138-Ba, 9-Bi, 7-Li, 100-Mo, 123-Sb, 120-Sn, 88-Sr, 205-Tl, 184-W, 90-Zr; resolution: low, 300 m/Δm;
38.	ICP-MS	ELAN 6000 quadrupole-based mass spectrometer (Perkin Elmer Sciex, Ontario, Canada); microconcentric MicroMist nebulizer (Model MicroMist	Rf power: 1350 W; cylindrical lens potential: 10.2 V; dwell time: 500 ms; mass range: 23 u - 238 u; scanning mode: peak hopping; optimization: max. $^{137}Ba^{+}$ intensity; detection system dead time: 53 ns; gas flow rates: 13.5

		AR30-1F02); minicyclonic spray chamber (both from Glass Expansion, Pty. Ltd., Camberwell, Victoria, Australia); ELAN 6000 mass flow controller (MKS Instruments); peristaltic pump (Perimax 12, Spetec GmbH, Erding, Germany);	l/min (coolant), 0.7 l/min (auxiliary); mass resolution: 300 m/Δm; solution uptake rates: 160 µl/min and 320 µl/min; nebulizer gas flow rate: 0.81 l/min and 0.76 l/min; no. of replicates: 8 and 10; measurement time: 3.2 min. and 4.0 min;
39.	ICP-MS	Thermo Elemental X7 ICP-MS spectrometer; normal flow, concentric, pneumatic nebulizer;	collision cell gas flow rate: 7.2 ml/min, 93% He - 7% H_2; Rf power: 1410 W; Ar gas flow rates: 13 L/min (plasma), 0.95 L/min (auxiliary), 0.84 L/min (nebulizer); sample uptake rate: 0.82 ml/min; isotopes: 52-Cr, 55-Mn, 56-Fe, 60-Ni, 65-Cu, 66-Zn, 85-Rb, 208-Pb;
	TXRF	Atomika Extra IIA TXRF spectrometer; line-focused X-ray tubes; energy dispersive Si(Li) detector;	Excitation: Mo Kα 17.4 keV; data acquisition live time: 1000 s; K lines were used for determination of: Cr, Mn, Fe, Ni, Cu, Zn and Rb; L line was used for determination of Pb.;
44.	GF-AAS	AA 6800G atomic absorption spectrometer (Shimadzu); graphite furnace atomizer (GFA-6500); autosampler (ASC-6100); bismuth hollow cathode lamp (Hamamatsu Photonics, L233 Series); Pyrolytic graphite-coated graphite tubes (P/N 206-69984-02) (Shimadzu);	analytical spectral line: 223.1 nm; spectral bandpass: 0.5 nm; hollow cathode lamp current: 10 mA; sample injection volume: 20 µl.
45.	ICP-OES	Labtest Plasmalab ICP-AES spectrometer (40 analytical channels plus monochromator); GMK-nebulizer with a Gilson Minipuls 2 pump; sample-loop injector.	Rf: 27.12 MHz; Rf power: 2 kW;
	GF-AAS	Model SIMAA 6000 multielement GF-AAS system (solid state detection, Echelle polychromator optics, transverse-heated graphite atomiser with longitudinal Zeeman-effect background correction; stabilised temperature platform furnace; true temperature control; AS-72 autosampler (Perkin-Elmer);	inert gas flow rate: Ar 250 ml/min; integration time: 5 s; experimental conditions on each step: 1) 110 °C, 1 ramp time/s, 20 hold time/s, internal flow 250 ml/min, 2) 130 °C, 5 ramp time/s, 45 hold time/s, internal flow 250 ml/min, 3) 600 °C, 10 ramp time/s, 20 hold time/s, internal flow 250 ml/min, 4) 1600 °C, 0 ramp time/s, 5 hold time/s, internal flow 0 ml/min, 5) 2300 °C, 1 ramp time/s, 3 hold time/s, internal flow 250 ml/min.
46.	ICP-OES	iCAP 6300 emission spectrometer (Thermo Electron Corp., Waltham, MA, US); Echelle type	range of recorded emission spectrum: 166.250 nm - 847.000 nm;

		monochromator; radio frequency - 27.12 MHz; radial/axial plasma observation;	
	CV-AAS	Solar MQZe atomic absorption spectrometer with vapor system VP100 Continuous Flow Vapor Accessory; mercury absorption cell (Thermo Electron Corp., Waltham, MA, US);	
47.	ICP-OES	ICP spectrometry source (2 kW, 27±3 MHz) (Beijing Second Broadcast Equipment Factory, China); conventional plasma torch; modified graphite furnace vaporizer; WDG-500-1A monochromator (Beijing Second Optics, Beijing, China); R456 type photo-multiplier tube (Hamamatsu, Japan); home-built direct current amplifier; U-135 recorder (Shimadzu, Japan);	incidient power: 1.1 kW; Ar gas flow rate: 0.5 L/min (carrier), 18 L/min (coolant); observation height: 12 mm; entrance slit width 25 μm; exit slit width: 25 μm; drying temperature: 100 °C, ramp 10 s, hold 20 s; ashing temperature: 500 °C, ramp 10 s, hold 50 s; vaporization temperature: 2400 °C; clear-out temperature: 2700 °C; vaporization time: 4 s; sample volume: 10 μl;
51.	GF-AAS	Varian atomic absorption spectrometer (Model 475, Sunnyvale, CA); graphite furnace atomizer (Model GTA-95);	analytical spectral line: 309.3 nm; bandpass: 0.5 nm; inert gas: Ar; volume of deposited sample: 20 mm^3; operating conditions: 1) drying - 120 °C, 20 ramp time/s, 25 hold time/s, 2) ashing - 1400 °C, 10 ramp time/s, 40 hold time/s, 3) atomizing - 2600 °C, 1 ramp time/s, 2 hold time/s, 4) cleaning - 2600 °C, 1 hold time/s;
53.	GF-AAS	Perkin-Elmer 1100B atomic absorption spectrometer; Perkin-Elmer HGA 700 graphite furnace; Perkin-Elmer AS 70 autosampler; Perkin-Elmer HGA 400 graphite furnace; Perkin-Elmer AS 40 autosampler; deuterium lamp as a background correction system; Pyrolytic graphite tubes; L'vov platform;	analytical spectral lines: 309.3 nm (Al), 279.5 nm (Mn); spectral bandwidth: 0.7 nm (Al), 0.2 nm (Mn); integration time: 3 s; peak-area measurements; D_2 lamp background corrector; injection volume: 20 ml; operating conditions: 1) drying - 150 °C, ramp time - 20 s; hold time - 15 s, Ar flow - 300 ml/min, 2) pyrolysis - 1500 °C (Al) and 1200 °C (Mn), ramp time - 10 s; hold time - 15 s, Ar flow - 300 ml/min, 3) atomization - 2500 °C (Al) and 2200 °C (Mn), ramp time - 0 s; hold time - 3 s, Ar flow - 200 ml/min (Al), 4) cleaning - 2600 °C, ramp time - 2 s; hold time - 2 s, Ar flow - 300 ml/min;
55.	GF-AAS	Varian Zeeman SpectrAA-300 AAS instrument (Varian Canada Inc.); pyrolytic coated graphite partition tube;	analytical spectral line: 251.6 nm; lamp current: 10 mA; sample volume: 10 μl; operating conditions: 1) 90 °C, furnace time 15 s, gas flow 3.0 L/min, 2) 95 °C, furnace time 10 s, gas flow 3.0 L/min, 3) 100 °C, furnace time 5 s, gas flow 3.0 L/min, 4) 300 °C, furnace time 5 s, gas flow 3.0 L/min, 5) 1400 °C, furnace time 19 s, gas flow 3.0 L/min, 6) 40 °C, furnace time 6.8 s, gas flow 0.2 L/min, 7) 2700 °C, furnace time 1.4 s,

			gas flow 0 L/min, 8) 2700 °C, furnace time 2.0 s, gas flow 0 L/min, 9) 2700 °C, furnace time 2.0 s, gas flow 3.0 L/min;
56.	GF-AAS ICP-OES	graphite furnace technique model AA-670; ICP-OES spectrometer (ULTIMA 2CE);	
57.	GF-AAS	AAnalyst600 atomic absorption spectrometer, transversely heated graphite atomizer (THGA), longitudinal Zeeman-effect background corrector, AS-800 autosampler, WinLab 32 software (Perkin Elmer, UK); standard THGA graphite tubes, integrated L'vov platform (Perkin Elmer, UK);	operating conditions: 1) drying - 110 °C, ramp time 10 s, hold time 40 s, internal gas flow rate 250 ml/min, 2) drying - 130 °C, ramp time 15 s, hold time 40 s, internal gas flow rate 250 ml/min, 3) pyrolysis - 500 °C, ramp time 10 s, hold time 10 s, internal gas flow rate 250 ml/min, 4) pyrolysis - 1200 °C, ramp time 10 s, hold time 15 s, internal gas flow rate 250 ml/min, 5) atomisation - 2300 °C, ramp time 0 s, hold time 5 s, internal gas flow rate 0 ml/min, 6) clean out - 2500 °C, ramp time 1 s, hold time 5 s, internal gas flow rate 250 ml/min;
59.	GF-AAS	Analyst 700 Perkin-Elmer atomic absorption spectrometer in conjunction with a graphite furnace model GF 3000 included PAL 3000 autosampler;	analytical spectral lines and slit-width: 283.3 nm and 1.3 nm (Pb), 228.8 nm and 1.3 nm (Cd), 357.9 nm and 1.3 nm (Cr), 232.0 nm and 0.2 nm (Ni); lamp current: 7.5 mA (Pb), 7.5 mA (Cd), 7.5 mA (Cr), 10 mA (Ni); background correction: D_2 lamp; cuvette: cup (Pb and Cd) and tube (Cr and Ni); carrier gas flow rate: 200 ml/min; sample volume: 10 µl; temperature conditions - dry: 80 °C - 120 °C /15 s (Pb, Cd, Cr, Ni); ash: 300 °C - 600 °C /15 s (Pb, Cd) and 300 °C - 700 °C /15 s (Cr, Ni); atomisation: 2000 °C - 2100 °C /5 s (Pb), 1500 °C - 1800 °C /5 s (Cd), 2600 °C - 2700 °C /5 s (Cr), 2500 °C - 2600 °C /5 s (Ni); cleaning: 2100 °C - 2400 °C /2 s (Pb), 1800 °C - 2000 °C /2 s (Cd), 2700 °C - 2900 °C /2 s (Cr), 2600 °C - 2800 °C /2 s (Ni);
60.	GF-AAS	Hitachi model 180-50 (Hitachi, Tokyo, Japan); Hitachi Model 056 recorder; hollow cathode lamps (Hitachi);	analytical spectral lines and slit-width: 193.8 nm and 2.6 nm (As), 240.7 nm and 0.2 nm (Co), 324.8 nm and 1.3 nm (Cu), 279.5 nm and 0.4 nm (Mn); lamp current: 10.0 mA (As), 10.0 mA (Co), 7.5 mA (Cu), 7.5 mA (Mn); background correction: D_2 lamp; cuvette: cup; carrier gas (Ar) flow rate: 200 ml/min; sample volume: 10 µl; temperature conditions - dry: 80 °C - 120 °C /10 s (As) and 80 °C - 120 °C /15 s (Co, Cu, Mn); ash: 300 °C - 400 °C /10 s (As), 400 °C - 600 °C /15 s (Co, Cu) and 400 °C - 500 °C /15 s (Mn); atomisation: 2700 °C - 2800 °C /5 s (As), 2600 °C - 2700 °C /5 s (Co, Cu), 2500 °C - 2600 °C /5 s (Mn); cleaning: 2800 °C - 2900 °C /3 s (As), 2700 °C - 2800 °C /2 s (Co, Cu), 2600 °C - 2800 °C /2 s (Mn)
63.	F-AAS	Perkin Elmer model AAnalyst 700 (Norwalk, CT) flame atomic absorption	analytical spectral line: 232.0 nm; spectral bandwidth: 0.7 nm; lamp current: 30 mA;

		spectrophotometer; hollow cathode lamp of Ni;	
64.	F-AAS	Perkin-Elmer Model AAnalyst 700 (Norwalk, CT, USA) flame atomic absorption spectrophotometer; hollow cathode lamp of Mn;	analytical spectral line: 279.5 nm; spectral bandwidth: 0.2 nm; lamp current: 2.0 mA; acetylene flow rate 1.6 L/min; air flow 8.0 L/min; burner height 7.0 mm;
69.	ICP-OES	Optima 3100-XL ICP-AES spectrometer (Perkin-Elmer, Norwalk, CT); concentric nebulizer; cyclonic spray chamber; axially-viewed system; segmented-array charge-coupled device; AS-91 auto-sampler;	analytical spectral lines: 317.99 nm (Ca), 238.20 nm (Fe), 279.08 nm (Mg); Rf power: 1.2 kW; gas flow rates: 15 l/min (outer Ar), 0.5 l/min (auxiliary Ar), 0.8 l/min (nebulizer); quantitative mode: peak area; background correction mode: two-point;
71.	ICP-OES	Labtest Plasmalab ICP spectrometer; pneumatically operated injection valve;	argon plasma; incident power: 1.3 kW; Rf: 27.12 MHz; observation height: 16 mm; volume of injected sample: 130 µl;
76.	ICP-MS	ICP-MS spectrometer Elan 9000 (PerkinElmer, Waltham, MA); nebulizer: cross flow type; spray chamber: double pass;	isotopes: 75-As, 111-Cd, 59-Co, 202-Hg, 98-Mo, 208-Pb, 82-Se; plasma Rf power: 1200W; gas flow rates: 15 l/min (plasma), 1.2 l/min (auxiliary), 1.0 l/min (nebulizer); auto lens: on; Dwell time: 200 ms; sweeps: 10; 3 replicates; read delay: 25 s; rinse delay: 25 s; pump rate: 13 rpm;
	ICP-OES	Varian MPX ICP-OES spectrometer; axial view mode; nebulizer: concentric - sea spray; spray chamber: cyclonic baffled;	analytical spectral lines: 324.754 nm (Cu), 213.857 nm (Zn); plasma Rf power: 1200 W; gas flow rates: 15 l/min (plasma), 1.5 l/min (auxiliary), 1.0 l/min (nebulizer); replicate read time: 30 s; fitted background correction;
77.	ICP-OES	ICP-OES spectrometer Spectro Genesis EOP II, Spectro Analytical Instruments (DmbH, Kleve, Germany);	analytical spectral lines: 394.401 nm (Al), 249.773 nm (B), 233.527 nm (Ba), 228.802 nm (Cd), 228.616 nm (Co), 205.552 nm (Cr), 324.754 nm (Cu), 259.941 nm (Fe), 184.950 nm (Hg), 460.289 nm (Li), 259.373 nm (Mn), 202.095 nm (Mo), 231.604 nm (Ni), 220.353 nm (Pb), 460.733 nm (Sr), 206.1919 nm (Zn);
78.	ICP-OES	Jobin-Yvon JY 48 instrument composed of a vacuum polychromator and a Plasma-Therm source; pneumatic nebulization;	analytical spectral lines: 455.40 nm (Ba), 393.37 nm (Ca), 324.75 nm (Cu), 259.94 nm (Fe), 766.49 nm (K), 279.55 nm (Mg), 403.08 nm (Mn), 386.41 nm (Mo), 589.0 nm (Na), 178.28 nm (P), 182.03 nm (S), 407.77 nm (Sr), 213.86 nm (Zn);
79.	ICP-OES	Vista simultaneous ICP-OES spectrometer (Varian - Mulgrave, Australia); axial viewing; charge coupled device solid state detector; V-Groove nebulizer; Sturman – master nebulization chamber;	analytical spectral lines: 226.502 nm (Cd); 238.203 nm (Fe); 327.398 nm (Cu); 280.267 nm (Mg); 220.354 nm (Pb); 196.026 nm (Se); 213.858 nm (Zn); Rf generator power: 1.3 kW; gas flow rates: 0.7 ml/min (nebulizer), 1.5 ml/min (auxiliary), 15 ml/min (plasma); signal integration time: 1.0 s; stabilization time: 15 min; reading time: 1 min; 3 replicates;

81.	ICP-OES	Optima 3100 XL spectrometer (Perkin Elmer, Norwalk, CT, USA); cross-flow nebulizer; Ryton Scott chamber; polychromator with echelle grating; detector: simultaneous solid-state segmented-array charged-coupled device;	analytical spectral lines: 393.3 nm (Ca); 324.7 nm (Cu); 259.9 nm (Fe); 279.5 nm (Mg); 251.6 nm (Si); 371.0 nm (Y), 213.8 nm (Zn); radiofrequency: 1.3 kW; argon gas flow rates: 13.0 l/min (plasma), 0.5 l/min (auxiliary), 0.7 l/min (nebulizer); max. resolution: 0.006 nm at 200 nm;
	ICP-MS	SF-ICP-MS spectrometer ELEMENT model from Thermo Finnigan (Bremen, Germany); torch guard electrode device; platinum interface cones; Meinhardt type glass nebulizer; water-cooled Scott chamber;	isotopes: 27-Al, 55-Mn; medium resolution mode: 3000m/Δm; radiofrequency power: 1.2 kW; gas flow rates: 14.0 l/min (plasma), 0.9 l/min (auxiliary), 0.85 l/min (nebulizer);
82.	ICP-OES	ULTIMA 2 ICP-OES spectrometer (Jobin Yvon, Longjumeau Cedex, France); radial viewing mode; Czerny-Turner monochromator; Meinhard nebulizer; cyclonic spray chamber;	analytical spectral lines: 167.02 nm (Al), 238.204 nm (Fe), 257.610 nm (Mn), 213.856 nm (Zn), 588.95 nm (Na), 670.784 nm (Li), 766.490 nm (K); argon flow rate: 12 l/min; optical bench temperature: 32 °C;
83.	ICP-OES	IRIS/AP ICP-AES spectrometer (Thermo Jarell-Ash, Franklin, MA, USA); charged injection device detector; axial viewing mode; microconcentric (Micromist) nebulizer (Glass Expansion Pty. Ltd., Australia); cyclone spray chamber;	analytical spectral lines: 396.152 nm (Al), 249.678 nm (B), 493.409 nm (Ba), 313.107 nm (Be), 214.438 nm (Cd), 237.862 nm (Co), 267.716 nm (Cr), 324.754 nm (Cu), 259.940 nm (Fe), 670.784 nm (Li), 257.610 nm (Mn), 231.604 nm (Ni), 220.353 nm (Pb), 196.090 nm (Se), 407.771 nm (Sr), 206.200 nm (Zn); plasma frequency: 27.12 MHz; Rf power: 1150 W; gas flow rates: 0.56 L/min (torch), 0.5 L/min (auxiliary), 0.56 L/min (nebulizer); nebulizer uptake: 0.5 ml/min; sample volume: 1.5 ml/2 repeats; flush time: 40 s; purge time: 90 s; signal integration time: 60 s (high wavelength) and 10 s (low wavelength);
84.	ICP-OES	ICP-OES spectrometer ICAP-61 (Thermo Jarrell Ash, USA); angular nebulizer;	analytical spectral lines: 308.215 nm (Al), 249.678 nm (B), 493.409 nm (Ba), 393.366 nm (Ca), 324.754 nm (Cu), 259.94 nm (Fe), 766.491 nm (K), 670.784 nm (Li), 279.553 nm (Mg), 257.61 nm (Mn), 588.995 nm (Na), 213.618 nm (P), 182.04 nm (S), 421.552 nm (Sr), 292.402 nm (V), 213.856 nm (Zn); generator output power: 1.200 W; reflected power: <5 W, gas flow rates 18 L/min (plasma), 0.9 L/min (auxiliary), 0.6 L/min (nebulizer), sample flow rate: 1.5 mL/min; zone height for plasma observation: 14 mm; integration time: 5 s;
86.	ICP-OES	JOBIN-YVON PANORAMA ICP-AES spectrometer; axial viewing configuration;	analytical spectral lines: 259.940 nm (Fe), 324.754 nm (Cu), 237.862 nm (Co), 213.856 nm (Zn), 232.003 nm (Ni), 228.802 nm (Cd), 257.610 nm (Mn), 220.353 nm (Pb); Rf Power:

			1.0 kW; nebulizer pressure: 3.0 bar; gas flow rates: 16 l/min (plasma), 1.7 l/min (auxiliary); sample uptake rate: 0.8 ml/min; stabilization time: 15 s; read time: 1 s;
89.	ICP-MS	HR-ICP-MS Thermo Finnigan Element II model (Bremen, Germany); concentric glass nebulizer; water-cooled Scott double-pass spray chamber; torch with guard electrode device and nickel interface cones;	isotopes: 11-B, 85-Rb, 88-Sr, 95-Mo, 111-Cd, 208-Pb (analysed in low resolution, 300 m/Δm), 27-Al, 51-V, 52-Cr, 55-Mn, 56-Fe, 59-Co, 63-Cu, 66-Zn (analysed in medium resolution, 4000 m/Δm), 75-As and 77-Se (analysed in high resolution, 10000 m/Δm); Rf power: 1280 W - 1300 W; argon gas flow rates: 16.0 L/min (cool), 0.94 L/min (auxiliary), 1.110 -1.200 L/min (sample); sample uptake rate: 0.1-0.2 mL/min;
90.	ICP-MS	ICP-MS/MS system Agilent ICP-QQQ-MS 8800 (Waldbronn, Germany); MicroMist nebulizer; Scott type spray chamber;	two modes: 1) on-mass mode: He as collision gas, 2) mass-shift mode: O_2 and H_2 as reaction/collision gas mixture; parameters for mode 1) forward power: 1550, gas flow rates: 15 L/min (cool), 0.9 L/min (auxiliary), 1 L/min (nebulizer), 3 ml/min (cell - He), m/z: 24-Mg, 44-Ca, 55-Mn, 56-Fe, 65-Cu, 66-Zn, 103-Rh, 111-Cd, 127-I; integration time: 0.3 s; replicates: 3 s; parameters for mode 2) cell gas flow rate: 0.4 mL/min (O_2), 1 mL/min (H_2); m/z: 75-As, 77-Se, 78-Se, 80-Se, 98-Mo, 103-Rh; 91AsO, 93-SeO, 94-SeO, 96-SeO, 114-MoO;
95.	ICP-MS	Elan 6000 ICP-MS spectrometer (Perkin Elmer, Sciex, Toronto, Canada); cross flow nebulizer; peristaltic pump; AS-91 autosampler fitted with a 152 position tray	isotopes: 111-Cd, 67-Zn;
96.	ICP-MS	Agilent 7500 ICP-MS (Agilent Technologies, Santa Monica, CA, USA); reaction mode: on;	Rf power: 1500 W; sampling depth: 7.2 mm; gas flow rates: 0.88 L/min (carrier, Ar), 0.25 L/min (makeup, Ar), 4.7 mL/min (He); integration time: 0.1 s;
98.	ICP-MS	ICP-MS spectrometer (Okamoto, 1997);	
99.	ICP-MS	ICP-MS spectrometer NexION 300D (Perkin Elmer, Waltham MA); Elemental Scientific Inc (ESI) SC2-DX autosampler (Omaha NE); platinum sampler and skimmer cones (Glass Expansion, West Melbourne, Australia); Microflow PFA-ST nebulizer (ESI); quartz cyclonic spray chamber with baffle (ESI) ;	two modes: 1) dynamic reaction cell mode with ammonia as a reactant gas, 2) kinetic energy discrimination with helium as an inert gas; power: 1600 W; cell gas flow rates: 0.6 mL/min (ammonia), 4.0 mL/min (helium); nebulizer gas flow rate: 0.8 L/min - 1.2 L/min; isotopes: 52-Cr, 51-V, 59-Co; Dwell time: 50 ms; sweeps: 5;
100.	ICP-MS	ICP-MS spectrometer (Elan DRC II PerkinElmer, Norwalk, CT); Meinhard concentric nebulizer	isotopes: 107-Ag, 27-Al, 75-As, 138-Ba, 9-Be, 111-Cd, 59-Co, 53-Cr, 63-Cu, 55-Mn, 98-Mo, 208-Pb, 82-Se, 205-Tl, 238-U, 51-V, 64-Zn; Rf power: 1200 W; data acquisition: 20

		(Spectron/Glass Expansion, Ventura, CA, USA); cyclonic spray chamber;	sweeps/reading, 1 reading/replicate; dwell time: 50 ms; Ar nebulizer gas flow rate: 0.5 L/min - 0.9 L/min; integration time: 1000 s;
101.	ICP-MS	ICP-MS spectrometer VGElemental PlasmaQuad SOption;	
102.	ICP-MS	ICP-MS spectrometer (X-SERIES II, Thermo Fisher, USA); interface: Nickel Xt; concentric glass nebulizer;	isotope: 90-Zr; Rf power: 1400 W; gas flow rates: 0.85 L/min (nebulizer), 13.0 L/min (cooling), 0.80 L/min (auxiliary); sampling depth: 150 steps; peristaltic pump speed: 30; 10 sweeps; 3 main runs; dwell time: 30 ms; acquisition mode: peak jumping;
105.	GF-AAS	4100 ZL atomic absorption spectrometer (Perkin Elmer, Germany); longitudinal Zeeman background correction; transversely heated graphite atomiser (THGA); end-capped graphite tubes; L'vov platform (PerkinElmer Part No. B3 000653); AS-70 autosampler; Intensitron hollow cathode lamp (Perkin Elmer)	analytical spectral line: 248.3 nm (Fe); slit width: 0.2 nm; lamp current: 30 mA; inert gas: Ar; flow rate: 250 ml/min; sample injection volume: 15 µl; matrix modifier injection volume: 5 µl; measurement mode: integrated absorbance; integration time: 5 s; baseline offset correction: 2 s; operating conditions: 1) dry: 110 °C, ramp 1 s, hold 30 s, 2) dry: 130 °C, ramp 15 s, hold 30 s, 3) pyrolysis: 1400 °C, ramp 10 s, hold 20 s, 4) atomisation: 2100 °C, ramp 0 s, hold 5 s, 5) cleaning: 2450 °C, ramp 1 s, hold 3 s; injection temperature: 20 °C;
108.	GF-AAS	Atomic absorption spectrometer 4110 ZL (Perkin-Elmer); Zeeman-effect background correction; chromium hollow-cathode lamp; transversely heated graphite tubes; Lvov platforms;	analytical spectral line: 357.9 nm (Cr); spectral band pass: 0.7 nm; pure gas: Ar; operating conditions: 1) dry: 110 °C, ramp 10 s, hold 20 s, 2) dry: 130 °C, ramp 15 s, hold 30 s, 3) pyrolysis: 1500 °C, ramp 10 s, hold 20 s, 4) atomisation: 2300 °C, ramp 0 s, hold 5 s, 5) clean: 2600 °C, ramp 1 s, hold 3 s;
110.	GF-AAS	Varian SpectrAA-300Z atomic absorption spectrophotometer (Victoria, Australia); graphite furnace and Zeeman background correction system; autosampler (Varian); Mn and Cu hollow cathode lamps; pyrolytically-coated partition graphite tubes (Varian);	analytical spectral lines: 324.8 nm (Cu), 279.5 nm (Mn); slit width: 0.5 nm (Cu), 0.2 nm (Mn); lamp current: 4 mA (Cu), 5 mA (Mn); volume of the injected to the graphite tube: 5 µl; operating conditions for Cu determination: 1) 120 °C, ramp 30 s, hold 10 s, Ar flow rate: 3.0 L/min, 2) 700 °C, ramp 30 s, hold 10 s, Ar flow rate: 3.0 L/min, 3) 2600 °C, ramp 1 s, hold 7 s, Ar flow rate: 0.0 L/min, 4) 40 °C, ramp 13 s, hold 2 s, Ar flow rate: 3.0 L/min; operating conditions for Mn determination: 1) 110 °C, ramp 35 s, hold 15 s, Ar flow rate: 3.0 L/min, 2) 650 °C, ramp 35 s, hold 20 s, Ar flow rate: 3.0 L/min, 3) 2500 °C, ramp 1 s, hold 67 s, Ar flow rate: 0.0 L/min, 4) 40 °C, ramp 10 s, hold 4 s, Ar flow rate: 3.0 L/min;
	F-AAS	Varian SpectrAA-20 flame atomic absorption spectrophotometer; deuterium background correction; zinc hollow cathode lamp;	analytical spectral line: 213.9 nm (Zn); slit width: 1.0 nm (Zn); lamp current: 5 mA (Zn);

118.	ICP-OES	iCAP 6300 duo plasma emission simultaneous spectrometer (Thermo Electron, Waltham, MA); detector: charge-injection device; observation mode: radial/axial (auto view); spray chamber: cyclonic with concentric nebulizer (Meinhard);	Rf power: 1.150 kW; Rf: 27.12 MHz; pump rate: 50 rpm; integration time: 15 s/15 s (low/high wavelength); gas flow rates: 0.5 L/min (auxiliary), 20 L/min (coolant); nebulizer gas pressure: 0.15 MPa;
119.	ICP-MS	ELEMENT 2 (Thermo Fisher Scientific, Bremen, Germany); sampling and skimmer cone: Pt; two sample introduction systems: 1) proposed: HPCN nebulizer (customized concentric type nebulizer body from ONIZUKA Glass/ST JAPAN, Tokyo, Japan, and a tapered liquid capillary made from a fused silica capillary, GL Sciences, Japan), IsoMist spray chamber, loop injection unit (KP-11 model, Ogawa. Co. Ltd., Japan), polypropylene micro syringe; 2) conventional: conical nebulizer (Glass expansion); cyclone chamber at room temperature (i.e. 27 ◦C);	Rf: 27.12 MHz; incident Rf power: 1.5 kW; reflected power: <2W; gas flow rates: 16 L/min (outer gas), 0.9 L/min (intermediate gas), 1.05 L/min (carrier gas for HPCN) and 0.95 L/min (carrier gas for conical nebulizer); sampling depth: -2mm; solution flow rate: 10 µl/min (HPCN), 1 ml/min (conventional); mass resolution: m/Δm 4000; scanning mode: E-scan; integrated mass window: 50%; data points: 20 points/peak; dwell time: 10 ms/point; integration: 5 times; repetition: 5 times; oxide formation ratio YO^+/Y^+: 0.5% (HPCN), 1.5% (conventional); m/z: 23-Na^+, 26-Mg^+, 31-P^+, 32-S^+, 39-K^+, 44-Ca^+, 52-Cr^+, 55-Mn^+ 56-Fe^+, 59-Co^+, 60-Ni^+, 63-Cu^+, 66-Zn^+, 89-Y^+, 95-Mo^+, 111-Cd^+, 137-Ba^+, 208-Pb^+;

ACS Chemical Neuroscience

pubs.acs.org/chemneuro

Research Article

Comparison of Elemental Anomalies Following Implantation of Different Cell Lines of Glioblastoma Multiforme in the Rat Brain: A Total Reflection X-ray Fluorescence Spectroscopy Study

Karolina Planeta,[#] Zuzanna Setkowicz,[#] Natalia Janik-Olchawa, Katarzyna Matusiak, Damian Ryszawy, Agnieszka Drozdz, Krzysztof Janeczko, Beata Ostachowicz, and Joanna Chwiej*

Cite This: https://dx.doi.org/10.1021/acschemneuro.0c00648

Read Online

ACCESS | Metrics & More | Article Recommendations | Supporting Information

ABSTRACT: Glioblastoma multiforme (GBM) is a primary brain tumor with a very high degree of malignancy and is classified by WHO as a glioma IV. At present, the treatment of patients suffering from GBM is based on surgical resection of the tumor with maximal protection of surrounding tissues followed by radio- and pharmacological therapy using temozolomide as the most frequently recommended drug. This strategy, however, does not guarantee success and has devastating consequences. Testing of new substances or therapies having potential in the treatment of GBM as well as detection of their side effects cannot be done on humans. Animal models of the disease are usually used for these purposes, and one possibility is the implantation of human tumor cells into rodent brains. Such a solution was used in the present study the purpose of which was comparison of elemental anomalies appearing in the brain as a result of implantation of different glioblastoma cell lines. These were two commercially available cell lines (U87MG and T98G), as well as tumor cells taken directly from a patient diagnosed with GBM. Using total reflection X-ray fluorescence we determined the contents of P, S, K, Ca, Fe, Cu, Zn, and Se in implanted-left and intact-right brain hemispheres. The number of elemental anomalies registered for both hemispheres was positively correlated with the invasiveness of GBM cells and was the highest for animals subjected to U87MG cell implantation, which presented significant decrease of P, K, and Cu levels and an increase of Se concentration within the left hemisphere. The abnormality common for all three groups of animals subjected to glioma cell implantation was increased Fe level in the brain, which may result from higher blood supply or the presence of hemorrhaging regions. In the case of the intact hemisphere, elevated Fe concentration may also indicate higher neuronal activity caused by taking over some functions of the left hemisphere impaired as a result of tumor growth.

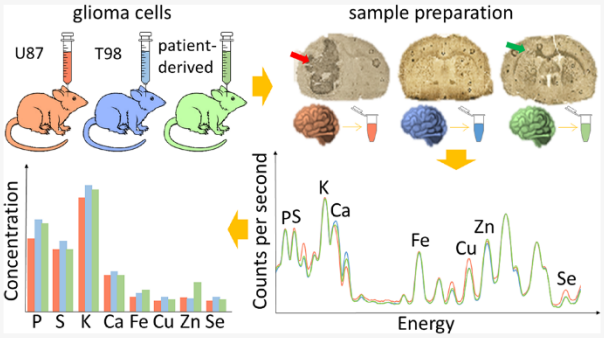

KEYWORDS: *glioblastoma multiforme, GBM, animal model of GBM, bulk elemental analysis of brain, total reflection X-ray fluorescence, U87MG, T98G*

INTRODUCTION

One of the most common primary brain tumors are gliomas, which usually develop from glial cells, non-neuronal cells supporting the functions of neurons. As different types of glial cells exist, various types of gliomas are distinguished,[1] but the most aggressive is glioblastoma multiforme (GBM), which accounts for about 54% of all glioma cases and represents about 16% of all brain tumors. The World Health Organization classified GBM to cancers with the highest (IV) degree of malignancy.[2]

Despite various therapies, median survival of patients suffering from GBM is 14−16 months and only 9.8% of them survive 5 years.[2] The high aggressiveness of GBM results from its complex nature, which includes the presence of necrotic and hemorrhagic regions or cellular atypia within the same tumor mass. GBM has high infiltrative potential and vascular proliferation ability, which lead to its great invasiveness.[3] Standard glioblastoma treatment includes surgical resection of the tumor, radiotherapy, and chemotherapy, usually based on temozolomide (TMZ). Despite such radical therapy, there is no significant improvement in the patient survival rate. The location and infiltrating nature of the tumor prevent its total resection and make precise radio-

Received: October 9, 2020
Accepted: November 9, 2020

Table 1. Limits of Detection and Intraday and Interday Precision Values Obtained for Analyzed Elements

parameter	P	S	K	Ca	Fe	Cu	Zn	Se
LOD (SD) [ppm]	12.96(0.45)	8.32(0.29)	4.41(0.16)	1.832(0.072)	0.1916(0.0082)	0.0852(0.0035)	0.1078(0.0042)	0.0297(0.0011)
intraday precision [%]	2.0	1.6	1.0	3.1	0.3	0.7	0.2	4.9
interday precision [%]	1.3	1.2	0.7	2.8	0.3	0.4	0.2	1.2

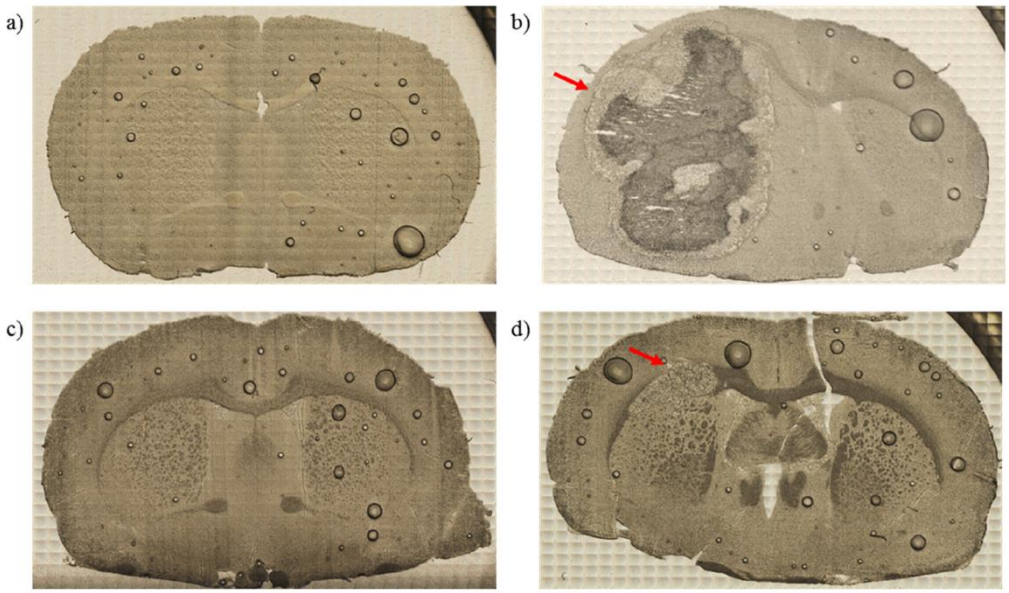

Figure 1. Microscopic images of unstained tissue slices taken from animals representing N (a), U (b), T (c), and P (d) groups. N group consisted of naive controls, while animals from groups U, T, and P were subjected to implantation into the brain of U87MG, T98G, and patient tumor-derived cells, respectively. Red arrows indicate developed tumor mass.

therapy difficult. In addition, its complexity and drug resistance capacity reduce the effectiveness of the treatment.[4] Due to lack of satisfactory results in the treatment of patients diagnosed with glioblastoma, new therapeutic strategies are still being sought.

To get better knowledge about tumor pathogenesis and progress, as well as to examine new therapeutic strategies before clinical trials, animal models of tumors are used.[5−7] A wide range of GBM animal models are available. Some are based on implantation of human cells from established tumor cell lines into animal brains. There is also possibility to implant tumor cells taken directly from a patient diagnosed with tumor. In both approaches, immunodeficient and immunosuppressed rodents are usually used as experimental animals.[8,9] As there is no one model that ideally reflects the nature of a human brain tumor, different models have been verified in order to assess their usability in preclinical studies.[10−12]

The existing literature shows that trace and minor elements may be involved in the pathogenesis and progress of different types of tumors. Bobko et al. indicated the significance of inorganic phosphorus for the metabolism of tumor cells, as well as the increased phosphorus demand by these cells associated with tumor growth.[13] Duan et al. found that sulfur inhibits proliferation of cells separated from prostate cancer developed *in vivo* in nude mice[14] while Eil et al. observed that immune response of tumor cells may be suppressed by high potassium levels.[15] The information about the levels of elements in pathologically changed tissue may serve as tumor biomarkers and prognostic factors allowing prediction of patient survival or success of the anticancer therapy.[16−19] The tissues taken from brain tumors were also analyzed with respect to the significance of different elements for pathogenesis and development of the tumor or to discover dependencies between elemental composition of the tumor and its malignancy grade.[20−24]

The aim of our research was to assess the elemental anomalies appearing in rat brain after intracranial implantation of different GBM cells. For the purposes of our experiment, we used two commercially available human GBM cell lines, namely, T98G and U87MG, and tumor cells taken directly from a patient diagnosed with primary GBM. Using the total reflection X-ray fluorescence (TXRF) method, we determined and compared the concentrations of P, S, K, Ca, Fe, Cu, Zn, and Se in glioma-implanted and intact hemispheres of the brain. Each of 4 groups of animals (3 groups subjected to implantation of different GBM cells and normal rats) consisted of 6 individuals from which 2 brain hemispheres were taken, prepared, and measured separately. As a result 12 samples were examined per animal population. This study, aimed at the determination of elemental changes specific for particular GMB cell lines, is necessary to start the next steps of research focused on elemental modifications occurring in animal brains as a result of different new therapies.

■ RESULTS AND DISCUSSION

Limits of Detection and Precision. The limit of detection (LOD) and precision (intraday and interday) obtained using TXRF method were calculated for each

https://dx.doi.org/10.1021/acschemneuro.0c00648
ACS Chem. Neurosci. XXXX, XXX, XXX−XXX

examined element. As one can notice from Table 1, the lowest values of LOD were obtained for selenium (0.0297 ppm) and the highest for phosphorus (12.96 ppm). The values of detection limit are lower for elements with higher atomic numbers. The detectability of elements with the uses of XRF is influenced by the efficiency of detection of the fluorescent radiation emitted by the elements. This, in turn, strongly depends on values of radiation energy, which increase with element atomic number.

Values of intraday precision were good and varied from 0.2% to 4.9% for Zn and Se, respectively. Interday precision values for all analyzed elements did not exceed 2.8%.

Microscopic Evaluation. In order to define the degree of invasiveness of different GBM cells, before tissue digestion, microscopic images of the brain slices were taken from the area of implantation. The exemplary pictures obtained for the animals representing each of the examined groups are presented in Figure 1. As one can see, the implantation on U87MG cell line led to the development of massive tumor, which in the most severe cases included the whole hemisphere subjected to implantation (Figure 1b). Also after implantation of cells taken directly from a patient diagnosed with GBM, tumors appeared in rat brains (Figure 1d); however their volumes were much smaller than in case of U87MG cells introduction. For T98G cells, morphological changes of the brain were not visible or were limited only to the area of implantation (Figure 1c).

Spectral Analysis. As a result of TXRF measurements, for each analyzed brain hemisphere the X-ray fluorescence spectrum was obtained. Energy calibration of the obtained TXRF spectra was carried out in the PyMCA program. The identification and quantitative analysis of P, S, K, Ca, Fe, Cu, Zn, and Se were performed based on their Kα lines. As an example, the mean TXRF spectrum recorded for the left hemisphere of normal brain is presented in Figure 2. The Kα lines of the elements taken for further quantitative analysis are indicated with red arrows.

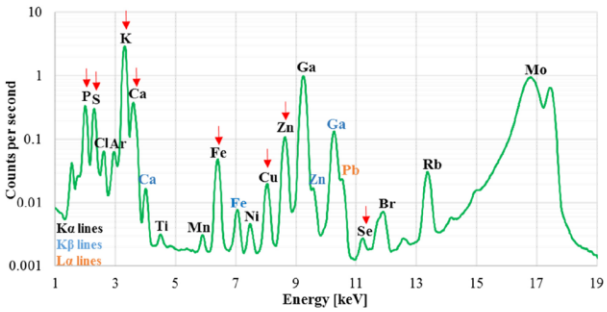

Figure 2. Mean TXRF spectrum recorded for left hemisphere of normal brain. The Kα lines of the analyzed elements (P, S, K, Ca, Fe, Cu, Zn, Se) are indicated with red arrows.

Elemental Anomalies Introduced by Implantation of GBM Cells in the Left (Implanted) Hemisphere. To identify local elemental anomalies introduced by tumor development, the levels of P, S, K, Ca, Fe, Cu, Zn, and Se in the left, glioma-implanted cerebral hemispheres were measured. Afterward, the median values of the concentrations were determined for each experimental group and together with the maximal and minimal values, as well as interquartile spans, they were presented as box-and-whiskers plots in Figure 3. To examine the significance of the observed anomalies, the *U* Mann−Whitney test was applied. For all identified statistically relevant differences (p-value < 0.05) between animals subjected to GBM cell implantation and normal controls, p-values of the *U* test are presented in Figure 3.

Many differences in the elemental composition of the left hemisphere were observed between animals subjected to glioma cell implantation and normal controls. However, it is not possible to indicate any elemental abnormality common for all animal models of GBM. As can be seen from Figure 3, implantation of U87MG cells led to a significant decrease of P, K, and Cu levels and an increase of Se concentration within the implanted hemisphere. In turn, the animals from the P group presented higher Fe and Zn contents and diminished Se level within the implanted hemisphere. The only difference compared to normal rats observed in animals subjected to implantation of T98G cells was the elevated Fe content.

Elemental Anomalies Introduced by Implantation of GBM Cells in Right (Intact) Hemisphere. The median values of elemental concentrations in right hemispheres were determined for each experimental group, and together with the maximal and minimal values as well as interquartile spans, they are presented in Figure 4. As can be seen, for all examined GBM models, the levels of iron within the intact hemispheres were elevated compared to the right hemispheres taken from normal rats. Additionally, for animals representing the U group, lower concentrations of K and Cu and a higher concentration of Ca were observed. In turn, the rats subjected to patient-derived cell implantation presented only lower K levels within the intact hemispheres.

Differences in Elemental Composition between Implanted and Intact Hemispheres. In the charts presented in Figure 5, the concentrations of P, S, K, Ca, Fe, Cu, Zn, and Se in the left and right hemispheres were compared for individual animal groups. As can be seen, no differences between the elemental composition of two hemispheres were observed in normal rats. Such differences, however, were found in animals subjected to GBM implantation, and most of them were detected in animals subjected to implantation of the most invasive U87MG cells. They included lower levels of P, Ca, Fe, Cu, and Zn, as well as higher concentration of Se in the implanted hemisphere. In rats representing P group, the implanted hemisphere was characterized by higher content of Zn and lower content of Se. In turn, in the left hemispheres taken from animals subjected to T98G cells implantation, lower contents of S and K were observed.

Discussion. The aim of our investigation was to assess the effects of GBM cells implanted in a rat cerebral hemisphere and of their further development on the elemental composition of the whole brain. The study was carried using two commercially available cell lines (U87MG and T98G), as well as tumor cells taken directly from a patient diagnosed with GBM. The degree of aggressiveness of the tumor developing from different GBM cells strongly differed and was the greatest for U87MG cell line. The intensive tumor growth and deteriorating condition of the animals representing the U group led to the decision about the earlier experiment termination.

Corresponding brain hemispheres taken from the experimental and control animals were compared regarding concentrations of elements. In addition, differences in the elemental composition between the implanted and non-

https://dx.doi.org/10.1021/acschemneuro.0c00648
ACS Chem. Neurosci. XXXX, XXX, XXX−XXX

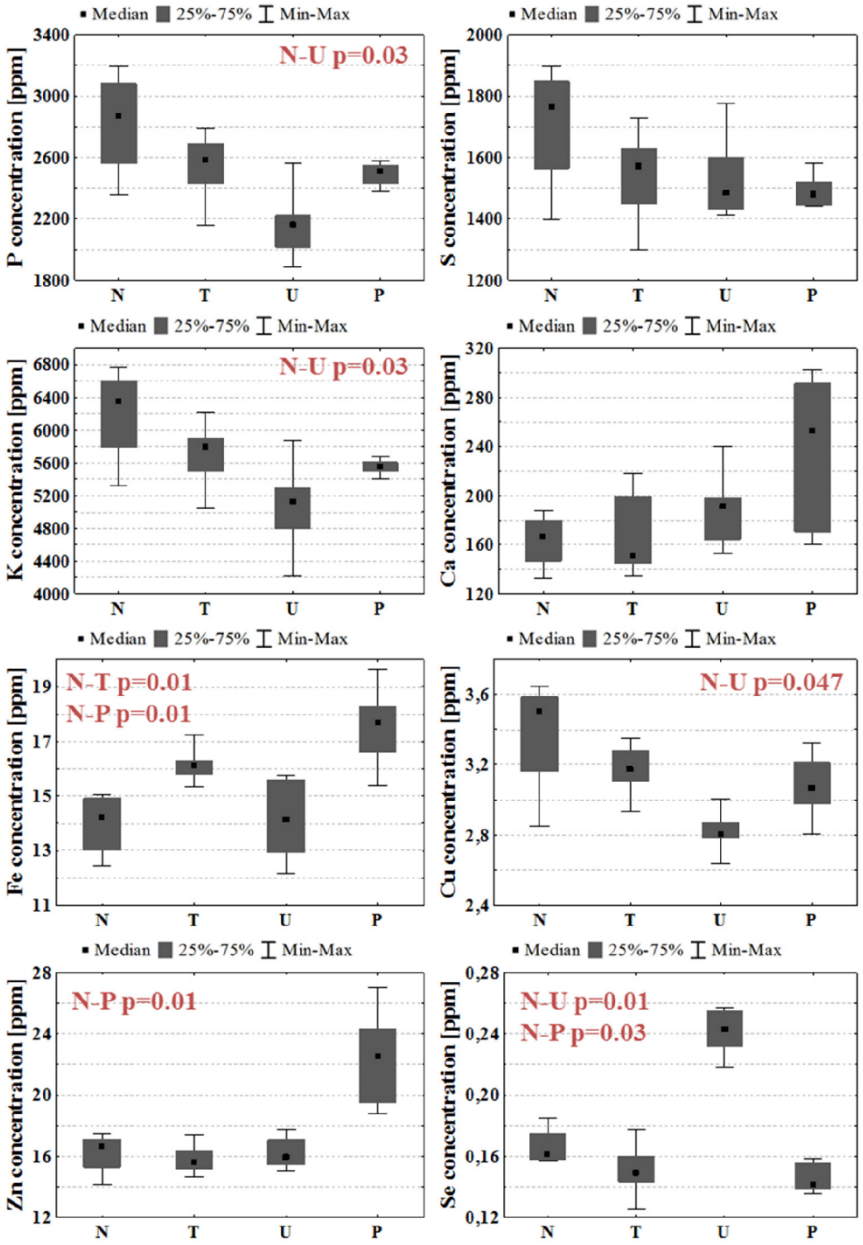

Figure 3. Median, minimal, and maximal values, as well as interquartile spans (gray boxes), of elemental concentrations in the left hemispheres of brain for N, T, U, and P groups. The statistically significant differences (p-value < 0.05) between animals subjected to GBM cell implantation and normal rats are marked in red.

implanted hemispheres were evaluated for each animal group. The concentrations of P, S, K, Ca, Fe, Cu, Zn, and Se were determined using the TXRF method. To prove the usefulness of this method for the elemental analysis of examined samples, validation parameters such as LOD and precision were determined. The obtained LOD values were low and varied from 0.0297 ppm for Se to 12.96 ppm for P. The precision of performed measurements was very good, and for most of the analyzed elements, intraday precision did not exceed 4.9%, while interday precision was no more than 2.8%.

For all examined experimental groups significant elemental anomalies were observed in both implanted and intact brain hemispheres; however the most changes were found for rats subjected to implantation of the most invasive U87MG cells. The smallest differences in elemental composition occurred for animals implanted with T98G cells, which confirms the manufacturer descriptions of the used commercial cell lines, where U87MG cell line was defined as tumorigenic while T98G was defined as nontumorigenic. According to our best knowledge, this is the first study where elemental anomalies occurring within the brain as a result of glioma cell implantation were analyzed. Therefore, in the discussion we confronted our results with literature data obtained for samples of both human and animal origin and concerning the elemental anomalies associated with malignant brain tumors. The reviewed studies were not based on bulk elemental analysis

https://dx.doi.org/10.1021/acschemneuro.0c00648
ACS Chem. Neurosci. XXXX, XXX, XXX−XXX

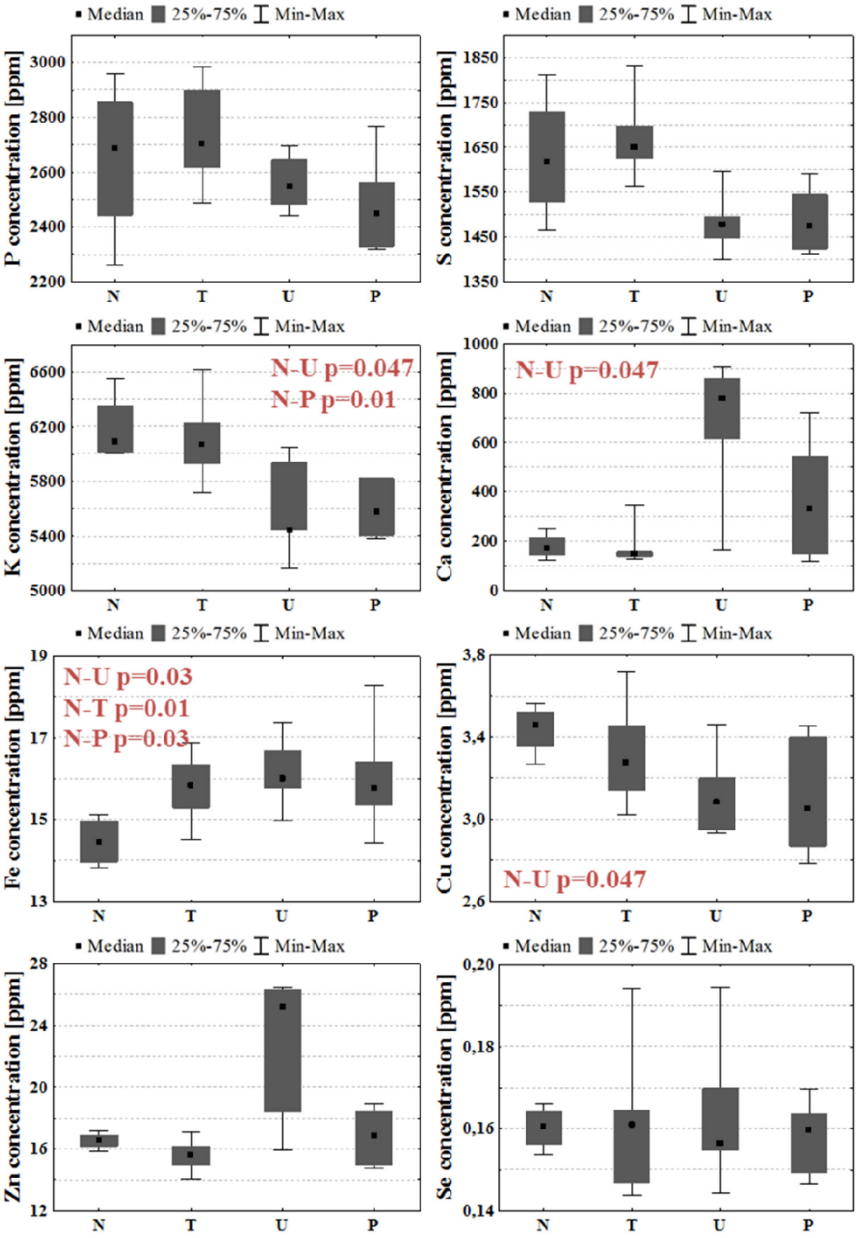

Figure 4. Median, minimal, and maximal values, as well as interquartile spans (gray boxes), of elemental concentrations in the right cerebral hemispheres for N, T, U, and P groups. Statistically significant differences (p-value < 0.05) between animal groups subjected to GBM cell implantation and normal rats are marked in red.

of the brain hemispheres, but concerned either the comparative analysis of tumor and normal tissue or the topographic elemental analysis of the brain affected with tumor. We also discussed the significance of the analyzed elements for the pathogenesis, progress, and treatment of GBM.

Phosphorus is a mineral the presence of which in body cells is crucial for their proper functioning. It constitutes a building component of nucleic acids, phospholipids, or phosphoproteins. Being a part of ATP, phosphorus plays a key role in energy metabolism processes.[25] It is also involved in cell signaling through phosphorylation reactions, which regulate activity of many types of enzymes.[26] Already in the mid-twentieth century, there were reports of increased uptake of radioactive phosphorus by malignant brain tumor cells.[27] It has been shown that compared to normal brain tissue, tumor tissue was characterized by diminished phosphorus concentration. This observation was correlated with a simultaneous decrease in phospholipid (cephalin, lecithin, and sphingomyelin) content in cancer tissue.[28] Based on conducted MR examinations Hubesch et al. observed that the content of phosphate metabolites (phosphomonoesters, phosphodiesters, and phosphocreatine) in brain tumor was decreased compared to a normal human brain.[29] From the other hand, Srivastava et al. revealed an increased phosphatidylcholine level in brain tumor compared to normal brain which indicated the

https://dx.doi.org/10.1021/acschemneuro.0c00648
ACS Chem. Neurosci. XXXX, XXX, XXX−XXX

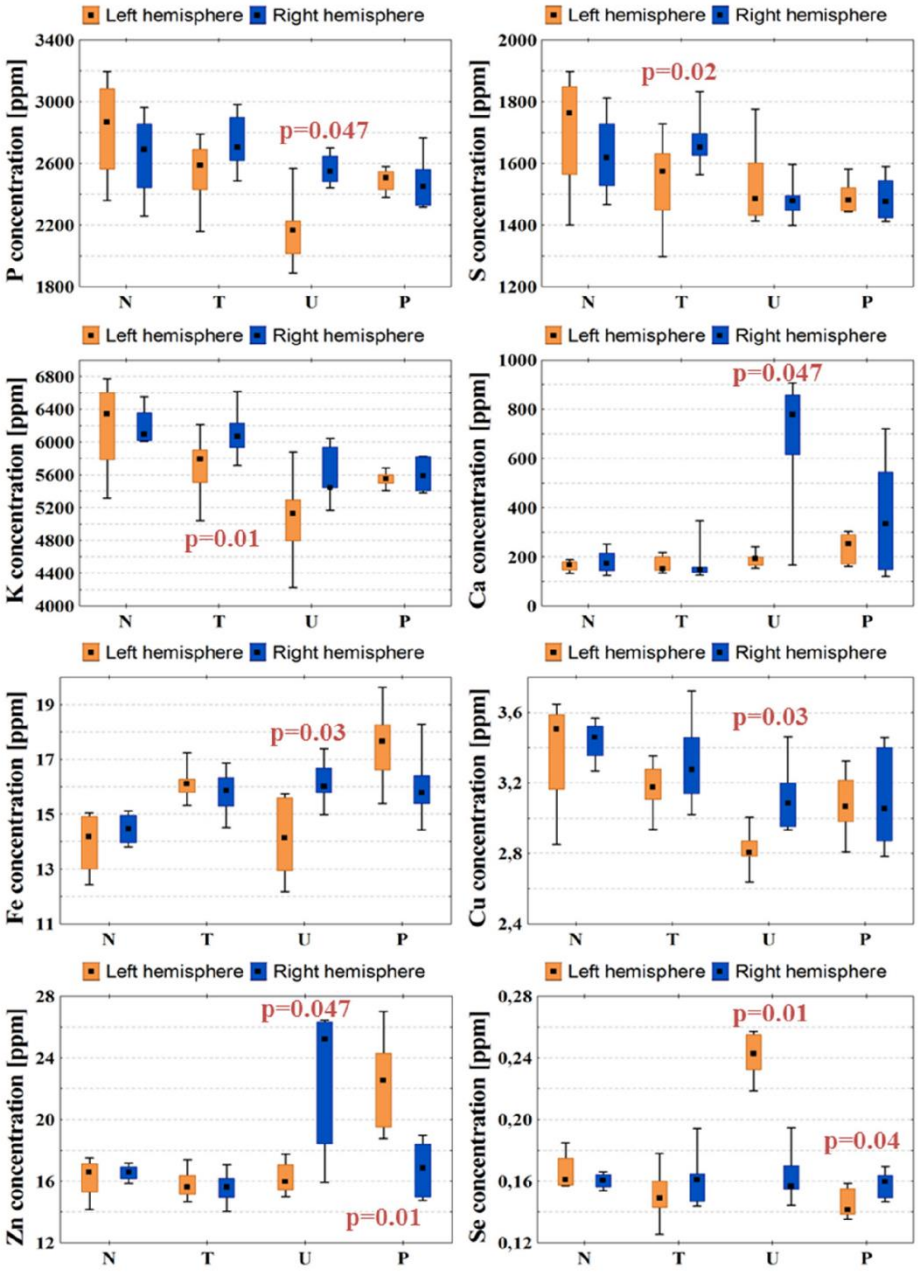

Figure 5. Concentrations of P, S, K, Ca, Fe, Cu, Zn, and Se in both brain hemispheres determined for N, T, U, and P groups. Median, interquartile range, and minimal and maximal values of concentrations are indicated. Left and right hemispheres are marked with orange and blue colors, respectively. Statistically significant differences in elemental composition between the two hemispheres were identified using the Mann−Whitney test and are marked with *p*-values of *U* test.

abnormal accumulation of this compound within the tumor.[30] Andrasi et al. compared elemental composition of various regions of brain with and without tumor and did not find differences in phosphorus level between analyzed samples.[31] Comparing the human samples taken from brains affected by tumors with different degrees of malignancy, Wandzilak et al. observed that the samples representing the highest malignant group (which included GBM samples) were characterized by decreased concentration of phosphorus.[24] Our results seem to agree with the last mentioned report, as we noticed a significant decrease of phosphorus level in the left hemisphere taken from animals subjected to the implantation of the most invasive GBM cell line. What is more, for the rats representing U group, a significantly diminished level of the element within the implanted hemisphere was noticed compared to the intact one. Following the papers of Selverstone and Moulton[28] as well as Hubesch et al.,[29] the lower level of phosphorus determined for U group may suggest disorders in metabolism processes or decreased content of the important phosphorus compounds, like phospholipids, in tumor tissue. Such a conclusion is in agreement with our new unpublished data

https://dx.doi.org/10.1021/acschemneuro.0c00648
ACS Chem. Neurosci. XXXX, XXX, XXX−XXX

showing significantly diminished content of lipids within tumor mass compared to the neighboring tissues.

Our study did not reveal any significant anomalies in calcium and sulfur levels within left hemispheres taken from animals subjected to implantation of various GBM cells. However, rats from group U presented increased calcium concentration within the right hemisphere compared to normal animals. What is more, in animals subjected to implantation of U87MG cells, the level of Ca in the right hemisphere exceeded that measured for the left one. Andrasi et al. did not observe the changes in calcium and sulfur levels between corresponding regions of brains with and without tumor.[31] However, in the literature one can find also reports on decreased concentrations of these elements in brain tumor tissue with a high grade of malignancy.[24] Calcium ions play a key role in cell signaling processes. It has been observed that calcium channels are characterized by altered expression in tumor tissues, including brain tumors with a high grade of malignancy.[32] Due to a proven link between expression of calcium channels and homeostasis, angiogenesis, and growth of glioma tumors, they are considered as a potential target of cancer therapy.[33] Xiao et al. observed that sulfur compounds (Na_2S) might have potential to increase the sensitivity of GBM cells (U87MG and T98G) to radiation therapy.[34] Sulfur and selenium prevent DNA damage caused by copper and iron, which are the two metals involved in the production of highly reactive hydroxyl radicals. Compounds of sulfur and selenium have the ability to bind copper and iron and thus prevent the risk of DNA impairment.[35] Wróbel et al. analyzed the content of sulfur compounds in tumor and normal brain tissue. They observed that compared to the other examined brain regions, malignant tumor tissue was characterized by an increased level of sulfane sulfur.[36]

Potassium is an essential mineral participating in regulation of the water and acid balance in cells. It plays a key role in electrical impulse transmission, due to active transport of its ions across he cell membrane.[37] Potassium is also involved in processes of cell death. It was shown that potassium ions suppress activity of a nuclease enzyme participating in apoptosis mechanisms, with complete inhibition at physiological potassium level found in living cells (150 mM).[38] Eil et al. observed that cells under necrotic conditions release to the extracellular environment potassium ions, which suppress the immune response of T-cells in tumors.[15] Results of various investigations indicate that potassium ion channels are abnormally expressed in glioma cells. Huang et al. found that ATP-sensitive potassium channels, overexpressed in glioma cells, regulate their proliferation.[39] Suppression of some classes of potassium channels in U87MG cells resulted in significant improvement of therapy with TMZ, the main chemotherapy drug used to treat brain tumors including GBM.[40] Ru et al. observed that blocking the voltage-gated potassium channels could induce apoptosis and inhibit proliferation of U87MG cells.[41] Szczerbowska-Boruchowska et al. and Wandzilak et al. compared concentrations of potassium within brain tumor samples of different stage of malignancy, but they did not find any significant differences between examined tumors. Nonetheless, they both determined potassium as the element of high importance for classification of brain tumors with respect to their malignancy.[22,24] Also Andrasi et al. did not observed differences in potassium levels between regions of brain with and without tumor.[31] Results of our experiment revealed a decrease of potassium level in both left and right brain hemispheres taken from rats subjected to implantation of U87MG cells. In animals from P group, such an effect was found only for the intact hemisphere, while animals representing T group presented differences between the element accumulation within left and right hemispheres but the measured potassium concentrations in both hemispheres did not differ from the normal levels. Overexpression of potassium channels in glioma cells may increase the flow of the ions of the element into the extracellular environment. This, in turn, may facilitate the removal of the element from tumor volume and could explain diminished levels of potassium observed in implanted hemispheres of the brain.

Iron is a fundamental element in the human body, and it is crucial for the proper course of many biological processes ensuring growth and development of body cells. It is involved in oxygen transport, as a part of hemoglobin, and participates in nucleic acid synthesis.[42] On the other hand, it may lead to DNA damage through reactive oxygen species formation. Therefore, regulation of iron levels is crucial for proper cell functioning.[43] Both iron overload and its deficiency may play important roles in the mechanisms of carcinogenesis.[44−46] Schonberg et al.[47] observed that stem-like GBM cells are characterized by increased iron uptake compared to the remaining GBM and normal brain cells, and this mechanism may affect tumor proliferation. They also found that it was connected with increased expression and synthesis of iron storage protein ferritin and higher level of ferritin was positively correlated with malignancy grade of the tumor.[47] As iron is involved in molecular processes of cell proliferation, including tumor cells, methods of its inhibition are tested as a promising strategy for GBM therapy.[48] Andrasi et al. did not find differences in iron concentration between regions of brain with and without tumor.[31] In turn, Wandzilak et al. observed a significant decrease of its content in samples of brain with high grade tumors compared to control tissues originating from non-brain-tumor patients.[24] In our study, the animals subjected to the implantation of U87MG cells presented increased levels of iron in the right hemisphere compared to the normal rats as well as in relation to the corresponding left hemisphere. For the remaining experimental groups (T and P), we observed elevated iron levels compared to controls for both brain hemispheres, and no differences in the element accumulation was observed between implanted and intact hemispheres. Increased levels of iron found in rat brains may be connected with higher blood supply, which in the case of the implanted hemisphere could be a result of intensified tumorigenesis processes. It must be remembered that glioma tumors very often contain hemorrhaging regions, which also can lead to iron accumulation. The greater iron content in the intact hemisphere may also indicate its higher neuronal activity, caused by taking over some functions of the left hemisphere impaired as a result of tumor increase.

Copper constitutes a part of proteins involved in cell signaling and oxygen transport. Due to its high oxidative potential, it plays a crucial role in redox reactions. Its redox activity is important for enzyme action, but through reactive-oxygen species (ROS) production, it may be toxic for many important biomolecules. Disturbances of copper homeostasis in cells can lead to different pathologies.[49] Research reports show that copper levels are elevated in many types of tumors, compared to controls, and targeting copper through chelation may be a potential direction for cancer therapy.[50] Higher copper levels promote growth of cancer cells, while copper

https://dx.doi.org/10.1021/acschemneuro.0c00648
ACS Chem. Neurosci. XXXX, XXX, XXX−XXX

chelation results in antiproliferative effect. What is more, different copper concentrations may modulate cell metabolic pathways by influencing oxidative phosphorylation.[51] Li et al. showed that subcytotoxic copper levels induce senescence of U87 GBM cells, and this could be a potential direction for new anticancer therapy.[52] Copper, due to the regulation of factors affecting growth of blood vessels, is an element involved in angiogenesis. Promoting angiogenesis, it may in turn influence the process of cancer development.[53] Brem et al. observed that a low copper diet combined with penicillamine, a copper chelating agent, resulted in the reduction of proliferation and vascularity of glioma in the rabbit model of tumor.[54] Jazayeri et al. found that the decrease of copper content in the diet of GBM patients led to the reduction of factors affecting angiogenesis processes.[55] In turn, in the work of Pérès et al. increased accumulation of copper-labeled compounds in hypoxic areas of glioma was shown, and the authors suggested that this may be connected with redox processes and overexpression of cellular transporters of copper under hypoxic conditions.[56] Yoshida et al. showed that higher copper concentrations are observed in malignant gliomas and metastatic brain tumor tissues compared to benign tumor and normal brain tissues. However, they did not specify if the analyzed malignant glioma corresponded to glioblastoma multiforme.[57] Contrary to this, Szczerbowska-Boruchowska et al. and Wandzilak et al. did not indicate any correlations between Cu concentration and the degree of malignancy of brain tumor. However, they mentioned the element as significant for the tumor sample classification.[22,24] Also Stojsavljević et al. did not observe any differences in Cu levels between brain malignant tumor samples, most of which were classified as GBM, and normal cerebral tissue.[58] Denhardt et al. studied distributions of elements in different regions of GBM specimens. They observed that concentration of Cu was higher in brain tissue surrounding the tumor (peritumoral zone) than in the solid tumor. This indicates a possible heterogeneous distribution of copper in tissue affected by a tumor.[21]

Taking all this into account, the assessment of changes of Cu level in brain tumor tissue still remains unclear. The results we observed for lower invasiveness glioma cells (T and P groups) seem to be in agreement with those of Stojsavljević et al. who did not detect any differences between malignant and normal cerebral tissues.[58] However, in case of the implantation of the most invasive U87MG cells, content of Cu within both hemispheres was significantly diminished compared to that in normal animals which may suggest some correlation between anomalies observed in the accumulation of the element and the degree of tumor malignancy. Further elemental study is necessary in this aspect and should involve topographic elemental analysis of tissues affected with glioma since copper distribution within tumor can be heterogeneous as was suggested in the study of Denhardt et al.[21]

Another micronutrient essential for proper functioning of living organisms is zinc. It is involved in activation and stabilization of a wide range of enzymes. Mainly in the ion form, zinc participates in synthesis and repair of DNA, apoptosis regulation, immune response and proliferation, differentiation, and signaling of cells. Due to its antioxidative property, zinc protects DNA and other biomolecules against damage caused by oxidative stress.[59] Many reports prove that zinc is involved in the process of cancer cell death; however, this is a cell-specific effect. In some types of cancers, zinc has antiapoptotic properties, while for others it may induce cell death.[60] Mehrian-Shai et al. found that p53 protein, which has cancer suppressing properties, is typically inactive in the U87MG cell line but can be activated through the addition of zinc.[61] Toren et al. discovered that the combination of zinc with TMZ enhances toxic effects of the drug on GBM cells *in vitro*, which manifests in reduction of cell proliferation and induction of apoptosis. Addition of Zn to TMZ resulted also in more effective inhibition of tumor growth *in vivo* than TMZ alone.[62] Takeda et al. observed increased accumulation of zinc in brain tumor developing in rats subjected to C6 glioma cells implantation. The uptake of zinc in the tumor mass was clearly higher than in other regions of the brain.[63,64] Szczerbowska-Boruchowska et al. and Wandzilak et al. included zinc in a group of elements with high significance for brain tumor classification with respect to their malignancy grade.[22,24] What is more, Wandzilak et al. observed a higher concentration of Zn in tumor tissue compared to the control brain tissue.[24] Andrasi et al. observed decreases in Zn concentration in various brain regions of humans diagnosed with GBM compared to the corresponding regions of the normal brain.[31] According to Cilliers et al., this may be connected with intensified uptake of Zn by tumor cells from surrounding brain tissue.[65] Stojsavljević et al. observed increased levels of zinc in samples of human brain tumor compared to a control tissue with a simultaneous decrease of its concentration in liquid samples, like serum and cerebrospinal fluid.[58] The results of both Andrasi et al. and Stojsavljević et al. seem to suggest that increased accumulation of zinc within the tumor mass may be connected to uptake of the element from the tumor neighborhood.[31,58] In turn, Denhardt et al. found that a higher concentration of Zn is specific rather for the tissue surrounding the tumor than for the tumor mass itself. They suggested that such localization of zinc may be evidence for the importance of this element for the tumor infiltration.[21] In our study, abnormalities of Zn accumulation were observed in the left brain hemisphere of rats implanted with cells taken from a patient suffering from GBM. The animals presented higher content of the element compared to the normal rats. Additionally, for P group, the level of Zn in the implanted hemisphere was higher than that in the intact one. In turn, the opposite relation was found for the U group.

Selenium is an essential microelement included in various chemical compounds responsible for proper functioning of the body, such as antioxidative processes or immune response.[66] It has high potential to prevent tumorigenesis including that developed in the brain.[67] Zhu et al. observed antiproliferative effect of selenium on human and rat glioblastoma cells.[68] In another paper, the authors suggest that apoptotic death of tumor cells, initiated by selenium, may be connected with formation of oxygen free radicals.[69] Rooprai et al. stated that selenium not only influences malignant human tumor cell death without affecting normal brain cells but can also reduce tumor invasiveness.[70] Harmanci et al. observed different effects of selenium supplementation on human GBM cells, depending on the dose of selenium. Low doses of Se induced tumor cell proliferation, while high doses promoted death of GBM cells.[71] Wang et al. showed that selenocysteine, an amino acid containing selenium, can inhibit the synthesis phase of the cell cycle of human glioma cells, blocking the process of DNA replication and resulting in decrease of cell proliferation.[72] Research on potential use of selenium in the treatment of malignant brain tumors was also conducted.[73−75] Zhang et al. observed a higher level of selenium in brain tumor regions

https://dx.doi.org/10.1021/acschemneuro.0c00648
ACS Chem. Neurosci. XXXX, XXX, XXX−XXX

compared to contralateral brain tissue of rats previously implanted with C6 glioma cells.[76] Also Stojsavljević et al. observed higher concentration of selenium in brain tumor tissue compared to control one. What is more, a decreased level of this element occurred in serum taken from patients with diagnosed malignant brain tumor. Authors suggested that tumor cells may be characterized by an increased demand for selenium.[58] Results of our experiment showed abnormalities in brain selenium accumulation for U and P groups. For animals from U group, the content of this element in the implanted hemisphere was elevated compared to the corresponding hemisphere taken from normal animals. The level of Se was also higher in the left than in the right hemisphere. The opposite relations were noticed for rats subjected to the patient-derived cell implantation. The results obtained for animals subjected to the implantation of the U87MG cells are in agreement with those obtained by Zhang et al. and Stojsavljevic et al. Such a conclusion, however, cannot be made in the case of tumor appearing as a result of patient-derived cell implantation.

Conclusions. GBM with its high aggressiveness and morbidity rate is the subject of many studies undertaken both for better understanding of its nature and for testing new therapeutic strategies. Animal models of glioma, applied in preclinical trials, are an invaluable tool in this kind of investigation. Due to the importance of different elements for tumor genesis and progression, confirmed by many studies, it seems necessary to perform elemental analysis of changes introduced through the developing tumor within the brain in various animal models of the disease. The largest number of elemental anomalies, both within implanted and intact hemispheres, was observed in rats subjected to implantation of U87MG cells. In turn, the lowest one was observed in animals after implantation of T98G cells. As the first cell line was characterized by the highest aggressiveness and the second by the lowest aggressiveness, we may try to connect the degree of elemental abnormalities with the extent of glioma invasiveness. The most of the observed elemental anomalies are specific for particular model of GBM; however the common hallmark of all experimental models of the disease is the elevated Fe level in the intact hemisphere. Within the implanted hemisphere, the level of this element was also higher for animals subjected to implantation of T98G and patient-derived cells. In turn, Se presented model specific accumulation there. It occurred at the normal level after T98G cells implantation, at a decreased level in animals subjected to the implantation of patient-derived cells, and at an increased level in the case of the most invasive cell line, U87MG.

The bulk elemental analysis performed by us using the TXRF method gave information about changes in elemental composition occurring in the whole examined brain hemispheres. Based on the obtained results, the elements that may play a role in GBM pathogenesis were identified. However, as the distribution of elements in the tissues affected by the tumor may be heterogeneous, further studies are necessary. Especially helpful would be here topographic elemental analysis of the tumor mass and its surrounding areas providing more specific information on the contribution of particular elements in the pathogenesis and development of GBM.

■ MATERIALS AND METHODS

Cell Lines. Three glioblastoma cell lines were used for this study: T98G, U87MG, and patient-derived tumor cells. T98G and U87MG cell lines were purchased from ATCC company and cultured according to the manufacturer protocol. The first cell line is characterized as GBM type, while the second as "likely" glioblastoma. Both T98G and U87MG are human brain-derived cells with fibroblastoid or epithelial morphology, respectively. U87MG cell line is described by the manufacturer as tumorigenic, while T98G is described as nontumorigenic. Patient-derived cells originated from primary tumor of a patient diagnosed with GBM. They were isolated from a 23 year old woman in the Clinic of Neurosurgery and Neurotraumatology of University Hospital in Bydgoszcz according to the consent of the Bioethics Commission for the use of cellular material collected from patients in neurooncological operations (Decision no. 535/2017 from 13th June 2017, issued by the Bioethical Commission at University of Nicolaus Copernicus in Toruń). Written informed consent was obtained from the patient and all the procedures were in agreement with relevant guidelines and regulations.

Suspensions of glioma cells for implantation were prepared in the Department of Cell Biology of the Faculty of Biophysics, Biochemistry, and Biotechnology of Jagiellonian University (JU). Dulbecco's modified Eagle medium was used for preparation of the suspensions. The concentration of administered suspension was equal 5×10^4 cells/μL for T98G cell line and patient-derived cells. For U87MG cell line, the concentration of cells was changed to 5×10^3 cells/μL as our previous observations showing high mortality of Wistar rats after implantation at higher concentrations.

Experimental Animals. Animal husbandry and all animal-use experiments, previously approved by the second Local Institutional Animal Care and Use Committee (agreement no. 119/2016), were performed in accordance with the international standards in the Department of Neuroanatomy of the Institute of Zoology and Biomedical Research JU. The subjects of our study were male Wistar albino rats. The animals had free access to water and standard rodent food (Labofeed, Morawski). At 9 weeks of age, the rats were divided into four groups: N, T, U, and P. Each group consisted of 6 individuals. The animals from groups T and U were subjected to the implantation into the brain of the T98G and U87MG cell lines, respectively. Animals included in P group obtained primary tumor cells taken directly from a patient diagnosed with GBM, while the N group consisted of naive controls.

Implantations. The main part of the animal experiment was the transcranial implantation of GBM cells into the rat brain. The day before and on the day of surgery, the animals were weighed and given cyclosporine intravenously (Sandimmun 50 mg/mL, Novartis Poland) at a dose of 10 mg/kg of body mass for immunosuppressive purposes. For the implantation, the animals were initially anesthetized in a desiccator filled with isoflurane (Aerrane, Baxter Poland). The same agent was administered by inhalation throughout the whole surgery, and its dose was monitored and adjusted to maintain general anesthesia. To precisely determine the place of implantation (Figure 6), the animals were immobilized in a stereotactic apparatus. The injection site was determined stereotaxically in the left hemisphere (coordinates antero-posterior, −0.30 mm; medio-lateral: 3.0 mm; dorso-ventral: 5.0 mm, Paxinos and Watson 1986). The first step was to drill a hole in the skull of the rat, where the needle (27 gauge needle on a Hamilton syringe) with the cell suspension was then placed. One minute after placing the needle, cell suspension in a volume of 5 μL was introduced to the brain, and 3 min later the needle was slowly removed. Afterward, the wound was sutured with a stapler and disinfected. Animals woke up from anesthesia a few minutes after the end of the implantation procedure.

After surgery, the animals were intravenously administered cyclosporine (Novartis Poland) at a daily dose of 5 mg/kg of body mass. Additionally, for the first 7 days after glioma implantation, the rats were given an antibiotic (Sul-Tridin 24%, ScanVet, Poland). The condition of animals was checked daily with particular attention to neurological deficits. The duration of the experiment, counted from the day of implantation, was 21 days for groups N, T, and P. In the case of the U group, due to very poor animal health revealed in deterioration of motor functions and body weight loss, and the

https://dx.doi.org/10.1021/acschemneuro.0c00648
ACS Chem. Neurosci. XXXX, XXX, XXX−XXX

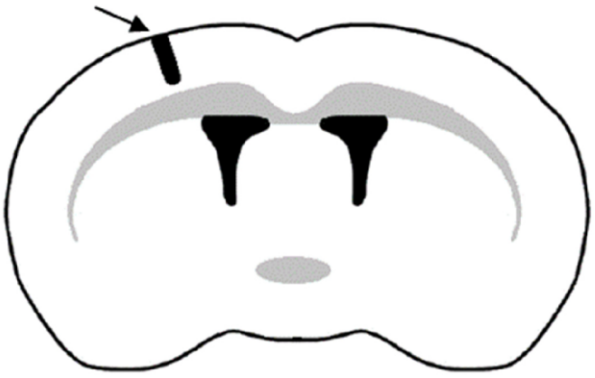

Figure 6. Location of the implantation site in the left cerebral hemisphere.

possibility of their premature death, the experiment was terminated 15 days after the surgery. Rats were sacrificed by intravenous administration of Euthasol-Vet (Euthasol vet. 400 mg/mL, Le Vet B. V.) at doses appropriate to their weights. After perfusion with physiological saline, the brains were rapidly removed from the skulls and divided in two hemispheres, which were separately placed in the storage bags, immediately frozen in liquid nitrogen and stored in the freezer until further preparations.

Sample Preparation. TXRF method was applied to determine the concentrations of P, S, K, Ca, Fe, Cu, Zn, and Se in both cerebral hemispheres. The elemental analysis using the TXRF spectrometry requires removal of the sample organic matrix and conversion of the sample from a solid (tissue) to a liquid form. For this purpose, microwave-assisted acid digestion was performed with the use of SpeedWave 4 digestion system (Berghof). Each hemisphere was placed in an individual Teflon vessel (DAP100) to which 5 mL of high purity nitric acid 65% (Suprapur, Merck) was added. The brain samples were digested by using program "Tissue, blood", for which values of digestion parameters were as follows: temperature 50−190 °C, pressure 0−30 bar, and power 0−870 W. One digestion cycle lasted about 45 min.

Apparatus and Measurement Conditions. Quantitative analysis using the TXRF method is based on the use of the internal standard and 1000 ppm gallium solution (Gallium ICP standard in HNO_3 2−3% 1000 mg/L Ga Certipur, Merck was used for this purpose). Typically, 100 μL of the internal standard was added to the entire sample volume (approximately 5 mL) and mixed thoroughly. Six microliters of this solution was taken and spotted on a Super Frost (Menzel) glass slide, which was then dried on a heating plate. Three slides were made for each sample. The Rigaku Nanohunter II TXRF spectrometer was used for measurements. The apparatus allows for high-sensitivity elemental analysis of liquids at ultratrace (ppb) levels of elements. It is equipped with a 600 W X-ray tube with molybdenum anode, excitation energy of which is 17.44 keV and silicon drift detector (SDD). The slides were placed in the 16-position cassette of the spectrometer, which allowed their automatic, sequential measurements. The acquisition time of a single slide was 1000 s. The voltage of the tube was equal to 50 kV, while its current was 12 mA. The measurements were performed at the glancing angle of 0.04°.

Quantitative Elemental Analysis. The concentration of each element i in the analyzed sample was determined based on relationship 1:

$$C_i = \frac{C_{IS} N_i}{N_{IS} S_i^r} \quad (1)$$

where C_i is the concentration of the element i in a sample [ppm], C_{IS} is the concentration of the added internal standard in a sample [ppm], N_i is the number of counts for the element i in the spectrum of the sample, N_{IS} is the number of counts for added internal standard in the spectrum of the sample, and S_i^r is the relative sensitivity of element i.

The relative sensitivities for analyzed elements were determined in the calibration process. Two standard solutions were used for this purpose: MERCK ICP multielement standard solution IV (23 elements diluted in nitric acid, 1000 mg/L) and phosphorus single-component standard (10000 μg/mL P in 0.05% HNO_3 from $NH_4H_2PO_4$) from High Purity Standards. The relative sensitivity coefficients of the elements, defined as the ratio of the sensitivity of a given element to the sensitivity of the internal standard, were determined based on formula 2:

$$S_i^r = \frac{S_i}{S_{IS}} = \frac{\frac{N_i^s}{C_i^s}}{\frac{N_{IS}^s}{C_{IS}^s}} = \frac{C_{IS}^s N_i^s}{N_{IS}^s C_i^s} \quad (2)$$

where S_i^r is the relative sensitivity of the element i, S_i is the sensitivity of the element i, S_{IS} is the sensitivity of the internal standard, C_i^s is the known concentration of element i in the standard solution [ppm], C_{IS}^s is the concentration of the internal standard in the standard solution [ppm], N_i^s is the number of counts of element i in the spectrum of the standard solution, and N_{IS}^s is the number of counts for the internal standard in the spectrum of the standard solution.

Based on a calculated relative sensitivity, a calibration curve was determined and, together with its equation, presented in Figure 7.

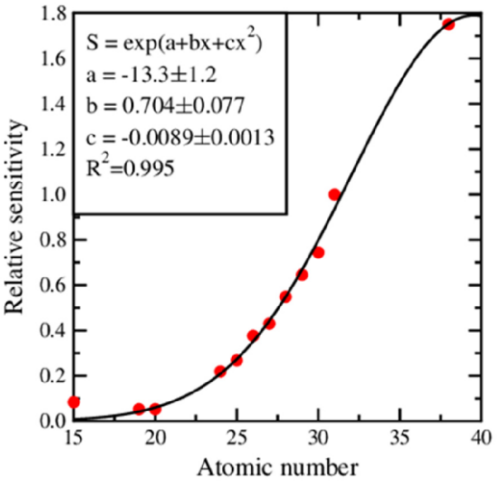

Figure 7. Relative sensitivity curve obtained from the measurements of Merck ICP multielement standard solution IV and phosphorus single-component standard from High Purity Standards.

Evaluation of limit of detection of elements in analyzed samples and precision of measurements was also performed. The limit of detection was calculated based on results obtained for all examined brain samples. The precision of measurements was calculated based on results for samples of normal brain. Depending on the time between measurements, intraday and interday precision were determined. Details concerning calculation of validation parameters and formulas used for this purpose are provided in Supporting Information.

■ ASSOCIATED CONTENT

Supporting Information

The Supporting Information is available free of charge at https://pubs.acs.org/doi/10.1021/acschemneuro.0c00648.

Methods to calculate limits of detection and precision (PDF)

https://dx.doi.org/10.1021/acschemneuro.0c00648
ACS Chem. Neurosci. XXXX, XXX, XXX−XXX

AUTHOR INFORMATION

Corresponding Author

Joanna Chwiej − *AGH University of Science and Technology, Faculty of Physics and Applied Computer Science, Krakow 30-059, Poland;* orcid.org/0000-0002-3792-7876; Email: joanna.chwiej@fis.agh.edu.pl

Authors

Karolina Planeta − *AGH University of Science and Technology, Faculty of Physics and Applied Computer Science, Krakow 30-059, Poland*

Zuzanna Setkowicz − *Jagiellonian University, Institute of Zoology and Biomedical Research, Krakow 31-007, Poland*

Natalia Janik-Olchawa − *AGH University of Science and Technology, Faculty of Physics and Applied Computer Science, Krakow 30-059, Poland*

Katarzyna Matusiak − *AGH University of Science and Technology, Faculty of Physics and Applied Computer Science, Krakow 30-059, Poland;* orcid.org/0000-0003-2211-8432

Damian Ryszawy − *Jagiellonian University, Faculty of Biochemistry, Biophysics, and Biotechnology, Krakow 31-007, Poland*

Agnieszka Drozdz − *AGH University of Science and Technology, Faculty of Physics and Applied Computer Science, Krakow 30-059, Poland*

Krzysztof Janeczko − *Jagiellonian University, Institute of Zoology and Biomedical Research, Krakow 31-007, Poland*

Beata Ostachowicz − *AGH University of Science and Technology, Faculty of Physics and Applied Computer Science, Krakow 30-059, Poland*

Complete contact information is available at: https://pubs.acs.org/10.1021/acschemneuro.0c00648

Author Contributions

#K.P. and Z.S. contributed equally. K.P. contributed to conceptualization, methodology, resources, investigation, validation, writing the original draft, and answers to the reviewers' remarks; Z.S. contributed to conceptualization, methodology, resources, supervision, and reviewing the manuscript; N.J.-O. contributed to methodology and investigation; K.M. contributed to methodology and investigation; D.R. contributed to methodology, resources, and reviewing the manuscript; A.D. contributed to methodology and investigation; K.J. contributed to reviewing manuscript; B.O. contributed to methodology and resources; J.C., as corresponding author, contributed to conceptualization, methodology, resources, validation, supervision, writing the original draft, and answers to the reviewers' remarks.

Notes

The authors declare no competing financial interest.

ACKNOWLEDGMENTS

This work was partially financed by the Polish Ministry of Science and Higher Education and by the Polish National Science Centre Grant No. UMO-2015/19/D/NZ3/00273. Karolina Planeta and Natalia Janik-Olchawa have been partially supported by the EU Project POWR.03.02.00-00-I004/16. Special thanks to Ph.D. Eng. Przemyslaw Wachniew from Faculty of Physics and Applied Computer Science, University of Science and Technology, in Krakow for providing access to chemical laboratory and sharing the mineralizer SpeedWave4.

REFERENCES

(1) Hanif, F., Muzaffar, K., Perveen, K., Malhi, S. M., and Simjee, S. U. (2017) Glioblastoma Multiforme: A Review of its Epidemiology and Pathogenesis through Clinical Presentation and Treatment. *Asian Pac. J. Cancer Prev. 18* (1), 3−9.

(2) Czapski, B., Baluszek, S., Herold-Mende, C., and Kaminska, B. (2018) Clinical and immunological correlates of long term survival in glioblastoma. *Wspolczesna Onkol. 22* (1A), 81−85.

(3) Holland, E. C. (2000) Glioblastoma multiforme: The terminator. *Proc. Natl. Acad. Sci. U. S. A. 97* (12), 6242−6244.

(4) Urbańska, K., Sokołowska, J., Szmidt, M., and Sysa, P. (2014) Glioblastoma multiforme - an overview. *Wspolczesna Onkol. 18* (5), 307−312.

(5) Henke, G., Meier, V., Lindner, L. H., Eibl, H., Bamberg, M., Belka, C., Budach, W., and Jendrossek, V. (2012) Effects of ionizing radiation in combination with Erufosine on T98G glioblastoma xenograft tumours: a study in NMRI nu/nu mice. *Radiat. Oncol. 7*, 172.

(6) Teicher, B. A., Menon, K., Álvarez, E., Galbreath, E., Shih, C., and Faul, M. M. (2001) Antiangiogenic and antitumor effects of a protein kinase Cbeta inhibitor in human T98G glioblastoma multiforme xenografts. *Clin. Cancer Res. 7* (3), 634−40.

(7) Uchida, H., Marzulli, M., Nakano, K., Goins, W. F., Chan, J., Hong, C. S., Mazzacurati, L., Yoo, J. Y., Haseley, A., Nakashima, H., Baek, H., Kwon, H., Kumagai, L., Kuroki, M., Kaur, B., Chiocca, E. A., Grandi, P., Cohen, J. B., and Glorioso, J. C. (2013) Effective Treatment of an Orthotopic Xenograft Model of Human Glioblastoma Using an EGFR-retargeted Oncolytic Herpes Simplex Virus. *Mol. Ther. 21* (3), 561−569.

(8) Lenting, K., Verhaak, R., Ter Laan, M., Wesseling, P., and Leenders, W. (2017) Glioma: experimental models and reality. *Acta Neuropathol. 133* (2), 263−282.

(9) Flávio Key, F. K., Alves, M. J. F., Rocha, M. C., da Silva, R., Oba-Shinjo, S. M., and Marie, S. K. N. (2010) Xenograft Transplantation of Human Malignant Astrocytoma Cells Into Immunodeficient Rats: An Experimental Model of Glioblastoma. *Clinics 65* (3), 305−309.

(10) Baklaushev, V. P., Kavsan, V. M., Balynska, O. V., Yusubalieva, G. M., Abakumov, M. A., and Chekhonin, V. P. (2012) New Experimental Model of Brain Tumors in Brains of Adult Immunocompetent Rats. *Br. J. Med. Med. Res. 2* (2), 206−215.

(11) Biasibetti, E., Valazza, A., Capucchio, M. T., Annovazzi, L., Battaglia, L., Chirio, D., Gallarate, M., Mellai, M., Muntoni, E., Peira, E., Riganti, C., Schiffer, D., Panciani, P., and Lanotte, M. (2017) Comparison of Allogeneic and Syngeneic Rat Glioma Models by Using MRI and Histopathologic Evaluation. *Comp. Med. 67* (2), 147−156.

(12) Strojnik, T., Kavalar, R., and Lah, T. T. (2006) Experimental Model and Immunohistochemical Analyses of U87 Human Glioblastoma Cell Xenografts in Immunosuppressed Rat Brains. *Anticancer Res. 26* (4B), 2887−2900.

(13) Bobko, A. A., Eubank, T., Driesschaert, B., Dhimitruka, I., Evans, J., Mohammad, R., Tchekneva, E. E., Dikov, M. M., and Khramtsov, V. (2017) Interstitial Inorganic Phosphate as a Tumor Microenvironment Marker for Tumor Progression. *Sci. Rep. 7*, 41233.

(14) Duan, F., Li, Y., Chen, L., Zhou, X., Chen, J., Chen, H., and Li, R. (2015) Sulfur inhibits the growth of androgen-independent prostate cancer in vivo. *Oncol. Lett. 9* (1), 437−441.

(15) Eil, R., Vodnala, S. K., Clever, D., Klebanoff, C. A., Sukumar, M., Pan, J. H., Palmer, D. C., Gros, A., Yamamoto, T. N., Patel, S. J., Guittard, G. C., Yu, Z., Carbonaro, V., Okkenhaug, K., Schrump, D. S., Linehan, W. M., Roychoudhuri, R., and Restifo, N. P. (2016) Ionic immune suppression within the tumour microenvironment limits T cell effector function. *Nature 537* (7621), 539−543.

(16) Callejón-Leblic, B., Arias-Borrego, A., Pereira-Vega, A., Gómez-Ariza, J. L., and García-Barrera, T. (2019) The Metallome of Lung Cancer and its Potential Use as Biomarker. *Int. J. Mol. Sci. 20* (3), 778.

(17) Jouybari, L., Saei Ghare Naz, M., Sanagoo, A., Kiani, F., Sayehmiri, F., Sayehmiri, K., and Hasanpour Dehkordi, A. (2018)

Toxic elements as biomarkers for breast cancer: a meta-analysis study. *Cancer Manage. Res. 10*, 69−79.
(18) Silva, M. P., Soave, D. F., Ribeiro-Silva, A., and Poletti, M. E. (2012) Trace elements as tumor biomarkers and prognostic factors in breast cancer: a study through energy dispersive x-ray fluorescence. *BMC Res. Notes 5*, 194.
(19) Zaichick, V., and Zaichick, S. V. (2018) Trace Elements of Expressed Prostatic Secretions as a Source for Biomarkers of Prostate Cancer. *J. Clin. Res. Oncol. 1* (1), 1−7.
(20) Zoriy, M. V., Dehnhardt, M., Reifenberger, G., Zilles, K., and Becker, J. S. (2006) Imaging of Cu, Zn, Pb and U in human brain tumor resections by laser ablation inductively coupled plasma mass spectrometry. *Int. J. Mass Spectrom. 257*, 27−33.
(21) Dehnhardt, M., Zoriy, M. V., Khan, Z., Reifenberger, G., Ekström, T., Sabine Becker, J., Zilles, K., and Bauer, A. (2008) Element distribution is altered in a zone surrounding human glioblastoma multiforme. *J. Trace Elem. Med. Biol. 22* (1), 17−23.
(22) Szczerbowska-Boruchowska, M., Lankosz, M., and Adamek, D. (2011) First step toward the 'fingerprinting' of brain tumors based on synchrotron radiation X-ray fluorescence and multiple discriminant analysis. *JBIC, J. Biol. Inorg. Chem. 16* (8), 1217−1226.
(23) Lankosz, M. W., Grzelak, M., Ostachowicz, B., Wandzilak, A., Szczerbowska-Boruchowska, M., Wrobel, P., Radwanska, E., and Adamek, D. (2014) Application of the total reflection X-ray fluorescence method to the elemental analysis of brain tumors of different types and grades of malignancy. *Spectrochim. Acta, Part B 101*, 98−105.
(24) Wandzilak, A., Czyzycki, M., Radwanska, E., Adamek, D., Geraki, K., and Lankosz, M. (2015) X-ray fluorescence study of the concentration of selected trace and minor elements in human brain tumours. *Spectrochim. Acta, Part B 114*, 52−57.
(25) Brown, R. B., and Razzaque, M. S. (2018) Endocrine Regulation of Phosphate Homeostasis, *Textbook of Nephro-Endocrinology*, pp 539−548, Elsevier, DOI: 10.1016/B978-0-12-803247-3.00032-5.
(26) Ardito, F., Giuliani, M., Perrone, D., Troiano, G., and Muzio, L. L. (2017) The crucial role of protein phosphorylation in cell signaling and its use as targeted therapy (Review). *Int. J. Mol. Med. 40* (2), 271−280.
(27) Selverstone, B., and Solomon, A. K. (1948) Radioactive isotopes in the study of intracranial tumors. Preliminary report of methods and results. *Trans. Am. Neurol. Assoc. 73*, 115−119.
(28) Selverstone, B., and Moulton, M. J. (1957) The phosphorus metabolism of gliomas: a study with radioactive isotopes. *Brain 80* (3), 362−375.
(29) Hubesch, B., Sappey-Marinier, D., Roth, K., Meyerhoff, D. J., Matson, G. B., and Weiner, M. W. (1990) P-31 MR spectroscopy of normal human brain and brain tumors. *Radiology 174* (2), 401−409.
(30) Srivastava, N. K., Pradhan, S., Gowda, G. A. N., and Kumar, R. (2009) In vitro, high-resolution 1H and 31P NMR based analysis of the lipid components in the tissue, serum, and CSF of the patients with primary brain tumors: one possible diagnostic view. *NMR Biomed. 23*, 113−122.
(31) Andrási, E., Suhajda, M., Sáray, I., Bezúr, L., Ernyei, L., and Réffy, A. (1993) Concentration of elements in human brain: glioblastoma multiforme. *Sci. Total Environ. 139−140*, 399−402.
(32) Morrone, F. B., Gehring, M. P., and Nicoletti, N. F. (2016) Calcium Channels and Associated Receptors in Malignant Brain Tumor Therapy. *Mol. Pharmacol. 90* (3), 403−409.
(33) Li, S., and Ding, X. (2017) TRPC Channels and Glioma. *Adv. Exp. Med. Biol. 976*, 157−165.
(34) Xiao, A. Y., Maynard, M. R., Piett, C. G., Nagel, Z. D., Alexander, J. S., Kevil, C. G., Berridge, M. V., Pattillo, C. B., Rosen, L. R., Miriyala, S., and Harrison, L. (2019) Sodium sulfide selectively induces oxidative stress, DNA damage, and mitochondrial dysfunction and radiosensitizes glioblastoma (GBM) cells. *Redox Biol. 26*, 101220.
(35) Zimmerman, M. T., Bayse, C. A., Ramoutar, R. R., and Brumaghim, J. L. (2015) Sulfur and selenium antioxidants: Challenging radical scavenging mechanisms and developing structure-activity relationships based on metal binding. *J. Inorg. Biochem. 145*, 30−40.
(36) Wróbel, M., Czubak, J., Bronowicka-Adamska, P., Jurkowska, H., Adamek, D., and Papla, B. (2014) Is Development of High-Grade Gliomas Sulfur-Dependent? *Molecules 19* (12), 21350−21362.
(37) Kowey, P. R. (2002) The Role of Potassium, *Women's Health and Menopause*, pp 151−157, Springer, Boston, MA, DOI: 10.1007/978-1-4615-1061-1_18.
(38) Hughes, F. M., Jr., and Cidlowski, J. A. (1999) Potassium is a critical regulator of apoptotic enzymes in vitro and in vivo. *Adv. Enzyme Regul. 39*, 157−171.
(39) Huang, L., Li, B., Li, W., Guo, H., and Zou, F. (2009) ATP-sensitive potassium channels control glioma cells proliferation by regulating ERK activity. *Carcinogenesis 30* (5), 737−744.
(40) Sales, T. T., Resende, F. F. B., Chaves, N. L., Titze-De-Almeida, S. S., Báo, S. N., Brettas, M. L., and Titze-De-Almeida, R. (2016) Suppression of the Eag1 potassium channel sensitizes glioblastoma cells to injury caused by temozolomide. *Oncol. Lett. 12* (4), 2581−2589.
(41) Ru, Q., Tian, X., Pi, M., Chen, L., Yue, K., Xiong, Q., Ma, B., and Li, C. (2015) Voltage-gated K+ channel blocker quinidine inhibits proliferation and induces apoptosis by regulating expression of microRNAs in human glioma U87-MG cells. *Int. J. Oncol. 46* (2), 833−840.
(42) Chen, Y., Fan, Z., Yang, Y., and Gu, C. (2019) Iron metabolism and its contribution to cancer (Review). *Int. J. Oncol. 54*, 1143−1154.
(43) Manz, D. H., Blanchette, N. L., Paul, B. T., Torti, F. M., and Torti, S. V. (2016) Iron and cancer: recent insights. *Ann. N. Y. Acad. Sci. 1368* (1), 149−161.
(44) Huang, X. (2003) Iron overload and its association with cancer risk in humans: evidence for iron as a carcinogenic metal. *Mutat. Res., Fundam. Mol. Mech. Mutagen. 533* (1−2), 153−171.
(45) Eckard, J., Dai, J., Wu, J., Jian, J., Yang, Q., Chen, H., Costa, M., Frenkel, K., and Huang, X. (2010) Effects of cellular iron deficiency on the formation of vascular endothelial growth factor and angiogenesis. Iron deficiency and angiogenesis. *Cancer Cell Int. 10*, 28.
(46) Hossein Davoodi, S., Jamshidi-Naeini, Y., Esmaeili, S., Sohrabvandi, S., and Mortazavian, A. M. (2016) The Dual Nature of Iron in Relation to Cancer: A Review. *Iran. J. Cancer Prev. 9*, No. e5494.
(47) Schonberg, D. L., Miller, T. E., Wu, Q., Flavahan, W. A., Das, N. K., Hale, J. S., Hubert, C. G., Mack, S. C., Jarrar, A. M., Karl, R. T., Rosager, A. M., Nixon, A. M., Tesar, P. J., Hamerlik, P., Kristensen, B. W., Horbinski, C., Connor, J. R., Fox, P. L., Lathia, J. D., and Rich, J. N. (2015) Preferential Iron Trafficking Characterizes Glioblastoma Stem-like Cells. *Cancer Cell 28* (4), 441−455.
(48) Gaur, K., Vázquez-Salgado, A. M., Duran-Camacho, G., Domínguez-Martínez, L., Benjamín-Rivera, J. A., Fernández-Vega, L., Sarabia, L. C., García, A. C., Pérez-Deliz, F., Román, J. A. M., Vega-Cartagena, M., Loza-Rosas, S. A., Acevedo, X. R., and Tinoco, A. D. (2018) Iron and Copper Intracellular Chelation as an Anticancer Drug Strategy. *Inorganics 6*, 126.
(49) Denoyer, D., Masaldan, S., La Fontaine, S., and Cater, M. A. (2015) Targeting copper in cancer therapy: 'Copper That Cancer'. *Metallomics 7* (11), 1459−1476.
(50) Gupte, A., and Mumper, R. J. (2009) Elevated copper and oxidative stress in cancer cells as a target for cancer treatment. *Cancer Treat. Rev. 35* (1), 32−46.
(51) Ishida, S., Andreux, P., Poitry-Yamate, C., Auwerx, J., and Hanahan, D. (2013) Bioavailable copper modulates oxidative phosphorylation and growth of tumors. *Proc. Natl. Acad. Sci. U. S. A. 110* (48), 19507−19512.
(52) Li, Y., Hu, J., Guan, F., Song, L., Fan, R., Zhu, H., Hu, X., Shen, E., and Yang, B. (2013) Copper induces cellular senescence in human glioblastoma multiforme cells through downregulation of Bmi-1. *Oncol. Rep. 29* (5), 1805−1810.
(53) Xie, H., and Kang, Y. (2009) Role of Copper in Angiogenesis and Its Medicinal Implications. *Curr. Med. Chem. 16* (10), 1304−1314.

https://dx.doi.org/10.1021/acschemneuro.0c00648
ACS Chem. Neurosci. XXXX, XXX, XXX−XXX

(54) Brem, S. S., Zagzag, D., Tsanaclis, A. M., Gately, S., Elkouby, M. P., and Brien, S. E. (1990) Inhibition of angiogenesis and tumor growth in the brain. Suppression of endothelial cell turnover by penicillamine and the depletion of copper, an angiogenic cofactor. *Am. J. Pathol. 137* (5), 1121−1142.
(55) Jazayeri, S., Feli, A., Bitaraf, M. A., Dodaran, M. S., Alikhani, M., and Hosseinzadeh-Attar, M. J. (2016) Effects of Copper Reduction on Angiogenesis-Related Factors in Recurrent Glioblastoma Cases. *Asian Pac. J. Cancer Prev. 17* (10), 4609−4614.
(56) Pérès, E. A., Toutain, J., Paty, L. P., Divoux, D., Ibazizène, M., Guillouet, S., Barré, L., Vidal, A., Cherel, M., Bourgeois, M., Bernaudin, M., and Valable, S. (2019) 64Cu-ATSM/64Cu-Cl2 and their relationship to hypoxia in glioblastoma: a preclinical study. *EJNMMI Res. 9*, 114.
(57) Yoshida, D., Ikeda, Y., and Nakazawa, S. (1993) Quantitative analysis of copper, zinc and copper/zinc ratio in selected human brain tumors. *J. Neuro-Oncol. 16*, 109−115.
(58) Stojsavljević, A., Vujotić, L., Rovčanin, B., Borković-Mitić, S., Gavrović-Jankulović, M., and Manojlović, D. (2020) Assessment of trace metal alterations in the blood, cerebrospinal fluid and tissue samples of patients with malignant brain tumors. *Sci. Rep. 10*, 3816.
(59) Skrajnowska, D., and Bobrowska-Korczak, B. (2019) Role of Zinc in Immune System and Anti-Cancer Defense Mechanisms. *Nutrients 11* (10), 2273.
(60) Franklin, R. B., and Costello, L. C. (2009) The important role of the apoptotic effects of zinc in the development of cancers. *J. Cell. Biochem. 106* (5), 750−757.
(61) Mehrian-Shai, R., Yalon, M., Simon, A. J., Eyal, E., Pismenyuk, T., Moshe, I., Constantini, S., and Toren, A. (2015) High metallothionein predicts poor survival in glioblastoma multiforme. *BMC Med. Genomics 8*, 68.
(62) Toren, A., Pismenyuk, T., Yalon, M., Freedman, S., Simon, A. J., Fisher, T., Moshe, I., Reichardt, J. K. V., Constantini, S., Mardor, Y., Last, D., Guez, D., Daniels, D., Assoulin, M., and Mehrian-Shai, R. (2016) Zinc enhances temozolomide cytotoxicity in glioblastoma multiforme model systems. *Oncotarget 7* (46), 74860−74871.
(63) Takeda, A., Tamano, H., Enomoto, S., and Oku, N. (2001) Zinc-65 Imaging of Rat Brain Tumors. *Cancer Res. 61* (13), 5065−5069.
(64) Takeda, A., Tamano, H., and Oku, N. (2003) Alteration of zinc concentrations in the brain implanted with C6 glioma. *Brain Res. 965* (1−2), 170−173.
(65) Cilliers, K., Muller, C. J. F., and Page, B. J. (2020) Trace Element Concentration Changes in Brain Tumors: A Review. *Anat. Rec. 303* (5), 1293−1299.
(66) Mehdi, Y., Hornick, J.-L., Istasse, L., and Dufrasne, I. (2013) Selenium in the Environment, Metabolism and Involvement in Body Functions. *Molecules 18* (3), 3292−3311.
(67) Yakubov, E., Buchfelder, M., Eyüpoglu, I. Y., and Savaskan, N. E. (2014) Selenium Action in Neuro-Oncology. *Biol. Trace Elem. Res. 161* (3), 246−254.
(68) Zhu, Z., Kimura, M., Itokawa, Y., Nakatsu, S., Oda, Y., and Kikuchi, H. (1995) Effect of selenium on malignant tumor cells of brain. *Biol. Trace Elem. Res. 49*, 1−7.
(69) Zhu, Z., Kimura, M., Itokawa, Y., Aoki, T., Takahashi, J. A., Nakatsu, S., Oda, Y., and Kikuchi, H. (1996) Apoptosis induced by selenium in human glioma cell lines. *Biol. Trace Elem. Res. 54* (2), 123−134.
(70) Rooprai, H. K., Kyriazis, I., Nuttall, R. K., Edwards, D. R., Zicha, D., Aubyn, D., Davies, D., Gullan, R., and Pilkington, G. J. (2007) Inhibition of invasion and induction of apoptosis by selenium in human malignant brain tumour cells in vitro. *Int. J. Oncol. 30* (5), 1263−1271.
(71) Harmanci, D., Erbayraktar, Z., Sayin, O., and Guner, G. A. (2017) In Vitro effects of Selenium on Human Glioblastoma Multiforme Cell Lines: A Preliminary Study. *ACTA Clin. Croat. 56*, 48−57.
(72) Wang, K., Fu, X., Li, Y., Hou, Y., Yang, M., Sun, J., Yi, S., Fan, C., Fu, X., Zhai, J., and Sun, B. (2016) Induction of S-Phase Arrest in Human Glioma Cells by Selenocysteine, a Natural Selenium-Containing Agent Via Triggering Reactive Oxygen Species-Mediated DNA Damage and Modulating MAPKs and AKT Pathways. *Neurochem. Res. 41* (6), 1439−1447.
(73) da Cruz, E. H. G., Silvers, M. A., Jardim, G. A. M., Resende, J. M., Cavalcanti, B. C., Bomfim, I. S., Pessoa, C., de Simone, C. A., Botteselle, G. V., Braga, A. L., Nair, D. K., Namboothiri, I. N. N., Boothman, D. A., and da Silva Júnior, E. N. (2016) Synthesis and antitumor activity of selenium-containing quinone-based triazoles possessing two redox centres, and their mechanistic insights. *Eur. J. Med. Chem. 122*, 1−16.
(74) Xu, B., Zhang, Q., Luo, X., Ning, X., Luo, J., Guo, J., Liu, Q., Ling, G., and Zhou, N. (2020) Selenium nanoparticles reduce glucose metabolism and promote apoptosis of glioma cells through reactive oxygen species-dependent manner. *NeuroReport 31* (3), 226−234.
(75) Ertilav, K., Nazıroğlu, M., Ataizi, Z. S., and Braidy, N. (2019) Selenium Enhances the Apoptotic Efficacy of Docetaxel Through Activation of TRPM2 Channel in DBTRG Glioblastoma Cells. *Neurotoxic. Res. 35* (4), 797−808.
(76) Zhang, Z., Miyatake, S., Saiki, M., Asahi, M., Yukawa, H., Toda, H., Kikuchi, H., Yoshimura, S., and Hashimoto, N. (2000) Selenium and Glutathione Peroxidase mRNA in Rat Glioma. *Biol. Trace Elem. Res. 73* (1), 67−76.

https://dx.doi.org/10.1021/acschemneuro.0c00648
ACS Chem. Neurosci. XXXX, XXX, XXX−XXX

Comparison of elemental anomalies following implantation of different cell lines of glioblastoma multiforme in the rat brain. A total reflection X-ray fluorescence spectroscopy study

Karolina Planeta (1)#, Zuzanna Setkowicz (2)#, Natalia Janik-Olchawa (1), Katarzyna Matusiak (1), Damian Ryszawy (3), Agnieszka Drozdz (1), Krzysztof Janeczko (2), Beata Ostachowicz (1), Joanna Chwiej (1)*

(1) AGH University of Science and Technology, Faculty of Physics and Applied Computer Science, Krakow, Poland

(2) Jagiellonian University, Institute of Zoology and Biomedical Research, Krakow, Poland

(3) Jagiellonian University, Faculty of Biochemistry Biophysics and Biotechnology, Krakow, Poland

# - Contributed equally

*joanna.chwiej@fis.agh.edu.pl

Supplementary materials

Limits of detection and precision

Limit of detection of the element i in the sample j was calculated based on the formula (S1):

$$LOD_{ij} = \frac{3 * C_{ij} * \sqrt{N_{BGij}}}{N_{ij}} \quad (S1)$$

where:

C_{ij} – concentration of the element i in the sample j [ppm],
N_{BGij} – area of the background under the K_α line of the element i in the sample j [a.u.],
N_{ij} – net peak area of the K_α line of the element i in the sample j [a.u.].
Final value of the detection limit LOD_i for the analysed element i was calculated as an average of the results obtained for all the analysed samples of the normal brain. Thus, the uncertainty of the final result was calculated as the standard deviation of LOD_i:

$$SD_{LOD_i} = \sqrt{\frac{\sum_1^n (LOD_{ij} - LOD_i)^2}{n * (n-1)}} \quad (S2)$$

where:

n – the number of analysed samples representing control group.

Precision was evaluated as an intra-day and inter-day precision, depending on the period between performed measurements. The intra-day precision was calculated based on the ten results obtained for one sample in one measurement series performed within one day. The inter-day precision was evaluated by measuring the same sample in five different days. Both intra-day and inter-day precision was calculated as coefficient of variation of obtained results, according to the formula (S3):

$$CV = \sqrt{\frac{\sum_1^k (a_{ij} - a_i)^2}{k * (k-1)}} * 100\% \quad (S3)$$

where:

j – the number of measurement,

a_{ij} – the concentration of the element i in a measurement j [ppm],

a_i – the mean value of the concentration of the element i [ppm],

k – the number of measurements.

International Journal of
Molecular Sciences

MDPI

Article

Altered Elemental Distribution in Male Rat Brain Tissue as a Predictor of Glioblastoma Multiforme Growth—Studies Using SR-XRF Microscopy

Karolina Planeta [1,†], Zuzanna Setkowicz [2,†], Mateusz Czyzycki [3], Natalia Janik-Olchawa [1], Damian Ryszawy [4,‡], Krzysztof Janeczko [2], Rolf Simon [5], Tilo Baumbach [3,5] and Joanna Chwiej [1,*]

1 Faculty of Physics and Applied Computer Science, AGH University of Science and Technology, Al. Mickiewicz 30, 30-059 Krakow, Poland; Karolina.Planeta@fis.agh.edu.pl (K.P.); Natalia.Janik-Olchawa@fis.agh.edu.pl (N.J.-O.)
2 Institute of Zoology and Biomedical Research, Jagiellonian University, Golebia 24, 31-007 Krakow, Poland; Zuzanna.Setkowicz-Janeczko@uj.edu.pl (Z.S.); K.Janeczko@uj.edu.pl (K.J.)
3 Laboratory for Applications of Synchrotron Radiation, Karlsruhe Institute of Technology, Kaiserstr. 12, D-76131 Karlsruhe, Germany; Czyzycki@kit.edu (M.C.); Tilo.Baumbach@kit.edu (T.B.)
4 Faculty of Biochemistry Biophysics and Biotechnology, Jagiellonian University, Golebia 24, 31-007 Krakow, Poland; Damian.Ryszawy@uj.edu.pl
5 Karlsruhe Institute of Technology, Institute for Photon Science and Synchrotron Radiation, Hermann-von-Helmholtz-Platz 1, D-76344 Eggenstein-Leopoldshafen, Germany; R.Simon@kit.edu
* Correspondence: Joanna.Chwiej@fis.agh.edu.pl
† These authors contributed equally to this work.
‡ The authors sadly announce that Damian Ryszawy, a young scientist and our good friend, suddenly passed away before this paper was finally prepared.

check for updates

Citation: Planeta, K.; Setkowicz, Z.; Czyzycki, M.; Janik-Olchawa, N.; Ryszawy, D.; Janeczko, K.; Simon, R.; Baumbach, T.; Chwiej, J. Altered Elemental Distribution in Male Rat Brain Tissue as a Predictor of Glioblastoma Multiforme Growth—Studies Using SR-XRF Microscopy. *Int. J. Mol. Sci.* **2022**, *23*, 703. https://doi.org/10.3390/ijms23020703

Academic Editor: Peter Hau

Received: 29 November 2021
Accepted: 5 January 2022
Published: 9 January 2022

Publisher's Note: MDPI stays neutral with regard to jurisdictional claims in published maps and institutional affiliations.

Abstract: Glioblastoma multiforme (GBM) is a particularly malignant primary brain tumor. Despite enormous advances in the surgical treatment of cancer, radio- and chemotherapy, the average survival of patients suffering from this cancer does not usually exceed several months. For obvious ethical reasons, the search and testing of the new drugs and therapies of GBM cannot be carried out on humans, and for this purpose, animal models of the disease are most often used. However, to assess the efficacy and safety of the therapy basing on these models, a deep knowledge of the pathological changes associated with tumor development in the animal brain is necessary. Therefore, as part of our study, the synchrotron radiation-based X-ray fluorescence microscopy was applied for multi-elemental micro-imaging of the rat brain in which glioblastoma develops. Elemental changes occurring in animals after the implantation of two human glioma cell lines as well as the cells taken directly from a patient suffering from GBM were compared. Both the extent and intensity of elemental changes strongly correlated with the regions of glioma growth. The obtained results showed that the observation of elemental anomalies accompanying tumor development within an animal's brain might facilitate our understanding of the pathogenesis and progress of GBM and also determine potential biomarkers of its extension. The tumors appearing in a rat's brain were characterized by an increased accumulation of Fe and Se, whilst the tissue directly surrounding the tumor presented a higher accumulation of Cu. Furthermore, the results of the study allow us to consider Se as a potential elemental marker of GBM progression.

Keywords: glioblastoma multiforme (GBM); animal models of GBM; multi-elemental analysis of rat brain; synchrotron X-ray fluorescence microscopy; U87mg; T98g

1. Introduction

Animal models of diseases have a great importance in experimental studies, which cannot be performed on humans for ethical reasons. They improve the knowledge about both physiological and pathological processes taking place in the organisms. Animal models are

commonly used for the study of disorders of different origins and also developing/testing new therapeutic substances or strategies.

Tumors of the central nervous system are the 10th most common cause of death among both men and women. Gliomas, originating from glial cells responsible for neurons support, constitute about 33% of all brain tumors. Depending on the cells' morphology, their proliferation ability and aggressiveness, four grades of malignancy are distinguished for gliomas. The group of gliomas with the highest degree of malignancy includes glioblastoma multiforme (GBM). GBM is a rapidly progressive and infiltrative brain tumor, characterized by an intensive formation of new blood vessels and the presence of necrotic and hemorrhagic foci within its structure. It accounts for 16% of all brain tumors and stands out by high mortality—the median survival of patients from diagnosis is about several months [1,2].

Many interdisciplinary research groups have been currently conducting investigations aiming at gaining more comprehensive knowledge about gliomas etiology and developing new and effective methods of its treatment. Some of the studies concerning the pathogenesis and the progress of GBM are conducted on tissue samples taken from humans suffering from GBM. In these cases, however, one should remember that the obtained results may be influenced by many factors including the applied therapy [3,4]. In turn, due to ethical considerations, the testing of new antitumor substances/drugs cannot be carried out on humans and therefore animal models, usually based on rodents, are used for both purposes [5–7].

Testing new therapies of GBM based on animal models of the disease requires a deep knowledge about the morphological and biomolecular changes introduced in the brain through the developing tumor. In this study, we compared topographic and quantitative elemental anomalies appearing in the brain as a result of the implantation of three different types of GBM cells. For this purpose, Wistar rats were subjected to the intracranial implantation of human GBM cell lines U87mg and T98g as well as patient-derived glioma cells. Then, we applied synchrotron radiation-based X-ray fluorescence (SR-XRF) spectrometry for the elemental mapping of brain tissue slices taken from the area of tumor implantation. SR-XRF is a valuable tool allowing for the investigation of changes in both the distribution and accumulation of elements. This sensitive and non-destructive method of multi-elemental analysis offers low detection limits and a short acquisition time. The above-mentioned properties enable the use of the analytical technique to investigate the elemental topography of biomedical samples [8–11]. As a result of the SR-XRF measurements, we obtained two-dimensional maps of P, S, K, Ca, Fe, Cu, Zn and Se distribution. In addition, we compared them with the corresponding microscopic images of the examined tissues in order to identify local anomalies specific for the animals implanted with particular GBM cells.

Each of the analyzed elements is important for the purposes of our study, in terms of their involvement in both the physiological as well as pathological processes occurring in the cells. Phosphorus is a macronutrient playing an important role in the cells' metabolism and constituting a building component of cell membranes. Sulfur compounds may increase the sensitivity of GBM cells to radiation therapy [12]. In turn, potassium channels are observed to be abnormally expressed in glioma cells [13]. The occurrence of calcium deposits is a feature accompanying intracranial tumors with a different grade of malignancy [14]. Copper is consider as a cofactor involved in the process of angiogenesis [15]. Iron and zinc are the elements essential for the proper regulation of cells' growth and DNA synthesis [16,17]. Furthermore, an increased iron uptake was observed for brain tumor cells [18]. Whilst selenium is crucial for the proper functioning of immune system cells and it is also involved in the processes of cell proliferation and apoptosis [19].

This is our second study concerning the elemental abnormalities of a rat's brain following the implantation of glioma cells. The first one, performed with the use of total reflection X-ray fluorescence (TXRF), provided us with information about tumor-induced changes in elemental concentrations averaged over the brain hemispheres. The obtained results allowed us to classify the U87mg cell line as the most aggressive among

the investigated GBM cells and to identify the elements potentially involved in tumor progression [20]. As the distribution of the elements in the analyzed tissues may not be homogenous, in the current study, we focused on the local elemental anomalies of the brain tissue and particular attention was directed toward the differences between the region of the tumor and its surrounding. This approach enabled us to obtain more precise information on the contribution of the analyzed elements to the process of GBM pathogenesis and progress.

2. Results

2.1. Outline of the Experiment

Five groups of male Wistar rats were the subject of the study. Three of them were intracranially implanted with human GBM cells of different origin (U87mg and T98g cell lines and patient-derived glioma cells) suspended in the culture medium. Two groups constituted the controls. One consisted of animals implanted with cells growth medium, whilst the second included naive normal rats. Three weeks after the procedure of implantation, the animals were sacrificed, and brain sections from the area of implantation were taken and prepared for measurements. Detailed descriptions of the experiment assumptions as well as the measurement conditions are included in the Materials and Methods section.

2.2. Data Analysis

As a result of the raster scanning of tissue slices with the X-ray beam, a set of XRF spectra, together with the information about the position of the beam for which they were recorded, were obtained for each sample. Spectral analysis was performed with the PyMca software ver. 5.0.2 [21], which enabled us to gather information about the net peak areas of the $K\alpha$ lines for the elements under interest and calculate the areal densities of the elements (M_T) for the examined tissue points in accordance with Equation (1).

$$M_T = \frac{Y_T}{S \times Y_T^N}, \quad (1)$$

M_T—the areal density of the analyzed element in the tissue sample (μg/cm^2);
Y_T—the net peak area of the $K\alpha$ line of the measured element for the tissue sample (a.u.);
S—sensitivity for the measured element (cm^2/μg);
Y_T^N—the incoming X-ray beam normalization factor for the tissue sample (a.u.).

The sensitivities S for the measured elements were determined in the calibration process and, for this purpose, the MICROMATTER XRF calibration standards (GaP, KCl, CaF_2, Ti, Fe, Cu, ZnTe, Se, CsBr, RbI, SrF_2) were used. Sensitivity values were quantified according to Equation (2)

$$S = \frac{Y_S}{M_S \times Y_S^N}, \quad (2)$$

Y_S—the net peak area of the $K\alpha$ line of the measured element for the standard sample (a.u);
M_S—the areal density of the analyzed element in the standard sample (μg/cm^2);
Y_S^N—the incoming X-ray beam normalization factor for the standard sample (a.u.).

The sensitivities S were then used to determine the calibration curve that is presented in Figure 1.

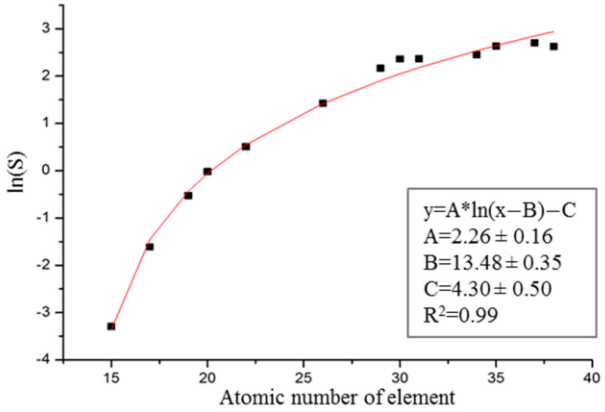

Figure 1. Sensitivity curve determined from the measurements of the MICROMATTER XRF calibration standards.

2.3. Limits of Detection

The limit of detection LOD_{ij} (μg/cm^2) for the element i in the tissue point j was calculated in accordance with Equation (3)

$$LOD_{ij} = 3.29 \times \frac{\sqrt{Y_{Bij}}}{Y_{Nij}} \times M_{Tij} \quad (3)$$

Y_{Bij}—the integrated area of the background under the $K\alpha$ line of element i in the spectrum recorded for tissue point j (a.u.);
Y_{Nij}—the net peak area of the $K\alpha$ line of element i in the spectrum recorded for tissue point j (a.u.);
M_{Tij}—the areal density of element i in tissue point j (μg/cm^2).

To estimate the detection limit of the element i for the brain tissue (LOD_i), the results obtained for the samples taken from normal rats were used. From each tissue slice, we randomly selected 30 points localized in the striatum region in the right hemisphere, calculated LOD_{ij} for each point, which was followed by averaging the results from all the points and for all the animals. The uncertainties of the determined LOD_i values were calculated as the standard deviation of the mean value, according to Equation (4).

$$SD_{LODi} = \sqrt{\frac{\sum_{1}^{n}(LOD_{ij} - LOD_i)^2}{n \times (n-1)}} \quad (4)$$

LOD_i—the detection limit of element i for the brain tissue, calculated as an average of the results for all the selected tissue points (μg/cm^2);
n—the number of examined points.

The final values of such calculated detection limits of elements, together with their uncertainties, are presented in Table 1.

Table 1. Detection limits of analyzed elements with uncertainties calculated as standard deviation of the mean value.

Element	P	S	K	Ca	Fe	Cu	Zn	Se
LOD (ng/cm^2)	355.4	122.7	39.36	12.25	2.695	1.126	1.544	0.4493
SD (ng/cm^2)	3.8	1.3	0.41	0.13	0.028	0.012	0.015	0.0073

2.4. Morphological Evaluation

A morphological evaluation of the tissues taken from the place of the implantation yielded the development grade of the tumors that originated from the used GBM cell lines. Examples of the microscopic images obtained for the representative samples from the five examined animal groups are presented in Figure 2. It can be seen that the implantation of both U87mg cells and patient-derived cells led to the development of a tumor within the affected rat's brain hemisphere. In the case of U87mg cells, a massive tumor, often involving the entire hemisphere, was observed. After implanting T98g cells, no signs of tumor development were found. However, in the regions where the glioma cells were implanted, similarly to the case of DMEM administration, morphological changes indicating nervous tissue damage were found.

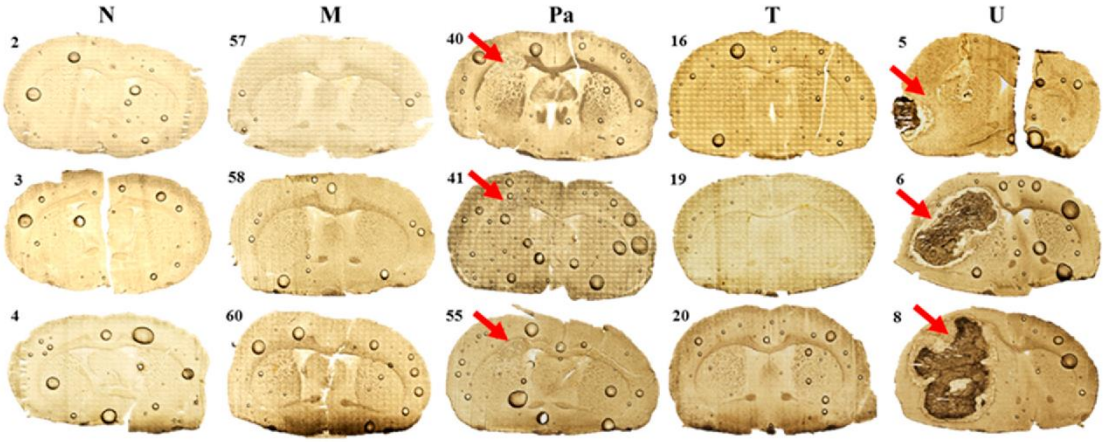

Figure 2. Microscopic images of tissue slices taken from the place of the implantation from 3 representative animals of each examined experimental group (N—normal rats; M—animals receiving DMEM; Pa, T and U—animals implanted with GBM cells taken from patient and T98g or U87mg cell lines, respectively). Red arrows indicate tumor bulk developed after the implantation of glioma cells.

2.5. Qualitative Elemental Analysis

Evaluating the distributions of the elements under interest (P, S, K, Ca, Fe, Cu, Zn and Se) in the scanned brain slices was the first step of our investigation. The results of the topographic elemental analysis for the representative samples that originated from all the experimental groups are provided in Figure 3.

As one can see from Figure 3a, a clear decrease in P accumulation in the implanted brain hemisphere and especially in the area of tumor development was found for the rats from the U group. A reduced element content was noted compared to the naive hemisphere within the same sample, as well as compared to the left hemisphere of the normal animals. A similar relation was observed for the animals implanted with patient-derived glioma cells. Additionally, for them, the area of the tumor determined from microscopic examinations corresponded with the region of a slight decrease in phosphorus accumulation. In the case of groups M and T, we did not observe any changes in P distribution in the regions of interest.

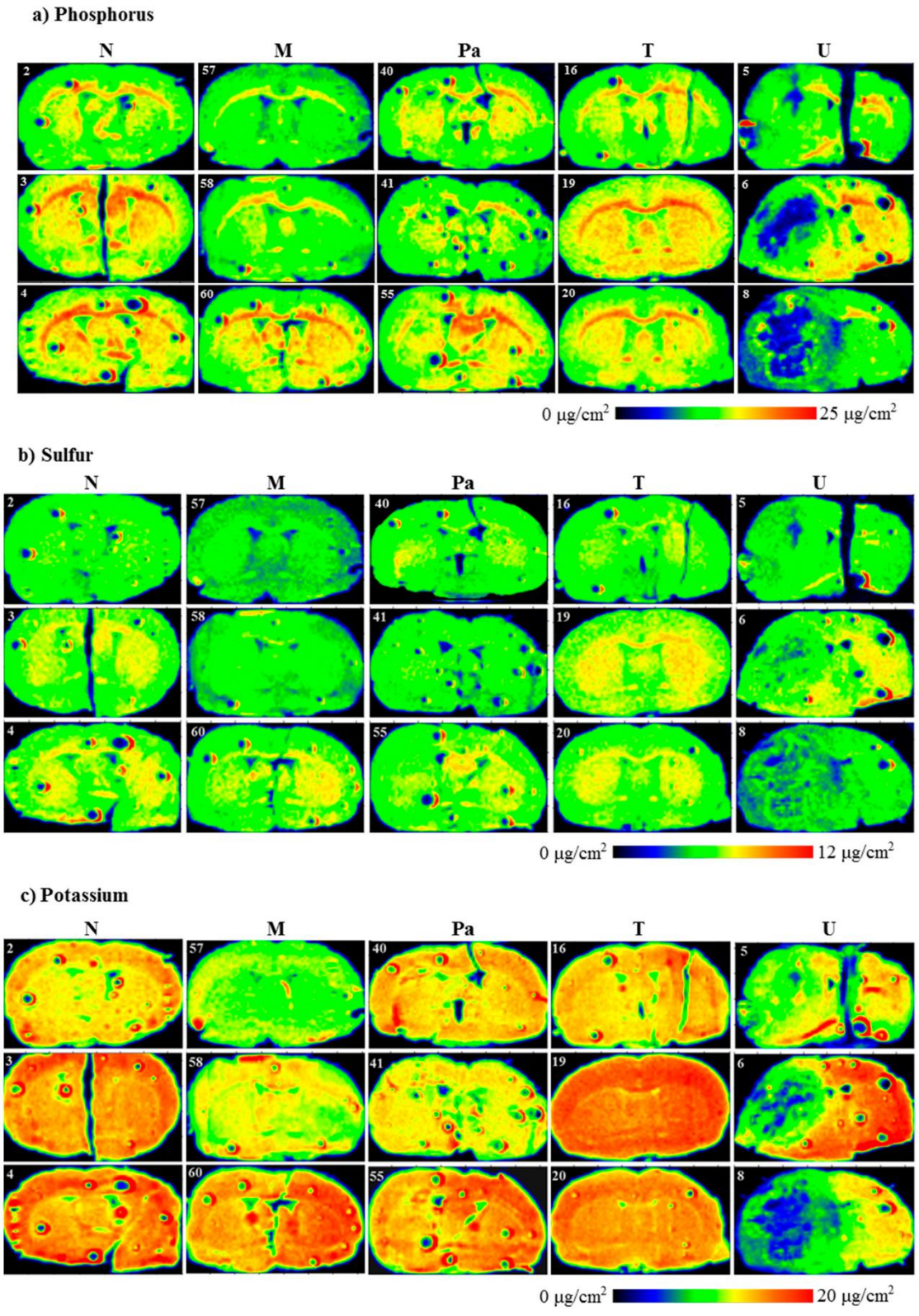

Figure 3. *Cont.*

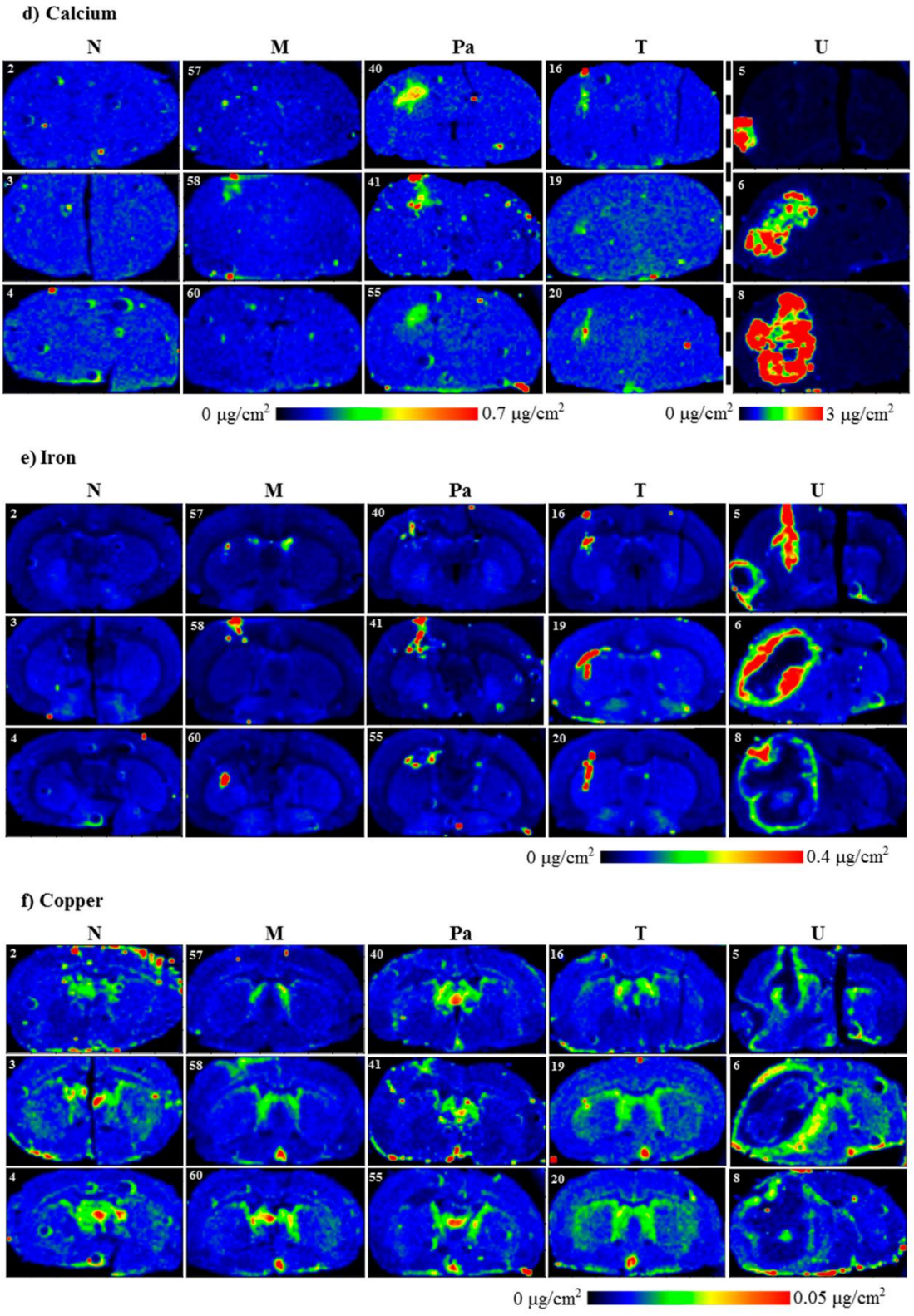

Figure 3. *Cont.*

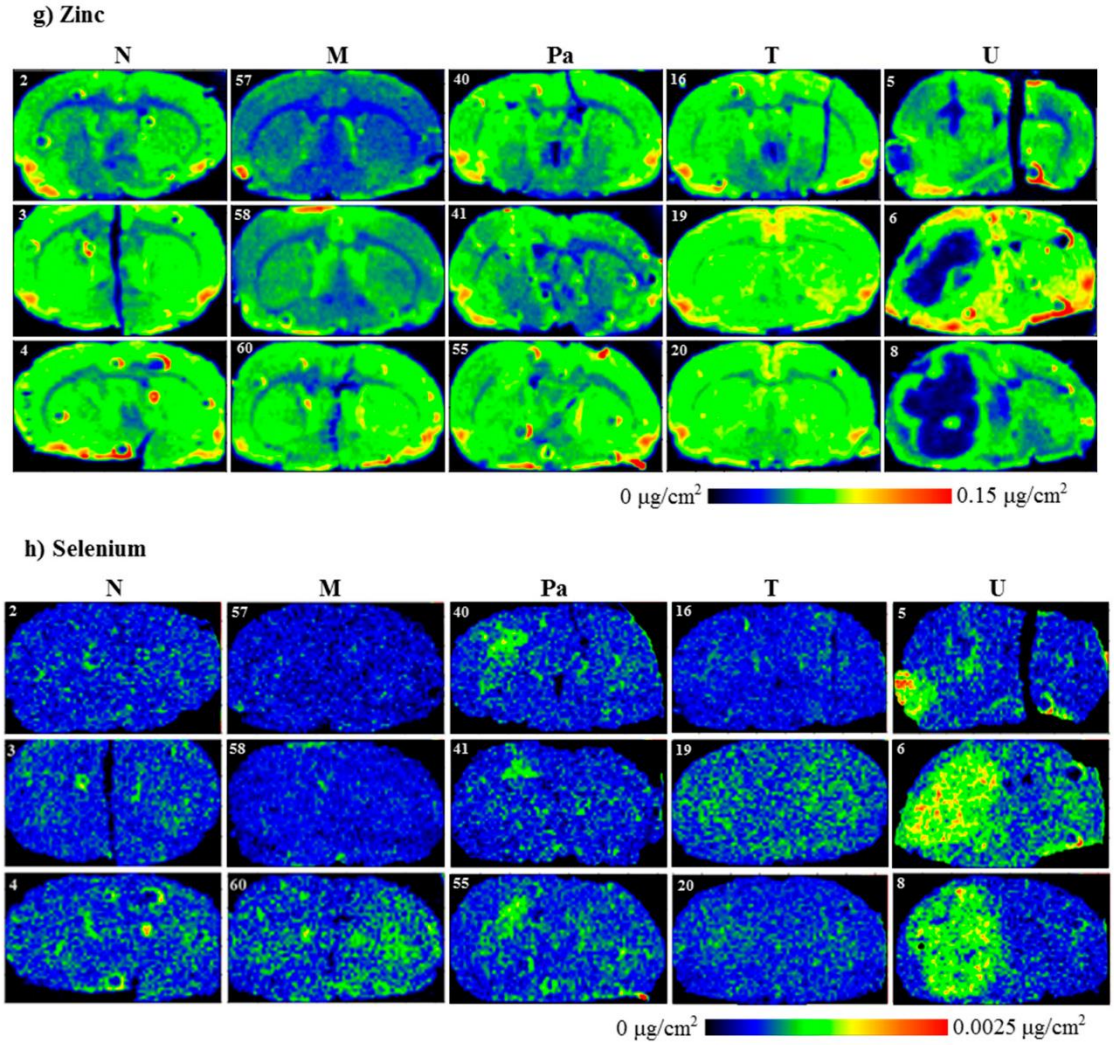

Figure 3. Topographic elemental maps of brain slices taken from the rats of all experimental groups for: (**a**) phosphorus, (**b**) sulfur, (**c**) potassium, (**d**) calcium, (**e**) iron, (**f**) copper, (**g**) zinc and (**h**) selenium. Color scales express areal densities of elements in µg/cm^2. In the case of Ca, large differences in areal densities were observed between groups N, M, Pa, T and group U. Two different scales were applied for better visualization of the distribution of this element.

Topographic analysis of the maps of S distribution (Figure 3b) illustrated changes in the accumulation of this element in the left hemispheres of the animals implanted with the U87mg cells. For this group of rats, the areas of the reduced S content, compared to the intact hemisphere as well as to the left hemispheres taken from the control rats, were observed. These differences were not found in the case of the remaining experimental groups. A similar observation was made in the case of K distributions. The clear decrease in its accumulation occurred only in the areas corresponding to the tumors developed in the brains of the animals from the U group.

Ca and Fe are two elements, the distribution of which was disturbed both within the place where the glioma cells were implanted and culture medium was administered. The accumulation of both elements increased in the regions of DMEM administration and T98g cells injection (M and T groups, respectively), as well as the tumor development in the case of the Pa and U groups.

The topographic maps recorded for Ca and Fe showed a great heterogeneity of element accumulation in the tumor bulk developed from U87mg cells. A significant increase in Ca content was found in the inner area of the tumor, while Fe accumulated more in its border layers. Furthermore, regions of an elevated accumulation of Ca and Fe corresponded with the tumor areas presenting a different morphological structure, which can be seen in Figure 2, illustrating microscopic images of the scanned tissue sections.

The results obtained for Cu showed a substantially elevated areal density of this element in the tissue directly adjacent to the tumor developed from the U87mg cells. Additionally, in the case of the U group, the distribution of Cu within the tumor was heterogeneous and its level was lower in the external layer than the inner region. In turn, the level of Cu was generally lower in the tumor compared to its surroundings for the samples taken from the animals belonging to the Pa group.

Zn accumulation showed anomalies in the samples taken from the animals representing the Pa and U groups. A decrease in this element content was recorded in the area of the tumor developed from the U87mg cells. Furthermore, the reduced Zn level occurred mainly in the inner part of the tumor and was usually correlated with the area of lower P accumulation. The tumor developed from patient-derived cells presented the heterogeneous Zn distribution with a slightly elevated content compared to the surroundings.

In the examined tissue slices, Se was selectively accumulated in the tumors developed in the animals from the Pa and U groups. Moreover, its distribution within the tumor bulk was generally homogenous and corresponded with the area of the tumor determined based on microscopic images.

2.6. Quantitative Elemental Analysis

The second step of our study consisted of performing quantitative elemental analysis for the examined brain samples. Its main purpose was to evaluate the statistical significance of the differences in elemental accumulation in the places where T98g cells or DMEM were administered and their surroundings as well as the tumors developed from implanting either patient cells or U87mg cells and their surroundings. In this investigation, the samples representing the M, T, Pa and U groups were taken into account.

First, based on the microscopic images of the tissues for the Pa and U groups, the areas corresponding to the place of tumor development were defined. When choosing the areas of interest for the samples originating from the M and T groups, we based the selections on the regions with the increased Fe accumulation that correlated with the places where T98g cells or DMEM were administered. For the brain samples taken from the rats representing the M, T and Pa groups, we defined two regions: first corresponding to the places where the medium or glioma cells were administered and second constituting their surroundings. In the case of the tumors developed from U87mg cells, due to the clear heterogeneity within their structure, we also defined an additional region inside the tumor bulk, which is further referred to as the tumor debris. The mentioned areas, marked in the elemental maps and microscopic images of the selected samples representing the Pa and U groups, are presented in Figure 4.

For each examined brain slice, the mean quantities of P, S, K, Ca, Fe, Cu, Zn and Se were calculated in the regions mentioned before. Then, based on the results obtained for the whole experimental group, the median, minimal and maximal values of areal densities of the analyzed elements were determined and the obtained results were presented in the form of box-and-whiskers plots in Figure 5. We applied the non-parametric Mann–Whitney U test at the confidence level of 95% [22] to evaluate the statistical significance of the differences in the elemental composition between the compared regions within a given animal group. All the statistically relevant differences were determined based on this test and are marked with their p-values in Figure 5.

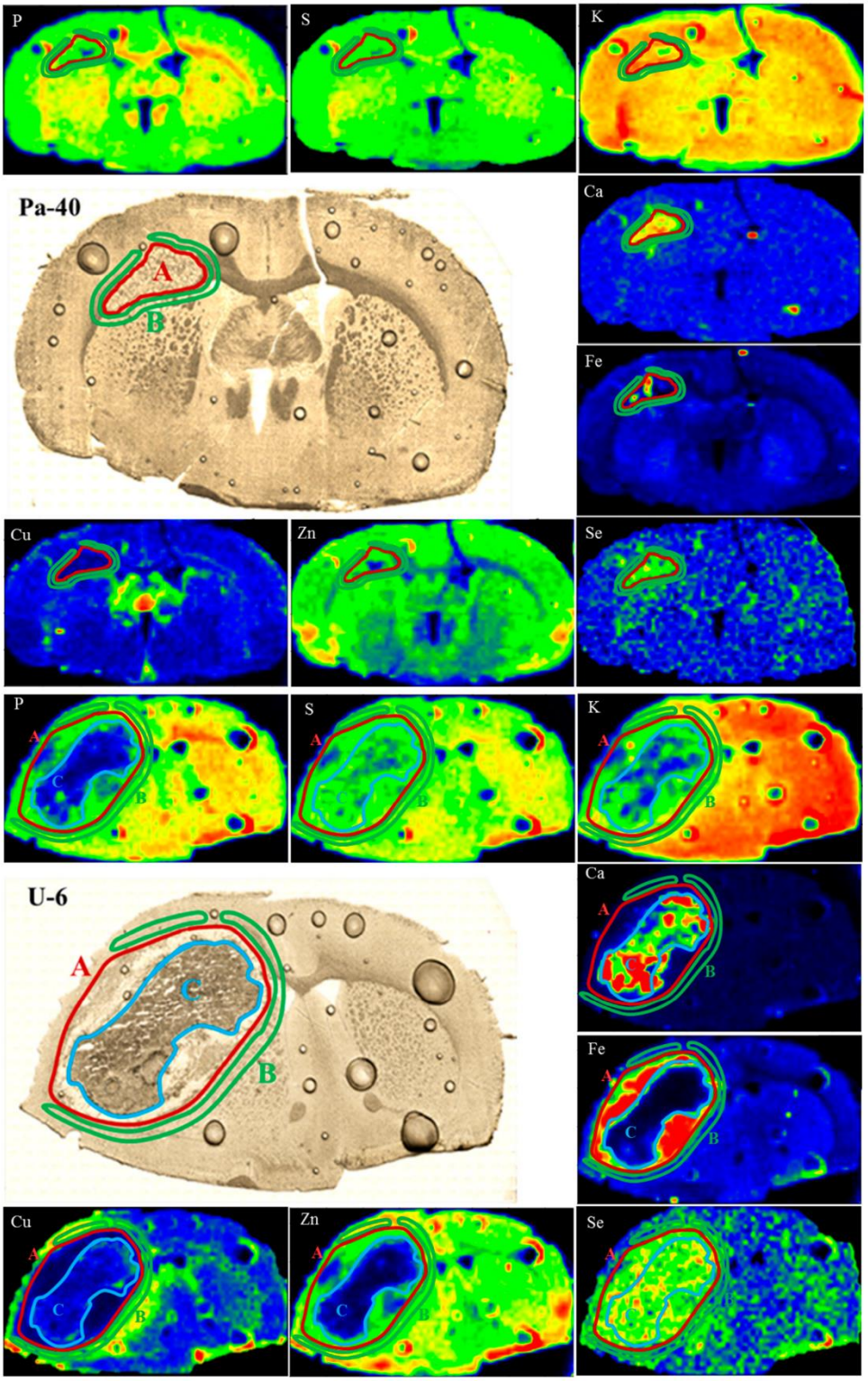

Figure 4. Regions of tumor (**A**), surrounding tissue (**B**) and tumor debris (**C**) marked in the maps of elemental distribution as well as microscopic images of brain slices taken from selected animals representing Pa and U groups.

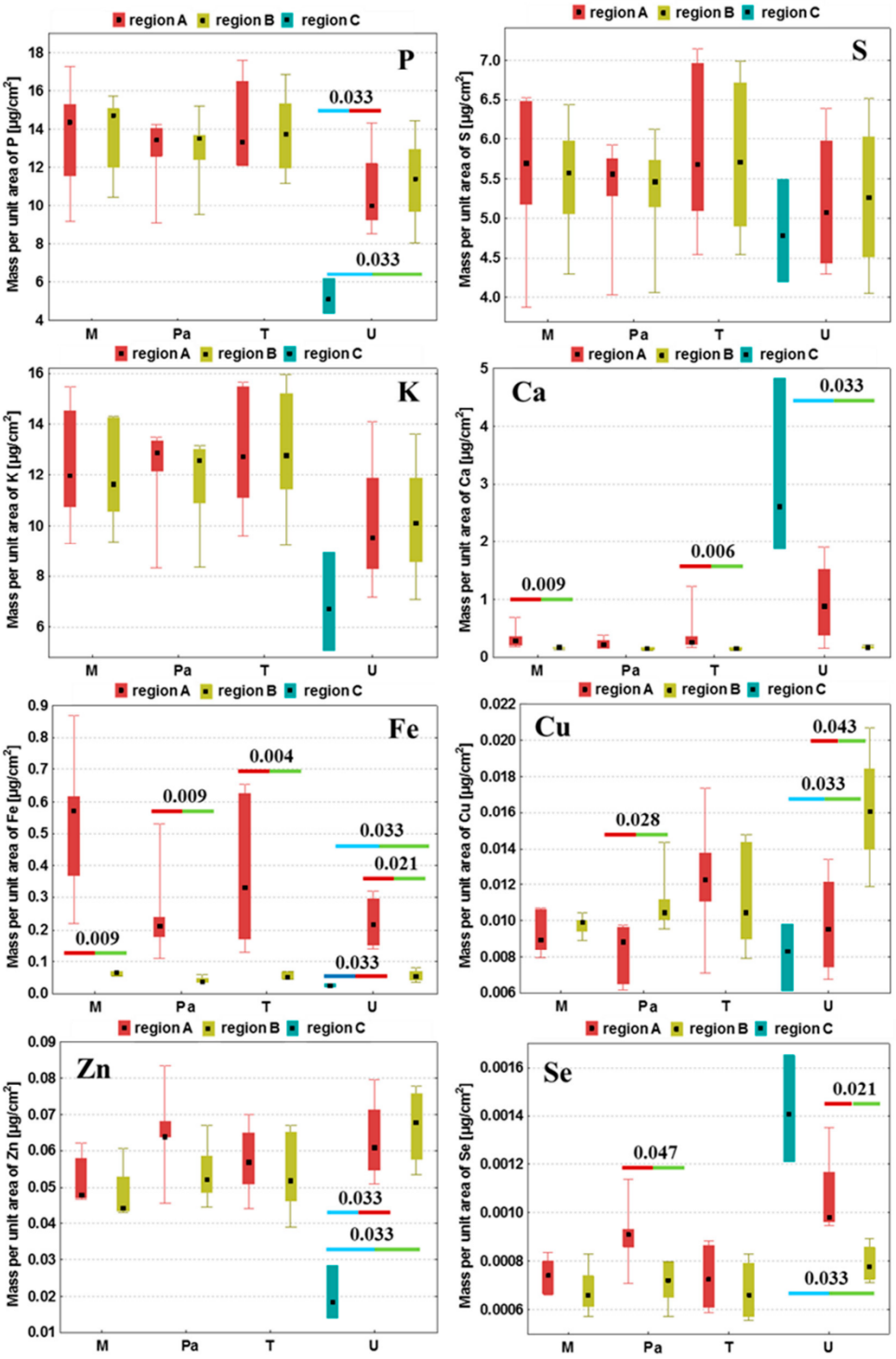

Figure 5. Medians, minimal and maximal values as well as interquartile spans of areal densities of P, S, K, Ca, Fe, Cu, Zn and Se in the examined tissue regions obtained for groups M, Pa, T and U. Region A—tumor (groups Pa and U) or place where DMEM/T98g cells were administered (groups M and T, respectively); region B—surroundings of the tumor or place where DMEM/T98g cells were administered; C—tumor debris defined in the case of the U group. Statistically significant differences between the compared areas within the same experimental group were marked with *p*-values of the *U* test.

As one can see from Figure 5, the tumors developed after the implantation of U87mg cells presented numerous statistically significant differences in the elemental distribution, both comparing to their surrounding and within the tumor bulk, which resulted from their heterogeneous structure. Defined for the U group, tumor debris was characterized by the diminished quantities of P, Fe and Zn compared both to the tumor as well as to the tissue adjacent tumor. Furthermore, in this region, we observed a reduced accumulation of Cu and an increased content of Ca and Se, in relation to the surrounding tissues.

The comparison of tumors developing in the animals representing the Pa and U groups showed a similar pattern of elemental differences between the tumor and its surroundings. The tumors developed from both U87mg cells and from patient-derived cells were characterized by a higher accumulation of Fe and Se compared to the adjacent tissues. In turn, the tumor's surroundings revealed an elevated content of Cu in relation to its bulk. Additionally, the M and T groups were similar one to the other in terms of the observed elemental anomalies. The places where the T98g cells or DMEM were administered presented an elevated Ca and Fe accumulation compared to the surrounding tissue.

Fe accumulation changes at the place of administration were common for the samples taken from all the experimental groups and the amount of this element was always higher there in relation to the surroundings.

3. Discussion

A significant number of publications cover the involvement of trace and major elements in the process of carcinogenesis. The differences in elemental accumulation between healthy and neoplastic tissues are observed in the case of various types of tumors [23–26]. They may result, among others, from an increased demand for some elements during the tumor development, which may, in turn, be associated with the changed metabolism of tumor cells or their higher proliferation ability [27–30]. With knowledge of the elemental abnormalities that are characteristic for a particular neoplasm, some elements or their inhibitors might be selected and then tested as potential agents supporting the treatment against the tumor [31–33].

The subject of our study was glioblastoma multiforme, one of the most aggressive brain tumors, characterized by very high mortality among patients. We selected two human GBM cell lines—U87mg and T98g—and implanted them into the left cerebral hemispheres of rats. Cells derived from a patient suffering from GBM were used in an identical manner. Our investigation presented in this study is the continuation of our previous study, where the TXRF method was applied to determine the mean concentrations of P, S, K, Ca, Fe, Cu, Zn and Se in brain hemispheres taken from rats that were implanted with the same glioma cells [20]. The results of the above-mentioned study provided us with a general view of the elemental changes caused by the tumor development and allowed us to associate the revealed anomalies with the degree of aggressiveness of the selected GBM cells. As TXRF spectrometry only enables a bulk analysis of the examined samples, there was still an open question about the local elemental anomalies within the GBM-affected brain tissues, especially within the tumor bulk and its surroundings. Therefore, we applied SR-XRF microscopy to perform the topographic and quantitative elemental analysis of the brain slices taken from the area where the glioma cells were implanted. Data concerning the distribution and accumulation of the examined elements were correlated with the information about the tissue histology. The quantitative analysis followed by statistical evaluation allowed us to determine the elements for which accumulation differs significantly between the tumor area and its surroundings. In the discussion presented below, based on evidence in the available literature, we try to indicate the possible causes of the observed elemental anomalies.

Based on histological examinations, Martin and Lemmen distinguished four calcification patterns of intracranial tumors. They classified benign lesions to groups that frequently show a tendency to calcification. In the case of high-grade gliomas and glioblastomas, calcifications were rarely seen [14]. However, cases of glioblastomas with the presence

of calcified regions were also reported [34–38]. In the literature, one can find reports on clinical cases, where imaging examinations performed few years before brain tumor diagnosis revealed calcifications in the area of cancer development [39,40]. Mallya et al. and Kroh et al. suggested that the presence of calcified regions may be associated with a longer survival period [36,37]. Bähr et al. analyzed the cases of patients suffering from GBM who had undergone therapy with Bevacizumab. The authors observed the occurrence of calcifications in gliomas after the treatment. Moreover, the median survival of patients in which tumor calcification occurred was higher than in those without such changes [41]. Similar observations were made by Blumenthal et al. [42]. These results appear to be in agreement with the in vitro investigation, revealing that Bevacizumab induces a specific death of endothelial cells connected with massive Ca accumulation [43]. Halpin and Kingsley described two clinical cases of patients with an intracranial tumor for which calcifications' disappearance was found. It was suggested that such a phenomenon might be a prognostic factor of high-grade tumor development and is probably associated with the progressive changes of tissue pH resulting from its growth [44].

In biological tissues, calcification foci usually state hydroxyapatite deposits composed of Ca and P. Our study showed, however, that the areas of increased Ca accumulation are usually correlated with the regions of diminished P amounts. This is especially visible for the tumor debris found in the U group. Such an observation is in agreement with the findings of Guisan et al., who also found the negative correlation between Ca and P quantities for brain tumor bulks [18]. We hypothesize that the alterations in Ca accumulation within the examined regions, revealed in our study, might be rather associated with the process of glutamate excitotoxicity. Glutamate is an excitatory neurotransmitter, whose concentration is normally regulated through the astrocytes' uptake. Ye and Sontheimer showed that GBM cells are characterized by the diminished absorption of glutamate compared to the normal astrocytes. Furthermore, they release considerable amounts of this neurotransmitter to the extracellular environment. According to the authors, glioma cells may be responsible for the death of surrounding neurons due to this excessive glutamate release [45]. Under the conditions of the increased glutamate in the cells' surroundings, glutamate-sensitive receptors are stimulated. Some of these receptors are permeable for Ca ions and their activation causes an elevated influx of this element into the cells. This, in turn, results in the activation of enzymes involved in the cell death and triggers a cascade of damaging processes, including the release of the reactive oxygen species, ATP depletion and membranes oxidation [45,46]. Clearly elevated Ca quantities, as well as inhomogeneity in its distribution, are observed within the tumor bulk developed from U87mg cells. This effect is mainly noticed in the region described as the tumor debris. Tumor debris probably constitutes a necrotic tissue, the presence of which is both one of the characteristic morphological features of GBM and a poor prognostic factor [47]. The decrease in the phosphorus content in the necrotic area may be explained by the depletion of ATP resources and the damage of cell membranes. Phosphorus is present in phospholipids' building membranes and, therefore, their disintegration may be responsible for the reduced content of the element compared to a healthy tissue.

The topographic analysis of the brain slices taken from the rats subjected to the implantation of patient-derived cells also showed an increased deposition of Ca within the tumor. However, the element distribution was quite homogenous, which probably results from the fact that, in this case, the debris area was not formed within the tumor bulk. This, in turn, probably results from the differences in the aggressiveness of implanted GBM cells, as the presence of necrotic regions usually indicates a higher degree of malignancy and progression ability.

Glutamate excitotoxicity and the resulting elevated Ca accumulation are the common outcomes of the nervous tissue injuries occurring following trauma or cerebral ischemia [48–50]. The procedures performed in our study, necessary for implanting glioma cells, might lead to nervous tissue damage. This finding is confirmed by an increased Ca accumulation in the place where the culture medium was administered. Probably, the same

effect is responsible for the significant increase in Ca observed within the area where the T98g cells were implanted.

Fe is a key micronutrient essential for cells' growth and division. It is part of many proteins that enable proper cell functioning and are involved in processes such as oxygen transport, metabolism and DNA synthesis. On the other hand, Fe may also be potentially toxic for living cells by mediating free radicals' formation. According to epidemiological reports, an elevated body content of Fe is associated with a higher cancer risk [16]. Guisun et al. found that the amount of Fe increases in brain tumors together with their malignancy [18]. Furthermore, it was shown that the expression of ferritin, the protein storing Fe within living cells, grows with the glioma grade. Transferrin is responsible for Fe transport in the blood plasma and its delivery to body cells [28]. Cancer cells of various origins, compared to healthy cells, are characterized with a overexpression of transferrin receptor 1 (TfR1), which is responsible for binding the Fe from the blood and, therefore, their uptake of Fe is higher [51]. In addition, Fe-chelators suppress the progression of tumors both in vitro and in vivo, what may indicate the significant role of the element in the process of carcinogenesis [52]. It was shown that in the case of gliomas, the overexpression of transferrin receptors (TfR) is associated with an enhanced tumor cell proliferation and neuronal death. An increased or decreased TfR expression results in the reduction in or acceleration of glioma progression, respectively. Furthermore, by promoting the release of glutamate, TfR stimulate the reduction in the neurons' mass and provide a space for glioma development [53]. The importance of Fe for the metabolism of gliomas may be proven by the fact that 68-Ga, binding similarly to Fe by TfR, was successfully applied for the imaging of these tumors with positron emission tomography [54]. Furthermore, it was shown that elevated Fe uptake is observed for GBM stem-like cells being the self-renewing population of glioma cells involved in the tumor progression [28]. Stem-like cells may be located within the glioma core (in peri-vascular and peri-necrotic niches) or in its periphery, where they are involved in tumor invasion [55]. In our study, we observed the increased accumulation of Fe within the place of administration for all the experimental groups. The elevated Fe deposition within tumors developed from the patient-derived and U87mg cells may point at the regions of intensified proliferation having invasive potential. Especially for the tumors developed in the rats from the U group, the peripherally localized areas of higher Fe accumulation may be associated with the presence of the invasion-supporting GBM stem-like cells. In the case of the animals subjected to an intracerebral DMEM injection but also in the rats implanted with T98g cells and for which a tumor did not develop, a higher Fe content may result from tissue damage as a result of needle insertion and/or the subsequent hemorrhage.

The region of tumor debris, observed for gliomas developed from U87mg cells, is characterized by a significantly diminished accumulation of Zn, which is an element crucial for the proper functioning of living cells and takes part in the regulation of cells' growth and division as well as DNA synthesis [17]. As previously mentioned, this region probably corresponds with the necrotic tissue where zinc-involving processes may just not occur and, because of this, the amount of the element may be lower there both compared to the tumor bulk and its surroundings.

Many studies indicate the involvement of Cu in the formation of new blood vessels. This process, referred to as angiogenesis, is crucial for the tumor development characterized by increased blood supply. Cu activates various proangiogenic factors and stimulates the proliferation of endothelial cells, which line the inner surfaces of vessels [15]. It was shown that the use of Cu chelators as well as the inhibition of its intracellular transport may suppress the process of angiogenesis in different types of tumors [56,57] and, therefore, clinical trials are conducted to verify if low-copper diets may improve the outcome of the anti-cancer treatment of patients [58]. An increased amount of Cu was found in the serum of patients suffering from neoplasms of various origins [59]. Similar observations were made in the case of patients diagnosed with inflammatory diseases as well as in animal models of

these disorders. A higher concentration of copper in serum is probably associated with the increased level of ceruloplasmin—an inflammatory protein transporting Cu to tissues [60].

The results of our study showed a specific non-homogenous distribution of Cu within the tumor-affected hemisphere. The highest accumulation of the element was observed in the peri-tumoral area, and this effect was most pronounced for the U group. Such a result may point at the infiltrative character of the tumor and/or the ongoing angiogenesis related with its progression. Similar observations concerning the increased amount of Cu in the region surrounding human GBM were made by Dehnhardt et al. The authors suggested that the elevated quantity of the element in the peri-tumoral zone may result from the neovascularization as well as from inflammatory processes caused by the tumor development [61]. In turn, the decreased Cu accumulation observed in our study within the tumor bulk and debris probably resulted from the limited vascularization due to the neurodegenerative processes ongoing there.

Se is a well-known micronutrient involved in immunity stimulation and cancer prevention. Some of the Se-containing proteins protect against the damages induced by reactive oxygen species (ROS) considered as the inflammation and mutagenic factors leading to the carcinogenesis. Furthermore, through the cell cycle modulations, Se is involved in the repair of DNA and the apoptosis process [19]. Harmanci et al. examined the influence of selenomethionine on GBM cells and found that at low doses it promotes cell proliferation, while its high amounts stimulate cellular death [62]. An elevated accumulation of Se, compared to the healthy brain tissue, was found in various brain tumors of both human and animal origin [18,63–65]. Additionally, an increased accumulation of Se in the bulk of human GBM was usually accompanied by its lower concentration within the serum, which may prove the greater demand of neoplastic cells for this element [63]. All these reports are in agreement with our results, pointing at a significantly higher accumulation of selenium within the tumor bulk compared to the surrounding tissues. It should be also noted that Se is the only element whose distribution is quite homogenous within the tumor developed from U87mg cells. The Se quantity is elevated both in the tumor as well as in the debris area. In addition, the increased accumulation of the element clearly distinguishes the tumor bulks developed for the U and Pa groups from the areas where DMEM or T98g cells were administered when tumor development and expansion were not observed. Furthermore, among all the analyzed elements, only the region of increased Se quantity coincides with the extent of the neoplastic area, determined based on histological examinations. All these observations allow us to consider selenium as a potential elemental marker of tumor progression. We also suppose that the elevated accumulation of Se within a glioma bulk may result from an increased demand of proliferating tumor cells for this element and/or it may be a result of the immune system response to the ongoing tumor expansion and inflammation.

4. Materials and Methods

Detailed information concerning the used GBM cell lines, laboratory animals, pharmaceuticals and conditions of the experiment, including the procedure of implantation, are reported elsewhere [20]. Here, the most important assumptions of the performed research were briefly presented.

We used the three types of human glioma cells for the purposes of our investigation. These were two commercially available GBM cell lines (T98g and U87mg, both purchased from ATCC company) and the cells extracted directly from the tumor of a patient diagnosed with GBM. Isolation procedure of the patient cells was approved by the Bioethics Commission for the use of cellular material collected from patients in neurooncological operations (Decision no. 535/2017 of 13 June 2017, issued by the Bioethical Commission at the University of Nicolaus Copernicus in Toruń, Poland).

The subjects of the study were five groups of male Wistar rats at 9 weeks of age and each group consisted of six animals. Detailed characteristics of the experimental groups are presented in Table 2. Animal experiments were approved by the 2nd Local Institutional

Animal Care and Use Committee (agreement no. 119/2016) and were performed with international standards.

Table 2. Characteristics of examined animal groups.

Animal Group	Characteristics
N	Naive, normal rats (without implantation)
M	Implantation of 5 µL of Dulbecco's Modified Eagle Medium (DMEM) used for preparation of cell suspensions
Pa	Implantation of human GBM cells extracted from a patient, suspended in 5 µL of DMEM, 50,000 cells/µl
T	Implantation of cultured human GBM cell line T98g, suspended in 5 µL of DMEM, 50,000 cells/µl
U	Implantation of cultured human GBM cell line U87mg, suspended in 5 µL of DMEM, 5000 cells/µl

Gender dependence in GBM is observed both in case of the occurrence and the survival rates, and men are more at risk that women rting GBM stem-like cells. p. uld be addressed [66]. An ideal animal model of GBM should involve both male and female individuals. Moreover, taking into account the variability of the sex hormones during the female life, such a study should include groups of animals at different developmental stages. Due to practical reasons and restrictions on the number of animals involved in the experiment, only male rats were used in this study. Nonetheless, due to the mentioned gender differences for GBM, we admit that similar research including female rats is needed and we plan to perform it in the future.

The procedure of implanting cells or administering DMEM into rat brains consisted of a few steps. The animals were pre-anesthetized and immobilized in a stereotactic apparatus. Next, after the induction of general anesthesia, a particular type of suspension was transcranially implanted/administered to their left brain hemispheres (coordinates antero-posterior: −0.30 mm; medio-lateral: 3.0 mm; dorso-ventral: 5.0 mm [67]). The initial stage was to drill a hole in the rat's skull, into which a needle (27-gauge needle on a Hamilton syringe) with the cell suspension was then placed. One minute after the insertion of the needle, a 5-microliter volume of cell suspension was injected into the brain, and the needle was slowly removed after 3 min. The wound was then stitched with a stapler and sanitized. Animals were awakened from anesthesia a few minutes after completing the implantation procedure. The rats subjected to the implantation of glioma cells were, afterwards, daily immunosuppressed with cyclosporine A (Novartis Poland at a daily dose of 5 mg/kg of body mass) and observed in terms of behavioral changes. In preliminary studies, taking into account the health status of the animals after the implantation (weight loss, neurological problems), the survival time was determined in the respective groups, 21 days for the Pa, T and M groups and 15 days for the U group. At the end of the experiment, the rats received a euthanasia agent (Euthasol vet. 400 mg/mL, Le Vet) and, afterwards, they were subjected to perfusion with a physiological saline of high analytical purity. The brains removed from the skulls were frozen in liquid nitrogen and subsequently cut into 20-micrometer-thick slices using cryomicrotome. Tissue sections taken from the place of implantation were used for further analysis. These specimens were mounted on the Ultralene foil and freeze-dried.

For the qualitative and quantitative elemental analysis of brain slices, the SR-XRF microscopy was applied. The measurements were performed at the FLUO beamline at the KIT Synchrotron Light Source in Karlsruhe, Germany [68]. The X-ray beam energy of 16 keV enabled efficient detection of the following elements: P, S, K, Ca, Fe, Cu, Zn and Se. A beam size of 200 µm × 200 µm was enough to differentiate the main brain structures as well as the area of tumor/implantation. Typically, the acquisition time of a single XRF spectrum was 5 s per pixel.

5. Conclusions

The local elemental anomalies observed in our study were correlated with the histological changes of brain tissue that resulted from tumor expansion. The tumors developing from U87mg cells and patient-derived cells were characterized with the increased accumulation of Fe and Se, whilst the tissue directly surrounding the tumor presented a higher areal density of Cu. The tissues taken from animals subjected to the implantation of T98g cells were similar to those taken from the rats that obtained the culture medium, in terms of both morphology and the elemental distribution. Although no signs of tumor development were found for these groups, the tissue damage connected with the administration of cells or culture medium was observed and characterized by an increased accumulation of Fe and Ca.

Author Contributions: Conceptualization, K.P., Z.S. and J.C.; Formal analysis, K.P. and J.C.; Investigation, K.P., M.C., N.J.-O. and J.C.; Methodology, K.P., Z.S., M.C., N.J.-O., D.R., R.S., T.B. and J.C.; Resources, K.P., Z.S., M.C., D.R., R.S., T.B. and J.C.; Supervision, Z.S. and J.C.; Validation, K.P. and J.C.; Writing—original draft, K.P. and J.C.; Writing—review and editing, Z.S., M.C., K.J. and R.S. All authors have read and agreed to the published version of the manuscript.

Funding: This work was partially financed by the Ministry of Education and Science (Poland). Karolina Planeta and Natalia Janik-Olchawa have been supported by the EU Project POWR.03.02.00-00-I004/16. For the evaluation of tissues morphology, the microscope purchased from the funds granted to the AGH UST in the frame of the "Excellence Initiative—Research University" program was applied.

Institutional Review Board Statement: The procedure of isolation of the patient cells was approved by the Bioethics Commission for the use of cellular material collected from patients in neurooncological operations (Decision no. 535/2017 of 13 June 2017, issued by the Bioethical Commission at the University of Nicolaus Copernicus in Toruń, Poland). Animal experiments were approved by the 2nd Local Institutional Animal Care and Use Committee (agreement no. 119/2016) and were performed with the international standards.

Informed Consent Statement: Informed consent was obtained from the patient for cell isolation and all the procedures were in agreement with relevant guidelines and regulations.

Data Availability Statement: The data that support the findings of this study will be made available after reasonable request. We may require the participation in the authorship after the use of the shared data.

Acknowledgments: The authors acknowledge Thomas Spangenberg, David Haas and Stefan Uhlemann who provided the technical support at the FLUO beamline at the KIT Synchrotron Light Source.

Conflicts of Interest: The authors declare no conflict of interest.

References

1. Czapski, B.; Baluszek, S.; Herold-Mende, C.; Kaminska, B. Clinical and immunological correlates of long term survival in glioblastoma. *Contemp. Oncol.* **2018**, *22*, 81–85. [CrossRef] [PubMed]
2. Ostrom, Q.T.; Patil, N.; Cioffi, G.; Waite, K.; Kruchko, C.; Barnholtz-Sloan, J.S. CBTRUS Statistical Report: Primary Brain and Other Central Nervous System Tumors Diagnosed in the United States in 2013–2017. *Neuro-Oncology* **2020**, *22*, iv1–iv96. [CrossRef]
3. Depciuch, J.; Tołpa, B.; Witek, P.; Szmuc, K.; Kaznowska, E.; Osuchowski, M.; Król, P.; Cebulski, J. Raman and FTIR spectroscopy in determining the chemical changes in healthy brain tissues and glioblastoma tumor tissues. *Spectrochim. Acta Part A Mol. Biomol. Spectrosc.* **2020**, *225*, 117526. [CrossRef]
4. Szczerbowska-Boruchowska, M.; Lankosz, M.; Adamek, D. First step toward the "fingerprinting" of brain tumors based on synchrotron radiation X-ray fluorescence and multiple discriminant analysis. *JBIC J. Biol. Inorg. Chem.* **2011**, *16*, 1217–1226. [CrossRef]
5. Gregory, J.V.; Kadiyala, P.; Doherty, R.; Cadena, M.; Habeel, S.; Ruoslahti, E.; Lowenstein, P.R.; Castro, M.G.; Lahann, J. Systemic brain tumor delivery of synthetic protein nanoparticles for glioblastoma therapy. *Nat. Commun.* **2020**, *11*, 5687. [CrossRef] [PubMed]
6. Song, X.; Shu, X.-H.; Wu, M.-L.; Zheng, X.; Jia, B.; Kong, Q.-Y.; Liu, J.; Li, H. Postoperative resveratrol administration improves prognosis of rat orthotopic glioblastomas. *BMC Cancer* **2018**, *18*, 871. [CrossRef]

7. Marrero, L.; Wyczechowska, D.; Musto, A.E.; Wilk, A.; Vashistha, H.; Zapata, A.; Walker, C.; Velasco-Gonzalez, C.; Parsons, C.; Wieland, S.; et al. Therapeutic Efficacy of Aldoxorubicin in an Intracranial Xenograft Mouse Model of Human Glioblastoma. *Neoplasia* **2014**, *16*, 874–882. [CrossRef] [PubMed]
8. Chwiej, J.; Patulska, A.; Skoczen, A.; Janeczko, K.; Ciarach, M.; Simon, R.; Setkowicz, Z. Elemental changes in the hippocampal formation following two different formulas of ketogenic diet: An X-ray fluorescence microscopy study. *JBIC J. Biol. Inorg. Chem.* **2015**, *20*, 1277–1286. [CrossRef]
9. Turyanskaya, A.; Rauwolf, M.; Pichler, V.; Simon, R.; Burghammer, M.; Fox, O.J.L.; Sawhney, K.; Hofstaetter, J.G.; Roschger, A.; Roschger, P.; et al. Detection and imaging of gadolinium accumulation in human bone tissue by micro- and submicro-XRF. *Sci. Rep.* **2020**, *10*, 6301. [CrossRef] [PubMed]
10. Osterode, W.; Falkenberg, G.; Ferenci, P.; Wrba, F. Quantitative trace element mapping in liver tissue from patients with Wilson's disease determined by micro X-ray fluorescence. *J. Trace Elem. Med. Biol.* **2019**, *51*, 42–49. [CrossRef]
11. Farquharson, M.J.; Al-Ebraheem, A.; Falkenberg, G.; Leek, R.; Harris, A.L.; Bradley, D.A. The distribution of trace elements Ca, Fe, Cu and Zn and the determination of copper oxidation state in breast tumour tissue using μSRXRF and μXANES. *Phys. Med. Biol.* **2008**, *53*, 3023–3037. [CrossRef]
12. Xiao, A.Y.; Maynard, M.R.; Piett, C.G.; Nagel, Z.D.; Alexander, J.S.; Kevil, C.G.; Berridge, M.V.; Pattillo, C.B.; Rosen, L.R.; Miriyala, S.; et al. Sodium sulfide selectively induces oxidative stress, DNA damage, and mitochondrial dysfunction and radiosensitizes glioblastoma (GBM) cells. *Redox Biol.* **2019**, *26*, 101220. [CrossRef] [PubMed]
13. Huang, L.; Li, B.; Li, W.; Guo, H.; Zou, F. ATP-sensitive potassium channels control glioma cells proliferation by regulating ERK activity. *Carcinogenesis* **2009**, *30*, 737–744. [CrossRef] [PubMed]
14. Martin, F.; Lemmen, L.J. Calcification in intracranial neoplasms. *Am. J. Pathol.* **1952**, *28*, 1107–1131. [PubMed]
15. Finney, L.; Vogt, S.; Fukai, T.; Glesne, D. Copper and angiogenesis: Unravelling a relationship key to cancer progression. *Clin. Exp. Pharmacol. Physiol.* **2009**, *36*, 88–94. [CrossRef] [PubMed]
16. Torti, S.V.; Torti, F.M. Iron and cancer: More ore to be mined. *Nat. Rev. Cancer* **2013**, *13*, 342–355. [CrossRef]
17. MacDonald, R.S. The Role of Zinc in Growth and Cell Proliferation. *J. Nutr.* **2000**, *130*, 1500S–1508S. [CrossRef]
18. Guisun, Z.; Yinson, W.; Mingguang, T.; Min, Z.; Yongjie, W.; Fulin, Z. Preliminary study of trace elements in human brain tumor tissues by instrumental neutron activation analysis. *J. Radioanal. Nucl. Chem. Artic.* **1991**, *151*, 327–335. [CrossRef]
19. Brozmanová, J.; Mániková, D.; Vlčková, V.; Chovanec, M. Selenium: A double-edged sword for defense and offence in cancer. *Arch. Toxicol.* **2010**, *84*, 919–938. [CrossRef]
20. Planeta, K.; Setkowicz, Z.; Janik-Olchawa, N.; Matusiak, K.; Ryszawy, D.; Drozdz, A.; Janeczko, K.; Ostachowicz, B.; Chwiej, J. Comparison of Elemental Anomalies Following Implantation of Different Cell Lines of Glioblastoma Multiforme in the Rat Brain: A Total Reflection X-ray Fluorescence Spectroscopy Study. *ACS Chem. Neurosci.* **2020**, *11*, 4447–4459. [CrossRef]
21. Solé, V.A.; Papillon, E.; Cotte, M.; Walter, P.; Susini, J. A Multiplatform Code for the Analysis of Energy-Dispersive X-ray Fluorescence Spectra. *Spectrochim. Acta Part B At. Spectrosc.* **2007**, *62*, 63–68. [CrossRef]
22. Nachar, N. The Mann-Whitney U: A Test for Assessing Whether Two Independent Samples Come from the Same Distribution. *Tutor. Quant. Methods Psychol.* **2008**, *4*, 13–20. [CrossRef]
23. Wandzilak, A.; Czyzycki, M.; Radwanska, E.; Adamek, D.; Geraki, K.; Lankosz, M. X-ray fluorescence study of the concentration of selected trace and minor elements in human brain tumours. *Spectrochim. Acta Part B At. Spectrosc.* **2015**, *114*, 52–57. [CrossRef]
24. Chiba, R.; Morikawa, N.; Sera, K.; Ishida, K.; Nagashima, H.; Shigeeda, W.; Deguchi, H.; Tomoyasu, M.; Hosokawa, T.; Saito, H.; et al. Elemental and mutational analysis of lung tissue in lung adenocarcinoma patients. *Transl. Lung Cancer Res.* **2019**, *8*, S224–S234. [CrossRef] [PubMed]
25. Al-Ebraheem, A.; Dao, E.; Geraki, K.; Farquharson, M.J. Emerging Patterns in the Distribution of Trace Elements in Ovarian, Invasive and In-Situ Breast Cancer. *J. Phys. Conf. Ser.* **2014**, *499*, 012014. [CrossRef]
26. Pamphlett, R.; Satgunaseelan, L.; Jew, S.K.; Doble, P.A.; Bishop, D.P. Elemental bioimaging shows mercury and other toxic metals in normal breast tissue and in breast cancers. *PLoS ONE* **2020**, *15*, e0228226. [CrossRef]
27. Selverstone, B.; Moulton, M.J. The phosphorus metabolism of gliomas: A study with radioactive isotopes. *Brain* **1957**, *80*, 362–375. [CrossRef]
28. Schonberg, D.L.; Miller, T.E.; Wu, Q.; Flavahan, W.A.; Das, N.K.; Hale, J.S.; Hubert, C.G.; Mack, S.C.; Jarrar, A.M.; Karl, R.T.; et al. Preferential Iron Trafficking Characterizes Glioblastoma Stem-like Cells. *Cancer Cell* **2015**, *28*, 441–455. [CrossRef]
29. Dejos, C.; Gkika, D.; Cantelmo, A.R. The Two-Way Relationship Between Calcium and Metabolism in Cancer. *Front. Cell Dev. Biol.* **2020**, *8*, 573747. [CrossRef]
30. Hsu, M.Y.; Mina, E.; Roetto, A.; Porporato, P.E. Iron: An Essential Element of Cancer Metabolism. *Cells* **2020**, *9*, 2591. [CrossRef] [PubMed]
31. Xiao, Y.; Chen, D.; Zhang, X.; Cui, Q.; Fan, Y.; Bi, C.; Dou, Q.P. Molecular study on copper-mediated tumor proteasome inhibition and cell death. *Int. J. Oncol.* **2010**, *37*, 81–87. [CrossRef] [PubMed]
32. Yu, Y.; Gutierrez, E.; Kovacevic, Z.; Saletta, F.; Obeidy, P.; Suryo Rahmanto, Y.; Richardson, D.R. Iron Chelators for the Treatment of Cancer. *Curr. Med. Chem.* **2012**, *19*, 2689–2702. [CrossRef] [PubMed]
33. Evans, S.O.; Khairuddin, P.F.; Jameson, M.B. Optimising Selenium for Modulation of Cancer Treatments. *Anticancer Res.* **2017**, *37*, 6497–6509.

34. Ishimura, M.; Yamamoto, Y.; Mitamura, K.; Norikane, T.; Nishiyama, Y. A Case of Glioblastoma With Calcified Region Imaged With 18F-NaF PET/CT. *Clin. Nucl. Med.* **2018**, *43*, 764–765. [CrossRef] [PubMed]
35. Kubota, T.; Kogure, Y.; Yamamoto, S.; Matsubara, S.; Kitano, T.; Hayashi, M. Calcification in glioblastoma multiforme of the cervical spinal cord. *Surg. Neurol.* **1986**, *26*, 183–186. [CrossRef]
36. Mallya, V.; Siraj, F.; Singh, A.; Sharma, K. Giant cell glioblastoma with calcification and long-term survival. *Indian J. Cancer* **2015**, *52*, 704. [CrossRef]
37. Kroh, H.; Matyja, E.; Marchel, A.; Bojarski, P. Heavily lipidized, calcified giant cell glioblastoma in an 8-year-old patient, associated with neurofibromatosis type 1 (NF1): Report of a case with long-term survival. *Clin. Neuropathol.* **2004**, *23*, 286–291.
38. Zeng, Y.; Zhu, X.; Wang, Y.; Liu, B.; Yang, X.; Wang, Q.; Du, J.; Ma, Y.; Lin, L.; Fu, P.; et al. Clinicopathological, Immunohistochemical and Molecular Genetic Study on Epithelioid Glioblastoma: A Series of Fifteen Cases with Literature Review. *OncoTargets Ther.* **2020**, *13*, 3943–3952. [CrossRef]
39. Bhatoe, H.S.; Kumar, H. Calcified occipital glioblastoma. *Neurol. India* **2004**, *52*, 130.
40. Broniscer, A.; Tatevossian, R.G.; Sabin, N.D.; Klimo, P.; Dalton, J.; Lee, R.; Gajjar, A.; Ellison, D.W. Clinical, radiological, histological and molecular characteristics of paediatric epithelioid glioblastoma: Epithelioid glioblastoma in children. *Neuropathol. Appl. Neurobiol.* **2014**, *40*, 327–336. [CrossRef]
41. Bähr, O.; Hattingen, E.; Rieger, J.; Steinbach, J.P. Bevacizumab-induced tumor calcifications as a surrogate marker of outcome in patients with glioblastoma. *Neuro-Oncology* **2011**, *13*, 1020–1029. [CrossRef]
42. Blumenthal, D.T.; Aisenstein, O.; Ben-Horin, I.; Ben Bashat, D.; Artzi, M.; Corn, B.W.; Kanner, A.A.; Ram, Z.; Bokstein, F. Calcification in high grade gliomas treated with bevacizumab. *J. Neuro-Oncol.* **2015**, *123*, 283–288. [CrossRef]
43. Weiseenthal, L.; Williamson, S.; Brunschwiler, C.; Rueff-Weisenthal, C. Bevacizumab-induced tumor calcifications can be elicited in glioblastoma microspheroid culture and represent massive calcium accumulation death (MCAD) of tumor endothelial cells. *Nat. Preced.* **2012**. [CrossRef]
44. Halpin, S.; Kingsley, D. Disappearance of cerebral calcification as a sign of tumor growth. *Am. J. Neuroradiol.* **1993**, *14*, 119–122.
45. Ye, Z.-C.; Sontheimer, H. Glioma Cells Release Excitotoxic Concentrations of Glutamate. *Cancer Res.* **1999**, *59*, 4383–4391. [PubMed]
46. Noch, E.; Khalili, K. Molecular mechanisms of necrosis in glioblastoma: The role of glutamate excitotoxicity. *Cancer Biol. Ther.* **2009**, *8*, 1791–1797. [CrossRef] [PubMed]
47. Liu, S.; Wang, Y.; Xu, K.; Wang, Z.; Fan, X.; Zhang, C.; Li, S.; Qiu, X.; Jiang, T. Relationship between necrotic patterns in glioblastoma and patient survival: Fractal dimension and lacunarity analyses using magnetic resonance imaging. *Sci. Rep.* **2017**, *7*, 8302. [CrossRef] [PubMed]
48. Chwiej, J.; Gabrys, H.; Janeczko, K.; Kutorasinska, J.; Gzielo-Jurek, K.; Matusiak, K.; Appel, K.; Setkowicz, Z. Elemental anomalies in the hippocampal formation after repetitive electrical stimulation: An X-ray fluorescence microscopy study. *J. Biol. Inorg. Chem.* **2014**, *19*, 1209. [CrossRef]
49. Deshpande, J.K.; Siesjö, B.K.; Wieloch, T. Calcium Accumulation and Neuronal Damage in the Rat Hippocampus following Cerebral Ischemia. *J. Cereb. Blood Flow Metab.* **1987**, *7*, 89–95. [CrossRef]
50. Dorsett, C.R.; McGuire, J.L.; DePasquale, E.A.K.; Gardner, A.E.; Floyd, C.L.; McCullumsmith, R.E. Glutamate Neurotransmission in Rodent Models of Traumatic Brain Injury. *J. Neurotrauma* **2017**, *34*, 263–272. [CrossRef] [PubMed]
51. Shen, Y.; Li, X.; Dong, D.; Zhang, B.; Xue, Y.; Shang, P. Transferrin receptor 1 in cancer: A new sight for cancer therapy. *Am. J. Cancer Res.* **2018**, *8*, 916–931.
52. Richardson, D.R. Iron chelators as therapeutic agents for the treatment of cancer. *Crit. Rev. Oncol./Hematol.* **2002**, *42*, 267–281. [CrossRef]
53. Chirasani, S.R.; Markovic, D.S.; Synowitz, M.; Eichler, S.A.; Wisniewski, P.; Kaminska, B.; Otto, A.; Wanker, E.; Schäfer, M.; Chiarugi, P.; et al. Transferrin-receptor-mediated iron accumulation controls proliferation and glutamate release in glioma cells. *J. Mol. Med.* **2009**, *87*, 153–167. [CrossRef]
54. Behr, S.C.; Villanueva-Meyer, J.E.; Li, Y.; Wang, Y.-H.; Wei, J.; Moroz, A.; Lee, J.K.L.; Hsiao, J.C.; Gao, K.T.; Ma, W.; et al. Targeting iron metabolism in high-grade glioma with 68Ga-citrate PET/MR. *JCI Insight* **2018**, *3*, e93999. [CrossRef]
55. Nishikawa, M.; Inoue, A.; Ohnishi, T.; Kohno, S.; Ohue, S.; Matsumoto, S.; Suehiro, S.; Yamashita, D.; Ozaki, S.; Watanabe, H.; et al. Significance of Glioma Stem-Like Cells in the Tumor Periphery That Express High Levels of CD44 in Tumor Invasion, Early Progression, and Poor Prognosis in Glioblastoma. *Stem Cells Int.* **2018**, *2018*, 5387041. [CrossRef] [PubMed]
56. Karginova, O.; Weekley, C.M.; Raoul, A.; Alsayed, A.; Wu, T.; Lee, S.S.-Y.; He, C.; Olopade, O.I. Inhibition of Copper Transport Induces Apoptosis in Triple-Negative Breast Cancer Cells and Suppresses Tumor Angiogenesis. *Mol. Cancer Ther.* **2019**, *18*, 873–885. [CrossRef] [PubMed]
57. Yoshida, D.; Ikeda, Y.; Nakazawa, S. Copper Chelation Inhibits Tumor Angiogenesis in the Experimental 9L Gliosarcoma Model. *Neurosurgery* **1995**, *37*, 287–293. [CrossRef]
58. Brewer, G.J.; Dick, R.D.; Grover, D.K.; LeClaire, V.; Tseng, M.; Wicha, M.; Pienta, K.; Redman, B.G.; Jahan, T.; Sondak, V.K.; et al. Treatment of Metastatic Cancer with Tetrathiomolybdate, an Anticopper, Antiangiogenic Agent: Phase I Study. *Clin. Cancer Res.* **2000**, *6*, 1–10. [PubMed]
59. Zowczak, M.; Iskra, M.; Torliński, L.; Cofta, S. Analysis of Serum Copper and Zinc Concentrations in Cancer Patients. *Biol. Trace Elem. Res.* **2001**, *82*, 001–008. [CrossRef]

60. Milanino, R.; Marrella, M.; Gasperini, R.; Pasqualicchio, M.; Velo, G. Copper and zinc body levels in inflammation: An overview of the data obtained from animal and human studies. *Agents Actions* **1993**, *39*, 195–209. [CrossRef]
61. Dehnhardt, M.; Zoriy, M.V.; Khan, Z.; Reifenberger, G.; Ekström, T.J.; Sabine Becker, J.; Zilles, K.; Bauer, A. Element distribution is altered in a zone surrounding human glioblastoma multiforme. *J. Trace Elem. Med. Biol.* **2008**, *22*, 17–23. [CrossRef]
62. Harmanci, D. In Vitro Effects of Selenium on Human Glioblastoma Multiforme Cell Lines: A Preliminary Study. *Acta Clin. Croat.* **2017**, *56*, 48–57. [CrossRef]
63. Stojsavljević, A.; Vujotić, L.; Rovčanin, B.; Borković-Mitić, S.; Gavrović-Jankulović, M.; Manojlović, D. Assessment of trace metal alterations in the blood, cerebrospinal fluid and tissue samples of patients with malignant brain tumors. *Sci. Rep.* **2020**, *10*, 3816. [CrossRef] [PubMed]
64. Civit, T.; Houdayer, A.J.; Kennedy, G. A search for trace elements in some human intracranial tumors by instrumental neutron activation analysis. *Biol. Trace Elem. Res.* **2000**, *74*, 203–210. [CrossRef]
65. Zhang, Z.; Chinen, Y.; Zhu, Z.; Kimura, M.; Itokawa, Y. Uptake and distribution of sodium selenite in rat brain tumor. *Biol. Trace Elem. Res.* **1995**, *48*, 45–50. [CrossRef] [PubMed]
66. Tian, M.; Ma, W.; Chen, Y.; Yu, Y.; Zhu, D.; Shi, J.; Zhang, Y. Impact of gender on the survival of patients with glioblastoma. *Biosci. Rep.* **2018**, *38*, BSR20180752. [CrossRef] [PubMed]
67. Paxinos, G.; Watson, C. *The Rat Brain in Stereotaxic Coordinates*; Academic Press: New York, NY, USA, 1986.
68. Simon, R.; Buth, G.; Hagelstein, M. The X-ray-fluorescence facility at ANKA, Karlsruhe: Minimum detection limits and micro probe capabilities. *Nucl. Instrum. Methods Phys. Res. Sect. B Beam Interact. Mater. At.* **2003**, *199*, 554–558. [CrossRef]

Spectrochimica Acta Part B: Atomic Spectroscopy

The first total reflection X-ray fluorescence round-robin test of mammalian tissue samples: preliminary results

--Manuscript Draft--

Manuscript Number:	SAPB-D-23-00065
Article Type:	Research Paper
Keywords:	total reflection X-ray fluorescence; element analysis; round-robin test; inter-comparison investigation; validation parameters
Corresponding Author:	Joanna Chwiej Krakow, Poland
First Author:	Karolina Olbrich
Order of Authors:	Karolina Olbrich
	Aldona Kubala-Kukus
	Eva Margui
	Ramon Fernández Ruiz
	Katarzyna Matusiak
	Jolanta Wudarczyk-Mocko
	Pawel Wrobel
	Zuzanna Setkowicz
	Joanna Chwiej
Abstract:	The study presented in this paper was carried out in the frame of the COST Action 18130 (European Network for Chemical Elemental Analysis by Total Reflection X-ray Fluorescence) and its purpose was performing a round-robin test for the element analysis of mammalian tissue samples using the total reflection X-ray fluorescence (TXRF). To achieve the goal of the study, the selected rat organs (kidney, heart, spleen and lung) were subjected to microwave digestion and, in the liquid form, were sent to four European laboratories participating in the inter-comparison investigation. There, using various commercially available TXRF spectrometers, their elemental composition was determined. The carried inter-laboratory comparisons involved the concentrations of macro (P, S and K), micro (Ca) and trace (Fe, Cu, Zn and Se) elements in the examined samples and the validation parameters such as the detection limits of the examined elements as well as the intra-day and inter-day precision. To verify the variation in the results acquired in participating laboratories, for all measured elements, the inter-laboratory precision was also evaluated. Results obtained by TXRF were also compared with the ones resulting from ICP-MS (Se) and ICP-OES analysis (P, S, K, Ca, Fe, Cu and Zn). The results obtained as part of the study confirmed the high usefulness of the TXRF method in the elemental analysis of animal tissues. As expected, the best results in terms of the examined validation parameters were obtained for elements with higher atomic numbers (Fe, Cu, Zn and Se). For these analytes, the round-robin test confirmed a good accuracy (around 100% for Fe, Cu, Zn) and precision (intra-day <6%, inter-day <12% and inter-laboratory <12%) what supports the use of TXRF for their determination in the mammalian tissue samples. The obtained results allowed, moreover, to indicate potential issues that require resolving in order to increase the usefulness of the method in case of the analysis of light elements such as P, S or K. It is worth mentioning here, inter alia, the improvement of the sample preparation procedures aiming at the reduction of self-absorption in its dried residue, optimization and/or unification of the sensitivity calibration and the spectra fitting procedures in particular laboratories.

The first total reflection X-ray fluorescence round-robin test of mammalian tissue samples: preliminary results

Karolina Olbrich (1), Aldona Kubala-Kukus (2)(3), Eva Marguí (4), Ramón Fernández-Ruiz (5), Katarzyna Matusiak (1), Jolanta Wudarczyk-Mocko (3), Pawel Wrobel (1), Zuzanna Setkowicz (6), Joanna Chwiej (1)*

(1) Faculty of Physics and Applied Computer Science, AGH University of Science and Technology, Krakow, Poland.
(2) Institute of Physics, Jan Kochanowski University, Kielce, Poland.
(3) Holy Cross Cancer Center, Kielce, Poland.
(4) Department of Chemistry, University of Girona, Girona, Spain.
(5) Interdepartmental Research Service (SIdI), Autonomous University of Madrid, Madrid, Spain.
(6) Institute of Zoology and Biomedical Research, Jagiellonian University, Krakow, Poland.

*Corresponding author:
joanna.chwiej@fis.agh.edu.pl

Abstract

The study presented in this paper was carried out in the frame of the COST Action 18130 (European Network for Chemical Elemental Analysis by Total Reflection X-ray Fluorescence) and its purpose was performing a round-robin test for the element analysis of mammalian tissue samples using the total reflection X-ray fluorescence (TXRF). To achieve the goal of the study, the selected rat organs (kidney, heart, spleen and lung) were subjected to microwave digestion and, in the liquid form, were sent to four European laboratories participating in the inter-comparison investigation. There, using various commercially available TXRF spectrometers, their elemental composition was determined. The carried inter-laboratory comparisons involved the concentrations of macro (P, S and K), micro (Ca) and trace (Fe, Cu, Zn and Se) elements in the examined samples and the validation parameters such as the detection limits of the examined elements as well as the intra-day and inter-day precision. To verify the variation in the results acquired in participating laboratories, for all measured elements, the inter-laboratory precision was also evaluated. Results obtained by TXRF were also compared with the ones resulting from ICP-MS (Se) and ICP-OES analysis (P, S, K, Ca, Fe, Cu and Zn).

The results obtained as part of the study confirmed the high usefulness of the TXRF method in the elemental analysis of animal tissues. As expected, the best results in terms of the examined validation parameters were obtained for elements with higher atomic numbers (Fe, Cu, Zn and Se). For these analytes, the round-robin test confirmed a good accuracy (around 100% for Fe, Cu, Zn) and precision (intra-day <6%, inter-day <12% and inter-laboratory <12%) what supports the use of TXRF for their determination in the mammalian tissue samples. The obtained results allowed, moreover, to indicate potential issues that require resolving in order to increase the usefulness of the method in case of the analysis of light elements such as P, S or K. It is worth mentioning here, *inter alia*, the improvement of the sample preparation procedures aiming at the reduction of self-absorption in its dried residue, optimization and/or unification of the sensitivity calibration and the spectra fitting procedures in particular laboratories.

Keywords:
total reflection X-ray fluorescence; element analysis; round-robin test; inter-comparison investigation; validation parameters

Introduction

As major, minor and trace elements play an important role in the proper functioning of living organisms and both their too low and too high concentrations in cells, tissues and organs may result in various pathological states, the accurate quantitative elemental analysis of biological samples constitutes a very important issue of biomedicine [i,ii,iii,iv,v]. Various instrumental methods are applied for this purpose, including flame and graphite furnace atomic absorption spectrometry (F-AAS and GF-AAS), inductively coupled plasma optical emission spectrometry (ICP-OES) and inductively coupled plasma mass spectrometry (ICP-MS) [vi,vii,viii]. The wide literature study, done in our previous paper, showed that the most frequently used methods of elemental analysis of biomedical samples are ICP-MS and ICP-AES, which, in contrary to F-AAS and GF-AAS, allow for simultaneous determination of many elements in the sample [ix].

The total reflection X-ray fluorescence (TXRF) spectroscopy, being the variant of conventional energy dispersive X-ray fluorescence in which the source-sample-detector geometry leads to significant decrease of the recorded background and simultaneous increase of the intensity of atomic fluorescence signals, also belongs to the instrumental methods of elemental analysis [x]. Among various analytical techniques based on X-ray fluorescence, TXRF is considered as highly useful for the study of biomedical samples. It is due to the fast and simultaneously multi-elemental analysis, wide range of concentrations of examined elements as well as small amounts of sample required for the measurement. Furthermore, the use of the total reflection geometry in the TXRF enables the measurements of liquid samples with reduction of the scattered radiation, which influences on the achievement of low detection limits, down to few ppb. The easy procedure of quantification, based on the internal standard method, is also significant [xii]. Compared to ICP-based techniques, widely applied in elemental analysis of biomedical samples, TXRF systems are cost-effective since they do not require gas or cooling media for function [ix]. Because all of its properties, during the last years the TXRF method gains more and more popularity in the studies of elemental composition of various biomedical samples [xi,xii,xiii,xiv,xv,xvi].

A round-robin test is a comparative inter-laboratory study perform either with different methods, routinely applied by cooperative laboratories, or with the same method but with different equipment. Its purpose is to test the performance of experimental procedure or the analytical method. In round-robin test, the aim of several cooperative laboratories may be determination of elements concentration in sample, performed under established conditions [xvii]. In the last years, extensive effort have been done for standardization of the TXRF method [xviii,xix,xx,xxi,xxii]. However, according to our best knowledge, the inter-laboratory test on TXRF analysis of biological samples have not been performed so far.

The present study was performed in the frame of the European Network for Chemical Elemental Analysis by Total Reflection X-ray Fluorescence (COST Action 18130, https://enforcetxrf.eu/). The purpose of this international collaboration was the evaluation of the result variability of tissue elemental analysis done by different laboratories with different TXRF spectrometers. For investigation we have chosen organs (kidney, heart, spleen and lung) taken from four naive normal rats, that constituted the control group in other our study [xxiii,xxiv]. The organs were subjected to microwave assisted digestion and after adding the internal standard sent to four European laboratories participating in the inter-comparison investigation. All the laboratories involved in the study had a long-term previous experience in

the elemental analysis of biological material using various spectroscopic methods, especially those based on the X-ray fluorescence [xxv,xxvi,xxvii,xxviii,xxix,xxx,ix,xxxi,xxxii,xxxiii,xxxiv,xxxv,xxxvi,xxxvii,xxxviii,xxxix].

For the realization of the purposes of the investigation, commercially available TXRF spectrometers were applied. These were two S2 PICOFOX Bruker Nano spectrometers with molybdenum (Mo) anode X-ray tube, the analogous system with tungsten (W) anode X-ray tube and Rigaku Nanohunter II spectrometer also equipped with Mo-anode X-ray tube.

Inter-laboratory comparisons were made for a broad spectrum of elements (atomic number from 15 to 34), the contents of which in the tissues varied in a very wide range. For all the samples we examined the content of both macro (P, S and K), micro (Ca) and trace (Fe, Cu, Zn and Se) elements [xl]. The quantitative data obtained in four laboratories were compared and the validation parameters including the detection limits of examined elements for various organs and intra-day as well as inter-day precision were calculated for them. Additionally, in order to verify the variation in the results acquired in frame of the carried inter-comparison investigation, for all measured elements the inter-laboratory precision was evaluated. Results obtained by TXRF were also compared with the ones resulting from ICP-MS (Se) and ICP-OES analysis (P, S, K, Ca, Fe, Cu and Zn).

Materials and methods

Experimental animals and sample preparation

The subject of the study was a group consisting of 4 normal male Wistar rats that originated from the colony of the Department of Experimental Neuropathology from the Institute of Zoology and Biomedical Research, Jagiellonian University, Krakow. Animal care and experiments were approved by the 2nd Local Institutional Animal Care and Use Committee in Krakow (agreement no. 119/2016) and were performed in accordance with international standards and ARRIVE guidelines. On the 60th day of postnatal life, the animals were perfused with 0.9% saline of high analytical purity and their organs (left kidney, heart, spleen and left lung) were excised from bodies, weighted and frozen in the liquid nitrogen. In total, 16 organs (4 rats x 4 organs per animal) were separately packed in sterile Whirl-pack® bags and stored in ultra-freezer in -80°C. Such procedure, that was used also in our previous studies, protects tissues against elemental changes during the period between organ collection and tissue digestion [xxiii,xxix,xxx].

For the purpose of elemental analysis using the TXRF method, the tissues were reweighted (information on the weight of examined organs were included in Table S1 of Supplementary materials) and digested in high purity 65% nitric acid (100441/Suprapur®, Merck Group). The typical volume of added acid was equal to 2.5 ml per 1g of tissue. The process was performed with the use of SpeedWave 4 microwave digestion system (Berghof). The conditions of the digestion process were chosen based on the recommendations of the system manufacturer and were in details described in our previous paper [xxiii]. The quantitative elemental analysis was based on the internal standard method and the 1000 mg/l gallium (Ga) solution (Ga ICP standard in HNO_3 2-3% 1000 mg/l Ga Certipur®, Merck) was used for this purpose. 100 µl of Ga solution was added to the entire volume of the digested sample, which was around 5 ml, and mixed thoroughly. Afterwards, from such prepared solution, four subsamples of 1 ml volume were taken to the separate vials and stored at the temperature of 5°C until they were sent to the cooperating laboratories. The transportation of the appropriately protected samples took no more than 5 days. After reaching the laboratory, until the TXRF measurements, the samples were kept in the fridge.

Participating laboratories, apparatus and measurement conditions

In this paper, we discuss the results obtained in the first inter-laboratory test on TXRF element analysis of mammalian tissue samples. The measurements were done in four European laboratories in frame of the ENFORCE TXRF COST Action 18130 and the details concerning the participants of the study are listed in Table 1. The spectrometers used for investigation as well as experimental conditions used in particular laboratories involved in cooperation are shown in the Table 2.

Table 1. Participants to the 1st inter-laboratory test on TXRF analysis of mammalian tissue samples.

Participant	City, country
Laboratory of X-ray Methods of the Center for Research and Analysis at the Jan Kochanowski University	Kielce, Poland
X-ray Fluorescence Laboratory of the Faculty of Physics and Applied Computer Science at the AGH University of Science and Technology	Krakow, Poland
TXRF Laboratory of the Interdepartmental Research Service at the Autonomous University of Madrid	Madrid, Spain
Laboratory of X-ray Analytical Applications of the Department of Chemistry, University of Girona	Girona, Spain

Table 2. Characteristics of apparatus and experimental conditions used in cooperating laboratories.

Laboratory	TXRF spectrometer	X-ray tube	Tube voltage [kV]	Tube current [mA]	Glancing angle [°]	Acquisition time [s]	Deposition volume [µl]
Lab 1	S2 PICOFOX Bruker Nano	Mo	50	0.6	<0.1	1000	6*
Lab 2	Rigaku Nanohunter II	Mo	50	12	0.04	1000	6**
Lab 3	S2 PICOFOX Bruker Nano	Mo	50	0.6	<0.1	500***	5*
Lab 4	S2 PICOFOX Bruker Nano	W	50	1	0.1	1000	6*

* samples deposited on the quartz glass carriers;
** samples deposited on the Super Frost (Menzel) microscope glass slides;
*** the reduction of acquisition time was done after the verification, that it does not influence significantly the evaluated analytical parameters in the examined kind of matrixes.

In Lab1, Lab3 and Lab4, the analyzed samples are deposited on quartz carriers. Their cleanliness is checked every time before sample deposition by registering X-ray spectrum using TXRF system and verification of the presence of characteristic X-ray lines of elements being possible impurities of carrier (usually Ca, Fe, Cu, Zn). If the number of counts for the element X-ray line is less than 150 cts for the measurement time of 500 s (which corresponds to a few ppb concentration and the same the level of the detection limit for TXRF), the sample carrier is classified as a clean. In opposite case, the it is washed again.

In case of disposable carriers used in Lab2, for each batch (50 pieces) a random carrier is checked for the purity. If the recorded count rates are lower than 1 cps (for elements with atomic number higher than this of Ca - usually Fe and As) the batch is considered as acceptable. Such low count rates are negligible in comparison with the fluorescence signals originating from the sample (above 100 cps).

Determination of element concentrations

To determine the concentrations of the elements, three measurements of each sample on separate carriers were done and the final concentrations in the sample were calculated as the medians from the results of these 3 repetitions. For this purpose 5-6 µl (depending on the laboratory) of a solution was transferred onto an appropriate sample carrier. Before sample deposition, the carriers were cleaned according to the producer recommendations and tested through the control measurements of background. Similar tests were done in case of single-use

glass carriers utilized in Rigaku Nanohunter II spectrometer. Deposited samples were dried on a heating plate and its temperature depended on the laboratory and varied from 40°C to 70°C. The elemental analysis was carried out for the dry sample residue. The concentrations of elements in the examined organs were determined using internal standard method what was described in details in our previous paper [xxiii].

Calculation of validation parameters

Limits of detection (LOD)

The detection limits of the elements were calculated separately for each analysed organ. The value of the detection limit for the element i in the analysed organ subsample j (LOD_{ij}) was calculated based on the formula (1):

$$LOD_{ij} = \frac{3 \cdot C_{ij} \cdot \sqrt{N_{BGij}}}{N_{ij}} \quad (1)$$

where:

C_{ij} – concentration of the element i in the organ subsample j $[\mu g/g]$,

N_{BGij} – area of the background under the K_α line of the element i in the subsample j $[cts]$,

N_{ij} – net peak area of the K_α line of the element i in the subsample j $[cts]$.

The final value of the detection limit for the analysed element i (LOD_i) was calculated as an average of the results obtained for all the analysed subsamples. The number of analysed subsamples was equal to 12 (organs were taken from 4 animals, and each sample of digested tissue was measured 3 times). In turn, the uncertainty of LOD_i was calculated as the standard deviation according to the equation (2):

$$SD_{LOD_i} = \sqrt{\frac{\sum_1^n \left(LOD_{ij} - LOD_i\right)^2}{n \cdot (n-1)}} \quad (2)$$

where:

n – the number of analysed subsamples, $n = 12$.

Intra-day and inter-day precision

Precision was evaluated as an intra-day and inter-day precision, depending on the period between the performed measurements, and selected heart sample was utilized for this purpose. The intra-day precision was calculated based on the 10 results obtained for one sample in one measurement series performed within one day. The inter-day precision was evaluated by measuring the same sample in five different days (5 measurements, one measurement per day, 3 repetitions per each measurement done on separate sample carriers). Both precisions were calculated as coefficients of variation of obtained results, according to the formula (3):

$$CV = \frac{1}{a_i} \sqrt{\frac{\sum_1^k \left(a_{ij} - a_i\right)^2}{k-1}} \cdot 100\% \quad (3)$$

where:

j – the number of measurement,

a_{ij} – the concentration of the element i in a measurement j $[\mu g/g]$,

a_i – the mean value of the concentration of the element i $[\mu g/g]$,

k – the number of measurements (10 and 5 for intra-day and inter-day precision, respectively).

Inter-laboratory precision

Inter-laboratory precision was evaluated for each element as a coefficient of variation of the results obtained in three cooperating laboratories, namely Lab 1, Lab 2 and Lab 3. Because for the spectrometer equipped with the W-anode X-ray tube (Lab 4), only four elements were determined, these results were not taken into account for inter-laboratory precision evaluation. The coefficients of variation were calculated according to the formula (5) for the individual elements, based on their concentrations obtained during determination of intra-day precision for mentioned three laboratories.

Results and discussion

Four normal adult rats were used for the study. From each of them the internal organs, including kidney, heart, spleen and lung, were taken and subjected to the microwave digestion. The obtained samples, after adding the internal standard, were examined using the TXRF method in four European laboratories. As a result of measurements, for each analysed sample the X-ray fluorescence spectrum was obtained. A complete, qualitative identification of the spectral lines of elements observed in the X-ray fluorescence spectrum of the control heart sample is presented in the Figure S1 of Supplementary materials. The identification and quantitative analysis of examined elements was performed based on their Kα lines. In the Figure 1, the exemplary spectra recorded for selected heart sample in four cooperating laboratories are presented.

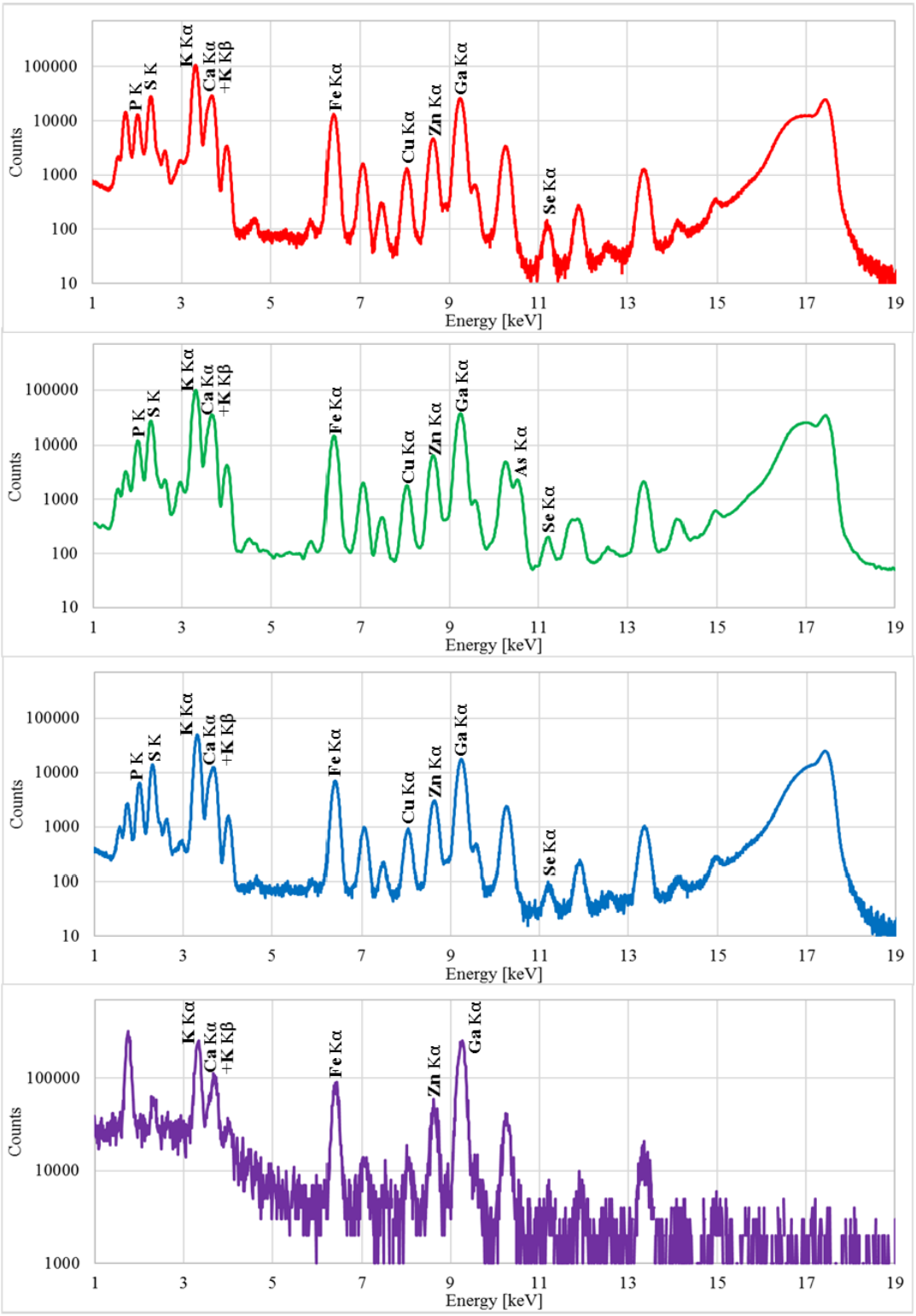
Counts
Energy [keV]
P K
S K
K Kα
Ca Kα
+K Kβ
Fe Kα
Cu Kα
Zn Kα
Ga Kα
As Kα
Se Kα

Figure 1. The X-ray fluorescence spectra recorded for selected heart sample in four cooperating laboratories. The Kα lines of the analysed elements and internal standard (Ga) were indicated. The As K-lines present in the spectra from Lab 2 originate from microscope glass slides.

Based on Figure 1, it can be noticed that the spectra measured in Lab 1, Lab 2 and Lab 3, where spectrometers equipped with Mo-anode X-ray tube were applied, did not differ significantly from each other. The analytical lines of all the elements under investigation (P, S, K, Ca, Fe, Cu, Zn and Se) were well visible in them and the recorded number of counts similar in the case of Lab 1 and Lab 2, where the same acquisition time (1000 s) was applied. In turn, the observed slight decrease of the number of counts in the spectrum obtained in Lab 3 may be caused by the reduced time of a single measurement (500 s).

The spectrum obtained in the Lab 4, registered with spectrometer equipped with W-anode X-ray tube, differed from the spectra measured in the three remaining laboratories. For similar measurement conditions (time of the measurement, deposited sample volume), the recorded analytical signal was not satisfactory for some of the elements under the analysis. This resulted from the specificity of the system equipped with W-anode X-ray tube, which application to the determination of elements with low and medium atomic number is limited [xli].

In order to illustrate the qualitative differences between the spectra obtained for analysed organs, the spectra of lung, heart, kidney and spleen samples, recorded in one selected laboratory, are compared in Figure 2. As on can see from this Figure, there is no significant differences in the spectral background between various matrices. Regarding the element content, is it interesting to note that Fe is higher in the spleen meanwhile Cu and Se are present at higher levels in kidney sample. These trends are easier to notice in Figure 3 where the box-and-whisker plots presenting the ranges of the element concentrations in the tested organs obtained for the examined animal group in particular laboratories are displayed.

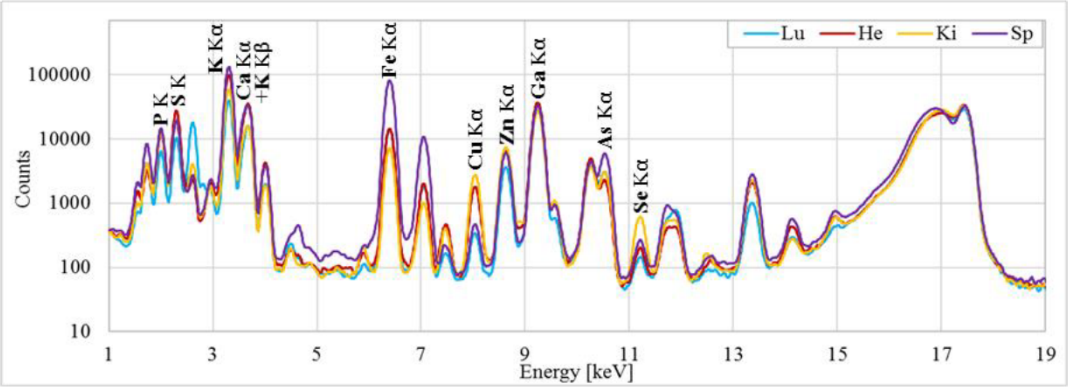

Figure 2. The comparison of spectra recorded in selected laboratory (Lab 2) for analysed organs (lung, heart, kidney, spleen) which were originated from one animal. Ga is the internal standard.

In the laboratories using TXRF spectrometers equipped with Mo-anode X-ray tube, the concentrations of P, S, K, Ca, Fe, Cu, Zn and Se were determined in the organ samples. In turn, in case of the S2 Picofox system with the W-anode X-ray tube, the contents of K, Ca, Fe and Zn were examined.

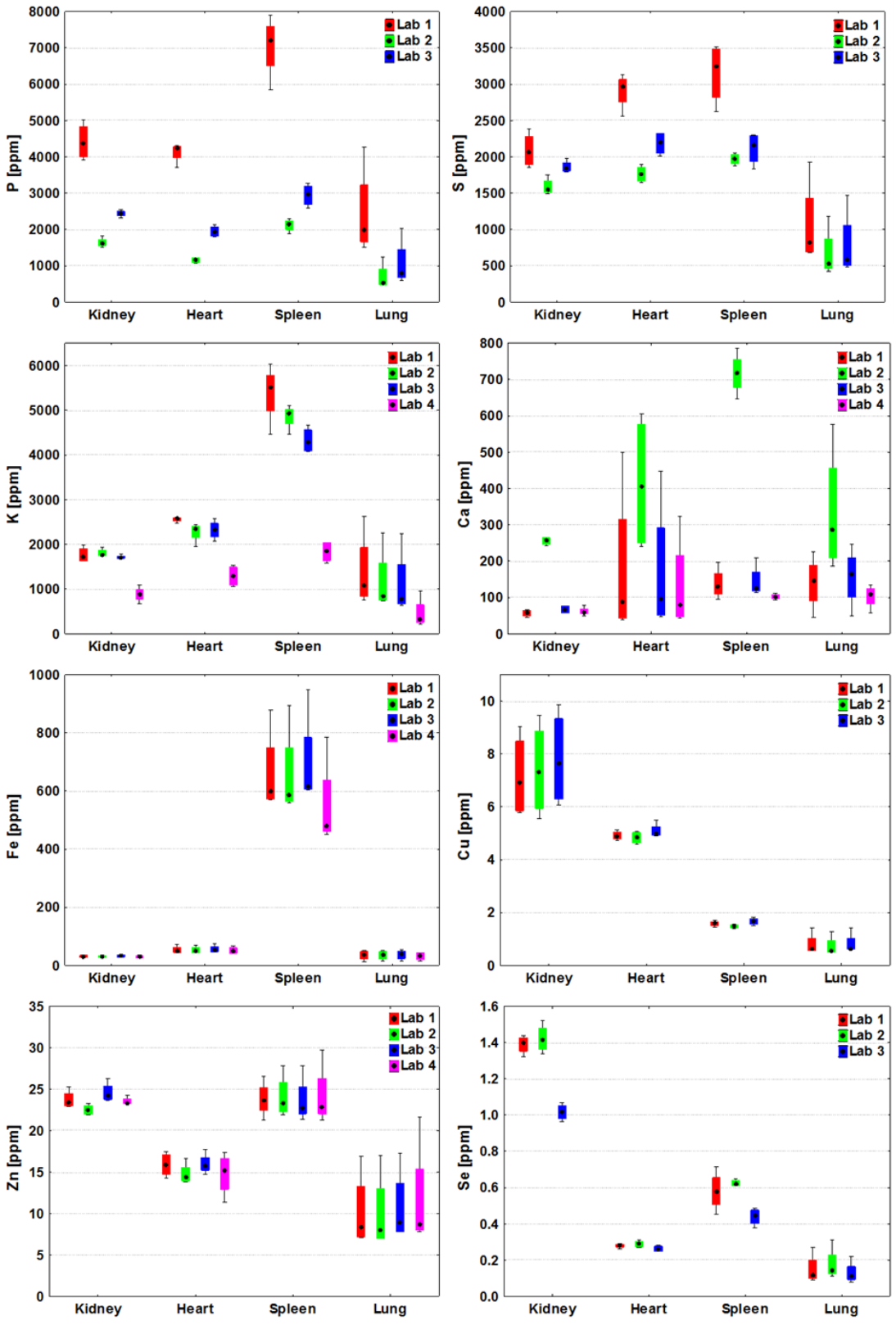

Figure 3. The box-and-whiskers plots presenting the ranges of P, S, K, Ca, Fe, Cu, Zn and Se concentrations in the organs of 4 normal rats that were obtained in the cooperating laboratories. Median, interquartile span and minimal-

maximal values determined for the animal group were marked as a little square, a box and whiskers, respectively. The concentrations of elements that were not measured or below the detection limits obtained in particular laboratory were not presented (P, S, Cu and Se for Lab 4).

As it can be seen from the Figure 3, apart from minor exceptions, the concentrations of heavier elements (Fe, Cu, Zn and Se) in organs, measured in the participating laboratories, were quite well consistent with each other. The situation was different in the case of light elements (especially P and S), for which discrepancies were observed in the results at the level of several dozen (S) and even several hundred percent (P). The source of the large discrepancies observed for these two elements may be different deconvolution algorithms used in particular laboratories for fitting X-ray spectra in the range of P and S characteristic radiation lines (1.5-3.0 keV). Spectrum complexity in this range, due to the presence of additional K series lines of Si (sample carrier material), Cl (from the sample) and Ar (from air), results in a particular sensitivity to the applied fit procedure. The fitting procedure is not the only reason for the observed discrepancies in the content of P and S determined in various laboratories. The other, probably even more significant reasons of discrepancies are various efficiency of the absorption of P and S X-ray fluorescence lines in dry sample residue and accuracy of calibration curve.

The K concentrations measured in Lab 4 presented systematically lower values than those obtained in the other laboratories. This is probably an effect of the lower signal to noise ratio of the X-ray fluorescence spectra recorded using the spectrometer equipped with the W X-ray tube in comparison to the systems with the Mo-anode. Underestimation of K concentrations in tissue samples, in case of the use of the spectrometer with W-anode and the internal standard method, is in agreement with our previous results obtained for foodstuff samples [xlii]. On the other hand, the opposite relation was observed for the Ca levels determined in Lab 2. In this laboratory disposable microscope slides, containing some amounts of Ca, are typically used as sample carriers. Therefore, the observed systematically higher Ca concentrations may be the result of the processes of dissolution and/or diffusion which cannot be excluded during the deposition of the acid digested samples.

The next step of the study was the determination of validation parameters, including LODs of elements as well as intra- and inter-day precisions, for particular laboratories. Additionally, for each examined element, inter-laboratory precision was calculated.

In the Table 3, the LODs for analysed tissues and measured elements, obtained in four participating laboratories, are compared. The lowest (the best) values were, additionally, marked in red. As it could be expected, LODs decreased with the atomic number of elements and was equal from 3.92 μg/g to 22.9 μg/g for P and from 0.0147 μg/g to 0.0352 μg/g for Se. LODs of the elements obtained in S2 PICOFOX Bruker Nano spectrometers with Mo-anode (Lab 1 and Lab 3) were similar, usually slightly better, to those determined for Rigaku Nanohunter II system (also equipped with Mo-anode X-ray tube). Much worse values of the mentioned parameter were obtained when W- instead of Mo-anode X-ray tube was applied for sample excitation.

The analysis of the values of intra-day precision, presented in Table 4, showed that in case of lighter elements (from P to Ca) the parameter did not exceed 19% for none of the cooperating laboratories. Much better values of intra-day precision, usually below 6%, were obtained for heavier elements (Fe, Cu, Zn and Se). The values of inter-day precision did not exceed 26% for lighter elements and were below 12% for heavier ones. What is more, the intra- and inter-day precision was in most cases better for spectrometers equipped with the Mo-anode X-ray tube comparing to the apparatus with W-anode.

Because, in case of the apparatus equipped with the W-anode X-ray tube, only 4 elements were measured in tissues, the values of inter-laboratory precision were calculated only based

on the data measured in Lab 1, Lab 2 and Lab 3. The obtained results are shown in Table 5. As one can see from this Table, K, Fe, Cu and Zn belonged to the elements for which the values of inter-laboratory precision were the best. For these elements, the mentioned parameter did not exceed 6%. Slightly worse results were obtained for S, Ca and Se. The worst and unsatisfactory inter-laboratory precision was found for P, in case of which the largest discrepancies in concentrations were observed between the cooperating laboratories. Such a result confirms the qualitative observations done based on the Figure 3, which shows that the P concentrations measured in various TXRF systems/laboratories may differ even several hundred percent.

Table 3. LOD values in [μg/g] obtained for examined elements in cooperating laboratories.

			P	S	K	Ca	Fe	Cu	Zn	Se
Kidney	Lab 1	LOD	10.97	3.38	0.620*	0.308	0.0417	0.0304	0.0294	0.0148
		SD	0.81	0.25	0.042	0.022	0.0030	0.0023	0.0022	0.0011
	Lab 2	LOD	8.06	4.94	1.416	0.872	0.0658	0.0437	0.0582	0.0249
		SD	0.39	0.25	0.070	0.041	0.0031	0.0023	0.0028	0.0013
	Lab 3	LOD	4.98	2.79	0.692	0.480	0.0758	0.0468	0.0404	0.0218
		SD	0.17	0.10	0.026	0.015	0.0031	0.0019	0.0016	0.00070
	Lab 4	LOD	-	-	26.6	18.3	1.51	-	0.778	-
		SD	-	-	2.7	1.8	0.16	-	0.074	-
Heart	Lab 1	LOD	13.40	3.89	0.766	0.374	0.0464	0.0325	0.0306	0.0151
		SD	0.94	0.34	0.052	0.032	0.0040	0.0025	0.0025	0.0012
	Lab 2	LOD	7.58	4.63	1.55	0.980	0.0677	0.0417	0.0538	0.0228
		SD	0.65	0.39	0.13	0.092	0.0059	0.0044	0.0054	0.0023
	Lab 3	LOD	5.16	2.51	0.833	0.433	0.0817	0.0493	0.0457	0.0213
		SD	0.45	0.22	0.067	0.042	0.0080	0.0049	0.0045	0.0018
	Lab 4	LOD	-	-	32.2	22.0	1.82	-	0.95	-
		SD	-	-	4.7	3.2	0.24	-	0.15	-
Spleen	Lab 1	LOD	22.9	7.31	1.50	0.699	0.1065	0.0558	0.0524	0.0307
		SD	1.7	0.53	0.11	0.050	0.0075	0.0040	0.0037	0.0022
	Lab 2	LOD	11.36	6.43	2.550	1.596	0.1664	0.0574	0.0683	0.0352
		SD	0.36	0.21	0.081	0.056	0.0035	0.0019	0.0021	0.0013
	Lab 3	LOD	6.46	3.62	0.933	0.670	0.1083	0.0534	0.0455	0.0254
		SD	0.43	0.25	0.057	0.042	0.0074	0.0035	0.0027	0.0019
	Lab 4	LOD	-	-	64	43.5	3.86	-	1.78	-
		SD	-	-	13	8.9	0.76	-	0.37	-
Lung	Lab 1	LOD	10.76	3.78	0.676	0.373	0.0437	0.0284	0.0270	0.0147
		SD	0.88	0.30	0.050	0.025	0.0042	0.0024	0.0022	0.0015
	Lab 2	LOD	6.58	4.34	1.38	0.896	0.0651	0.0397	0.0492	0.0230
		SD	0.67	0.39	0.14	0.092	0.0049	0.0032	0.0037	0.0020
	Lab 3	LOD	3.92	2.12	0.550	0.391	0.0629	0.0384	0.0343	0.0172
		SD	0.46	0.25	0.066	0.045	0.0068	0.0039	0.0034	0.0019
	Lab 4	LOD	-	-	52	24.4	2.94	-	1.35	-
		SD	-	-	10	3.5	0.55	-	0.27	-

*The lowest LOD values of element obtained for particular organ were marked in red.

Table 4. Intra-day and inter-day precision values obtained for selected heart sample in cooperating laboratories.

	Intra-day precision values [%]							
	P	S	K	Ca	Fe	Cu	Zn	Se
Lab 1	16.64	17.38	8.25	13.46	1.46	1.61	1.78	5.75
Lab 2	2.30	3.64	2.95	12.11	0.64	2.14	5.79	4.54
Lab 3	0.47	0.62	0.53	0.56	0.38	1.58	0.42	4.60
Lab 4	-	-	18.97	16.23	8.45	-	2.99	-
	Inter-day precision values [%]							
	P	S	K	Ca	Fe	Cu	Zn	Se
Lab 1	7.94	8.18	5.34	11.85	1.13	0.63	0.41	1.29
Lab 2	0.41	1.88	2.33	16.11	0.91	1.38	0.31	5.44
Lab 3	3.34	0.86	1.74	2.18	1.05	1.24	0.80	11.09
Lab 4	-	-	21.45	25.67	7.11	-	5.55	-

*The best intra- and inter-day precision values for particular element were marked in red.

Table 5. The values of inter-laboratory precision obtained for selected heart sample.

Inter-laboratory precision values [%]							
P	S	K	Ca	Fe	Cu	Zn	Se
53.50	14.97	2.64	16.88	1.45	5.36	2.94	11.16

For comparison purposes, the selected heart sample was also analysed by another, independent method, called the reference method (ICP-OES for P, S, K, Ca, Fe, Cu and Zn determination and ICP-MS for Se determination). The details concerning the used instruments, measurement conditions and procedure of quality control for both ICP systems are included in Tables S2 and S3 of Supplementary materials. The results measured using TXRF in four cooperating laboratories together with the data obtained using the reference method are presented in Table 6.

Table 6. The concentrations of analysed elements in selected heart sample determined using TXRF in four cooperating laboratories together with the results obtained with the reference method. Before analysis, digested tissue samples were diluted with the ratio 1:10.

Element		Concentration [µg/g]					Trueness [%]*			
		Ref. method	Lab 1	Lab 2	Lab 3	Lab 4	Lab 1	Lab 2	Lab 3	Lab 4
P	C [ppm]	1810	3500	1223.5	1864.0	-	193	68	**103**	-
	ΔC [ppm]**	3	180	8.9	2.8	-	10	1	**<1**	-
S	C [ppm]	2138.7	2590	1913	2366.8	-	121	**89**	**111**	-
	ΔC [ppm]	2.2	140	22	4.7	-	7	**1**	**<1**	-
K	C [ppm]	2117	2411	2446	2536.9	1062	**114**	116	120	50
	ΔC [ppm]	18	63	23	4.3	64	**3**	1	1	3
Ca	C [ppm]	388.3	436	597	471.10	234	**112**	154	121	60
	ΔC [ppm]	2.4	19	23	0.84	12	**5**	6	**1**	3
Fe	C [ppm]	72.76	70.97	70.30	72.322	57.4	97	96	**99**	79
	ΔC [ppm]	0.52	0.33	0.14	0.088	1.5	1	1	**1**	2
Cu	C [ppm]	5.221	5.160	5.048	5.583	-	**99**	97	107	-
	ΔC [ppm]	0.069	0.026	0.034	0.028	-	**1**	1	2	-
Zn	C [ppm]	17.10	17.80	16.93	17.839	18.12	104	**99**	104	106
	ΔC [ppm]	0.13	0.10	0.31	0.024	0.17	1	**2**	1	1
Se	C [ppm]	0.1914#	0.2882	0.3190	0.2549	-	151	167	**134**	-
	ΔC [ppm]	0.0064	0.0052	0.0046	0.0037	-	6	6	**5**	-

* Trueness [%]=(experimental value/reference value)*100;
**The uncertainty of elemental concentration was calculated as standard deviation of mean value obtained from measured replicates of the sample, whilst the uncertainty of trueness was estimated based on the law of propagation of uncertainties;
ICP-OES was mostly used as a reference method, only Se concentration was determined using ICP-MS.

The analysis of the results presented in Table 6 showed the most satisfactory compliance with the reference method for Lab 3. One may notice a tendency to overestimate the light elements (P, S) content in Lab 1 and their underestimation in Lab 2. In case of K and Ca the best trueness values were obtained for Lab 1. In turn, in case of Fe, Cu and Zn the trueness values were satisfactory for all participating laboratories. The worse trueness values, significantly exceeding 100%, were found for Se. However, as one can see from the Table S3 of Supplementary materials, the Se trueness calculated for ICP-MS based on the measurements of the reference material was also not impressive and equalled to 70%. Therefore, the values of

the concentration obtained for Se with the use of the reference method are, probably, significantly underestimated and also for this element, occurring in tissues at the trace level, the TXRF seems to give the satisfactory results.

Conclusions

Reassuming, the results of the inter-comparison investigation showed acceptable consistency of the results obtained in participating laboratories for mid and heavier elements such as Fe, Cu, Zn and Se. The discrepancies found for the elements with lower atomic number were larger but probably could be strongly limited by optimization of sample treatment procedures that would limit the self-absorption phenomenon in its dried residue as well as the unification of calibration procedures and spectra deconvolution process used in particular laboratories.

Data availability

The datasets used and/or analysed during the current study are available from the corresponding author on reasonable request.

Acknowledgements

The authors would like to acknowledge the contribution of the COST ACTION CA18130. This work also was partially financed by the Ministry of Education and Science of Poland and the statutory research fund no. N18/DBW/000018 of the Laboratory of Experimental Neuropathology (Institute of Zoology and Biomedical Research, Jagiellonian University). Karolina Olbrich has been partly supported by the EU Project POWR.03.02.00-00-I004/16.

Authors Contributions

Karolina Olbrich: conceptualization, methodology, resources, investigation, validation, writing original draft, Aldona Kubala-Kukus: resources, investigation, validation, reviewing manuscript, Eva Marguí: resources, investigation, validation, reviewing manuscript, Ramón Fernández-Ruiz: resources, investigation, validation, reviewing manuscript, Katarzyna Matusiak: methodology, investigation, Jolanta Wudarczyk-Mocko: investigation, validation, Pawel Wrobel: resources, validation, reviewing manuscript, Zuzanna Setkowicz: methodology, resources, investigation, Joanna Chwiej: conceptualization, supervision, resources, validation, writing original draft, corresponding author.

Competing Interests Statement

The authors report no conflicts of interest.

References

i. Gruber A, Müller R, Wagner A, Colucci S, Spasić MV, Leopold K (2020) Total reflection X-ray fluorescence spectrometry for trace determination of iron and some additional elements in biological samples. Anal Bioanal Chem 412(24):6419-6429. doi: 10.1007/s00216-020-02614-8.

ii. Jeffery J, Frank AR, Hockridge S, Stosnach H, Costelloe SJ (2019) Method for measurement of serum copper, zinc and selenium using total reflection X-ray fluorescence spectroscopy on the PICOFOX analyser: Validation and comparison with atomic absorption spectroscopy and

inductively coupled plasma mass spectrometry. Ann Clin Biochem 56(1):170-178. doi: 10.1177/0004563218793163.
iii. Johnson-Davis KL, Farnsworth C, Law C, Parker R (2020) Method validation for a multi-element panel in serum by inductively coupled plasma mass spectrometry (ICP-MS). Clin Biochem 82:90-98. doi: 10.1016/j.clinbiochem.2020.05.002.
iv. Rahil-Khazen R, Henriksen H, Bolann BJ, Ulvik RJ (2000). Validation of inductively coupled plasma atomic emission spectrometry technique (ICP-AES) for multi-element analysis of trace elements in human serum. Scand J Clin Lab Invest 60(8):677-86. doi: 10.1080/00365510050216402.
v. Dudek-Adamska D, Lech T, Konopka T, Kościelniak P (2021) Nickel Content in Human Internal Organs. Biol Trace Elem Res 199(6):2138-2144. doi: 10.1007/s12011-020-02347-w.
vi. Boulyga S F, Becker J S, Malenchenko A F, Dietze H-J (2000) Application of ICP-MS for multielement analysis in small sample amounts of pathological thyroid tissue. Mikrochim Acta 134:215–222. doi: 10.1007/S006040050069.
vii. Harrington J M, Young D J, Essader A S, Sumner S J, Levine K E (2014) Analysis of human serum and whole blood for mineral content by ICP-MS and ICP-OES: development of a mineralomics method. Biol Trace Elem Res 160(1):132-42. doi: 10.1007/s12011-014-0033-5.
viii. Mold M, Umar D, King A, Exley C. Aluminium in brain tissue in autism (2018) J Trace Elem Med Biol 46:76-82. doi: 10.1016/j.jtemb.2017.11.012.
ix. Planeta K, Kubala-Kukus A, Drozdz A, Matusiak K, Setkowicz Z, Chwiej J (2021) The assessment of the usability of selected instrumental techniques for the elemental analysis of biomedical samples. Sci Rep 11(1):3704. doi: 10.1038/s41598-021-82179-3.
x. Klockenkämper R, von Bohlen A (2015) Total reflection X-ray fluorescence analysis and related methods. 2nd ed. Hoboken: Wiley and Sons.
xi. Kubala-Kukus A, Braziewicz J, Pajek M (2004) Total-reflection X-ray fluorescence studies of trace elements in biomedical samples. Spectrochim Acta Part B At Spectrosc 59:1283-9. doi:10.1016/j.sab.2004.05.020.
xii. Fernandez-Ruiz R (2022) TXRF spectrometry in the bioanalytical sciences: A brief review. X-Ray Spectrom 51:279-93. doi: 10.1002/xrs.3243.
xiii. Carvalho ML, Magalhães T, Becker M, von Bohlen A (2007) Trace elements in human cancerous and healthy tissues: A comparative study by EDXRF, TXRF, synchrotron radiation and PIXE. Spectrochim Acta Part B At Spectrosc 62(9):1004-1011. doi:10.1016/j.sab.2007.03.030
xiv. Magalhães T, von Bohlen A, Carvalho ML, Becker M (2006) Trace elements in human cancerous and healthy tissues from the same individual: A comparative study by TXRF and EDXRF. Spectrochim Acta Part B At Spectrosc 61(10-11):1185-1193. doi:10.1016/j.sab.2006.06.002
xv. Magalhães T, Becker M, Carvalho ML, von Bohlen A (2008) Study of Br, Zn, Cu and Fe concentrations in healthy and cancer breast tissues by TXRF. Spectrochim Acta Part B At Spectrosc 63B(12):1473-1479. doi:10.1016/j.sab.2008.10.014
xvi. Wrobel PM, Bala S, Czyzycki M, Golasik M, Librowski T, Ostachowicz B, Piekoszewski W, Surowka A, Lankosz M (2016) Combined micro-XRF and TXRF methodology for quantitative elemental imaging of tissue samples. Talanta 162:654-659. doi:10.1016/j.talanta.2016.10.043
xvii. Hund E, Massart DL, Smeyers-Verbeke J (2000) Inter-laboratory studies in analytical chemistry. Anal Chim Acta 423(2):145-165. doi: 10.1016/S0003-2670(00)01115-6
xviii. Unterumsberger R, Beckhoff B, Gross A, Stosnach H, Nowak S, Stenzel YP, Kr¨amer M, von Bohlen A (2021) A round robin test for total reflection X-ray fluorescence analysis using

preselected and well characterized samples. J Anal At Spectrom 36:1933-1945. doi: 10.1039/d1ja00103e
xix. Borgese L, Bilo F, Federici S, Margui E, Hase T, Huang Y, Beckhoff B, Depero LE (2019) Summary of ISO standard 20289: Total reflection X-ray fluorescence analysis of water. Surf Interface Anal 52(3):119-123. doi: 10.1002/sia.6720
xx. Rink I, Rostam-Khani P, Knoth J, Schwenke H, de Gendt S, Wortelboer R (2001) Calibration of straight total reflection X-ray fluorescence spectrometry - Results of a European Round Robin test. Spectrochim Acta Part B At Spectrosc 56(11):2283-2292. doi: 10.1016/S0584-8547(01)00297-X
xxi. Nutsch A, Beckhoff B, Altmann R, Polignano ML, Cazzini E, Codegoni D, Borionetti G, Kolbe M, Mueller M, Mantler C (2009) Comparability of TXRF Systems at Different Laboratories. ECS Transactions 25(3):325-335 doi:10.1149/1.3204423
xxii. International Atomic Energy Agency Results of the IAEA proficiency test PTXRFIAEA10: Determination of Major, Minor and Trace Elements in a Sandy Soil, IAEA Laboratories, Seibersdorf, 2013
xxiii. Planeta K, Setkowicz Z, Janik-Olchawa N, Matusiak K, Ryszawy D, Drozdz A, Janeczko K, Ostachowicz B, Chwiej J (2020) Comparison of elemental anomalies following implantation of different cell lines of glioblastoma multiforme in the rat brain: A total reflection X-ray fluorescence spectroscopy study. ACS Chem Neurosci 11(24):4447-4459. doi: 10.1021/acschemneuro.0c00648.
xxiv. Planeta K, Setkowicz Z, Czyzycki M, Janik-Olchawa N, Ryszawy D, Janeczko K, Simon R, Baumbach T, Chwiej J (2022) Altered elemental distribution in male rat brain tissue as a predictor of glioblastoma multiforme growth-studies using SR-XRF microscopy. Int J Mol Sci 23(2):703. doi: 10.3390/ijms23020703.
xxv. Chwiej J, Sarapata A, Janeczko K, Stegowski Z, Appel K, Setkowicz Z (2011) X-ray fluorescence analysis of long-term changes in the levels and distributions of trace elements in the rat brain following mechanical injury. J Biol Inorg Chem 16(2):275-83. doi: 10.1007/s00775-010-0724-0.
xxvi. Chwiej J, Kutorasinska J, Janeczko K, Gzielo-Jurek K, Uram L, Appel K, Simon R, Setkowicz Z (2012) Progress of elemental anomalies of hippocampal formation in the pilocarpine model of temporal lobe epilepsy-an X-ray fluorescence microscopy study. Anal Bioanal Chem 404(10):3071-80. doi: 10.1007/s00216-012-6425-5.
xxvii. Chwiej J, Gabrys H, Janeczko K, Kutorasinska J, Gzielo-Jurek K, Matusiak K, Appel K, Setkowicz Z (2014) Elemental anomalies in the hippocampal formation after repetitive electrical stimulation: an X-ray fluorescence microscopy study. J Biol Inorg Chem 19(7):1209-20. doi: 10.1007/s00775-014-1177-7.
xxviii. Chwiej J, Patulska A, Skoczen A, Janeczko K, Ciarach M, Simon R, Setkowicz Z (2015) Elemental changes in the hippocampal formation following two different formulas of ketogenic diet: an X-ray fluorescence microscopy study. J Biol Inorg Chem 20(8):1277-86. doi: 10.1007/s00775-015-1306-y.
xxix. Matusiak K, Skoczen A, Setkowicz Z, Kubala-Kukus A, Stabrawa I, Ciarach M, Janeczko K, Jung A, Chwiej J (2017) The elemental changes occurring in the rat liver after exposure to PEG-coated iron oxide nanoparticles: total reflection X-ray fluorescence (TXRF) spectroscopy study. Nanotoxicology 11(9-10):1225-1236. doi: 10.1080/17435390.2017.1408151.
xxx. Skoczen A, Matusiak K, Setkowicz Z, Kubala-Kukuś A, Stabrawa I, Ciarach M, Janeczko K, Chwiej J (2018) Low doses of polyethylene glycol coated iron oxide nanoparticles cause significant elemental changes within main organs. Chem Res Toxicol 31(9):876-884. doi: 10.1021/acs.chemrestox.8b00110.
xxxi. Marguí E, Queralt I, García-Ruiz E, García-González E, Rello L, Resano M (2018). Energy dispersive X-ray fluorescence spectrometry for the direct multi-element analysis of

dried blood spots. Spectrochim Acta Part B At Spectrosc 139:13-9. doi: 10.1016/j.sab.2017.11.003.
xxxii. Bongiovanni GA, Pérez RD, Mardirosian M, Pérez CA, Marguí E, Queralt I (2019) Comprehensive analysis of renal arsenic accumulation using images based on X-ray fluorescence at the tissue, cellular, and subcellular levels. Appl Radiat Isot 150:95-102. doi: 10.1016/j.apradiso.2019.05.018.
xxxiii. Marguí E, Ricketts P, Fletcher H, Karydas AG, Migliori A, Leani JJ, Hidalgo M, Queralt I, Voutchkov M (2017) Total reflection X-ray fluorescence as a fast multielemental technique for human placenta sample analysis. Spectrochim Acta Part B At Spectrosc 130:53-9. doi: 10.1016/j.sab.2017.02.008.
xxxiv. Marguí E, Jablan J, Gerić M, Inić S, Domijan AM, Janušić R, Šarčević B, Queralt I, Garaj-Vrhovac V (2019) Critical evaluation of the use of total reflection X-ray fluorescence spectrometry for the analysis of whole blood samples: application to patients with thyroid gland diseases. Anal Bioanal Chem 411(8):1659-70. doi: 10.1007/s00216-019-01618-3.
xxxv. Jablan J, Besalú E, Žarak M, Dumić J, Marguí E (2021) Analytical potential of total reflection X-ray fluorescence spectrometry for simultaneous determination of iron, copper and zinc in human blood serum and plasma. Talanta 233:122553. doi: 10.1016/j.talanta.2021.122553.
xxxvi. Marguí E, Jablan J, Queralt I, Bilo F, Borgese L (2022) Potential of total-reflection X-ray spectrometry for multielement analysis of biological samples using dilution or suspension sample preparation techniques. X-Ray Spectrom 51(3):230. doi: 10.1002/xrs.3230.
xxxvii. Fernández-Ruiz R, Tornero JD, González VM, Alonso C (1999) Quantification of Pt bound to DNA using total-reflection X-ray fluorescence (TXRF). Analyst 124:583-5. doi: 10.1039/A900725C.
xxxviii. González M, Tapia L, Alvarado M, Tornero JD, Fernández R (1999) Intracellular determination of elements in mammalian cultured cells by total reflection X-ray fluorescence spectrometry. J Anal At Spectrometry 14:885-90. doi: 10.1039/A808748B.
xxxix. Fernández-Ruiz R, Redrejo MJ, Friedrich EJ, Ramos M, Fernández T (2014) Evaluation of bioaccumulation kinetics of gold nanorods in vital mammalian organs by means of total reflection X-ray fluorescence spectrometry. Anal Chem 86(15):7383-90. doi: 10.1021/ac5006475.
xl. Fernández-Ruiz R, von Bohlen A, Friedrich KEJ, Redrejo MJ (2018) Analysis of coke beverages by total-reflection X-ray fluorescence. Spectrochim Acta Part B At Spectrosc 145:99-106. doi: 10.1016/j.sab.2018.04.013.
xli. Dalipi R, Marguí E, Borgese L, Bilo F, Depero LE (2016) Analytical performance of benchtop total reflection X-ray fluorescence instrumentation for multielemental analysis of wine samples. Spectrochim Acta Part B At Spectrosc 120:37-43. doi: 10.1016/j.sab.2016.04.001.
xlii. Dalipi R, Marguí E, Borgese L, Depero LE (2017) Multi-element analysis of vegetal foodstuff by means of low power total reflection X-ray fluorescence (TXRF) spectrometry. Food Chem 218:348-355. doi: 10.1016/j.foodchem.2016.09.022.

Declaration of interests

☒The authors declare that they have no known competing financial interests or personal relationships that could have appeared to influence the work reported in this paper.

☐The authors declare the following financial interests/personal relationships which may be considered as potential competing interests:

Spectrochimica Acta Part A: Molecular and Biomolecular Spectroscopy

Vibrational spectroscopy methods for investigation of the animal models of glioblastoma multiforme

--Manuscript Draft--

Manuscript Number:	SAA-D-23-00547
Article Type:	VSI: CSI XLII 2022
Section/Category:	Biomolecular and Biomedical Spectroscopy
Keywords:	Glioblastoma multiforme (GBM); animal models; vibrational spectroscopy; Fourier transform infrared microspectroscopy (FTIR); Raman microscopy; X-ray fluorescence (XRF) spectrometry; principal component analysis (PCA)
Corresponding Author:	Joanna Chwiej AGH University of Science and Technology Krakow, POLAND
First Author:	Karolina Olbrich
Order of Authors:	Karolina Olbrich
	Zuzanna Setkowicz
	Kamil Kawon
	Mateusz Czyzycki
	Natalia Janik-Olchawa
	Ilaria Carlomagno
	Giuliana Aquilanti
	Joanna Chwiej
Abstract:	Glioblastoma multiforme (GBM) is the most common and devastating primary brain tumor among adults. It is highly lethal disease, as only 25% of patients survive longer than 1 year and only 5% more than 5 years from the diagnosis. To search for the new, more effective methods of treatment, the understanding of mechanisms underlying the process of tumorigenesis is needed. The new light on this problem may be shed by the analysis of biochemical anomalies of tissues affected by tumor growth. Therefore, in the present work, we applied the Fourier transform infrared (FTIR) and Raman microspectroscopy to evaluate changes in the distribution and structure of biomolecules appearing in the rat brain as a result of glioblastoma development. In turn, synchrotron X-ray fluorescence microscopy was utilized to determine the elemental anomalies appearing in the nervous tissue. To achieve the assumed goals of the study animal models of GBM were used. The rats were subjected to the intracranial implantation of glioma cells with different degree of invasiveness. For spectroscopic investigation brain slices taken from the area of cancer cells administration were used. The obtained results revealed, among others, the decrease content of lipids and compounds containing carbonyl groups, compositional and structural changes of proteins as well as abnormalities in the distribution of low atomic number elements within the region of tumor.

Vibrational spectroscopy methods for investigation of the animal models of glioblastoma multiforme

Karolina Olbrich (1)#, Zuzanna Setkowicz (2)#, Kamil Kawon (1), Mateusz Czyzycki (3), Natalia Janik-Olchawa (2), Ilaria Carlomagno (4), Giuliana Aquilanti (4), Joanna Chwiej (1)*

(1) Faculty of Physics and Applied Computer Science, AGH University of Science and Technology, Krakow, Poland
(2) Institute of Zoology and Biomedical Research, Jagiellonian University, Krakow, Poland
(3) Institute for Photon Science and Synchrotron Radiation, Karlsruhe Institute of Technology, Hermann-von-Helmholtz-Platz 1, 76344 Eggenstein-Leopoldshafen, Germany
(4) Elettra Sincrotrone Trieste SCpA, Trieste, Italy

#Equally contributed;
*Corresponding author, email: Joanna.Chwiej@fis.agh.edu.pl

Abstract

Glioblastoma multiforme (GBM) is the most common and devastating primary brain tumor among adults. It is highly lethal disease, as only 25% of patients survive longer than 1 year and only 5% more than 5 years from the diagnosis. To search for the new, more effective methods of treatment, the understanding of mechanisms underlying the process of tumorigenesis is needed.

The new light on this problem may be shed by the analysis of biochemical anomalies of tissues affected by tumor growth. Therefore, in the present work, we applied the Fourier transform infrared (FTIR) and Raman microspectroscopy to evaluate changes in the distribution and structure of biomolecules appearing in the rat brain as a result of glioblastoma development. In turn, synchrotron X-ray fluorescence microscopy was utilized to determine the elemental anomalies appearing in the nervous tissue. To achieve the assumed goals of the study animal models of GBM were used. The rats were subjected to the intracranial implantation of glioma cells with different degree of invasiveness. For spectroscopic investigation brain slices taken from the area of cancer cells administration were used.

The obtained results revealed, among others, the decrease content of lipids and compounds containing carbonyl groups, compositional and structural changes of proteins as well as abnormalities in the distribution of low atomic number elements within the region of tumor.

Keywords

Glioblastoma multiforme (GBM), animal models, vibrational spectroscopy, Fourier transform infrared microspectroscopy (FTIR), Raman microscopy, X-ray fluorescence (XRF) spectrometry, principal component analysis (PCA)

1. Introduction

Methods of vibrational spectroscopy, including Fourier transform infrared (FTIR) and Raman microspectroscopy, are frequently used to probe biochemical composition of various types of cells and tissues. These analytical techniques combine features of optical microscopy, giving the spatial information about the sample at micrometer resolution, with the spectral details regarding its biochemical structure [1]. Besides identifying the biomolecules building the sample such as lipids, proteins or nucleic acids, FTIR and Raman microspectroscopy allow to study their conformation, what has a great importance in biomedical research [2–4]. What is more, analysis performed with vibrational spectroscopy techniques requires only minimal sample preparation, without its staining, and the measurements are usually not destructive [5, 6]. All these properties make FTIR and Raman microspectroscopy valuable analytical tools widely applied in the research of biological samples [7–13]. The methods found their particular applications in studies of the biochemical processes occurring in the tissues as a result of tumor formation. More precisely, they have a potential in discriminating tumors with various grade of malignancy [14–17], investigating the heterogeneity in their structure [18–22] and finding biomarkers, which allow distinguishing neoplastic from healthy tissues [23–29]. Because pathological states of the cells and tissues may be reflected in the abnormalities at the molecular level, FTIR and Raman microspectroscopy are considered as methods with high diagnostic potential [30, 31].

Glioblastoma multiforme (GBM) is the most common and aggressive primary brain tumor with a median survival of patients about 15 months and five-year survival rate equal only 4-5% [32]. Extreme invasiveness, intensified proliferation and infiltration, as well as high recurrence of GBM determine its classification to the group of the tumors with IV grade of malignancy. The weak prognosis for patients diagnosed with GBM follows from e.g., late-state detection, the limited possibilities of treatment and the morphological differentiation of tumor cells [33]. Clinical disorders coexisting with GBM development are not specific and include increasing intracranial pressure, headaches, ataxia, visual disturbances and frequent fainting [34, 35]. Currently, the conventional GBM therapy relies on concomitant radiotherapy with a total radiation dose of 60 Gy [36] and chemotherapy with temozolomide an alkylating agent [37] or bevacimuzab the monoclonal humanised antibody against vascular endothelial growth factor (VEGF) [38]. Diffuse tumor growth, heterogeneity of the neoplastic cells, intensified neovascularization and modifications of extracellular matrix result in GBM remains resistant to the most of standard treatment methods. As glioblastoma continues to be highly lethal for patients, new approaches of treatment are urgently needed. Finding novel biomarkers and fingerprints of this malignancy may help to understand its biology, what may be a key factor in developing effective methods of diagnosis and therapy.

In the present study, we try to verify whether glioma development causes compositional and structural changes of major biological molecules in the brain tissue. For this purpose we used animal models of the tumor. We selected three, different types of glioma cells (patient-derived tumor cells as well as T98G and U87MG commercial cell lines) and implanted them into rat brains. First, the tissues were subjected to imaging with FTIR microspectroscopy what allowed us to obtain two dimensional maps of the biomolecules distribution and to indicate differences in their accumulation between healthy and tumor-changed regions. Next, using FTIR and Raman microspectroscopy we performed detailed, spectral analysis of specific brain regions (i.e. cortex, white matter and tumor) for both implanted and healthy brain hemispheres. The obtained data were subjected to advanced statistical evaluation with the use of principal component analysis (PCA). Additionally, we used synchrotron radiation-based X-ray fluorescence (SR-XRF) spectrometry method to identify alterations in the distribution of low atomic number elements (e.g. Na, Mg, Cl) in rat brain that may be linked with the glioma growth.

The results presented in this paper constitute an important part of our main research topic, which is the use of various spectroscopic methods for the determination of potential biomarkers of glioblastoma development and growth. Our previous studies, performed with X-ray fluorescence methods, showed that development of the glioma in rat brain leads to significant elemental anomalies in the tissues affected with the tumorigenesis process. Gliomas were characterized by an elevated accumulation of Fe and Se, and the tissues surrounding the tumor mass presented an increased level of Cu [39, 40]. Furthermore, we observed that a morphologically changed region of the brain in the place of the T98G cells implantation is rather the result of the tissue damage connected with cells injection than the development of the tumor [40]. Herein, by using methods of vibrational spectroscopy, we determined the changes in brain biomolecular composition resulted from GBM growth.

2. Materials and methods

2.1. Animal experiment

Details on experimental animals, GBM cells, the procedure of implantation as well as all used pharmaceuticals were reported in our previously published papers [39, 40]. In this work, only the most important information concerning performed experiment was summarized.

The subject of our study were four groups of male Wistar rats and three of them (Pa, T and U) were intracranially implanted with the GBM cells of different origin. The N animal group consisted of naive controls. Description of the examined animal groups is presented in Table 1.

Table 1 – Description of animal groups

Group	Number of animals	Type of implanted GBM cells	Cell suspension
N	4	No implantation	-
Pa	4	Patient-derived GBM cells	5 µL of DMEM, 50000 cells/µl
T	4	T98G cell line (ATCC company)	5 µL of DMEM, 50000 cells/µl
U	3	U87MG cell line (ATCC company)	5 µL of DMEM, 5000 cells/µl

The procedure of GBM cells implantation into rat brain started with initial anesthesia of animals, next immobilization in stereotactic apparatus and finally induction of general anesthesia. Afterwards, a prepared cell suspension was transcranially implanted into the left hemisphere of rat brain. The animals woke up from anesthesia few minutes after the end of the procedure. All rats subjected to implantation were daily immunosuppressed and observed in terms of behavioral changes. The duration of experiment (counted from the day of tumor cells implantation to the animal death) was determined during the preliminary studies based on the observation of animal health. The survival time was 21 days for groups N, P and T and 15 days for the group U. After that time, the rats were perfused with physiological saline solution and after it, the brains were removed from the skulls and frozen in liquid nitrogen.

Procedures with animals were approved by the 2nd Local Institutional Animal Care and Use Committee (agreement no. 119/2016) and performed in agreement with international standards. The isolation of cells originated from human patients was approved by the Bioethics Commission for the use of cellular material collected from patients in neurooncological operations (Decision no. 535/2017 of 13 June 2017, issued by the Bioethical Commission at the University of Nicolaus Copernicus in Torun, Poland).

Our earlier study concerning the elemental anomalies of brain resulted from GBM development showed that the lesion appearing after T98G cells administration is rather an effect of nervous tissue damage occurring during implantation than the development of tumor. Therefore, in this paper we use the term "place of T98G cells implantation" instead of "tumor" in case of the T experimental group [40].

2.2. Sample preparation

The brains taken from animals were cut using a cryomicrotome into 20 and 8 µm thick slices for SR-XRF microscopy and FTIR/Raman microspectroscopy, respectively. The sections taken from the place of implantation were mounted on the appropriate carriers: Ultralene foil for SR-XRF measurements and CaF_2 windows for FTIR/Raman microscpectroscopy examinations. Finally, all prepared samples were freeze-dried.

2.3. Fourier transform infrared microspectroscopy

The measurements were performed using a FTIR microscope Nicolet iN10 MX (Thermo Fisher Scientific) at the Department of Medical Physics and Biophysics, Faculty of Physics and Applied Computer Science, AGH University of Science and Technology in Krakow, Poland. The brain samples deposited on CaF_2 windows were measured in transmission mode and the spectra were recorded for the wavenumber range of 900-4000 cm^{-1}. The measurements of the whole brain sections were performed with Ultra-Fast Mapping system (one scan per spectrum, spectral resolution of 16 cm^{-1}) and the liquid nitrogen cooled imaging array detector was used for this purpose. The chosen experimental conditions allowed to obtain large chemical maps with a spatial resolution of 25 µm x 25 µm.

For detailed examinations of selected brain regions (cortex, white matter, tumor mass and place of T98G cells implantation) the liquid nitrogen cooled MCT-A detector was used. The samples were subjected to raster scanning with the 25 µm x 25 µm IR beam, using the same step size in both directions. Number of scans averaged per single spectrum was 32 and they were recorded with spectral resolution of 8 cm^{-1}.

2.4. Raman microscopy

Raman measurements were also conducted at the Department of Medical Physics and Biophysics. For the study we used the confocal Raman microscope WITec Alpha 300R equipped with the 532 nm excitation laser module, the 100x air objective (Zeiss EC Epiplan-Neofluar, numerical aperture NA = 0.9), the UHTS 300 spectrometer (600 gratings/mm) and thermoelectrically cooled spectroscopy

camera. The laser power on the samples was 5 mW whilst the integration time was 0.5 s. Raman mapping was carried out for the samples placed on CaF_2 windows and for exactly the same areas as those subjected to detailed FTIR imaging.

2.5. Synchrotron radiation-based X-ray fluorescence microscopy

Two-dimensional elemental mapping of the brain samples was performed with synchrotron radiation-based X-ray fluorescence method and the measurements were conducted at the XRF beamline of the Elettra synchrotron in Trieste, Italy [41]. A sample environment used for element mapping was an advanced X-ray spectrometry beamline endstation developed by the International Atomic Energy Agency [42, 43]. Each tissue slice was subjected to the raster scanning using the exciting X-ray beam with the energy of 10 keV. The size of the X-ray beam on the samples was 200 μm x 200 μm. The tissues were measured in vacuum, at a pressure of 10^{-7} mbar, at the room temperature. For the detection of the X-ray fluorescence spectra a Bruker XFlash SDD detector was employed. The typical time of acquisition was 5 s/spectrum. The obtained spectral data were processed with the PyMca software to get information about net peak areas of the Kα spectral lines of Na, Mg, Al and Cl. Such net areas were used to get the maps of the elemental spatial distribution within the examined tissues [44].

2.6. Spectral and statistical analysis

The topographic biochemical analysis was based on the chemical mapping of the main absorption bands or their ratios and was carried out using the OMNIC Picta software (Thermo Scientific, version 9.2.0.86). The software was also used for the extraction and preprocessing of spectra for further statistical analysis. In the case of FTIR data, the preprocessing of spectra involved the atmospheric and the baseline correction as well as vector-normalization. For Raman spectra, the normalization to the maximal intensity and baseline correction were applied.

For the statistical evaluation of the preprocessed spectral data the principal component analysis (PCA) was utilized. The calculations were done in the Origin software (version 9.7.5.184) with dedicated plug-in for PCA of spectra.

3. Results

The verification of the biochemical and elemental changes occurring in the hemisphere with engrafted GBM cells included the following steps: (1) the topographic biomolecular analysis of subjected to the implantation and healthy hemispheres, (2) the detailed biochemical analysis of selected brain areas (cortex, white matter, place of T98G cells implantation as well as solid and debris tumor tissue), (3) statistical evaluation of the spectral data using PCA, (4) the analysis of low atomic number elements distribution in brain tissues.

3.1. Topographic biochemical analysis

The first step of the study was to verify if the implantation of GBM cells influences the distribution and accumulation of biomolecules within the rat brains. To achieve this goal, we performed the chemical mapping of selected absorption bands for the analyzed tissues. The details concerning investigated biochemical parameters are collected in Table 2. The exemplary maps of distribution of selected absorption bands (or their ratios) for examined brain samples together with their microscopic images are presented in Figure 1.

Table 2 – Examined biochemical parameters [7, 45–53].

Absorption band (or ratio of absorption bands)	Biochemical parameter
1080 cm^{-1} **1240 cm^{-1}**	distribution of compounds containing phosphate groups (nucleic acids, phospholipids, phosphorylated carbohydrates) and differences in the degree of phosphorylation of carbohydrates and glycoproteins
1360-1480 cm^{-1}	distribution of lipids, cholesterol esters and cholesterol
1658 cm^{-1}	distribution of proteins (amide I band)
1635 cm^{-1}/1658 cm^{-1}	structural changes of proteins (β-sheet to α-helix ratio)
1740 cm^{-1}	distribution of compounds containing carbonyl groups including phospholipids, cholesterol esters and ketone bodies
2924 cm^{-1}/2955 cm^{-1}	structural changes of saturated lipids (saturation level of lipids, changes in the length of fatty acid chains and the degree of their branching)
2800-3000 cm^{-1}	distribution of lipids

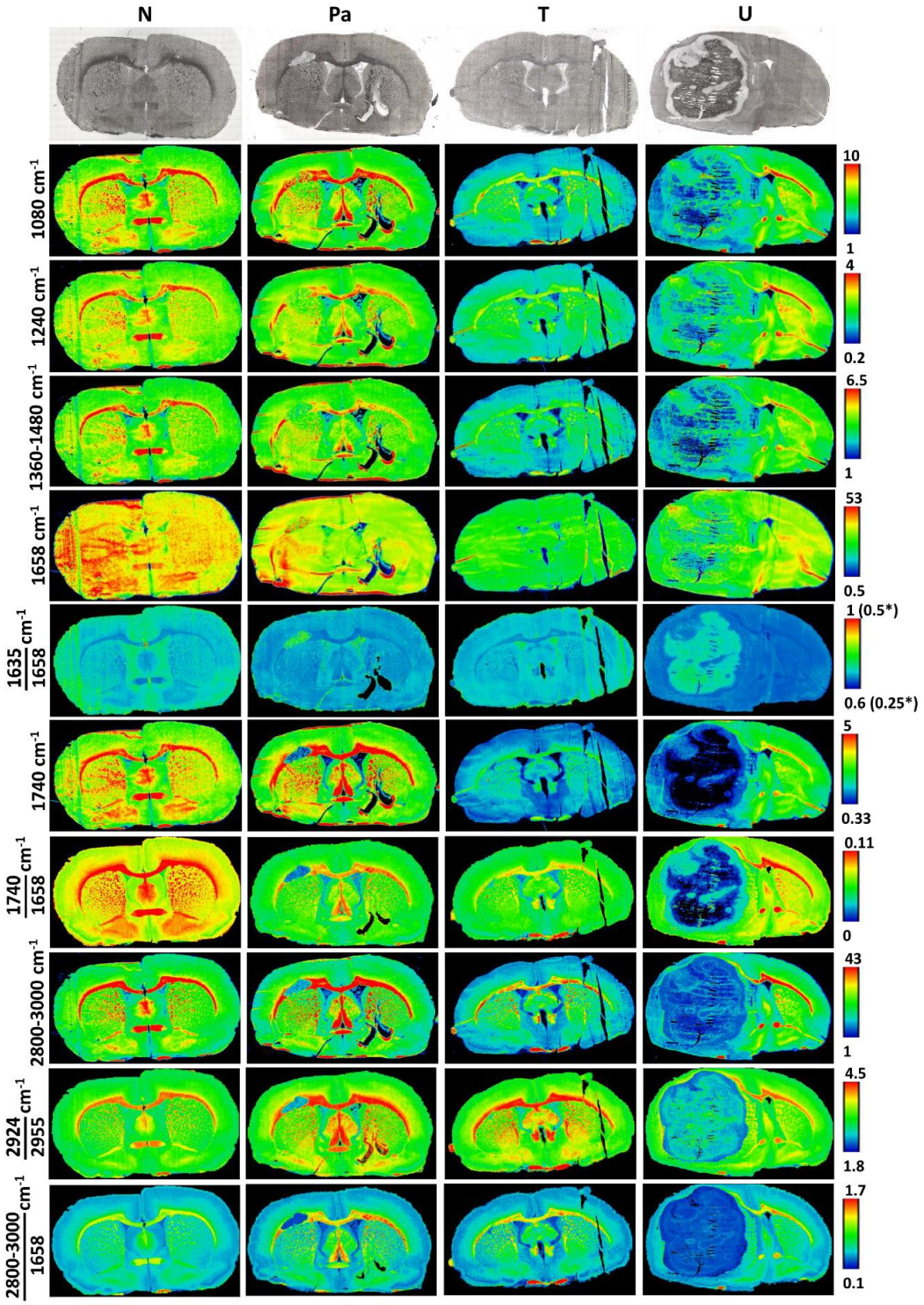

Figure 1 - The exemplary chemical maps obtained for examined brain samples together with the microscopic images of measured tissues. The sections were taken from the area of GBM cells implantation (for groups Pa, T and U) and the corresponding brain area in case of the group N. For most of the maps, the color scales, presenting relative/absolute integrated intensities of particular absorption bands, were unified. The exception is the map presenting the distribution of the ratio of absorbance at 1635 and 1658 cm^{-1} obtained for the group U, where for better visualization and interpretation of the data a different scale was applied (values in brackets).

Referring to the biochemical maps presented in Figure 1 one may notice clear changes in the distribution of compounds containing phosphate groups in the area of tumor development. The decrease of the intensity of bands at 1080 and 1240 cm^{-1} is the most pronounced for the samples taken from animals representing the group U - the diminished accumulation occurs within the whole hemisphere subjected to the implantation. What is more, a greater decrease in the intensity of these bands appears inside the tumor (tumor debris) than in its outer regions. A diminished accumulation of the compounds containing phosphate groups concerns also the tumor developing from the human patient cells. However, some differences are observed here between the intensities of the 1080 and 1240 cm^{-1} bands. The intensity of 1240 cm^{-1} band is clearly diminished within the tumor mass. In turn, in case of the band at 1080 cm^{-1} the differences comparing to the surrounding white matter area are much less pronounced.

Analysis of the distribution of lipids, cholesterol, and cholesterol esters was based on the binding vibrations of methyl and methylene group manifesting in the spectrum as a massif within the wavenumber range 1360-1460 cm^{-1}. As one can see from Figure 1, for all the experimental groups the intensity of the massif decreases in the regions of tumor development. Again, the most pronounced reduction of absorbance, covering the entire implanted hemisphere, is observed for the group U.

Alterations in the distribution and structure of proteins, resulted from GBM development, are visible for the samples taken from the Pa and U groups. The tumor developed from patient-derived cells is characterized with an elevated intensity of the amide I band. In turn for the group U, and particularly for the inner area of the tumor, one may observe a diminished intensity of that absorption band. The relative content of proteins with the β-type secondary structure is clearly elevated in the tumors developed both from the patient and U87MG line cells. For the Pa group, the increased ratio of absorbance at 1635 and 1658 cm^{-1} is observed in the entire region of the tumor, while in the case of the U group only in its debris area.

Analysis of the chemical maps presenting the absolute and relative intensity of 1740 cm^{-1} band clearly points at changes in the accumulation of compounds containing carbonyl groups in the region of the tumor for the Pa and U groups as well as the place of T98G cells implantation. The highly pronounced decrease of absorbance allows for a precise indication of tumor area and its separation from the surrounding tissues. What one should also notice is a strongly nonhomogeneous distribution of compounds containing carbonyl groups within the tumor both in case of the Pa and U groups. Extremely low levels of these compounds are observed in the necrotic regions of the tumor developed from U87MG cells.

As one can see from Figure 1, for the Pa, T and U groups the reduction in the absolute (2800-3000 cm^{-1}) and relative (2800-3000 cm^{-1}/amide I) accumulation of lipids is observed in the areas of the tumor development and T98G cells implantation. What is more, these regions are characterized with the structural abnormalities of lipids manifesting as the changes of intensity ratio of bands at 2924 and 2955 cm^{-1}. Based on the chemical maps presenting the accumulation and structural changes of lipids it is possible to precisely indicate the areas of tumors developed after the GBM cells implantation.

3.2. Detailed spectral analysis

The FTIR and Raman spectra for a detailed qualitative and statistical analysis were taken from the same, microscopically identified, tissue areas. The brain regions selected for spectral analysis included cortex, white matter and solid tumor or the place of glioma cells implantation for the Pa, U and T groups as well as, additionally, the tumor debris area for the U group. The collected spectra after appropriate preprocessing were subjected to an advanced statistical analysis utilizing PCA [54].

3.2.1. Spectral analysis of FTIR data

The first step of the study was to verify if the introduction of GBM cells and/or tumor development result in any biochemical changes of brain areas distant from the implantation site. For this purpose, for both brain hemispheres, we recorded the IR spectra in the cortex and white matter regions not affected with GBM growth. The average absorption spectra and their second derivatives calculated for the examined areas for all the experimental groups were compared in Figures 2a and 2b, respectively. One may observe that the intensity and shape of the absorption bands do not differ between the experimental groups. No differences in the recorded spectra were also noticed between the corresponding areas of the left and right hemispheres within a given animal group. This may suggest that the development of GBM

in the rat brain does not result in remote changes in the distribution of analyzed biomolecules, even in the case of a widespread tumor developed from the U87MG cells.

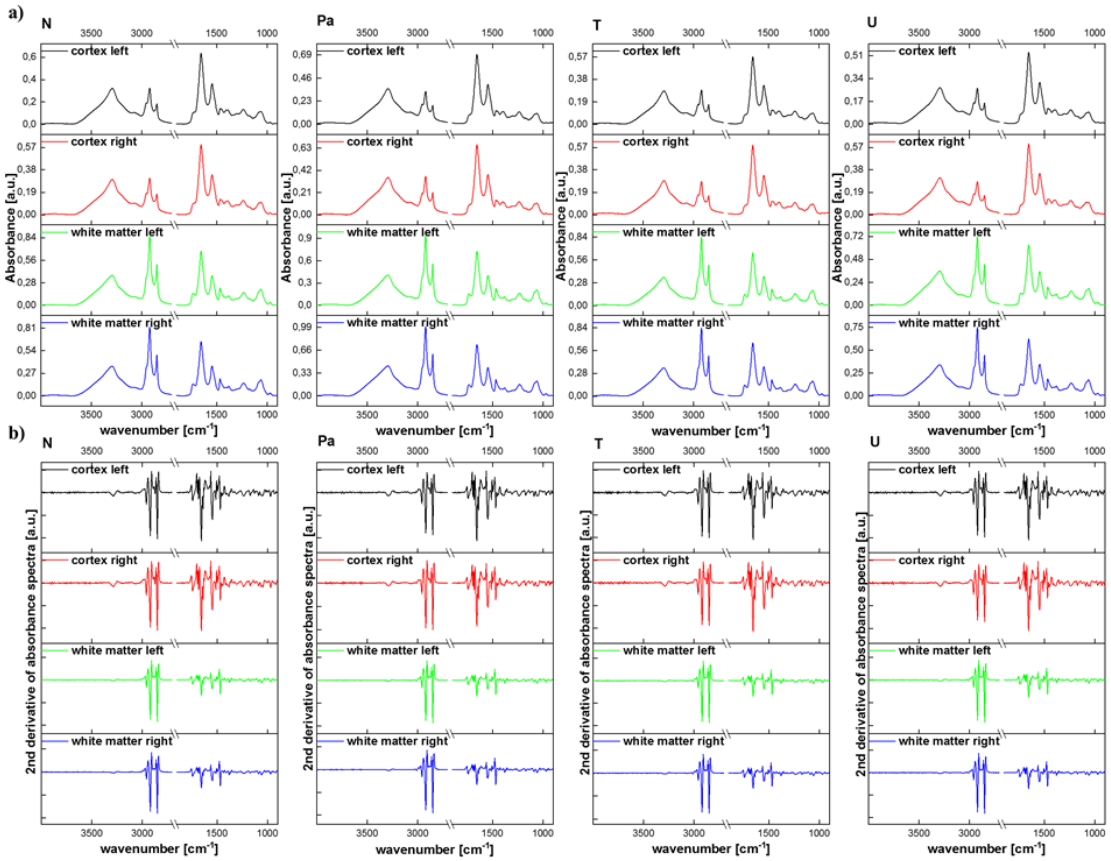

Figure 2 - The averaged absorption spectra (a) and their second derivatives (b) obtained for the regions of cortex and white matter from the left and right hemispheres for all the experimental groups.

In the further part of our investigation, we focused on the local changes in biomolecules distribution caused by GBM development. We compared the absorption spectra recorded in selected areas from the left (implanted) hemisphere, namely brain cortex, white matter and tumor as well as the place of glioma cells implantation in the case of the group T. The average spectra and their second derivatives obtained for the animals subjected to the implantation of various GBM cells are stated in Figures 3a and 3b, respectively. Based on the presented spectra, we could indicate clear differences in the intensity and/or shape of the absorption bands characteristic for analyzed biomolecules between the region of the tumor and healthy areas of the cortex and white matter. The spectra obtained for tumors in the Pa and U groups and the implantation site in the group T were characterized with a diminished absorbance within the lipid massif and with the absence of the IR band characteristic for compounds containing carbonyl groups. Furthermore, the changes in the shape of the band specific for phosphate groups were found for them.

For the statistical confirmation of the observations we found, using the vector-normalized second derivative spectra, we performed PCA and presented results in Figures 3c and 3d. As it can be seen, the spectra registered for cortex, white matter and tumor, in case of the Pa and U groups, are well separated in the space of the first two principal components. In the case of the group T, spectra recorded for the cortex and the place of implantation present a quite large similarity, while the ones measured for the white matter are well separated from them. Next, we compared the tumors developed from the U87MG and the patient-derived cells with the area of injury appearing after the introduction of T98G cells. Based on the PCA plot presented in Figure 3d one may observe that the probability circles (containing 95% of

cases representing a given group) for the compared areas overlap with each other in a large part, which indicates their high similarity.

Gliomas developed after the U87MG cells implantation were characterized by large heterogeneity of their structure, what allowed us to indicate two specific regions present within the tumor – the solid and debris areas. In Figure 4, one may see the absorption spectra registered in the mentioned regions, their second derivatives as well as the results of PCA. As one can see from Figure 4c, the solid and debris areas of the tumor are almost completely separated in the space of the first two principal components, what means they differ significantly from each other in relation to their biomolecular composition. This observation confirms the results of the earlier topographic analysis of the examined tissues.

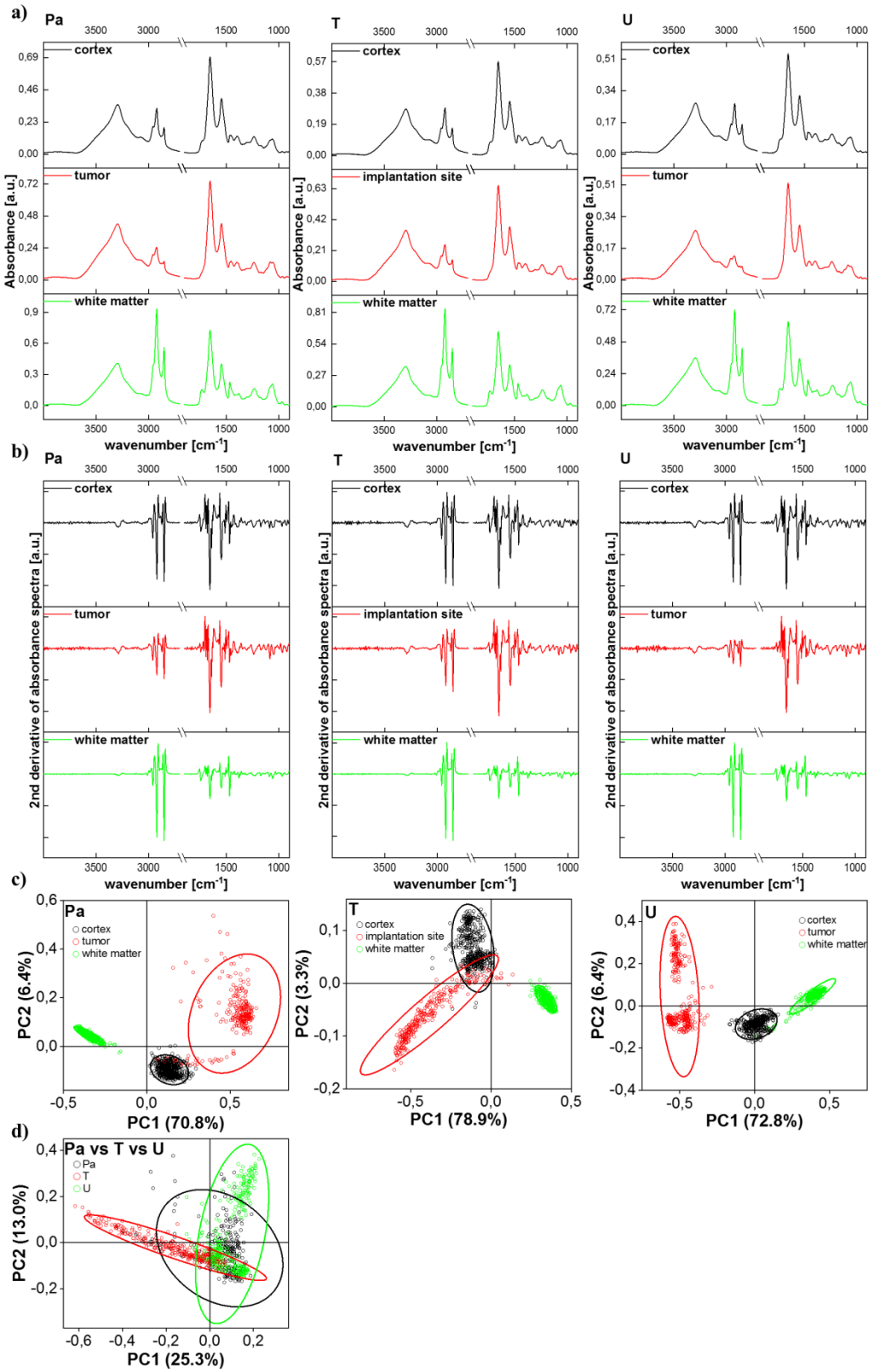

Figure 3 - Averaged absorption spectra (a) and their second derivatives (b) obtained for the regions of cortex, white matter and tumor or the place of glioma cells introduction for the animals subjected to the implantation. The results of PCA carried out on the vector-normalized second derivative spectra from the examined areas (c, d).

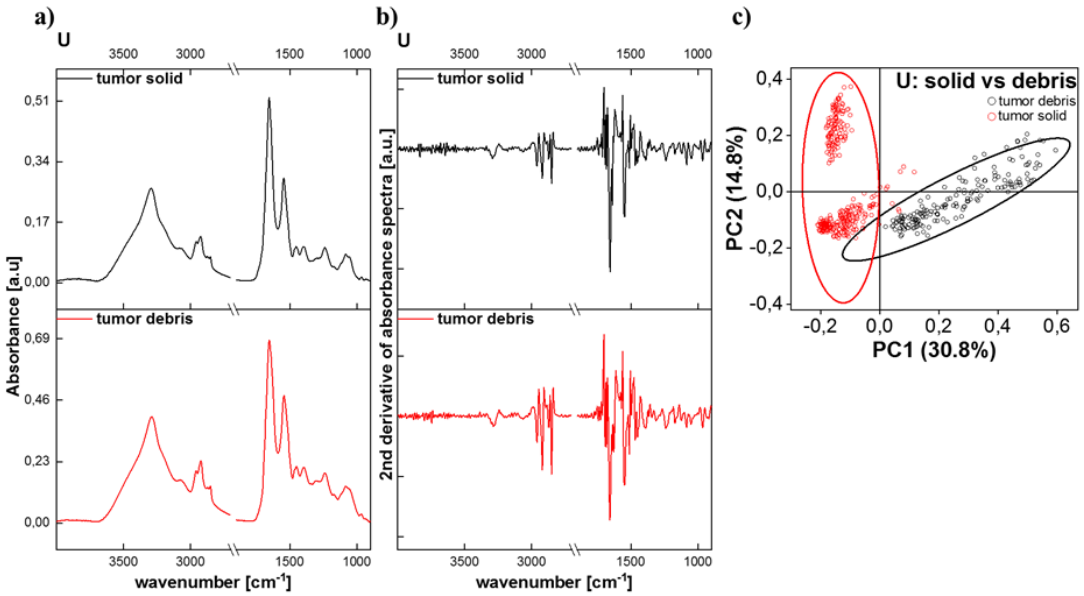

Figure 4 - Averaged absorption spectra (a) and their second derivatives (b) obtained for the solid and debris areas of the tumors developed from the U87MG cells. Results of PCA carried out on the vector-normalized second derivative spectra for the examined regions (c).

3.2.2. Spectral analysis of Raman data

The farther step of the study was to confirm, with a complementary technique of Raman microscopy, that the development of tumor does not affect the biochemical composition of far-distant regions of brain. The spectral analysis performed for the areas of brain cortex and white matter (Figure 5) showed that there is no substantial differences between the average Raman spectra obtained for the hemisphere with developed tumor and the healthy one.

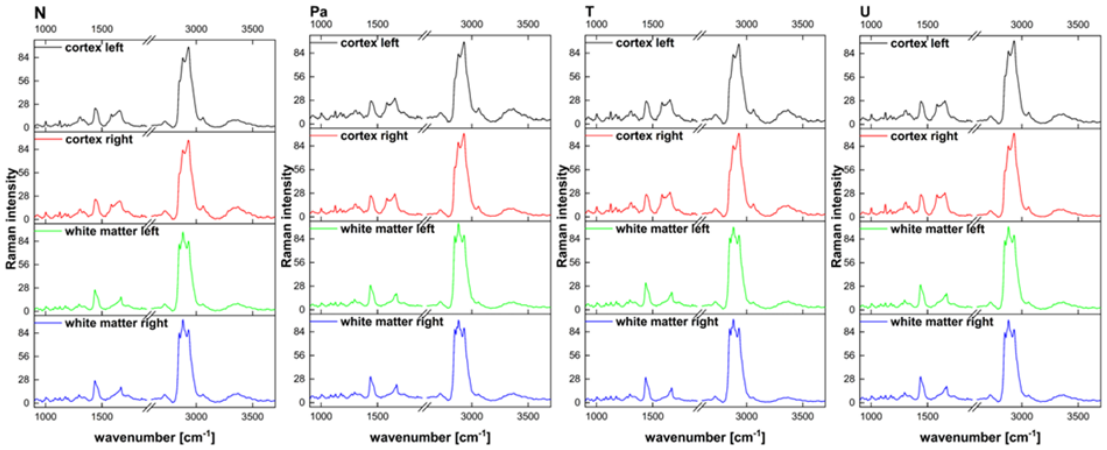

Figure 5 - Averaged Raman spectra obtained for the regions of cortex and white matter from the left and right hemispheres for all the experimental groups.

On the other hand, distinctive differences between the Raman spectra recorded for the cortex and white matter are apparent. They concern the relative intensity of lipid band at 1442 cm^{-1} and the shape of the massif at the wavenumber range 2800-3000 cm^{-1}. What is more, the Raman spectra of white matter are characterized by a diminished intensity of the band specific to phenylalanine and appearing at 1585 cm^{-1}.

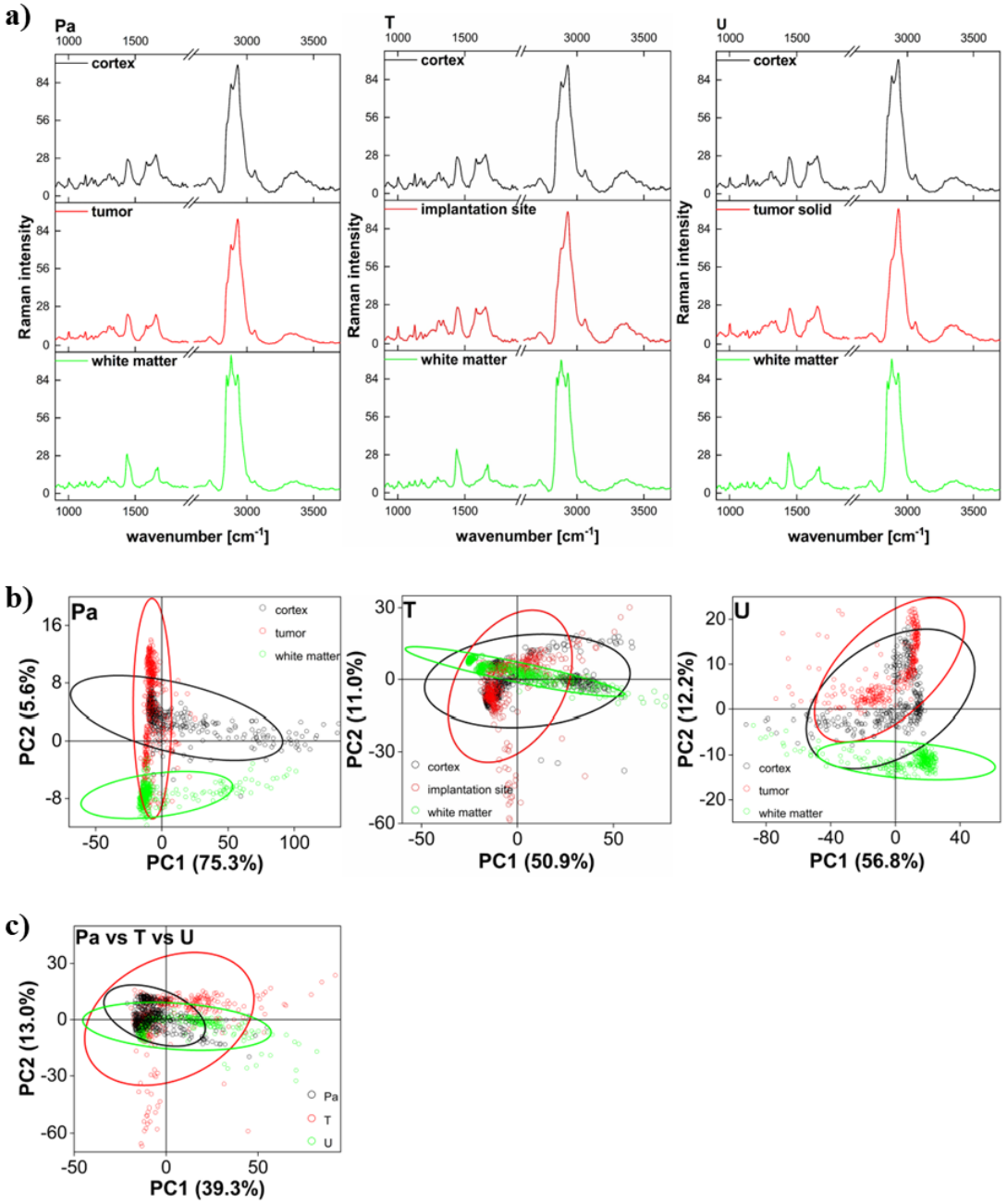

Figure 6 - Averaged Raman spectra obtained for the regions of cortex, white matter and tumor or the place of glioma cells introduction for the animals subjected to the implantation (a). Results of PCA carried out on the normalized Raman spectra from the examined areas (b, c).

The purpose of the next part of the study was the verification, if the Raman spectra recorded within the tumor/implantation area and white matter and brain cortex differ significantly from each other. To achieve this goal, the averaged and normalized Raman spectra from the mentioned brain regions are compared in Figure 6a. The wavenumber ranges of 2840-3020, 2861-2901 and 1200-1400 cm^{-1} in the tissue spectra are characteristic for the organic matter, lipids and proteins, respectively. The comparison of Raman spectra recorded in the GBM affected and healthy (cortex and white matter) tissues showed the differences in the shape of the massif characteristic for proteins. Within this wavenumber range, at around 1337 cm^{-1}, the band characteristic for tryptophan is, among others, observed [74, 75]. More

pronounced differences were found for the wavenumber range specific for lipids, where tumor spectra presented much lower intensity of Raman signal comparing to the surrounding white matter and cortex. Such a result is in a good agreement with the data obtained with the use of FTIR microscopy.

To evaluate the statistical significance of the observed differences, PCA was performed on the normalized Raman spectra. Its results were presented in Figures 6b and 7. As one can see from the Figure 6b, for none of the GBM model, it was possible to separate (in the space of the first two principal components) the tumor spectra from those recorded within white matter and cortex.

To verify the diagnostic potential of Raman microscopy, we also checked whether the spectra obtained for the tumor/implantation site appearing after the introduction of various glioma cells can be separated using PCA. The results of PCA, which one can see in Figure 6c, showed that the spectra from the implantation area do not differ significantly between the examined models of GBM. The probability circles obtained for the three examined spectra populations overlapped themselves in the space of the first two principal components.

As one can see from Figure 7, in contrast to PCA conducted on the data from the FTIR microscopy, the multivariate statistical analysis performed on Raman normalized spectra did not show any pivotal differences between the solid and debris regions of the tumor developing after the U87MG cells implantation.

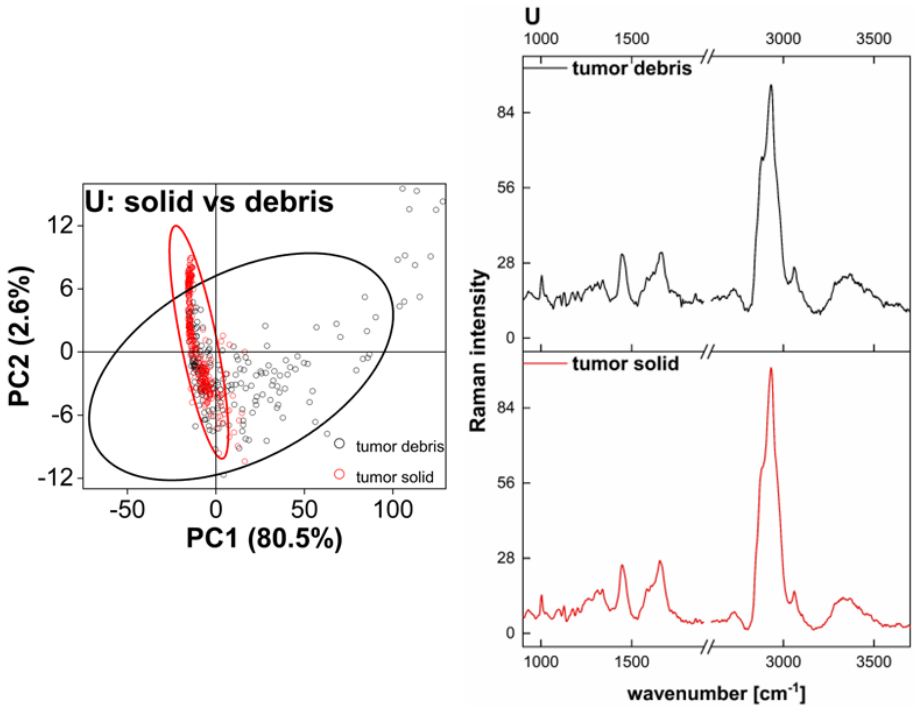

Figure 7 - Results of PCA carried out on the normalized Raman spectra from the solid and debris areas of the tumors developed from U87MG cells.

3.3. Topographic analysis of low atomic number elements

The last part of our investigation was to assess the changes in the distribution of Na, Mg and Cl in the examined tissues. Topographic elemental maps obtained for representative rat brain samples are presented in Figure 8. The most pronounced anomalies were found for the group U, where the greatest tumor growth occurred. The increase in the accumulation of Na was observed there mainly in the outer regions of the tumor, while elevated levels of Cl were noticed in its whole mass. Furthermore, a decreased accumulation of Mg was observed in the tumor debris area. In the case of other animal groups, only slightly elevated level of Cl was found in the tumor developed from the patient-derived GBM cells.

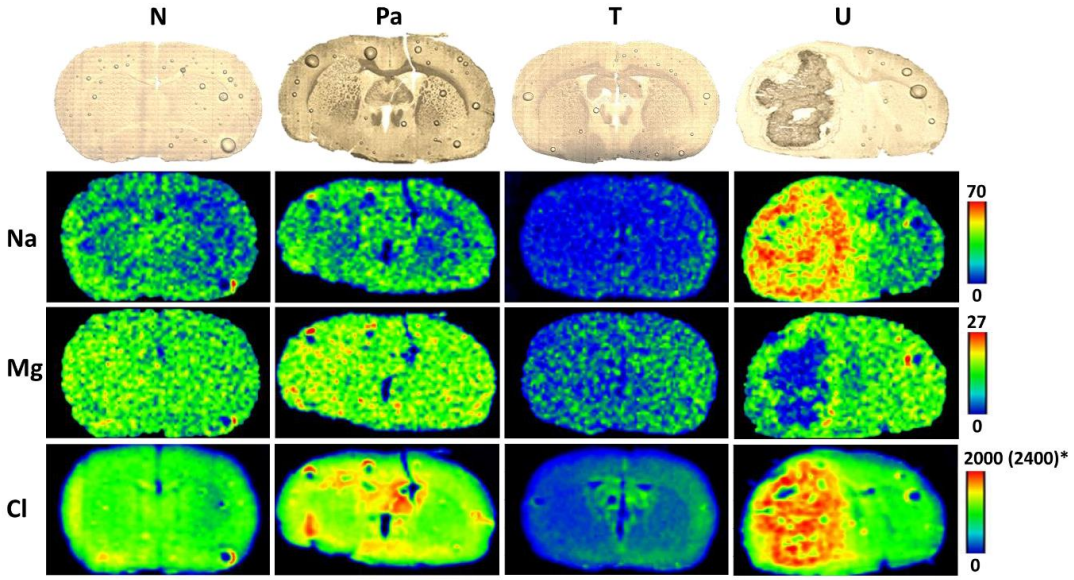

Figure 8 - Elemental maps obtained for the brain slices taken from the rats representing the examined animal groups. Distributions of Na, Mg, Al and Cl were compared with histological images. On color scales net intensity K-α lines was presented (* for the sample originated from the group U a different scale was applied).

4. Discussion

In our work, two methods of vibrational microspectroscopy coupled with PCA were used as experimental tools supporting brain tumor diagnosis. Such approach is widely used by numerous research groups [55]. Rat brains taken from animals subjected to various GBM cells implantation and control brain samples were raster scanned using FTIR and Raman microscopes. The preprocessed vibrational spectra recorded in selected brain/tumor areas were then subjected to PCA.

Brain tumor development is linked with a number of tissular and cellular alterations and with the use of FTIR mapping it is possible to visualize some of them at the tissue level. The absorption bands at 1080 and 1240 cm^{-1} give an information about the level of compounds containing phosphate groups like phospholipids or nucleic acids which are pivotal biochemical components of healthy cells. Therefore, the changes in their intensity may be linked with tumor mass growth and diminishing healthy cells.

The absorption bands at 1080 and 1240 cm^{-1} testify also about the presence of RNA and DNA in the analyzed sample. Both topographic and spectral FTIR analysis showed differences in the intensity and structure of the mentioned bands between glioma and normal tissue, observed mainly in the group Pa and U. The reduced bands intensity in the region of tumor development may be associated with the damage of nucleic acids. The results of our investigation are in agreement with the findings of Depciuch *et al.*, who observed a diminished intensity of absorption bands corresponding to the presence of RNA and DNA in the human glioma samples [56]. On the other hand, in the literature one may also find studies with animal models of glioma, which indicate the increase of nucleic acid content in the region of glioma growth, compared to a healthy brain tissue [22, 57].

The topographic biochemical analysis of brain slices revealed differences in the distribution of the intensity of the band at 1080 cm^{-1} between the samples originated from the Pa and U groups. For tumors developed from the patient-derived cells, the intensity of this band did not differ considerably from the surrounding white matter area. In turn, in the case of the group U, one may observe a significantly decreased absorbance within the tumor and, in particular, in its necrotic region.

Besides the nucleic acids, the mentioned spectral region is also associated with the presence of carbohydrates, including glucose [58]. Tumor cells of different origin, including glioma cells, are characterized by an increased uptake of glucose compared to normal ones, what results from intensified metabolic processes [59]. Therefore, we should rather expect a higher absorbance in this wavenumber range for the solid tumor, compared to the normal tissues. In turn, the observed decrease intensity of

1080 cm^{-1} band in the core of the tumor developed from the U87MG cells, may reflect changes in the glucose metabolism resulted from necrosis of the cells.

The results of the topographic analysis carried out for proteins indicate the differences in their accumulation between healthy and tumor-changed regions. The intensity of amid I band was elevated in the gliomas developed from the patient-derived cells and in the areas of the T98G cells implantation. These findings are in agreement with the literature reports. Krafft *et al.* showed that human brain tumors are characterized by a higher protein level than the normal brain tissue [60]. Similar observation, for the animal model of GBM, was made by Bambery *et al.*, who found the highest intensity of the amid I band in the tumor site [57]. During cancer progression, many cellular and extracellular processes occur. One of them is the excretion of extracellular matrix proteins (collagen, laminin, metalloproteinase) creating the favorable conditions to expand the tumor volume [61]. The mentioned process may explain the increased level of proteins as well as diminished relative content of other biomolecules within the tumor area.

We did not observe any significant differences in protein accumulation between healthy brain tissue and the solid region of the tumor for the group U. On the other hand, the necrotic region, observed in the tumors developed from the U87MG cells, was characterized by the areas with a reduced protein accumulation.

The analysis of tissues taken from the animals representing the Pa and U groups showed significant differences in the relative secondary structure of proteins between the area of the tumor and surrounding tissues. In case of the group U, the differences in the conformation of proteins were noticed also between the solid and debris region of the tumors. The increased ratio of absorbance at the wavenumbers of 1635 and 1658 cm^{-1} in the area of glioma indicates the higher content of proteins with β sheet structure in relation to these with α helical conformation. Protein structure determines their biological functions, and therefore, any changes may reflect in the proper functioning of the cells. The investigation performed *in vitro* by Kong *et al.* showed that, based on the secondary structure of proteins, it is possible to distinguish glial cells from glioma cells. Authors stated, moreover, that conformational changes of proteins in the examined cells are related to the process of tumorigenesis [62]. The anomalies in the secondary structure of proteins observed in the glioma-changed tissue may be a result of the gene mutations related with the process of tumor development [56, 63].

The increase of the relative content of proteins with _-type secondary structure may be linked with the elevated secretion of proteoglycan NG2 in GBM cells [64]. The NG2 proteoglycan belongs to chondroitin sulfate proteoglycans (CSPGs), that are involved in interactions with constituents of extracellular matrix, adhesion of the cells and binding of the receptors [65]. The NG2 proteoglycan influences the increase of the invasive capabilities of GBM cells enabling them binding with extracellular matrix proteins and its protein core has the secondary structure of β-sheets [66, 67].

Roemer *et al.* reported a case of a patient diagnosed with GBM and the development of the tumor was associated with the presence of inflammatory demyelination. The result of this process is a damage of the myelin sheaths, which surround neurons and ensure their proper functioning. Authors found that brain region affected with demyelination was characterized by a lower content of lipids and structural changes of the proteins, consisting in the modification of their conformation in the direction of β sheet secondary structure [68]. These finding is in agreement with the results of the FTIR analysis performed in the frame of our investigation. Due to similarities between inflammatory demyelination and high grade gliomas, observed during neuroimaging, cases of initial misdiagnosis were reported [69, 70].

The results of our investigation clearly point that tumors developed in the rat brains from the U87MG cells and the patient GBM cells, as well as the place of T98G cells implantation, are characterized with a diminished level of lipids, compared to both surrounding and normal brain tissue. The topographic and spectral analysis showed a noticeable decrease in the total lipid content and changes of their structure within the area of tumor. These differences were clearly visible on the biochemical maps obtained with the FTIR imaging and based on them it was possible to distinguish the region of the glioma from the tissue not affected with the tumor.

Based on the lipid distribution maps obtained for the group U we may conclude that the reduced lipid level concerns both the solid and debris regions of the tumor. Our observations are in agreement with the results obtained by Krafft *et al.* Authors used a near infrared Raman spectroscopy for examination of the samples of brain tumors, including gliomas. They found that a tumor-affected tissue contains less lipids than normal brain tissue [60]. Other studies showed that the decrease in the lipid

content in the glioma is correlated with an increased grade of its malignancy. What is more, a lipid to protein ratio within the area of the tumor is lower while comparing to the normal brain tissue [71, 72]. This finding is in agreement, also, with our investigation, that showed the clear decrease in the intensity ratio of lipid massif and amide I band (2800-3000 cm^{-1}/1658 cm^{-1}) within the tumors developing from all the examined GBM cells.

Alterations in the content and structure of lipids, that we observed in the solid regions of the glioma, may be associated with the development and growth of tumor cells. Both processes are connected with a higher energy demand, which may lead to the reduction in the lipid content in the proliferating tumor cells, compared to the normal ones [22, 73].

Another important factor which may influence the lipid content in the tumor tissue may be the presence of abnormalities in the composition of cell membranes. Changes in their structure were observed during the tumorigenesis and were associated with the higher grade of glioma malignancy [74]. One of the key lipid components of the cell membrane, that affects its integrity, are phospholipids. Their occurrence in the analyzed tissues manifests in the infrared spectra, mainly by the presence of the absorption band at ~1740 cm^{-1}, attributed to stretching vibrations of C=O groups, as well as the bands at ~1080 and 1240 cm^{-1}, which originate from the antisymmetric and symmetric stretch vibrations of phosphate groups [75]. Analyzing the infrared spectra recorded from the tumors developed from all the GBM cells, one may notice the lack of the absorption band at 1740 cm^{-1}. A significant reduction of the intensity of this band within the area of tumor is also visible in the chemical maps recorded from the examined tissues. Depciuch *et al.*, who used FTIR to analyze human glioma samples, made the same conclusions [56]. Similar observation was done by Beljebbar *et al.* based on the animal model of glioma. The authors found that the intensity of the 1740 cm^{-1} absorption band is diminished or the band is not visible in the tumor spectra [22]. They also suggested that the reduction in the content of some types of phospholipids (phosphatidylcholine, phosphatidylserine) in the glioma compared to other brain regions may be caused by their degradation. This, in turn, may affect structural changes of the cell membranes and finally may lead to disturbances in their functioning [22].

The chemical maps for the spectral region 1360-1480 cm^{-1} correspond to the distribution of fatty acids, cholesterol esters and cholesterol in the examined tissues. In the areas of tumor development, a reduced intensity of this massif, compared to the surrounding and normal brain tissues, was noticed. Similar observation was made by Beljebbar *et al.*, who found the lack of cholesterol in both the vital and necrotic region of animal glioma [22]. A decreased level of cholesterol in human brain tumors, compared to the normal brain tissue, was also reported [60]. Investigations on cholesterol metabolism in gliomas indicate its alterations in tumor-changed tissues and suggest a potential use of cholesterol-target therapy [76]. Pinacho-Garcia *et al.* found that cultured glioma cells, both of animal and human origin, use cholesterol for synthesis of corticosteroids that influence the tumor progression [77]. Because of an increased proliferation rate and the associated larger energy consumption, cancer cells require higher amounts of cholesterol [78]. The elevated demand for cholesterol of cancer cells may result in its decreased content in tumor compared to the normal tissues. Besides being the precursor of many hormones, cholesterol is one of the major components of the cell membranes and myelin sheaths [79]. Therefore, degradation of these structures or changes in their composition, also may affect the cholesterol level in the nervous tissue.

The detailed spectral analysis of the FTIR data confirmed the results of the chemical mapping. It showed, among others, that the development of GBM in the rat brain does not result in the remote changes in the accumulation of biomolecules, although the spectra recorded from the tumor area significantly differ from those measured in the surrounding tissues. Moreover, it was found that the observed spectral anomalies are common for various animal models of GBM. The significance of all the mentioned spectral differences was confirmed by the statistical analysis, and PCA was successfully used for this purpose.

In the frame of the study we also verified whether glioma development influences the distribution of low atomic number elements within brain. Alterations in their accumulation were mainly visible for the tumors developed from the U87MG cells. Higher levels of Na and Cl were observed in these tumors, however one has to take into account the fact that after death rats were perfused with physiological saline. We may, however, suppose that the glioma cells are characterized by an elevated uptake of these elements, compared to the normal cells. An increase of Na occurred in the cells with high proliferation

ability, what may explain its intensified accumulation in the vital region of the tumor [80]. In turn, in the necrotic region of the glioma, a decreased accumulation of Mg was observed.

5. Conclusions

The application of FTIR and Raman microspectroscopy allowed us to indicate the changes in the distribution and the structure of biomolecules that appear in rat brains as the result of GBM development. The observed anomalies were usually correlated with the histological changes of the tissue and their extent was dependent on the implanted glioma cell line. Decreased levels of lipids, nucleic acids and compounds containing carbonyl groups were observed within the regions of GBM growth, as well as changes in the content and structure of proteins. In addition, the elemental analysis carried out with SR-XRF revealed that in the most extensive tumors (developed from the U87MG cell line) there is an increase in the content of Na and Cl and a decrease in Mg compared to the surrounding tissues.

Author contributions:

Karolina Olbrich: Conceptualization, Methodology, Resources, Investigation, Formal analysis, Visualization, Writing - original draft. **Zuzanna Setkowicz**: Conceptualization, Methodology, Resources, Supervision, Writing - review & editing. **Kamil Kawon**: Methodology, Investigation, Formal analysis, Visualization, Writing - original draft. **Mateusz Czyzycki**: Methodology, Investigation. **Natalia Janik-Olchawa**: Methodology, Investigation. **Ilaria Carlomagno**: Methodology, Resources, Investigation. **Giuliana Aquilanti**: Methodology, Resources. **Joanna Chwiej**: Conceptualization, Methodology, Resources, Investigation, Supervision, Writing - original draft.

Declaration of Competing Interest:

The authors declare that they have no known competing financial interests or personal relationships that could have appeared to influence the work reported in this paper.

Acknowledgements:

This work was partially financed by the Ministry of Education and Science of Poland and the subvention no. N18/DBS/000018 of the Laboratory of Experimental Neuropathology (Institute of Zoology and Biomedical Research, Jagiellonian University in Krakow, Poland). Part of the presented results were obtained with the WITec Alpha300R Raman microscope purchased from the funds granted to the AGH UST in the frame of the "Excellence Initiative – Research University" project. Karolina Olbrich and Natalia Janik-Olchawa have been supported by the EU Project POWR.03.02.00-00-I004/16. Kamil Kawon has been partially supported by the program "Excellence Initiative – Research University" granted to AGH UST. The access to the XRF beamline has been supported by the project CALIPSOplus under Grant Agreement 730872 from the EU Framework Programme for Research and Innovation HORIZON 2020 (proposal 20195109) .

References

1. Carter EA, Tam KK, Armstrong RS, Lay PA (2009) Vibrational spectroscopic mapping and imaging of tissues and cells. Biophys Rev 1:95–103. https://doi.org/10.1007/s12551-009-0012-9

2. Severcan M, Haris PI, Severcan F (2004) Using artificially generated spectral data to improve protein secondary structure prediction from Fourier transform infrared spectra of proteins. Analytical Biochemistry 332:238–244. https://doi.org/10.1016/j.ab.2004.06.030

3. Leray A, Clément J-E, Bouhélier A, Finot E (2019) Conformational Changes and Charge Transfer in Biomolecules Resolved Using Dynamic Enhanced Raman Correlation Spectroscopy. J Phys Chem B 123:1931–1938. https://doi.org/10.1021/acs.jpcb.8b10803

4. Lewis RNAH, McElhaney RN (2013) Membrane lipid phase transitions and phase organization studied by Fourier transform infrared spectroscopy. Biochimica et Biophysica Acta (BBA) - Biomembranes 1828:2347–2358. https://doi.org/10.1016/j.bbamem.2012.10.018

5. Votteler M, Carvajal Berrio DA, Pudlas M, Walles H, Stock UA, Schenke-Layland K (2012) Raman spectroscopy for the non-contact and non-destructive monitoring of collagen damage within tissues. Journal of Biophotonics 5:47–56. https://doi.org/10.1002/jbio.201100068

6. Baker MJ, Trevisan J, Bassan P, Bhargava R, Butler HJ, Dorling KM, Fielden PR, Fogarty SW, Fullwood NJ, Heys KA, Hughes C, Lasch P, Martin-Hirsch PL, Obinaju B, Sockalingum GD, Sulé-Suso J, Strong RJ, Walsh MJ, Wood BR, Gardner P, Martin FL (2014) Using Fourier transform IR spectroscopy to analyze biological materials. Nature Protocols 9:1771–1791. https://doi.org/10.1038/nprot.2014.110

7. Chwiej JG, Ciesielka SW, Skoczen AK, Janeczko KJ, Sandt C, Planeta KL, Setkowicz ZK (2019) Biochemical Changes Indicate Developmental Stage in the Hippocampal Formation. ACS Chemical Neuroscience 10:628–635. https://doi.org/10.1021/acschemneuro.8b00471

8. Rugiel MM, Setkowicz ZK, Drozdz AK, Janeczko KJ, Kutorasińska J, Chwiej JG (2021) The Use of Fourier Transform Infrared Microspectroscopy for the Determination of Biochemical Anomalies of the Hippocampal Formation Characteristic for the Kindling Model of Seizures. ACS Chemical Neuroscience 12:4564–4579. https://doi.org/10.1021/acschemneuro.1c00642

9. Kawon K, Setkowicz Z, Drozdz A, Janeczko K, Chwiej J (2021) The methods of vibrational microspectroscopy reveals long-term biochemical anomalies within the region of mechanical injury within the rat brain. Spectrochimica Acta Part A: Molecular and Biomolecular Spectroscopy 263:120214. https://doi.org/10.1016/j.saa.2021.120214

10. Janik-Olchawa N, Drozdz A, Wajda A, Sitarz M, Planeta K, Setkowicz Z, Ryszawy D, Kmita A, Chwiej J (2022) Biochemical changes of macrophages and U87MG cells occurring as a result of the exposure to iron oxide nanoparticles detected with the Raman microspectroscopy. Spectrochimica Acta Part A: Molecular and Biomolecular Spectroscopy 278:121337. https://doi.org/10.1016/j.saa.2022.121337

11. Staritzbichler R, Hunold P, Estrela-Lopis I, Hildebrand PW, Isermann B, Kaiser T (2021) Raman spectroscopy on blood serum samples of patients with end-stage liver disease. PLOS ONE 16:e0256045. https://doi.org/10.1371/journal.pone.0256045

12. Nallala J, Lloyd GR, Shepherd N, Stone N (2016) High-resolution FTIR imaging of colon tissues for elucidation of individual cellular and histopathological features. Analyst 141:630–639. https://doi.org/10.1039/C5AN01871D

13. Tombolesi N, Altara R, da Silva GJJ, Tannous C, Zouein FA, Stensløkken K-O, Morresi A, Paolantoni M, Booz GW, Cataliotti A, Sassi P (2022) Early cardiac-chamber-specific fingerprints in heart failure with preserved ejection fraction detected by FTIR and Raman spectroscopic techniques. Scientific Reports 12.: https://doi.org/10.1038/s41598-022-07390-2

14. Crow P, Stone N, Kendall CA, Uff JS, Farmer JAM, Barr H, Wright MPJ (2003) The use of Raman spectroscopy to identify and grade prostatic adenocarcinoma in vitro. British Journal of Cancer 89:106–108. https://doi.org/10.1038/sj.bjc.6601059

15. Tiwari S, Falahkheirkhah K, Cheng G, Bhargava R (2022) Colon Cancer Grading Using Infrared Spectroscopic Imaging-Based Deep Learning. Applied Spectroscopy 76:475–484. https://doi.org/10.1177/00037028221076170

16. Krafft C, Sobottka SB, Geiger KD, Schackert G, Salzer R (2007) Classification of malignant gliomas by infrared spectroscopic imaging and linear discriminant analysis. Analytical and Bioanalytical Chemistry 387:1669–1677. https://doi.org/10.1007/s00216-006-0892-5

17. Kopec M, Błaszczyk M, Radek M, Abramczyk H (2021) Raman imaging and statistical methods for analysis various type of human brain tumors and breast cancers. Spectrochimica Acta Part A: Molecular and Biomolecular Spectroscopy 262:120091. https://doi.org/10.1016/j.saa.2021.120091

18. Amharref N, Beljebbar A, Dukic S, Venteo L, Schneider L, Pluot M, Manfait M (2007) Discriminating healthy from tumor and necrosis tissue in rat brain tissue samples by Raman spectral imaging. Biochimica et Biophysica Acta (BBA) - Biomembranes 1768:2605–2615. https://doi.org/10.1016/j.bbamem.2007.06.032

19. Yamada T, Miyoshi N, Ogawa T, Akao K, Fukuda M, Ogasawara T, Kitagawa Y, Sano K (2002) Observation of Molecular Changes of a Necrotic Tissue from a Murine Carcinoma by Fourier-Transform Infrared Microspectroscopy. Clin Cancer Res 8:2010–2014

20. Koljenović S, Choo-Smith L-P 'ing, Bakker Schut TC, Kros JM, van den Berge HJ, Puppels GJ (2002) Discriminating Vital Tumor from Necrotic Tissue in Human Glioblastoma Tissue Samples by Raman Spectroscopy. Laboratory Investigation 82:1265–1277. https://doi.org/10.1097/01.LAB.0000032545.96931.B8

21. Bitar RA, Martinho H da S, Tierra-Criollo CJ, Zambelli Ramalho LN, Netto MM, Martin AA (2006) Biochemical analysis of human breast tissues using Fourier-transform Raman spectroscopy. Journal of Biomedical Optics 11:054001. https://doi.org/10.1117/1.2363362

22. Beljebbar A, Amharref N, Lévèques A, Dukic S, Venteo L, Schneider L, Pluot M, Manfait M (2008) Modeling and quantifying biochemical changes in C6 tumor gliomas by Fourier transform infrared imaging. Anal Chem 80:8406–8415. https://doi.org/10.1021/ac800990y

23. Barnas E, Skret-Magierlo J, Skret A, Kaznowska E, Depciuch J, Szmuc K, Łach K, Krawczyk-Marć I, Cebulski J (2020) Simultaneous FTIR and Raman Spectroscopy in Endometrial Atypical Hyperplasia and Cancer. Int J Mol Sci 21.: https://doi.org/10.3390/ijms21144828

24. Zhang J, Fan Y, He M, Ma X, Song Y, Liu M, Xu J (2017) Accuracy of Raman spectroscopy in differentiating brain tumor from normal brain tissue. Oncotarget 8:36824–36831. https://doi.org/10.18632/oncotarget.15975

25. Amharref N, Beljebbar A, Dukic S, Venteo L, Schneider L, Pluot M, Vistelle R, Manfait M (2006) Brain tissue characterisation by infrared imaging in a rat glioma model. Biochimica et Biophysica Acta (BBA) - Biomembranes 1758:892–899. https://doi.org/10.1016/j.bbamem.2006.05.003

26. Mehrotra R, Tyagi G, Jangir DK, Dawar R, Gupta N (2010) Analysis of ovarian tumor pathology by Fourier Transform Infrared Spectroscopy. J Ovarian Res 3:27. https://doi.org/10.1186/1757-2215-3-27

27. de Jong BWD, Bakker Schut TC, Maquelin K, van der Kwast T, Bangma CH, Kok D-J, Puppels GJ (2006) Discrimination between Nontumor Bladder Tissue and Tumor by Raman Spectroscopy. Anal Chem 78:7761–7769. https://doi.org/10.1021/ac061417b

28. Lyng FM, Traynor D, Nguyen TNQ, Meade AD, Rakib F, Al-Saady R, Goormaghtigh E, Al-Saad K, Ali MH (2019) Discrimination of breast cancer from benign tumours using Raman spectroscopy. PLoS One 14.: https://doi.org/10.1371/journal.pone.0212376

29. Wehbe K, Pineau R, Eimer S, Vital A, Loiseau H, Déléris G (2010) Differentiation between normal and tumor vasculature of animal and human glioma by FTIR imaging. Analyst 135:3052–3059. https://doi.org/10.1039/C0AN00513D

30. Finlayson D, Rinaldi C, Baker MJ (2019) Is Infrared Spectroscopy Ready for the Clinic? Analytical Chemistry 91:12117–12128. https://doi.org/10.1021/acs.analchem.9b02280

31. Kong K, Kendall C, Stone N, Notingher I (2015) Raman spectroscopy for medical diagnostics — From in-vitro biofluid assays to in-vivo cancer detection. Advanced Drug Delivery Reviews 89:121–134. https://doi.org/10.1016/j.addr.2015.03.009

32. Ampie L, Woolf EC, Dardis C (2015) Immunotherapeutic Advancements for Glioblastoma. Front Oncol 0.: https://doi.org/10.3389/fonc.2015.00012

33. Carlsson SK, Brothers SP, Wahlestedt C (2014) Emerging treatment strategies for glioblastoma multiforme. EMBO Mol Med 6:1359–1370. https://doi.org/10.15252/emmm.201302627

34. Lakhan SE, Harle L (2009) Difficult diagnosis of brainstem glioblastoma multiforme in a woman: a case report and review of the literature. J Med Case Reports 3:87. https://doi.org/10.1186/1752-1947-3-87

35. Levine S, McKeever P, Greenberg H (1987) Primary cerebellar glioblastoma multiforme. Journal of neuro-oncology 5:231–6. https://doi.org/10.1007/BF00151226

36. Barani IJ, Larson DA (2015) Radiation therapy of glioblastoma. Cancer Treat Res 163:49–73. https://doi.org/10.1007/978-3-319-12048-5_4

37. Kislin KL, McDonough WS, Eschbacher JM, Armstrong BA, Berens ME (2009) NHERF-1: modulator of glioblastoma cell migration and invasion. Neoplasia 11:377–387. https://doi.org/10.1593/neo.81572

38. Specenier P (2012) Bevacizumab in glioblastoma multiforme. Expert Rev Anticancer Ther 12:9–18. https://doi.org/10.1586/era.11.179

39. Planeta K, Setkowicz Z, Janik-Olchawa N, Matusiak K, Ryszawy D, Drozdz A, Janeczko K, Ostachowicz B, Chwiej J (2020) Comparison of Elemental Anomalies Following Implantation of Different Cell Lines of Glioblastoma Multiforme in the Rat Brain: A Total Reflection X-ray Fluorescence Spectroscopy Study. ACS Chem Neurosci 11:4447–4459. https://doi.org/10.1021/acschemneuro.0c00648

40. Planeta K, Setkowicz Z, Czyzycki M, Janik-Olchawa N, Ryszawy D, Janeczko K, Simon R, Baumbach T, Chwiej J (2022) Altered Elemental Distribution in Male Rat Brain Tissue as a Predictor of Glioblastoma Multiforme Growth—Studies Using SR-XRF Microscopy. International Journal of Molecular Sciences 23:703. https://doi.org/10.3390/ijms23020703

41. Jark W, Eichert D, Luehl L, Gambitta A (2014) Optimisation of a compact optical system for the beamtransport at the x-ray fluorescence beamline at Elettra for experiments with small spots. Proceedings Volume 9207, Advances in X-Ray/EUV Optics and Components IX; 92070G (2014) 92070G. https://doi.org/10.1117/12.2063009

42. Karydas AG, Czyzycki M, Leani JJ, Migliori A, Osan J, Bogovac M, Wrobel P, Vakula N, Padilla-Alvarez R, Menk RH, Gol MG, Antonelli M, Tiwari MK, Caliri C, Vogel-Mikuš K, Darby I, Kaiser RB (2018) An IAEA multi-technique X-ray spectrometry endstation at Elettra Sincrotrone Trieste: benchmarking results and interdisciplinary applications. Journal of Synchrotron Radiation 25:189–203. https://doi.org/10.1107/S1600577517016332

43. Wrobel PM, Bogovac M, Sghaier H, Leani JJ, Migliori A, Padilla-Alvarez R, Czyzycki M, Osan J, Kaiser RB, Karydas AG (2016) LabVIEW interface with Tango control system for a multi-technique X-ray spectrometry IAEA beamline end-station at Elettra Sincrotrone Trieste. Nuclear

Instruments and Methods in Physics Research Section A: Accelerators, Spectrometers, Detectors and Associated Equipment 833:105–109. https://doi.org/10.1016/j.nima.2016.07.030

44. Solé VA, Papillon E, Cotte M, Walter P, Susini J (2007) A multiplatform code for the analysis of energy-dispersive X-ray fluorescence spectra. Spectrochimica Acta Part B: Atomic Spectroscopy 62:63–68. https://doi.org/10.1016/j.sab.2006.12.002

45. Chwiej J, Dulinska J, Janeczko K, Dumas P, Eichert D, Dudala J, Setkowicz Z (2010) Synchrotron FTIR micro-spectroscopy study of the rat hippocampal formation after pilocarpine-evoked seizures. Journal of Chemical Neuroanatomy 40:140–147. https://doi.org/10.1016/j.jchemneu.2010.03.008

46. Szczerbowska-Boruchowska M, Dumas P, Kastyak MZ, Chwiej J, Lankosz M, Adamek D, Krygowska-Wajs A (2007) Biomolecular investigation of human substantia nigra in Parkinson's disease by synchrotron radiation Fourier transform infrared microspectroscopy. Arch Biochem Biophys 459:241–248. https://doi.org/10.1016/j.abb.2006.12.027

47. Petibois C, Deleris G (2006) Chemical mapping of tumor progression by FT-IR imaging: towards molecular histopathology. Trends in Biotechnology 24:455–462. https://doi.org/10.1016/j.tibtech.2006.08.005

48. Petibois C, Déléris G (2006) Chemical mapping of tumor progression by FT-IR imaging: towards molecular histopathology. Trends in Biotechnology 24:455–462. https://doi.org/10.1016/j.tibtech.2006.08.005

49. Kneipp J, Lasch P, Baldauf E, Beekes M, Naumann D (2000) Detection of pathological molecular alterations in scrapie-infected hamster brain by Fourier transform infrared (FT-IR) spectroscopy. Biochimica Et Biophysica Acta-Molecular Basis of Disease 1501:189–199. https://doi.org/10.1016/S0925-4439(00)00021-1

50. Kneipp J, Miller LM, Joncic M, Kittel M, Lasch P, Beekes M, Naumann D (2003) In situ identification of protein structural changes in prion-infected tissue. Biochimica Et Biophysica Acta-Molecular Basis of Disease 1639:152–158. https://doi.org/10.1016/j.bbadis.2003.08.005

51. Miller LM, Wang Q, Telivala TP, Smith RJ, Lanzirotti A, Miklossy J (2006) Synchrotron-based infrared and X-ray imaging shows focalized accumulation of Cu and Zn co-localized with beta-amyloid deposits in Alzheimer's disease. Journal of Structural Biology 155:30–37. https://doi.org/10.1016/jjsb.2005.09.004

52. Kretlow A, Wang Q, Kneipp J, Lasch P, Beekes M, Miller L, Naumann D (2006) FTIR-microspectroscopy of prion-infected nervous tissue. Biochimica Et Biophysica Acta-Biomembranes 1758:948–959. https://doi.org/10.1016/j.bbamem.2006.05.026

53. Diem M, Boydston-White S, Chiriboga L (1999) Infrared spectroscopy of cells and tissues: Shining light onto a novel subject. Applied Spectroscopy 53:148A–161A

54. Gautam R, Vanga S, Ariese F, Umapathy S (2015) Review of multidimensional data processing approaches for Raman and infrared spectroscopy. EPJ Techn Instrum 2:1–38. https://doi.org/10.1140/epjti/s40485-015-0018-6

55. Klamminger GG, Frauenknecht K, Mittelbronn M, Kleine Borgmann F (2022) From Research to Diagnostic Application of Raman Spectroscopy in Neurosciences: Past and Perspectives. 19. https://doi.org/10.17879/freeneuropathology-2022-4210

56. Depciuch J, Tołpa B, Witek P, Szmuc K, Kaznowska E, Osuchowski M, Król P, Cebulski J (2020) Raman and FTIR spectroscopy in determining the chemical changes in healthy brain

tissues and glioblastoma tumor tissues. Spectrochimica Acta Part A: Molecular and Biomolecular Spectroscopy 225:117526. https://doi.org/10.1016/j.saa.2019.117526

57. Bambery KR, Schültke E, Wood BR, Rigley MacDonald ST, Ataelmannan K, Griebel RW, Juurlink BHJ, McNaughton D (2006) A Fourier transform infrared microspectroscopic imaging investigation into an animal model exhibiting glioblastoma multiforme. Biochim Biophys Acta 1758:900–907. https://doi.org/10.1016/j.bbamem.2006.05.004

58. Balan V, Mihai C-T, Cojocaru F-D, Uritu C-M, Dodi G, Botezat D, Gardikiotis I (2019) Vibrational Spectroscopy Fingerprinting in Medicine: from Molecular to Clinical Practice. Materials 12:2884. https://doi.org/10.3390/ma12182884

59. Xu J, Guo Y, Ning W, Wang X, Li S, Chen Y, Ma L, Qu Y, Song Y, Zhang H (2021) Comprehensive Analyses of Glucose Metabolism in Glioma Reveal the Glioma-Promoting Effect of GALM. Front Cell Dev Biol 9:717182. https://doi.org/10.3389/fcell.2021.717182

60. Krafft C, Miljanić S, Sobottka S, Schackert G, Salzer R (2003) Near-infrared Raman spectroscopy to study the composition of human brain tissue and tumors. Proceedings of SPIE - The International Society for Optical Engineering. https://doi.org/10.1117/12.500469

61. Hay ED (1981) Extracellular matrix. J Cell Biol 91:205s–223s. https://doi.org/10.1083/jcb.91.3.205s

62. Kong D, Peng W, Zong R, Cui G, Yu X (2020) Morphological and Biochemical Properties of Human Astrocytes, Microglia, Glioma, and Glioblastoma Cells Using Fourier Transform Infrared Spectroscopy. Med Sci Monit 26:e925754. https://doi.org/10.12659/MSM.925754

63. Zhou Y, Liu C-H, Wu B, Yu X, Cheng G, Zhu K, Wang K, Zhang C, Zhao M, Zong R, Zhang L, Shi L, Alfano RR (2019) Optical biopsy identification and grading of gliomas using label-free visible resonance Raman spectroscopy. J Biomed Opt 24:1–12. https://doi.org/10.1117/1.JBO.24.9.095001

64. Jones LL, Yamaguchi Y, Stallcup WB, Tuszynski MH (2002) NG2 Is a Major Chondroitin Sulfate Proteoglycan Produced after Spinal Cord Injury and Is Expressed by Macrophages and Oligodendrocyte Progenitors. J Neurosci 22:2792–2803

65. Busch SA, Silver J (2007) The role of extracellular matrix in CNS regeneration. Current Opinion in Neurobiology 17:120–127. https://doi.org/10.1016/j.conb.2006.09.004

66. Yadavilli S, Hwang EI, Packer RJ, Nazarian J (2016) The Role of NG2 Proteoglycan in Glioma. Transl Oncol 9:57–63. https://doi.org/10.1016/j.tranon.2015.12.005

67. Tamburini E, Dallatomasina A, Quartararo J, Cortelazzi B, Mangieri D, Lazzaretti M, Perris R (2019) Structural deciphering of the NG2/CSPG4 proteoglycan multifunctionality. The FASEB Journal 33:3112–3128. https://doi.org/10.1096/fj.201801670R

68. Roemer SF, Scheithauer BW, Varnavas GG, Lucchinetti CF (2011) Tumefactive demyelination and glioblastoma: a rare collision lesion. Clin Neuropathol 30:186–191. https://doi.org/10.5414/np300201

69. Hayashi T, Kumabe T, Jokura H, Fujihara K, Shiga Y, Watanabe M, Higano S, Shirane R (2003) Inflammatory demyelinating disease mimicking malignant glioma. J Nucl Med 44:565–569

70. Toh CH, Wei K-C, Ng S-H, Wan Y-L, Castillo M, Lin C-P (2012) Differentiation of tumefactive demyelinating lesions from high-grade gliomas with the use of diffusion tensor imaging. AJNR Am J Neuroradiol 33:846–851. https://doi.org/10.3174/ajnr.A2871

71. Krafft C, Sobottka SB, Schackert G, Salzer R (2004) Analysis of human brain tissue, brain tumors and tumor cells by infrared spectroscopic mapping. Analyst 129:921–925. https://doi.org/10.1039/b408934k

72. Gajjar K, Heppenstall LD, Pang W, Ashton KM, Trevisan J, Patel II, Llabjani V, Stringfellow HF, Martin-Hirsch PL, Dawson T, Martin FL (2012) Diagnostic segregation of human brain tumours using Fourier-transform infrared and/or Raman spectroscopy coupled with discriminant analysis. Anal Methods 5:89–102. https://doi.org/10.1039/C2AY25544H

73. Wang J-S, Shi J-S, Xu Y-Z, Duan X-Y, Zhang L, Wang J, Yang L-M, Weng S-F, Wu J-G (2003) FT-IR spectroscopic analysis of normal and cancerous tissues of esophagus. World J Gastroenterol 9:1897–1899. https://doi.org/10.3748/wjg.v9.i9.1897

74. Campanella R (1992) Membrane lipids modifications in human gliomas of different degree of malignancy. J Neurosurg Sci 36:11–25

75. Dreissig I, Machill S, Salzer R, Krafft C (2009) Quantification of brain lipids by FTIR spectroscopy and partial least squares regression. Spectrochim Acta A Mol Biomol Spectrosc 71:2069–2075. https://doi.org/10.1016/j.saa.2008.08.008

76. Guo X, Zhou S, Yang Z, Li Z-A, Hu W, Dai L, Liang W, Wang X (2022) Cholesterol metabolism and its implication in glioblastoma therapy. J Cancer 13:1745–1757. https://doi.org/10.7150/jca.63609

77. Pinacho-Garcia LM, Valdez RA, Navarrete A, Cabeza M, Segovia J, Romano MC (2020) The effect of finasteride and dutasteride on the synthesis of neurosteroids by glioblastoma cells. Steroids 155:108556. https://doi.org/10.1016/j.steroids.2019.108556

78. Cairns RA, Harris IS, Mak TW (2011) Regulation of cancer cell metabolism. Nat Rev Cancer 11:85–95. https://doi.org/10.1038/nrc2981

79. Zhang J, Liu Q (2015) Cholesterol metabolism and homeostasis in the brain. Protein Cell 6:254–264. https://doi.org/10.1007/s13238-014-0131-3

80. Cameron IL, Smith NK, Pool TB, Sparks RL (1980) Intracellular concentration of sodium and other elements as related to mitogenesis and oncogenesis in vivo. Cancer Res 40:1493–1500

Declaration of interests

☒The authors declare that they have no known competing financial interests or personal relationships that could have appeared to influence the work reported in this paper.

☐The authors declare the following financial interests/personal relationships which may be considered as potential competing interests: